The Astrophysical Journal, 818:47 (69pp), 2016 February 10
doi:10.3847/0004-637X/818/1/47

THE SINFONI BLACK HOLE SURVEY: THE BLACK HOLE FUNDAMENTAL PLANE REVISITED AND THE PATHS OF (CO)EVOLUTION OF SUPERMASSIVE BLACK HOLES AND BULGES

R. P. Saglia[1,2], M. Opitsch[1,2,3], P. Erwin[1,2], J. Thomas[1,2], A. Beifiori[1,2], M. Fabricius[1,2], X. Mazzalay[1,2], N. Nowak[4], S. P. Rusli[1,2], and R. Bender[1,2]
[1] Max-Planck-Institut für extraterrestrische Physik, Giessenbachstrasse, D-85748 Garching, Germany
[2] Universitäts-Sternwarte München, Scheinerstrasse 1, D-81679 München, Germany
[3] Exzellenzcluster Universe, Boltzmannstr. 2, D-85748 Garching, Germany
[4] Stockholm University, Department of Astronomy, Oskar Klein Centre, AlbaNova, SE-10691 Stockholm, Sweden
Received 2015 May 28; accepted 2015 December 12; published 2016 February 8

ABSTRACT

We investigate the correlations between the black hole (BH) mass $M_{\rm BH}$, the velocity dispersion σ, the bulge mass $M_{\rm Bu}$, the bulge average spherical density $\rho_{\rm h}$, and its spherical half-mass radius $r_{\rm h}$, constructing a database of 97 galaxies (31 core ellipticals, 17 power-law ellipticals, 30 classical bulges, and 19 pseudobulges) by joining 72 galaxies from the literature to 25 galaxies observed during our recent SINFONI BH survey. For the first time we discuss the full error covariance matrix. We analyze the well-known $M_{\rm BH}$–σ and $M_{\rm BH}$–$M_{\rm Bu}$ relations and establish the existence of statistically significant correlations between $M_{\rm Bu}$ and $r_{\rm h}$ and anticorrelations between $M_{\rm Bu}$ and $\rho_{\rm h}$. We establish five significant bivariate correlations ($M_{\rm BH}$–σ–$\rho_{\rm h}$, $M_{\rm BH}$–σ–$r_{\rm h}$, $M_{\rm BH}$–$M_{\rm Bu}$–σ, $M_{\rm BH}$–$M_{\rm Bu}$–$\rho_{\rm h}$, $M_{\rm BH}$–$M_{\rm Bu}$–$r_{\rm h}$) that predict $M_{\rm BH}$ of 77 core and power-law ellipticals and classical bulges with measured and intrinsic scatter as small as ≈0.36 dex and ≈0.33 dex, respectively, or 0.26 dex when the subsample of 45 galaxies defined by Kormendy & Ho is considered. In contrast, pseudobulges have systematically lower $M_{\rm BH}$ but approach the predictions of all of the above relations at spherical densities $\rho_{\rm h} \geqslant 10^{10}\,M_\odot\,{\rm kpc}^{-3}$ or scale lengths $r_{\rm h} \leqslant 1$ kpc. These findings fit in a scenario of coevolution of BH and classical-bulge masses, where core ellipticals are the product of dry mergers of power-law bulges and power-law ellipticals and bulges the result of (early) gas-rich mergers and of disk galaxies. In contrast, the (secular) growth of BHs is decoupled from the growth of their pseudobulge hosts, except when (gas) densities are high enough to trigger the feedback mechanism responsible for the existence of the correlations between $M_{\rm BH}$ and galaxy structural parameters.

Key words: galaxies: bulges – galaxies: elliptical and lenticular, cD – galaxies: fundamental parameters – galaxies: spiral – quasars: supermassive black holes

1. INTRODUCTION

The last two decades have made clear that supermassive black holes (BHs) are ubiquitous at the centers of galaxies with bulges. The galaxy velocity dispersion σ (Ferrarese & Merritt 2000; Gebhardt et al. 2000; Gültekin et al. 2009b; McConnell et al. 2011; McConnell & Ma 2013), luminosity (Dressler 1989; Kormendy 1993; Kormendy & Richstone 1995; Kormendy & Gebhardt 2001; Marconi & Hunt 2003), bulge mass $M_{\rm Bu}$ (Magorrian et al. 1998; Häring & Rix 2004), and the mass of the BH $M_{\rm BH}$ are proportional with a scatter of a factor of 2, which implies that galaxy bulges and BHs somehow grew in lock step. Important clues concerning this interconnection are encoded in the steepness and intrinsic scatter of scaling laws like the $M_{\rm BH}$–σ and the $M_{\rm BH}$–$M_{\rm Bu}$ relations. Kormendy & Ho (2013, and references therein) rederive the global correlations with BH mass and review the interpretation framework of these findings. When BHs accrete mass, they shine as quasars or active galactic nuclei (AGNs), and this activity interferes with the star formation that contributes to bulge growth. Gas can make it to the central region of a galaxy, where a BH might sit, when nonaxisymmetric distortions or temporal variations of the gravitational potential are strong enough. This can happen through secular evolution of a disk, possibly related to the formation and dissolution of bars, which also leads to the build-up of a pseudobulge. These pseudobulges structurally resemble disks, for example in their flattening and rotational support. Mergers are another channel to funnel material toward the central region of a galaxy. Mergers produce classical bulges and elliptical galaxies. Different regimes of the $M_{\rm BH}$–σ and $M_{\rm BH}$–$M_{\rm Bu}$ scaling relations isolate different stages and modes of BH or bulge growth (Kormendy et al. 2011; Mathur et al. 2012; Kormendy & Ho 2013). At the low-mass end, galaxies are disk dominated (possibly with pseudobulges), mergers are unimportant, and those few scaling relations that do exist mostly probe secular evolution processes in disks. At the high-mass end, gas-poor mergers dominate and drive the formation of core ellipticals, where the most massive BHs live. Here, the averaging effect of a succession of major mergers is expected to reduce the fractional dispersion of the $M_{\rm BH}$–$M_{\rm Bu}$ relation (Peng 2007). Core ellipticals have stellar densities mildly increasing toward the center (Faber et al. 1997; Kormendy et al. 2009), a result of binary BH scouring (Ebisuzaki et al. 1991; Milosavljević & Merritt 2001) that also leaves a dynamic imprint on the stellar orbits (Thomas et al. 2014) and generates a tight correlation between core radius and BH mass (Kormendy & Bender 2009; Kormendy et al. 2009; Rusli et al. 2013a). Core ellipticals are also slow rotators and mildly triaxial (Nieto & Bender 1989; Kormendy & Bender 1996; Faber et al. 1997; Emsellem et al. 2007; Lauer 2012), a further clue to their dry merger origin. In between the two extremes, early, gas-rich, dissipational mergers of disk galaxies are responsible for the formation of classical bulges and power-law ellipticals and the lock-step accretion on the central BHs mirrored in the $M_{\rm BH}$–σ and $M_{\rm BH}$–$M_{\rm Bu}$ relations (King 2003; Hopkins et al. 2007a, 2007b). Power-law ellipticals have stellar densities steeply increasing toward the center, a result of star formation in the high-density central gas concentration originating during a gas-rich merger (Faber et al. 1997; Kormendy et al. 2009). They are axisymmetric and fast rotators (Nieto et al. 1991; Faber et al. 1997; Emsellem et al. 2007), reminiscent of the structure and dynamics of disk galaxies (Bender 1988; Kormendy & Bender 1996).

Here we reconsider this scenario by discussing the relationship between the residuals from the $M_{\rm BH}$–σ and $M_{\rm BH}$–$M_{\rm Bu}$ relations and the average spherical stellar-mass density (or scale length) of the classical or pseudobulges and pay particular attention to the families of galaxies discussed above, core and power-law ellipticals, classical and pseudobulges, and the possible presence of bars. Attempts to detect a "second parameter" or "BH fundamental plane" (BH FP)[5] are numerous and contradictory. Feoli & Mele (2005) ask whether the black hole masses correlate with the kinetic energy of elliptical galaxies. Aller & Richstone (2007) claim based on a sample of ~20 galaxies that the BH masses best correlate with $E_g^{0.6}$, where $E_g \sim M_{\rm Bu}^2/r_{\rm h}$ is the bulge gravitational binding energy. With $M_{\rm Bu} \sim r_{\rm h}\sigma^2$ and $\rho \sim M_{\rm Bu}/r_{\rm h}^3$ this implies $M_{\rm BH} \sim \rho^{0.2} M_{\rm Bu} \sim r_{\rm h}^{-0.6} M_{\rm Bu}^{1.2} \sim M_{\rm Bu}^{0.6}\sigma^{1.2} \sim \rho^{-0.3}\sigma^3 \sim r_{\rm h}^{0.6}\sigma^{2.4}$, where ρ is the mean density of the bulge and $r_{\rm h}$ its scale length. A further empirical study of the BH FP is given by Barway & Kembhavi (2007).

Hopkins et al. (2007a, 2007b) investigate the BH FP with the help of hydrodynamical simulations, finding that the empirical relations $M_{\rm BH} \sim \sigma^{3.0\pm0.3} R_e^{0.43\pm0.19}$ and $M_{\rm BH} \sim M_{\rm Bu}^{0.54\pm0.17}\sigma^{2.2\pm0.5}$ can be explained theoretically by noting that the BH mass should scale as $M_{\rm Bu}^{0.5}\sigma^2$. Graham (2008) reports that the BH FP is possibly driven by the barred galaxies in the sample. Nevertheless, Graham et al. (2001) and more recently Savorgnan et al. (2013) argue for a strong correlation between BH mass and galaxy concentration. Feoli & Mancini (2009) and Mancini & Feoli (2012) investigate the relation between BH mass and kinetic energy of the bulge $M_{\rm BH} \sim M_{\rm Bu}\sigma^2$, discussing the existence of a main-sequence-like diagram. Soker & Meiron (2011) propose that the BH masses should correlate with $M_{\rm Bu}\sigma$. In contrast, Sani et al. (2011) fail to detect bivariate correlations. Beifiori et al. (2012) find only weak evidence for bivariate correlations by analyzing 49 galaxies from Gültekin et al. (2009b) and a large sample of galaxies with upper limits to BH masses from Beifiori et al. (2009). Finally, Graham & Scott (2013) claim that "Sérsic galaxies" follow a quadratic more than a linear $M_{\rm BH}$–$M_{\rm Bu}$ relation. We will see that to settle the issue it is important to consider a large database with dynamically measured BH masses and accurate bulge plus disk decompositions, and to distinguish between the different families of objects (core and power-law ellipticals, classical bulges and pseudobulges, barred objects), which to some extent obey different residual correlations.

The structure of the paper is as follows. In Section 2 we describe the data sample and the methods used to measure the bulge average densities. In Section 3 we discuss the error matrix, exploring the covariances between the parameters. In Section 4 we discuss the method adopted to investigate multivariate correlations between our parameters. In Section 5 we present the results of our correlation analysis. In Section 6 we investigate which of the quantities $M_{\rm Bu}^{0.5}\sigma^2$, $M_{\rm Bu}\sigma^2$, and $M_{\rm Bu}\sigma$ best correlate with BH masses and discuss the implications for the coevolution of bulges and BHs. In Section 7 we draw our conclusions. Four appendices discuss how we measure effective velocity dispersions (Appendix A), how we determine the luminosity profiles and the mass-to-light ratios (hereafter M/Ls) of bulges (Appendix B), and how we compute simple Jeans M/L values for some of our galaxies (Appendix C). Appendix D lists correlation results for a restricted sample of galaxies.

2. THE DATA SAMPLE

2.1. Distances, BH Masses, and Velocity Dispersions

Our sample includes galaxies from Gültekin et al. (2009b), Sani et al. (2011), McConnell et al. (2011), McConnell & Ma (2013), and Kormendy & Ho (2013). We tested various combinations of these data sets, obtaining compatible results. Here, we start with the database (morphological type, distances, BH masses, velocity dispersions, and their errors) of Kormendy & Ho (2013), without those galaxies belonging to our SINFONI BH survey (see below). We supplement this list with eight galaxies (NGC 2974, NGC 3079, NGC 3414, NGC 4151, NGC 4552, NGC 4621, NGC 5813, NGC 5846) that are quoted by Sani et al. (2011). References to the original sources can be found in these two papers. We estimate the errors on distances from the NASA Extragalactic Database (NED); they amount typically to 9%. We compute symmetrized logarithmic errors for BH masses and velocity dispersions.

We do not consider three galaxies with upper limits on their black hole masses (namely NGC 2778, NGC 4382, IC 2560). Furthermore, we exclude the following objects. Cygnus A has an uncertain BH mass and velocity dispersion (Kormendy & Ho 2013); moreover, the strong internal dust absorption prevents the derivation of a reliable photometric profile. IC 1481 is undergoing a merger, which makes the derivation of a reliable photometric profile difficult. The determination of the extremely large BH mass of NGC 1277 (van den Bosch et al. 2012) has been questioned by Emsellem (2013). For NGC 4945, the "binding mass of $\sim 10^6\,M_\odot$ within 0.3 pc" quoted in the abstract and the conclusions of Greenhill et al. (1997) come from maser measurements that point to a non-Keplerian rotation.

We complement these measurements with the 25 determinations from our SINFONI BH survey; nine of these values are currently unpublished. They are all based on the stellar dynamical analysis of our SINFONI kinematics, coupled with extended long-slit or integral field stellar kinematics of the outer regions of the galaxies. A detailed description of the SINFONI data set, the methods, and some specific cases can be found in Nowak et al. (2007, 2008, 2010), Rusli et al. (2011, 2013b), Mazzalay et al. (2015), J. Thomas et al. (2016, in preparation), P. Erwin et al. (2016, in preparation), and R. Bender et al. (2016, in preparation). In summary, our SINFONI BH sample consists of 30 galaxies that we observed with Spectrograph for INtegral Field Observations in the Near Infrared (SINFONI; Eisenhauer et al. 2003; Bonnet et al. 2003) at the UT4 of the Very Large Telescope under nearly diffraction-limited conditions. The sample was selected to explore poorly populated regions of the $M_{\rm BH}$–σ and $M_{\rm BH}$–$M_{\rm Bu}$ correlations, with particular attention to high-velocity-dispersion early-type galaxies, low-velocity-dispersion and pseudobulge galaxies, and mergers and galaxies with low-luminosity AGNs. Through our Schwarzschild axisymmetric

---

[5] This is different from the FP of BH activity discovered by Merloni et al. (2003).

code (Thomas et al. 2004, 2005), we determine the best-fitting BH mass $M_{\rm BH}$ (and the M/L of the stellar component(s)), taking into account the bulge and disk components of the galaxies separately when necessary. The appropriate dark matter potential is also considered when necessary (Rusli et al. 2013b). We summarize in Figure 36 the resulting M/L and $M_{\rm BH}$ for the nine galaxies that will be discussed in the papers in preparation quoted above; see also Appendix B.

Distances for the SINFONI sample are directly measured (from Cepheids or surface-brightness fluctuations) or computed from the redshifts using the standard cosmology ($\Omega = 0.3$, $\Lambda = 0.7$, $H_0 = 70$). We determine the σ for our SINFONI galaxies using the long-slit and integral field stellar kinematics used in the modeling (see Appendix A).

2.2. Bulge Masses, Sizes, and Densities

For all galaxies except the Milky Way, we compute bulge masses, half-light radii, and densities from the photometry of the galaxies, decomposed into a bulge and further components (a disk, a bar, a ring) when necessary. For some galaxies we find evidence for composite (classical plus pseudo) bulges (Erwin et al. 2015): in these cases we consider the classical component of the two. We note that some other disk galaxies identified as having pseudobulges may prove to have composite bulges as well, but the necessary data for a proper assessment are currently lacking for many. We use the dynamically determined M/L values taken from the literature or our own modeling to convert light into mass. For the Milky Way we use the axisymmetric bulge density profile of McMillan (2011), which we integrate spherically to get $M_{\rm MW}(<r)$. A detailed description of the methods and procedures is given in Appendices B and C; here we give a short summary only.

We measure surface-brightness profiles from images taken from the *Spitzer* archive or Sloan Digital Sky Survey (SDSS) (York et al. 2000) and the ESO Key Program described in Scorza et al. (1998), or we take them from the literature. Bulge–disk decompositions, when necessary, are taken from Fisher & Drory (2008), Gadotti (2008), Sani et al. (2011), Beifiori et al. (2012), and Vika et al. (2012) or are performed by us (in 16 cases) using the program of Erwin (2015) or the procedures of Fisher & Drory (2008). The *M/L*s come from different types of dynamical modeling, which can be based on spherical distribution functions (Kronawitter et al. 2000), Schwarzschild modeling (Schulze & Gebhardt 2011), Jeans equations (Häring & Rix 2004), or gas dynamics (Dalla Bontà et al. 2009). If none of this is available, they are computed by matching the stellar kinetic energy profiles $\sqrt{v^2(R) + \sigma^2(R)}$ or the central velocity dispersion through spherical Jeans equations (see Appendix B). When not already done by the authors, we correct the M/L for galactic extinction (GE) following Schlegel et al. (1998), and we transform them to the band of the available surface-brightness profiles using the galaxy colors from the Hyperleda database (Paturel et al. 2003). We adopt this approach to test whether dynamically determined M/Ls can deliver bulge masses and densities that better correlate (i.e., with smaller scatter) with BH masses. Kormendy & Ho (2013) consider M/L determinations from colors, deriving a $M_{\rm BH}$–$M_{\rm Bu}$ relation with impressively small scatter (0.29 dex). In principle, stellar population M/L determinations could be uncertain because they depend on the proper choice of the stellar initial mass function (Thomas et al. 2011; Cappellari et al. 2013) and internal dust corrections; see the discussion in Rusli et al. (2013a). We investigate this issue using the bulge masses quoted by Kormendy & Ho (2013) for the 45 galaxies used in their fits (see below).

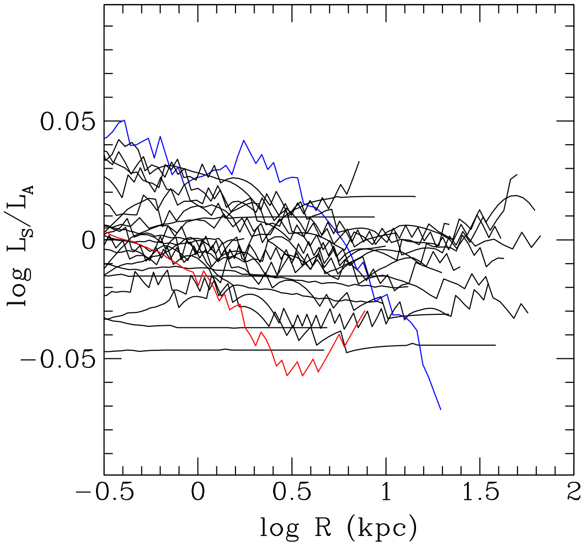

Figure 1. Comparison between the spherical luminosity profiles derived using Equations (1) and (2) for the SINFONI galaxies. The red (NGC 4486a) and blue (NGC 4751) lines show the most deviant profiles.

We circularize the bulge photometry and deproject it assuming spherical symmetry to derive the spherical luminosity density $l_{\rm S}(r)$. We then compute the spherical luminosity:

$$L_{\rm S}(<r) = \int_0^r 4\pi r^2 l_{\rm S}(r) dr. \quad (1)$$

For the SINFONI sample of galaxies we have also performed an axisymmetric deprojection of the (decomposed bulge and disk) surface-brightness profiles and derived the axisymmetric luminosity density $l_A(r, \theta, i)$, where r and θ are spherical coordinates and i the assumed inclination angle. We spherically integrate l_A to get a second estimate of the spherical luminosity L_A:

$$L_A(<r) = \int_{{\rm Sphere}(r)} l_A dV. \quad (2)$$

Figure 1 compares the spherical luminosity profiles derived using Equations (1) and (2). The luminosities $L_{\rm S}$ and L_A are similar within 0.05 dex, with typical deviations less than 0.02 dex. The most deviant profiles are for flattened galaxies seen nearly edge-on.

The spherical mass profile of the bulge is $M(<r) = L(<r) \times M/L$, where the M/L is determined dynamically. We discuss in Appendix B on a case-by-case basis the applied transformations necessary to homogenize the photometry used and M/L.

We extend $M(<r)$ to large radii using a spline extrapolation of the surface brightness, adding a further point to the measured profile at very large radii (typically several tens to hundreds of arcseconds depending on the size of the bulges) and with a surface brightness of 70 mag arcsec^{-2}. This generates a deprojected density decreasing as r^{-3} at large radii; see Figure 4. Then we get the bulge mass as

$$M_{\rm Bu} = M(<\infty) = M(<r_{\rm max}) + M_{\rm extrap}, \quad (3)$$

where $r_{\rm max}$ is the distance of the last measured surface-brightness point, and $M_{\rm extrap}$ is the light contribution due to the extrapolation to the last computed deprojected density point. We define the half-light radius $r_{\rm h}$ of the bulge component as the radius where $M(<r_{\rm h}) = M_{\rm Bu}/2$. The bulge's averaged density within $r_{\rm h}$ is

$$\rho_{\rm h} = \frac{M_{\rm Bu}/2}{4\pi r_{\rm h}^3/3}. \qquad (4)$$

Figure 4 shows that the bulge masses (to the precision given in Table 1) are reached at approximately $20\,r_{\rm h}$, where we effectively cut the density profiles to not have to worry about the logarithmic divergence of the mass profile implied by the r^{-3} behavior of our extrapolation.

In addition, for all galaxies except the Milky Way we compute the projected circularized half-luminosity radius R_e of the bulge from the curve of growth of the projection along the line of sight of the luminosity density profile. Examples of the procedure are given in Figure 2 discussed below. We get $R_e/r_{\rm h} = 0.74$ on average, with rms = 0.01.

Figure 2 shows four examples of our surface-brightness profiles to clarify the role of extrapolation in the determination of R_e and $r_{\rm h}$. For these galaxies, our derived R_e values differ by more than 0.3 dex from the r_e values quoted by Rusli et al. (2013a), Table 2, from a core-Sérsic fit (see comments in Appendix B). By construction, our procedure reproduces the observed profile perfectly. This is not always true, when, for example, Sérsic or core-Sérsic fits are used to derive scale radii, as done in Rusli et al. (2013a). We quantify the amount of extrapolation involved in our analysis in Section 2.3.

We compute spherically averaged densities for all classes of objects in our sample in order to have a homogeneous data set. But is it physically meaningful to consider spherical half-mass radii and spherically averaged densities also for pseudobulges? Our current understanding (Erwin et al. 2015, and references therein) is that these structures are more similar to disks than spheroids. Therefore, for these objects (except the Milky Way) we also estimate cylindrical average densities:

$$\rho_{{\rm h},c} = \frac{M_{\rm Bu}/2}{\pi a_e^2 h_z}, \qquad (5)$$

where $a_e = R_e(a/b)^{1/2}$ is the projected half-luminosity radius along the major axis (the proper scale length of an inclined disk), a/b the major to minor axis ratio of the bulge (taken from the decompositions described in Appendix B), and h_z an estimate of the thickness. We consider the case of (1) a fixed thickness of $h_z = 0.2$ kpc or (2) a thickness $h_z = 0.2a_e/1.67$, which is 20% of the exponential scale length of the disk $h = a_e/1.67$. Figure 3 shows the results. On average, the scale lengths do not change much ($\langle \log a_e/r_{\rm h}\rangle = -0.016$) because the a/b dependency compensates for the $R_e/r_{\rm h}$ ratio. However, the cylindrical densities are one order of magnitude larger ($\langle \log \rho_{{\rm h},c}/\rho_{\rm h}\rangle = 1.31$ for $h_z = 0.2a_e/1.67$).

Table 1 lists the galaxy names (column 1), the galaxy type (column 2), a series of flags (columns 3 to 8; see description in the footnote of the table), the distance used (column 9), and the logarithms of the measured values of the parameters $M_{\rm BH}$ (in $M_\odot$), σ (in km s^{-1}), $M_{\rm Bu}$ (in $M_\odot$), $\rho_{\rm h}$ (in $M_\odot$ kpc^{-3}), and $r_{\rm h}$ (in kpc) with their errors in columns 10 to 14 (see also Section 3), plus the values of R_e (in arcsec) in column 15. Table 2 lists the cylindrical average quantities for pseudobulges, with galaxy names (column 1), the logarithms of a_e (in kpc), and $\rho_{c,h}$ (in $M_\odot$ kpc^{-3}, computed with $h_z = 0.2a_e/1.67$). As discussed above, we also consider the bulge masses quoted by Kormendy & Ho (2013) for the 45 galaxies used in their fits, hereafter KH45. They are given in Table 3, coupled to our sizes $r_{\rm h}$ to derive color-based density estimates. This procedure is uncertain since we do not know how the bulge plus disk decompositions of Kormendy & Ho (2013) were performed. In detail, Table 3 gives the names of the galaxies of the KH45 sample (column 1), the bulge masses (column 2, computed from luminosities using M/L_C derived from colors), and the spherical bulge densities (column 4) computed using the $r_{\rm h}$ of Table 1. The logarithmic errors (column 3 and 5) are computed as described in Section 3.

2.3. Errors on r_h, ρ_h, and M_{Bu}

We now turn to the errors affecting the quantities $r_{\rm h}$, $\rho_{\rm h}$, and $M_{\rm Bu}$. Errors on the distance affect all of them, as do the errors coming from the extrapolation to compute total luminosities. Errors on $M_{\rm Bu}$ and $\rho_{\rm h}$ have a further component that is due to the M/L factor (see Section 3). We estimate the fractional error on the bulge mass due to extrapolation as $\delta M_{\rm Bu}/M_{\rm Bu} = M_{\rm extrap}/M_{\rm Bu}$. It is on average 9%. We then determine the logarithmic derivates $a_{rM} = d\log r/d\log M$, $a_{\rho M} = d\log\rho/d\log M$, and $a_{\rho r} = d\log\rho/d\log r$ at $r = r_{\rm h}$ by a least-squares fit in a region ± 0.1 dex around the mass point $\log M_{\rm Bu}/2$. The logarithmic errors on $M_{\rm Bu}$, $r_{\rm h}$, and $\rho_{\rm h}$ due to extrapolation are then $d\log M_{\rm Bu} = \delta M_{\rm Bu}/M_{\rm Bu} \times \log e$, $d\log r_{\rm h} = a_{rM}\, d\log M_{\rm Bu}$, and $d\log\rho_{\rm h} = a_{\rho M}\, d\log M_{\rm Bu}$. Figure 4 shows the bulge density and mass profiles of our galaxy sample. Figure 5 shows the histograms of the values of the parameters a_{rM}, $a_{\rho M}$, and $a_{\rho r}$. Their values can be derived from Table 1 using the equations given in Table 4 (see Section 3 for a full description of this table). On average, we have $\rho \sim r^{-2.3}$ near $r \sim r_{\rm h}$, which implies $M \sim r^{3-2.3} = r^{0.7}$, or $r \sim M^{1.5}$ and $\rho \sim M^{-2.3\times 1.5} = M^{-3.5}$. Therefore, the logarithmic errors on $r_{\rm h}$ due to the extrapolation are on average 1.5 times larger than the ones on $M_{\rm Bu}$, while the logarithmic errors on $\rho_{\rm h}$ are 3.5 times larger.

2.4. External Comparisons

In Figure 6 we compare our bulge masses to the ones reported by McConnell & Ma (2013), Kormendy & Ho (2013) (where we exclude pseudobulges with classical components), Rusli et al. (2013b) (where we show only galaxies fitted by one component), and Erwin et al. (2015). They compare reasonably well, with an rms scatter of ≈0.2 dex and estimated error bars of 0.1 dex. The most deviant point in the comparison with McConnell & Ma (2013) is NGC 3245. The difference stems from their large assumed bulge-to-total ratio (B/T) (0.76). The Kormendy & Ho (2013) points deviating more strongly are pseudobulges, in particular NGC 4388 and NGC 6323 and the classical bulge of NGC 4526; see discussion in Appendix B. The fits discussed in Section 5 and presented in Tables 13 and 14 show that using the bulge masses of Kormendy & Ho (2013), which are derived using M/L from colors, does not change our conclusions. The differences with the masses of Rusli et al. (2013a) are within the estimated errors due to the extrapolation. The four most deviant galaxies are discussed in detail in Figure 2. Some of the masses of Erwin et al. (2015)

Table 1

Galaxy Sample with the Values of the Measured Parameters

Galaxy	Type	S	T	m	b	B	M	D (Mpc)	$\log M_{\rm BH}$ ($M_\odot$)	$\log \sigma$ (km s^{-1})	$\log M_{\rm Bu}$ ($M_\odot$)	$\log \rho_{\rm h}$ ($M_\odot$ kpc^{-3})	$\log r_{\rm h}$ (kpc)	R_e ($''$)
MW	Sbc	0	3	0	1	1	0	0.008 ± 0.001	6.633 ± 0.048	2.021 ± 0.084	10.375 ± 0.069	9.283 ± 0.111	0.056 ± 0.052	⋯
Circinus	SABb:	0	3	0	1	1	2	2.820 ± 0.470	6.057 ± 0.105	1.898 ± 0.017	9.170 ± 0.089	10.611 ± 0.153	−0.788 ± 0.072	8.9
A 1836	BCGE	0	0	0	0	0	4	152.400 ± 8.426	9.573 ± 0.061	2.459 ± 0.021	12.026 ± 0.135	7.392 ± 0.187	1.237 ± 0.060	17.2
IC 1459	E4	0	0	0	0	0	2	28.920 ± 3.739	9.394 ± 0.079	2.520 ± 0.007	11.401 ± 0.076	8.800 ± 0.153	0.559 ± 0.069	18.6
IC 4296	BCGE	0	0	0	0	0	1	49.200 ± 3.628	9.114 ± 0.073	2.508 ± 0.022	12.026 ± 0.110	6.995 ± 0.355	1.369 ± 0.146	68.1
NGC 0221	E2	0	1	0	0	0	2	0.805 ± 0.030	6.389 ± 0.193	1.886 ± 0.017	8.627 ± 0.022	10.546 ± 0.042	−0.947 ± 0.019	21.2
NGC 0224	Sb	0	2	0	1	1	2	0.774 ± 0.032	8.155 ± 0.161	2.228 ± 0.021	10.445 ± 0.021	9.558 ± 0.038	−0.012 ± 0.018	192.9
NGC 0524	S0	0	2	0	0	0	1	24.220 ± 2.234	8.938 ± 0.053	2.393 ± 0.021	11.630 ± 0.073	8.108 ± 0.156	0.867 ± 0.066	47.1
NGC 0821	S0	0	1	0	0	0	1	23.440 ± 1.837	8.217 ± 0.210	2.320 ± 0.021	11.111 ± 0.108	7.994 ± 0.382	0.731 ± 0.158	34.8
NGC 1023	SB0	0	2	0	1	1	1	10.810 ± 0.797	7.616 ± 0.055	2.312 ± 0.021	10.423 ± 0.032	10.339 ± 0.064	−0.280 ± 0.032	7.5
NGC 1068	Sb	0	3	0	1	2	2	15.900 ± 9.411	6.924 ± 0.245	2.179 ± 0.020	9.254 ± 0.300	12.288 ± 0.519	−1.319 ± 0.244	0.5
NGC 1194	S0/	0	2	0	0	1	3	57.980 ± 6.299	7.850 ± 0.051	2.170 ± 0.071	10.929 ± 0.205	8.333 ± 0.222	0.558 ± 0.048	9.5
NGC 1300	SBbc	0	3	0	1	1	4	21.500 ± 9.384	7.878 ± 0.343	1.944 ± 0.015	9.730 ± 0.184	9.464 ± 0.368	−0.219 ± 0.184	4
NGC 1399	E1	0	0	0	0	0	1	20.850 ± 0.672	8.945 ± 0.306	2.498 ± 0.004	11.789 ± 0.021	7.353 ± 0.059	1.171 ± 0.025	103.7
NGC 2273	SBa	0	3	0	1	1	3	29.500 ± 1.903	6.935 ± 0.036	2.097 ± 0.031	9.875 ± 0.145	10.635 ± 0.153	−0.561 ± 0.028	1.5
NGC 2549	S0/	0	2	0	0.5	1	1	12.700 ± 1.642	7.161 ± 0.367	2.161 ± 0.021	10.250 ± 0.087	9.747 ± 0.237	−0.140 ± 0.101	8.6
NGC 2748	Sc	0	3	0	0.5	1	2	23.400 ± 8.244	7.647 ± 0.240	2.061 ± 0.019	9.582 ± 0.156	9.456 ± 0.303	−0.266 ± 0.150	3.6
NGC 2787	SB0/a	0	3	0	1	1	2	7.450 ± 1.241	7.610 ± 0.088	2.276 ± 0.021	9.733 ± 0.076	11.131 ± 0.154	−0.774 ± 0.076	3.5
NGC 2960	E2	0	3	1	0	1	3	67.100 ± 7.120	7.033 ± 0.049	2.220 ± 0.042	10.470 ± 0.126	9.845 ± 0.149	−0.099 ± 0.046	1.8
NGC 2974	E4	0	1	0	0	0	1	21.500 ± 2.381	8.230 ± 0.091	2.356 ± 0.021	11.140 ± 0.058	8.732 ± 0.133	0.493 ± 0.060	21.6
NGC 3031	Sb	0	2	0	1	1	2	3.604 ± 0.133	7.813 ± 0.129	2.155 ± 0.021	10.424 ± 0.065	9.535 ± 0.156	−0.011 ± 0.066	41.4
NGC 3079	SBcd	0	3	0	1	1	2	15.900 ± 1.246	6.398 ± 0.049	2.164 ± 0.021	9.898 ± 0.057	10.690 ± 0.082	−0.572 ± 0.034	2.6
NGC 3115	S0/	0	2	0	0.5	1	2	9.540 ± 0.396	8.953 ± 0.095	2.362 ± 0.021	11.072 ± 0.110	8.865 ± 0.389	0.428 ± 0.163	42.2
NGC 3227	SBa	0	3	0	1	1	1	23.750 ± 2.630	7.322 ± 0.232	2.124 ± 0.039	9.754 ± 0.067	9.776 ± 0.129	−0.315 ± 0.057	3.1
NGC 3245	S0	0	2	0	0	1	2	21.380 ± 1.972	8.378 ± 0.114	2.312 ± 0.021	10.288 ± 0.061	10.350 ± 0.094	−0.329 ± 0.042	3.5
NGC 3377	E5	0	1	0	0	0	1	10.990 ± 0.456	8.250 ± 0.253	2.161 ± 0.021	10.460 ± 0.083	8.172 ± 0.332	0.455 ± 0.132	39.1
NGC 3379	E1	0	0	0	0	0	1	10.700 ± 0.542	8.619 ± 0.113	2.314 ± 0.021	10.940 ± 0.045	8.522 ± 0.113	0.498 ± 0.047	45.2
NGC 3384	SB0	0	3	0	1	1	1	11.490 ± 0.741	7.033 ± 0.214	2.164 ± 0.021	10.080 ± 0.039	9.895 ± 0.076	−0.246 ± 0.035	7.6
NGC 3393	SABa	0	3	0	1	1	3	49.200 ± 8.194	7.196 ± 0.330	2.170 ± 0.029	10.263 ± 0.111	9.959 ± 0.167	−0.206 ± 0.072	2
NGC 3414	S0pec	0	2	0	1	1	1	25.200 ± 2.738	8.400 ± 0.071	2.312 ± 0.021	11.100 ± 0.081	8.409 ± 0.239	0.589 ± 0.098	23.3
NGC 3585	S0	0	2	0	0	1	1	20.510 ± 1.702	8.517 ± 0.127	2.328 ± 0.022	10.948 ± 0.176	8.307 ± 0.491	0.573 ± 0.219	27.4
NGC 3607	E1	0	0	0	0	0	1	22.650 ± 1.775	8.137 ± 0.157	2.360 ± 0.021	11.521 ± 0.074	8.110 ± 0.224	0.829 ± 0.092	45
NGC 3608	E1	0	0	0	0	0	1	22.750 ± 1.468	8.667 ± 0.098	2.260 ± 0.021	10.909 ± 0.092	7.589 ± 0.397	0.799 ± 0.158	42.7
NGC 3842	E1	0	0	0	0	0	1	92.200 ± 10.638	9.959 ± 0.139	2.431 ± 0.044	12.022 ± 0.152	7.085 ± 0.597	1.338 ± 0.242	35.3
NGC 3998	S0	0	2	0	1	1	4	14.300 ± 1.253	8.927 ± 0.052	2.439 ± 0.011	10.580 ± 0.277	10.595 ± 0.287	−0.313 ± 0.042	5.2
NGC 4026	S0	0	2	0	0.5	1	1	13.350 ± 1.726	8.255 ± 0.123	2.255 ± 0.022	10.358 ± 0.080	9.840 ± 0.142	−0.135 ± 0.064	8.4
NGC 4151	Sa	0	2	0	1	1	1	20.000 ± 2.772	7.813 ± 0.076	2.193 ± 0.022	9.988 ± 0.075	9.729 ± 0.128	−0.221 ± 0.060	4.6
NGC 4258	SABbc	0	2	0	1	1	1	7.270 ± 0.503	7.577 ± 0.030	2.061 ± 0.038	9.790 ± 0.034	9.471 ± 0.062	−0.201 ± 0.030	13.3
NGC 4261	E2	0	0	0	0	0	2	32.360 ± 2.835	8.723 ± 0.097	2.498 ± 0.021	11.887 ± 0.131	7.775 ± 0.502	1.063 ± 0.205	54.2
NGC 4291	E2	0	0	0	0	0	1	26.580 ± 3.931	8.990 ± 0.155	2.384 ± 0.022	10.950 ± 0.105	8.993 ± 0.241	0.345 ± 0.102	12.5
NGC 4342	S0	0	2	0	0.5	1	1	22.910 ± 1.372	8.656 ± 0.188	2.352 ± 0.021	10.358 ± 0.072	9.818 ± 0.231	−0.128 ± 0.090	4.9
NGC 4374	E1	0	0	0	0	0	1	18.510 ± 0.597	8.966 ± 0.046	2.471 ± 0.021	11.740 ± 0.052	7.750 ± 0.209	1.022 ± 0.084	84
NGC 4388	SBbc	0	3	0	1	1	3	16.530 ± 1.601	6.864 ± 0.043	1.996 ± 0.044	10.422 ± 0.102	8.552 ± 0.171	0.316 ± 0.067	19.2
NGC 4459	E2	0	1	0	0	0	1	16.010 ± 0.516	7.843 ± 0.086	2.223 ± 0.021	10.880 ± 0.041	8.254 ± 0.115	0.568 ± 0.048	35.2
NGC 4473	E5	0	1	0	0	0	1	15.250 ± 0.492	7.954 ± 0.239	2.279 ± 0.021	11.131 ± 0.071	8.538 ± 0.283	0.557 ± 0.111	35.7
NGC 4486	E1	0	0	0	0	0	1	16.680 ± 0.615	9.789 ± 0.031	2.511 ± 0.027	11.869 ± 0.071	7.222 ± 0.249	1.241 ± 0.095	158.4
NGC 4526	S0/	0	2	0	1	1	4	16.440 ± 1.786	8.654 ± 0.124	2.346 ± 0.022	10.120 ± 0.058	9.660 ± 0.100	−0.154 ± 0.047	6.5
NGC 4552	E	0	0	0	0	0	1	15.300 ± 0.987	8.699 ± 0.051	2.401 ± 0.021	11.420 ± 0.107	7.714 ± 0.604	0.928 ± 0.232	82.6
NGC 4564	S0	0	2	0	0	1	2	15.940 ± 0.514	7.945 ± 0.124	2.210 ± 0.021	10.671 ± 0.069	9.126 ± 0.177	0.207 ± 0.074	15.3
NGC 4594	Sa	0	2	0	0.5	1	1	9.870 ± 0.819	8.823 ± 0.045	2.380 ± 0.022	11.704 ± 0.037	7.975 ± 0.080	0.936 ± 0.039	133.6
NGC 4596	SB0	0	2	0	1	1	2	16.530 ± 6.229	7.885 ± 0.260	2.134 ± 0.019	10.423 ± 0.166	9.170 ± 0.333	0.110 ± 0.164	11.9
NGC 4621	E5	0	1	0	0	0	1	18.300 ± 2.962	8.602 ± 0.085	2.352 ± 0.021	11.120 ± 0.119	8.272 ± 0.401	0.643 ± 0.167	36.7
NGC 4649	E2	0	0	0	0	0	1	16.460 ± 0.607	9.674 ± 0.099	2.580 ± 0.022	11.849 ± 0.093	7.827 ± 0.373	1.033 ± 0.150	99.5
NGC 4697	E5	0	1	0	0	0	1	12.540 ± 0.404	8.305 ± 0.112	2.248 ± 0.020	11.021 ± 0.056	7.889 ± 0.179	0.736 ± 0.072	65.8

Table 1

(Continued)

Galaxy	Type	S	T	m	b	B	M	D (Mpc)	$\log M_{\rm BH}\,(M_\odot)$	$\log \sigma$ (km s^{-1})	$\log M_{\rm Bu}\,(M_\odot)$	$\log \rho_{\rm h}\,(M_\odot$ kpc$^{-3})$	$\log r_{\rm h}$ (kpc)	$R_e\,('')$
NGC 4736	Sab	0	3	0	1	1	2	5.000 ± 0.786	6.831 ± 0.123	2.079 ± 0.022	9.482 ± 0.081	10.373 ± 0.143	−0.605 ± 0.068	7.7
NGC 4826	Sab	0	3	0	0	1	2	7.270 ± 1.177	6.193 ± 0.131	2.017 ± 0.013	10.038 ± 0.087	8.597 ± 0.153	0.173 ± 0.072	31.3
NGC 4889	E4	0	0	0	0	0	1	102.000 ± 5.169	10.320 ± 0.437	2.540 ± 0.006	12.305 ± 0.102	6.861 ± 0.307	1.507 ± 0.123	47.1
NGC 5077	E3	0	0	0	0	0	4	38.700 ± 8.442	8.932 ± 0.268	2.346 ± 0.022	11.055 ± 0.114	8.453 ± 0.212	0.560 ± 0.099	14
NGC 5128	E	0	0	1	0	0	1	3.620 ± 0.200	7.755 ± 0.084	2.176 ± 0.020	10.636 ± 0.107	8.930 ± 0.129	0.261 ± 0.040	76.9
NGC 5576	E3	0	1	0	0	0	1	25.680 ± 1.657	8.436 ± 0.126	2.262 ± 0.021	11.060 ± 0.073	8.178 ± 0.171	0.653 ± 0.065	26.1
NGC 5813	E1-2	0	0	0	0	0	1	32.200 ± 2.672	8.851 ± 0.058	2.362 ± 0.021	11.770 ± 0.089	7.981 ± 0.220	0.954 ± 0.096	42.4
NGC 5845	E3	0	1	0	0	0	1	25.870 ± 4.067	8.688 ± 0.157	2.378 ± 0.020	10.459 ± 0.101	10.213 ± 0.205	−0.226 ± 0.096	3.6
NGC 5846	E0-1	0	0	0	0	0	1	24.900 ± 2.297	9.041 ± 0.058	2.375 ± 0.022	11.620 ± 0.156	7.196 ± 0.691	1.168 ± 0.281	89.4
NGC 6086	E	0	0	0	0	0	1	138.000 ± 11.452	9.573 ± 0.167	2.502 ± 0.003	11.227 ± 0.075	8.397 ± 0.102	0.636 ± 0.038	4.8
NGC 6251	E1	0	0	0	0	0	2	108.400 ± 8.996	8.788 ± 0.155	2.462 ± 0.021	11.970 ± 0.092	7.810 ± 0.270	1.079 ± 0.110	16.5
NGC 6264	SBb	0	3	0	1	1	3	147.600 ± 16.035	7.489 ± 0.047	2.199 ± 0.041	10.497 ± 0.099	8.805 ± 0.128	0.256 ± 0.047	1.9
NGC 6323	SBab	0	3	0	1	1	3	113.400 ± 12.320	7.004 ± 0.048	2.199 ± 0.072	10.691 ± 0.147	7.990 ± 0.176	0.593 ± 0.053	5.3
NGC 7052	E3	0	0	0	0	0	2	70.400 ± 8.449	8.598 ± 0.230	2.425 ± 0.021	11.357 ± 0.110	7.700 ± 0.270	0.911 ± 0.118	17.4
NGC 7457	S0	0	2	0	0	1	2	12.530 ± 1.214	6.954 ± 0.302	1.826 ± 0.019	9.518 ± 0.062	9.037 ± 0.097	−0.148 ± 0.043	8.7
NGC 7582	SBab	0	3	0	1	1	3	22.300 ± 9.845	7.741 ± 0.205	2.193 ± 0.053	9.480 ± 0.217	10.058 ± 0.388	−0.500 ± 0.186	2.2
NGC 7768	E4	0	0	0	0	0	1	116.000 ± 27.495	9.127 ± 0.181	2.410 ± 0.044	11.982 ± 0.190	6.970 ± 0.615	1.363 ± 0.255	30
UGC 3789	SABab	0	3	0	1	1	3	49.900 ± 5.421	6.985 ± 0.085	2.029 ± 0.049	10.053 ± 0.105	9.513 ± 0.133	−0.128 ± 0.047	2.3
NGC 0307	S0	1	2	0	0.5	1	1	52.800 ± 5.736	8.602 ± 0.060	2.310 ± 0.007	10.510 ± 0.050	10.120 ± 0.096	−0.178 ± 0.047	1.9
NGC 1316	SAB0	1	2	1	0	0	1	18.600 ± 0.600	8.176 ± 0.254	2.363 ± 0.004	11.150 ± 0.262	8.883 ± 0.684	0.447 ± 0.314	65.2
NGC 1332	S0	1	2	0	0	1	1	22.300 ± 1.851	9.161 ± 0.076	2.467 ± 0.010	11.000 ± 0.048	10.000 ± 0.079	0.025 ± 0.036	7.3
NGC 1374	E3	1	1	0	0	0	1	19.230 ± 0.655	8.763 ± 0.062	2.225 ± 0.009	10.700 ± 0.073	8.377 ± 0.199	0.466 ± 0.082	23.1
NGC 1398	SBab	1	2	0	1	1	1	24.770 ± 4.125	8.033 ± 0.083	2.369 ± 0.007	10.160 ± 0.074	10.200 ± 0.145	−0.322 ± 0.072	3
NGC 1407	E0	1	0	0	0	0	1	28.050 ± 3.367	9.653 ± 0.079	2.442 ± 0.003	11.740 ± 0.157	7.418 ± 0.469	1.134 ± 0.204	71.8
NGC 1550	SA0	1	0	0	0	0	1	51.570 ± 5.603	9.568 ± 0.067	2.436 ± 0.016	11.700 ± 0.108	7.918 ± 0.337	0.954 ± 0.137	26.2
NGC 3091	E3	1	0	0	0	0	1	51.250 ± 8.296	9.556 ± 0.072	2.477 ± 0.017	11.630 ± 0.106	8.044 ± 0.300	0.889 ± 0.130	22.4
NGC 3368	SABab	1	3	0	1	2	1	10.400 ± 0.959	6.875 ± 0.076	2.122 ± 0.003	8.483 ± 0.068	11.350 ± 0.097	−1.264 ± 0.040	0.8
NGC 3489	SAB0	1	3	0	1	2	1	12.100 ± 0.837	6.778 ± 0.051	1.949 ± 0.002	8.725 ± 0.036	10.830 ± 0.063	−1.009 ± 0.030	1.2
NGC 3627	SAB(s)b	1	3	0	1	1	1	10.050 ± 1.092	6.929 ± 0.048	2.088 ± 0.002	9.050 ± 0.048	11.020 ± 0.095	−0.967 ± 0.047	1.7
NGC 3923	E4	1	1	1	0	0	1	20.880 ± 2.700	9.449 ± 0.115	2.347 ± 0.020	11.560 ± 0.093	7.435 ± 0.245	1.069 ± 0.103	85.3
NGC 4371	SB0$\hat{+}$(r)	1	3	0	1	2	1	16.900 ± 1.481	6.845 ± 0.074	2.154 ± 0.005	9.901 ± 0.040	9.344 ± 0.078	−0.122 ± 0.038	6.9
NGC 4472	E2	1	0	0	0	0	1	17.140 ± 0.592	9.398 ± 0.037	2.482 ± 0.011	11.910 ± 0.069	7.137 ± 0.263	1.282 ± 0.106	168.3
NGC 4486a	E2	1	1	0	0	0	1	16.000 ± 0.516	7.100 ± 0.147	2.160 ± 0.006	10.280 ± 0.082	9.750 ± 0.281	−0.131 ± 0.119	7.2
NGC 4486b	cE0	1	1	0	0	0	1	16.550 ± 0.610	8.602 ± 0.024	2.172 ± 0.026	9.847 ± 0.027	10.700 ± 0.043	−0.593 ± 0.018	2.3
NGC 4501	SA(rs)b	1	3	0	0	1	1	16.500 ± 1.141	7.301 ± 0.080	2.197 ± 0.008	9.909 ± 0.038	9.798 ± 0.064	−0.271 ± 0.030	5
NGC 4699	SABb	1	3	0	1	2	1	18.900 ± 2.053	8.246 ± 0.052	2.258 ± 0.010	9.816 ± 0.057	10.770 ± 0.099	−0.627 ± 0.047	1.9
NGC 4751	E	1	1	0	0.5	0	1	26.920 ± 2.925	9.146 ± 0.056	2.558 ± 0.016	11.070 ± 0.087	8.566 ± 0.256	0.526 ± 0.109	18.9
NGC 5018	E3	1	1	1	0	0	1	40.550 ± 4.867	8.021 ± 0.078	2.321 ± 0.007	11.120 ± 0.063	8.222 ± 0.175	0.659 ± 0.077	17
NGC 5328	E	1	0	0	0	0	1	64.100 ± 6.964	9.672 ± 0.158	2.523 ± 0.002	11.750 ± 0.195	7.519 ± 0.997	1.101 ± 0.393	29.4
NGC 5419	E	1	0	0	0	0	1	56.200 ± 6.106	9.860 ± 0.144	2.565 ± 0.011	12.010 ± 0.151	7.170 ± 0.275	1.306 ± 0.103	53.8
NGC 5516	E	1	0	0	0	0	1	58.440 ± 6.349	9.519 ± 0.058	2.522 ± 0.015	11.790 ± 0.069	7.546 ± 0.214	1.107 ± 0.093	32.6
NGC 6861	E	1	1	0	0	0	1	27.300 ± 4.547	9.301 ± 0.084	2.590 ± 0.003	11.540 ± 0.116	8.918 ± 0.554	0.565 ± 0.220	20.5
NGC 7619	E	1	0	0	0	0	1	51.520 ± 7.380	9.398 ± 0.108	2.469 ± 0.007	11.780 ± 0.136	7.379 ± 0.493	1.159 ± 0.204	42.1

Note. Column 1: galaxy name; column 2: galaxy type; column 3: flag *S*; $S = 0$ flag identifies galaxies from the literature, $S = 1$ identifies galaxies belonging to the SINFONI sample. Column 4: flag *T*; $T = 0$ for core ellipticals, 1 for power-law ellipticals, 2 for classical bulges, 3 for pseudobulges. Column 5: flag *m*; $m = 1$ identifies merger remnants. Column 6: flag *b*; $b = 1$ identifies barred galaxies, $b = 0.5$ if a bar cannot be excluded because the galaxy is edge-on. Here we follow the strategy of classifying a galaxy as barred even when discrepant opinions are present; see comments in Appendix B. Column 7: flag *B*; $B = 0$ identifies galaxies where $M_{\rm Bu}$ comes from the measured photometric profile, $B = 1$ identifies galaxies where $M_{\rm Bu}$ is computed after a bulge plus disk decomposition, $B = 2$ identifies composite galaxies where both a classical and a pseudobulge are present. In these cases $M_{\rm Bu}$ is the mass of the classical bulge component. Column 8: flag *M*, $M = 0$ indicates the special case of the Milky Way (see text), $M = 1$ indicates that the M/L was computed from the distribution function or Schwarzschild modeling, $M = 2$ from Jeans modeling of stellar kinematics profiles, $M = 3$ from Jeans modeling of central stellar velocity dispersions, $M = 4$ from gas dynamics. See Appendix B for comments on single galaxies. Column 9: distance and its error. Column 10: black hole mass and its error. Column 11: velocity dispersion and its error. Column 12: bulge mass and its error. Column 13: bulge spherical average density and its error. Column 14: bulge spherical half-mass radius and its error. Column 15: bulge cylindrical half-mass radius.

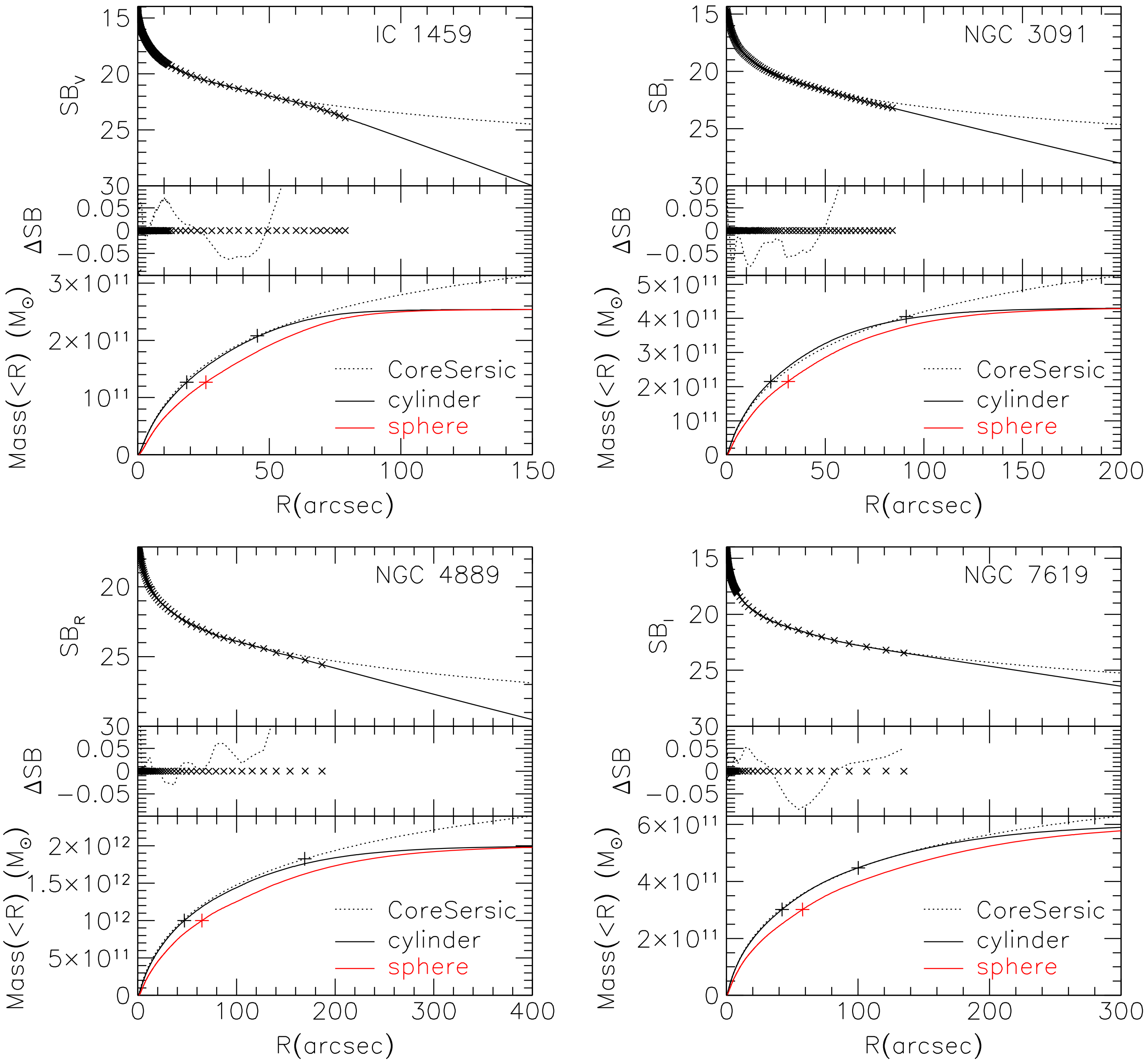

Figure 2. For each of the core ellipticals IC 1459, NGC 3091, NGC 4889, and NGC 7619 we present three plots. The plots at the top show the observed circularized surface-brightness profiles (crosses), together with the projection along the light of sight of the luminosity density we derived (solid line). The dotted lines show the best-fitting core-Sérsic profile of Rusli et al. (2013a). The plots in the middle show the differences in surface brightness between the data and the projected luminosity density profiles (crosses) and the core-Sérsic fits (dotted lines) of Rusli et al. (2013a). The plots at the bottom show three lines: our spherical (solid red lines) and cylindrical (solid black lines) mass profiles and the (cylindrical) mass profile implied by the core-Sérsic fits of Rusli et al. (2013a). The three crosses show the positions of $r_{\rm h}$ and R_e listed in Table 1 and r_e from Table 2 of Rusli et al. (2013a).

come from the sample of Laurikainen et al. (2011), who did not publish distances; the latter were provided to us by E. Laurikainen (2015, private communication). For five galaxies, Erwin et al. (2015) quote (bulge) masses a factor of 10 smaller than what we get. The differences originate mainly from the amount of extrapolation (see below). In addition, Erwin et al. (2015) derive stellar masses based on M/L from colors.

Figure 7, upper left, shows the comparison between our bulge masses and the ones reported by Scott et al. (2013). The latter are not based on proper bulge plus disk decompositions, but are instead derived from total $K_{\rm S}$-band magnitudes by applying a statistical bulge-to-disk correction that depends on morphological type. In addition, their conversion of light into mass involves (dust-corrected) M/L values derived from $(B-K)$ colors. The overall scatter in Figure 7 (0.36 dex) matches the total uncertainty quoted by Scott et al. (2013). For galaxies where we measure $\log M_{\rm Bu} < 10.8$ the agreement is fair (the average difference is 0.05 dex). However, at larger masses, Scott et al. (2013) derive values 0.34 dex smaller. This and the missing distinction between classical and pseudobulges drive the steepening of the $M_{\rm BH}$–$M_{\rm Bu}$ relation at small bulge masses of "Sérsic galaxies" noticed by Graham & Scott (2013).

Figure 7, upper right, shows the comparison between our bulge masses and the ones reported by the ATLAS3D collaboration (Cappellari et al. 2013) for the galaxies where we do not apply a decomposition. Cappellari et al. (2013) do not attempt any extrapolation; this probably explains most of the measured average shift of −0.11 dex. The measured scatter matches our error estimates. Similar conclusions are reached

Table 2
Cylindrical Parameters of the Pseudobulges

Galaxy	$\log a_e$ (kpc)	$\log \rho_{h,c}$ ($M_\odot$ kpc^{-3})
Circinus	−0.8313	11.95
IC 2560	−0.06558	10.81
NGC 1300	−0.3074	10.87
NGC 2273	−0.5796	11.93
NGC 2748	−0.3778	10.86
NGC 2960	−0.1376	11.19
NGC 3079	−0.3559	11.77
NGC 3227	−0.3287	11.1
NGC 3384	0.02405	10.92
NGC 3393	−0.3002	11.33
NGC 4388	0.3326	9.84
NGC 4736	−0.6902	11.75
NGC 4826	0.09586	9.985
NGC 6264	0.183	10.17
NGC 6323	0.4727	9.418
NGC 7582	−0.5045	11.35
UGC 3789	−0.2014	10.87
NGC 3627	−0.9195	12.27
NGC 4501	−0.2367	11.07

Note. Column 1: galaxy name. Column 2: bulge cylindrical major axis half-mass radius. Column 3: bulge cylindrical average density.

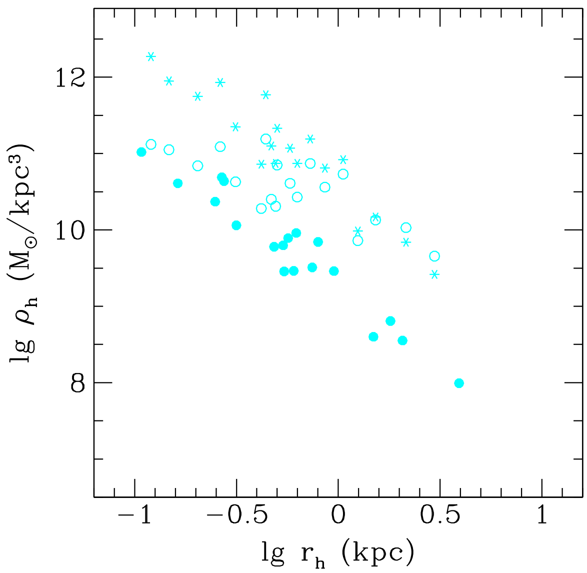

Figure 3. Cylindrical averaged scale lengths and densities of pseudobulges, assuming vertical scale height $h_z = 0.2$ kpc (open circles) or $h_z/h = 0.2$ (stars); see Equation (5), cases (1) and (2), respectively. The filled points show the spherical average quantities.

when we compare the half-mass radii (Figure 7, bottom left). Finally and for completeness, Figure 7, bottom right, shows the comparison between the velocity dispersions used here and the σ_e values reported by Cappellari et al. (2013). The ATLAS3D are systematically smaller by ≈10%; the scatter is a bit larger than the errors.

Figure 8 compares our bulge circularized half-luminosity radii R_e to literature values from Laurikainen et al. (2010), Sani et al. (2011), Beifiori et al. (2012), Vika et al. (2012), Rusli et al. (2013b), and Läsker et al. (2014). We use the fitted bulge axis ratios (b/a) tabulated by Sani et al. (2011) to transform their major-axis bulge half-luminosity radii a_e into $R_e = a_e \times (b/a)^{0.5}$. Laurikainen et al. (2010), Vika et al. (2012), and Läsker et al. (2014) did not publish their fitted b/a values, so we adopt the axis ratios $(b/a)_{25}$ given by Hyperleda and compute $R_e = a_e \times (b/a)_{25}^{0.5}$. The observed spread is larger than our estimated errors, with several galaxies where our bulge R_e differs by more than 0.3 dex from the literature values. We discuss these objects in Appendix B, where we justify our choices. Some discrepancies stem from differences in the photometric band and the assumed ellipticity. Often the differences in R_e correlate with the fitted value of $n_{\rm Ser}$: they are small when $n_{\rm Ser} \approx 3 - 5$, which matches approximately our assumed extrapolation. Our R_e are larger than the literature values when $n_{\rm Ser} \leqslant 3$ and smaller when $n_{\rm Ser} \geqslant 5$. However, the major contributors are the fitting procedures adopted.

If we perform the same check for the 16 galaxies discussed in Appendix B, Tables 20–33, where we perform multi-component fits, we find that the R_e we give in Table 1 (that are derived from the curve of growth of the spherical densities projected along the line of sight) agree with the ones from the fits to within 9%.

3. THE ERROR MATRIX

In Section 2 we described the data sample. For each galaxy we collected the distance D, the central BH mass $M_{\rm BH}$, the average velocity dispersion σ, the bulge mass $M_{\rm Bu}$ and M/L, the bulge half-light radius $r_{\rm h}$, and the bulge average density $\rho_{\rm h}$ within $r_{\rm h}$. We also computed errors on each quantity. We now discuss how we estimated the total error covariances on the decimal logarithms of the parameters σ, $M_{\rm BH}$, $M_{\rm Bu}$, $r_{\rm h}$, and $\rho_{\rm h}$. All BH correlation analyses performed in the past have ignored covariances, although some are obvious (e.g., BH and bulge masses scale with the distance). Here we attempt to quantify them systematically to assess their importance (or lack thereof). This is not always possible in a rigorous way: some error correlations are hidden in the modeling procedure (e.g., the anticorrelation between *M/L* and BH mass) and cannot be reconstructed from the published material; what follows is sometimes simply our best guess. Tables 4 and 5 summarize our results for the two cases where the bulge masses are computed from *M/L*s derived dynamically or from colors. In the first case we have the following:

1. Since dynamically determined M/L ratios scale as the square of velocities, we consider an additional error term on $(\delta \log M/L)^2$ of $4f\,(\delta \log \sigma)^2$ when we see that the quoted error on M/L given in Table 34 is too small given the kinematics available. Here f is a fudge factor that can be either 0 or 1 and is listed in Table 4. Therefore we use an effective error $(\delta M/L)_{\rm eff}$, where we add in quadrature the two error contributions.
2. The total error on the BH mass $\log M_{\rm BH}$ comes from the fitting procedure and the error on the distance discussed in Section 2. We add both terms in quadrature. Depending on the type of data and their spatial resolution, the errors on $M_{\rm BH}$ and on the M/L can be anticorrelated (Rusli et al. 2013b): $\delta \log M_{\rm BH}^{\rm fit} = a_{\rm BH}\,\delta \log M/L$ with $a_{\rm BH} \leqslant 0$. This dependency is important when computing the covariances $\delta \log M_{\rm BH}\,\delta \log \sigma$ and $\delta \log M_{\rm BH}\,\delta \log \rho_{\rm h}$. We list the adopted values of $a_{\rm BH}$ (which can be 0, −1, or −2) in Table 4: black hole masses not coming from stellar dynamical data (e.g., maser or gas dynamics measurements) must have $a_{\rm BH} = 0$. The values

Table 3
Bulge Masses and Densities of Kormendy & Ho (2013)

Galaxy	$\log M_{\mathrm{Bu},C}\,(M_\odot)$	$\delta\log M_{\mathrm{Bu},C}\,(M_\odot)$	$\log\rho_{\mathrm{h},C}\,(M_\odot\ \mathrm{kpc}^{-3})$	$\log\rho_{\mathrm{h},C}\,(M_\odot\ \mathrm{kpc}^{-3})$
IC 1459	11.6	0.1459	8.999	0.142
NGC 0221	9.05	0.1053	10.97	0.1041
NGC 0224	10.35	0.09694	9.462	0.09182
NGC 0524	11.26	0.1247	7.737	0.1585
NGC 0821	10.98	0.144	7.864	0.3854
NGC 1023	10.53	0.1105	10.45	0.09558
NGC 1194	10.64	0.1305	8.044	0.1046
NGC 1399	11.5	0.09493	7.064	0.1045
NGC 2549	9.71	0.1518	9.207	0.2301
NGC 3115	10.92	0.1394	8.713	0.3955
NGC 3245	10.69	0.1209	10.75	0.1012
NGC 3377	10.5	0.1177	8.212	0.3394
NGC 3379	10.91	0.1032	8.492	0.1362
NGC 3585	11.26	0.2011	8.619	0.4923
NGC 3608	11.01	0.1313	7.69	0.4016
NGC 3998	10.67	0.1187	10.68	0.1064
NGC 4026	10.33	0.1453	9.812	0.127
NGC 4258	9.86	0.1082	9.54	0.09493
NGC 4291	10.85	0.1627	8.893	0.2214
NGC 4374	11.62	0.1033	7.63	0.2246
NGC 4473	10.85	0.1078	8.256	0.2925
NGC 4486	11.72	0.104	7.072	0.2571
NGC 4526	11.02	0.1303	10.56	0.1017
NGC 4564	10.38	0.1059	8.835	0.1915
NGC 4594	11.47	0.1156	7.74	0.1031
NGC 4649	11.64	0.1235	7.618	0.3796
NGC 4697	10.97	0.1018	7.838	0.1947
NGC 5077	11.28	0.2094	8.677	0.1506
NGC 5576	11	0.1096	8.119	0.1767
NGC 5845	10.57	0.1733	10.32	0.1849
NGC 6086	11.69	0.1155	8.86	0.1013
NGC 7457	9.56	0.1232	9.08	0.1009
NGC 7768	11.75	0.2579	6.737	0.5879
NGC 1332	11.26	0.1152	10.26	0.09697
NGC 1374	10.63	0.1078	8.313	0.2112
NGC 1407	11.71	0.194	7.386	0.4655
NGC 1550	11.31	0.1476	7.528	0.3321
NGC 3031	10.42	0.1065	9.531	0.1725
NGC 3091	11.58	0.1789	7.99	0.2851
NGC 4486a	9.92	0.1207	9.39	0.2922
NGC 4472	11.86	0.1107	7.092	0.2741
NGC 4751	10.99	0.1439	8.486	0.256
NGC 5516	11.65	0.1387	7.404	0.2169
NGC 6861	11.21	0.1925	8.587	0.5468
NGC 7619	11.61	0.1879	7.211	0.487

Note. Column 1: galaxy name; columns 2 and 3: bulge masses from Kormendy & Ho (2013) derived from colors with our error estimates; columns 4 and 5: bulge densities derived from colors using the r_{h} of Table 1 and errors.

$a_{\mathrm{BH}} = -1$ or -2 come from typical χ^2 contour plots as a function of $\log M_{\mathrm{BH}}$ and $\log M/L$ (see Nowak et al. 2010; Rusli et al. 2011, 2013b). In Figure 9 we show the case of NGC 3923, for which we assign $a_{\mathrm{BH}} = -1$.

3. The total error on the bulge mass $\log M_{\mathrm{Bu}}$ comes from the residual extrapolation of Equation (3), the error on the distance discussed above, and the error on the mass-to-light ratio. We add the three terms in quadrature. The external comparisons performed in the previous section show that this error estimate is probably too small. Therefore we also consider solutions where we add 0.15 dex in quadrature to $\delta\log M_{\mathrm{Bu}}$.
4. The total error on the half-luminosity radius r_{h} comes from the extrapolation in Equation (3) and the error on the distance. We add both terms in quadrature, weighting the mass extrapolation term with the correlation coefficient a_{rM}^2.
5. The total error on the average density ρ_{h} within the half-luminosity radius comes from the extrapolation in Equation (3), the error(s) on M/L (see above), and the error on the distance. We add the four terms in quadrature, weighting the mass extrapolation term with the correlation coefficient $a_{\rho M}^2$ and the distance error by a factor of 2^2 (since $\rho \sim M/r^3 \sim D^{-2}$). Following the reasoning applied to $\delta\log M_{\mathrm{Bu}}$, we also consider solutions where we add 0.15 dex in quadrature to $\delta\log\rho_{\mathrm{h}}$.

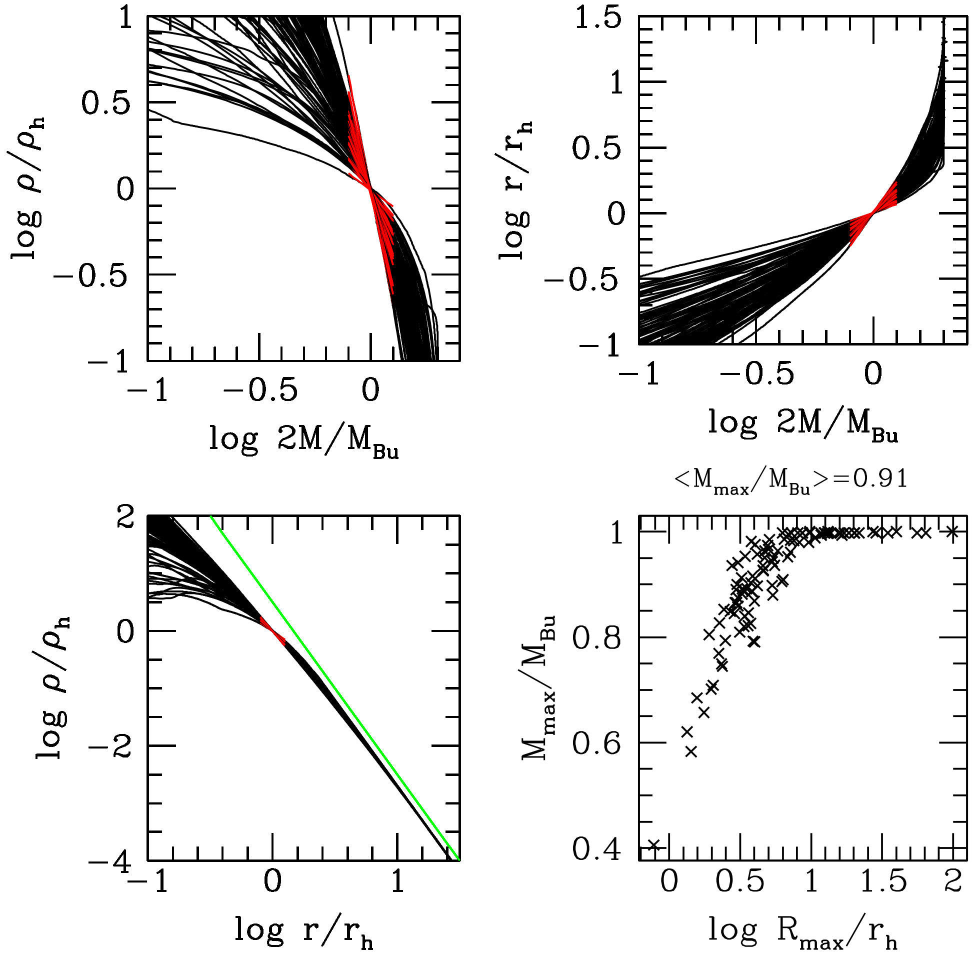

Figure 4. Bulge density and mass profiles of our galaxy sample. The red lines show the region where the logarithmic derivatives $a_{\rho M}$ (top left), a_{rM} (top right), and $a_{\rho r}$ (bottom left) are fitted. The green line shows $\rho \propto r^{-3}$. Bottom right: the correlation between the radial extent of the profile in units of r_h and the fractional bulge mass sampled. On average, our profiles probe ≈91% of the bulge mass.

6. The errors on $M_{\rm BH}$ and σ can be correlated through the M/L term, which scales as the square of velocity (see above).
7. The errors on $M_{\rm BH}$ and $M_{\rm Bu}$ are correlated through the distance and possibly anticorrelated through the M/L term (since $a_{\rm BH}$ is negative).
8. The errors on $M_{\rm BH}$ and $r_{\rm h}$ are correlated through the distance.
9. The errors on $M_{\rm BH}$ and $\rho_{\rm h}$ are anticorrelated through the distance and possibly through the M/L term.
10. The errors on $M_{\rm Bu}$ and σ are correlated through the M/L term; see above.
11. The errors on $M_{\rm Bu}$ and $r_{\rm h}$ are correlated through the mass extrapolation term and the distance.
12. Errors on $M_{\rm Bu}$ and $\rho_{\rm h}$ are correlated through the mass extrapolation and the M/L terms and anticorrelated through the distance. Moreover, when we consider solutions where we add 0.15 dex in quadrature to $\delta \log M_{\rm Bu}$ and $\delta \log \rho$, we augment the covariance element $\delta \log M_{\rm Bu} \delta \log \rho_{\rm h}$ by the same amount in quadrature.
13. Errors on $\log r_{\rm h}$ and $\log \rho_{\rm h}$ are correlated through the mass extrapolation term and anticorrelated through the distance.
14. Errors on $\log \rho_{\rm h}$ and $\log \sigma$ are correlated through the M/L term.

For some galaxies the BH mass is determined independently from the bulge M/L, for example from maser or gas rotation curves. In this case $a_{\rm BH} = 0$. For some galaxies setting $a_{\rm BH} = -2$ and $f = 1$ produces covariance matrices with negative determinants. In these cases we increase $a_{\rm BH}$ to -1 or 0, or we set $f = 0$. Table 4 reports the values of the terms averaged over the sample. The most poorly determined parameter is $\rho_{\rm h}$, followed by $M_{\rm BH}$. On average, the off-diagonal terms of the covariance matrix are smaller than the diagonal terms; therefore ignoring them, as done in the past, is not a bad approximation.

Tables 1 and 6 list the values of each term for each galaxy of the sample.

In the case of *M/L*s derived from colors, we get the following:

1. We assume that the error on the $\log M/L_C$ from colors is equal to the error on bulge masses quoted by Kormendy & Ho (2013).
2. The total error on the BH mass $\log M_{\rm BH}$ is unchanged and is as described above.
3. The total error squared on the bulge mass $\log M_{{\rm Bu},C}$ has an increased dependence on the distance error that now goes as $4(\delta \log D)^2$. This is because the *M/L* derived from colors is distance-independent, and therefore bulge

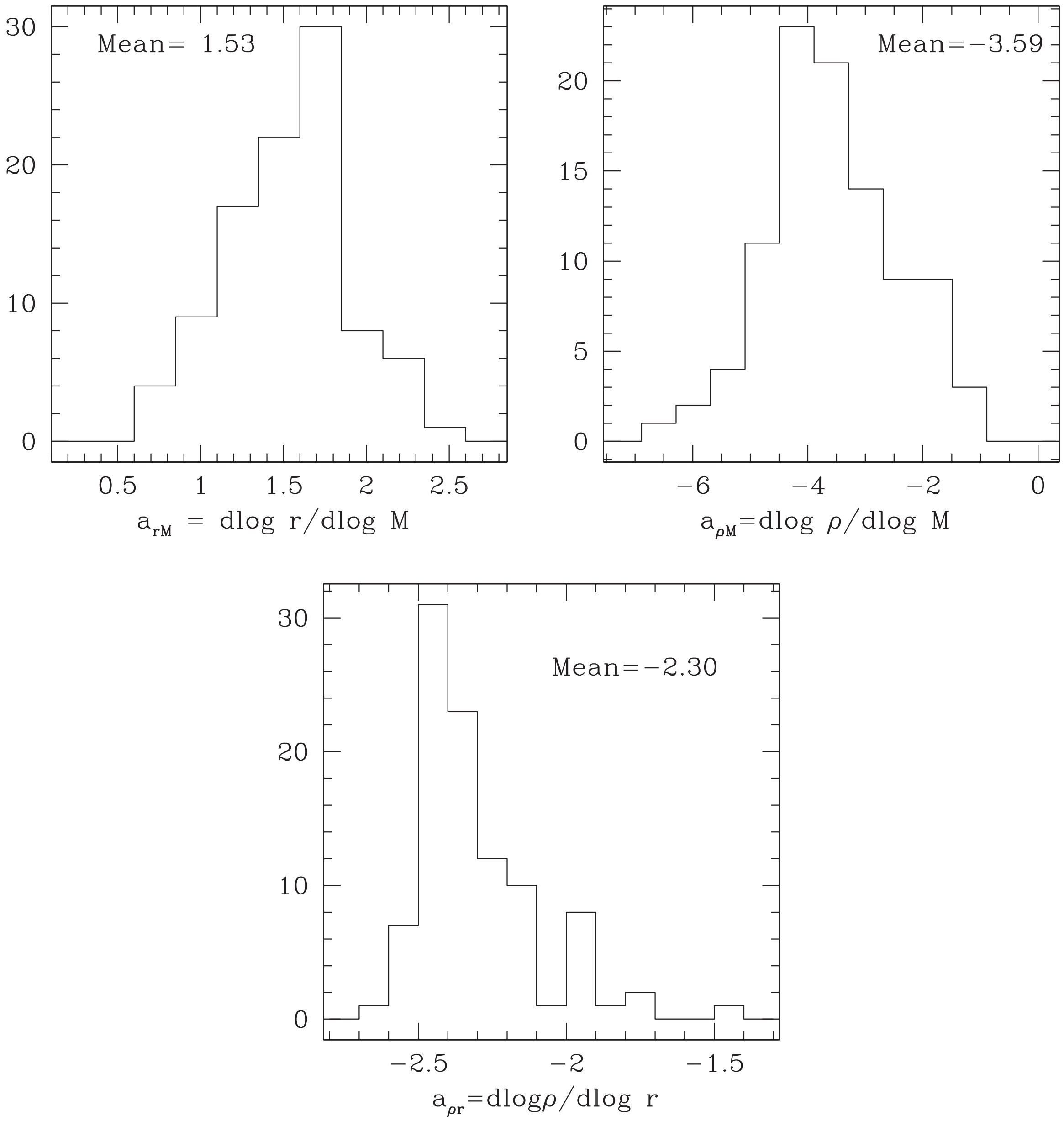

Figure 5. Histograms of the values of the logarithmic derivatives a_{rM} (top left), $a_{\rho M}$ (top right), and $a_{\rho r}$ (bottom).

masses scale as luminosities with the square of the distance.

4. The total error on $\log r_{\rm h}$ is unchanged and is as described above.
5. The total error squared on $\log \rho_{{\rm h},C}$ has a reduced dependence on the distance error that now goes as $(\delta \log D)^2$. This stems from the increased dependence on distance of the bulge mass (see point 3).
6. Errors on $\log M_{\rm BH}$ and $\log \sigma$ can be correlated through the M/L as above and are unchanged.
7. The correlation between the errors on $\log M_{\rm BH}$ and $\log M_{{\rm Bu},C}$ is only due to the distance and amounts to $2(\delta \log D)^2$ because of the dependence of bulge masses on distance (see above).
8. Errors on $\log M_{\rm BH}$ and $\log r_{\rm h}$ are correlated through the distance as before.
9. The anticorrelation between the errors on $\log M_{\rm BH}$ and $\log \rho_{{\rm h},C}$ is only due to the distance and amounts to $-(\delta \log D)^2$ because of the dependence of bulge masses on distance (see above).
10. There is no correlation between the errors on $\log M_{{\rm Bu},C}$ and on $\log \sigma$.
11. The errors on $\log M_{{\rm Bu},C}$ and $\log r_{\rm h}$ are correlated through the mass extrapolation term and with a stronger dependence on the distance error squared (as $2(\delta \log D)^2$) from the D^2 scaling of bulge masses.
12. The errors on $\log M_{{\rm Bu},C}$ and $\log \rho_{{\rm h},C}$ are correlated through the mass extrapolation term and the M/L_C dependency and anticorrelated through the distance, as in the previous case.
13. The errors on $\log r_{\rm h}$ and $\log \rho_{{\rm h},C}$ are correlated through the mass extrapolation term and anticorrelated (with the reduced dependency $-(\delta \log D)^2$) through the distance.
14. The errors on $\log \rho_{{\rm h},C}$ and $\log \sigma$ are not correlated.

Table 4
Error Correlations between the Parameters for Mass-to-light Ratios Derived Dynamically

N	Quantity	Mean Value
0	$(\delta \log \sigma)^2$	0.0006
1	$(\delta \log M/L)^2_{\rm eff} = (\delta \log M/L)^2 + 4f(\delta \log \sigma)^2$	0.0038
2	$(\delta \log M_{\rm BH})^2 = (\delta \log M^{\rm fit}_{\rm BH})^2 + (\delta \log D)^2$	0.023
3	$(\delta \log M_{\rm Bu})^2 = (\delta \log M^{\rm ext}_{\rm Bu})^2 + (\delta \log D)^2 + (\delta \log M/L)^2_{\rm eff}$	0.012
4	$(\delta \log r_{\rm h})^2 = a^2_{rM}(\delta \log M^{\rm ext}_{\rm Bu})^2 + (\delta \log D)^2$	0.015
5	$(\delta \log \rho_{\rm h})^2 = a^2_{\rho M}(\delta \log M^{\rm ext}_{\rm Bu})^2 + (\delta \log M/L)^2_{\rm eff} + 4(\delta \log D)^2$	0.087
6	$\delta \log M_{\rm BH} \delta \log \sigma = 2fa_{\rm BH}(\delta \log \sigma)^2$	−0.0003
7	$\delta \log M_{\rm BH} \delta \log M_{\rm Bu} = (\delta \log D)^2 + a_{\rm BH}(\delta \log M/L)^2_{\rm eff}$	0.0023
8	$\delta \log M_{\rm BH} \delta \log r_{\rm h} = (\delta \log D)^2$	0.0037
9	$\delta \log M_{\rm BH} \delta \log \rho_{\rm h} = -2(\delta \log D)^2 + a_{\rm BH}(\delta \log M/L)^2_{\rm eff}$	−0.009
10	$\delta \log M_{\rm Bu} \delta \log \sigma = 2f(\delta \log \sigma)^2$	0.0005
11	$\delta \log M_{\rm Bu} \delta \log r_{\rm h} = a_{rM}(\delta \log M^{\rm ext}_{\rm Bu})^2 + (\delta \log D)^2$	0.01
12	$\delta \log M_{\rm Bu} \delta \log \rho_{\rm h} = a_{\rho M}(\delta \log M^{\rm ext}_{\rm Bu})^2 + (\delta \log M/L)^2_{\rm eff} - 2(\delta \log D)^2$	−0.0185
13	$\delta \log r_{\rm h} \delta \log \rho_{\rm h} = a_{\rho M} a_{rM}(\delta \log M^{\rm ext}_{\rm Bu})^2 - 2(\log D)^2$	−0.035
14	$\delta \log \rho_{\rm h} \delta \log \sigma = 2f(\delta \log \sigma)^2$	0.0005

The average values of the covariance matrix elements listed in Tables 4 and 5 are similar, with $\delta \log M_{{\rm Bu},C}$ larger than $\delta \log M_{\rm Bu}$.

Tables 3 and 7 list the values of each term for each galaxy of the sample of Kormendy & Ho (2013) considered here.

4. EXPLORING MULTIVARIATE CORRELATIONS

In the following we investigate the correlations between all measured parameters. We assume that the n measured values of the dependent variable η_i (with i running from 1 to n) can be expressed as

$$\eta_i = \boldsymbol{\alpha}^T \cdot \boldsymbol{\xi}_i + ZP + N(0, \epsilon), \tag{6}$$

where $\boldsymbol{\xi}_i$ are the measured values of the independent vector of the variables, $N(0, \epsilon)$ is a normal random variable with zero mean and variance ϵ^2, with ϵ representing the intrinsic scatter in η_i, and ZP and $\boldsymbol{\alpha}$ are the zero point and the multilinear coefficients. We compute ZP, $\boldsymbol{\alpha}$, and ϵ following Kelly (2007) and making use of his IDL routines. To this purpose we compute the covariance error matrices:

$$C_i = \begin{pmatrix} \delta^2\eta_i & \delta\eta_i\delta\boldsymbol{\xi}_i \\ \delta\eta_i\delta\boldsymbol{\xi}_i & \delta\boldsymbol{\xi}_i\delta\boldsymbol{\xi}_i \end{pmatrix}. \tag{7}$$

The square roots of their diagonal terms are given in Tables 1 and 3; the off-diagonal terms can be found in Tables 6 and 7.

Kelly's routines provide the posterior probabilities $P(\boldsymbol{\alpha}, ZP, \epsilon)$ of the fitted parameters $\boldsymbol{\alpha}$, ZP, ϵ. We quote as best-fit parameters the averages of these distributions with errors given by the rms. We show two examples of this procedure in Figures 10 and 11. Figure 10 shows the one-dimensional case of the $\log M_{\rm BH} = a \log \sigma + ZP$ relation for the subsample CorePowerEClassPC (see below and Table 8). As expected, the errors in the slope and the zero point are highly correlated.

Figure 11 shows the two-dimensional case of the $\log M_{\rm BH} = a \log \sigma + b \log \rho_{\rm h} + ZP$ relation discussed below, again for the subsample CorePowerEClassPC. Strong error correlations are present between the two fitted slopes and the zero point. By integrating the posterior probability for positive values of b ($P(b > 0) = 0.9999$), we show that we have detected this bivariate correlation robustly. Furthermore, to assess whether we are overfitting the data by considering bivariate correlations involving BH masses, we also compute the corrected Akaike information criterion (cAIC; Akaike et al. 1973; Hurvich & Tsai 1989). It is defined as

$${\rm cAIC}(k) = {\rm AIC}(k) + \frac{2k(k+1)}{n-k-1}, \tag{8}$$

where n is the number of data points, k is the number of free parameters ($k = 3$ for monovariate correlations and $k = 4$ for bivariate correlations), and AIC is the Akaike information criterion:

$${\rm AIC}(k) = 2k - 2\ln P_{\rm best}(k), \tag{9}$$

where $P_{\rm best}$ is the likelihood of the best-fitting solution with k parameters. There is evidence for bivariate correlations if

$$\Delta{\rm cAIC} = {\rm cAIC}(k=4) - {\rm cAIC}(k=3) < 0. \tag{10}$$

The relative probability of the two solutions is $RP = \exp(\Delta{\rm cAIC}/2)$, so the bivariate correlation is strongly preferred when $\Delta{\rm cAIC} < -2$. Equivalent conclusions are obtained by considering the Bayesian information criterion ${\rm BIC} = -2\ln P_{\rm best} + k\ln n$ (Schwarz 1978) and $\Delta{\rm BIC} = {\rm BIC}(k=4) - {\rm BIC}(k=3)$.

We implement this schema as follows. We marginalize the posterior probability of the bivariate fits $P(a, b, ZP, \epsilon)$ over (b, ZP, ϵ) or (a, ZP, ϵ) to get the posterior distribution of a, $P_{k=4}(a)$, or b, $P_{k=4}(b)$, respectively. This is well approximated by a Gaussian, $P_{k=4}(a) = \frac{1}{\sqrt{2\pi}\delta a_{\rm best}}\exp[-\frac{(a-a_{\rm best})^2}{2\delta a^2_{\rm best}}]$ or $P_{k=4}(b) = \frac{1}{\sqrt{2\pi}\delta b_{\rm best}}\exp[-\frac{(b-b_{\rm best})^2}{2\delta b^2_{\rm best}}]$ (see Figure 11), where $a_{\rm best}$ and $\delta a_{\rm best}$, $b_{\rm best}$ and $\delta b_{\rm best}$ are given in Tables 12, 14, and 37, where we omit the label "best" for simplicity. Therefore the probability of our best-fitting bivariate solutions is $P_{{\rm best},k=4} = \frac{1}{\sqrt{2\pi}\delta a_{\rm best}}$ or $\frac{1}{\sqrt{2\pi}\delta b_{\rm best}}$. We compare this to the probability of one of the two possible best-fitting monovariate (i.e., $k = 3$) solutions for each combination of parameters we considered, having either $a = 0$ or $b = 0$. We choose the one

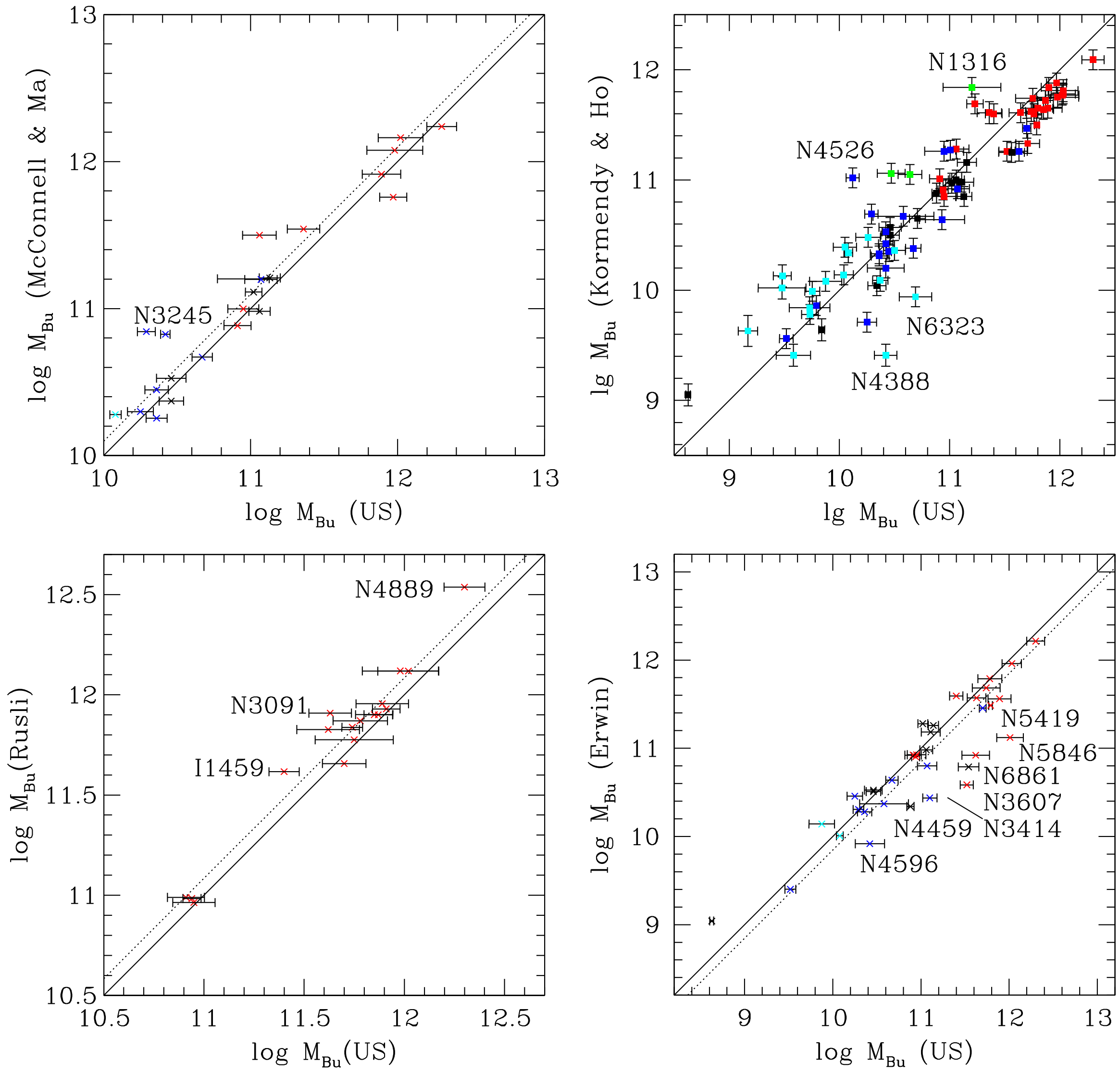

Figure 6. Bulge masses compared to the values of McConnell & Ma (2013, top left), Kormendy & Ho (2013, top right), Rusli et al. (2013a, bottom left), and Erwin et al. (2015b, bottom right). Red points are core ellipticals, black points are power-law ellipticals, blue points are classical bulges, cyan points are pseudobulges, and green points are mergers. In the upper left plot we exclude the galaxies where we consider the classical component of a composite (pseudo plus classical) bulge. In the bottom right plot we show only galaxies fitted by one component. The solid line shows the one-to-one relation, and the dotted line is shifted to fit the data points on average (indistinguishable from the solid line for the sample of Kormendy & Ho 2013).

with the smallest intrinsic and measured scatter. In this way we are sure to get the most stringent test for the evidence of bivariate correlations. For instance, in the case of the M_{BH}–M_{Bu}–σ correlation, this is M_{BH}–σ, which corresponds to the bivariate solution with $a = 0$. In all other cases we consider the bivariate solution with $b = 0$.

In practice, we compute the marginalized posterior distribution $P_{k=4}(a, b)$, verifying that the maximum of $P_{k=4}(a = 0, b)$ is reached for $b = b_{\text{best},k=3}$ for the M_{BH}–M_{Bu}–σ correlation and that the maximum of $P_{k=4}(a, b = 0)$ is reached for $a = a_{\text{best},k=3}$ for all the other correlations, where $a_{\text{best},k=3}$ or $b_{\text{best},k=3}$ are given in Tables 11, 13, and 36, listing our monovariate (i.e., $k = 3$) solutions (where again we dropped the label "*best*, $k = 3$" for simplicity). Then we set $P_{\text{best},k=3} = P_{\text{best},k=4}(a = 0) = \frac{1}{\sqrt{2\pi}\,\delta a_{\text{best}}} \exp[-(a_{\text{best}}/\delta a_{\text{best}})^2/2]$ for the M_{BH}–M_{Bu}–σ correlation or $P_{\text{best},k=3} = P_{\text{best},k=4}(b = 0) = \frac{1}{\sqrt{2\pi}\,\delta b_{\text{best}}} \exp[-(b_{\text{best}}/\delta b_{\text{best}})^2/2]$ for all other correlations.

Finally we get

$$2\ln[P_{\text{best}}(k = 4)/P_{\text{best}}(k = 3)] = (b_{\text{best}}/\delta b_{\text{best}})^2 \qquad (11)$$

or

$$2\ln[P_{\text{best}}(k = 4)/P_{\text{best}}(k = 3)] = (a_{\text{best}}/\delta a_{\text{best}})^2 \qquad (12)$$

for the the M_{BH}–M_{Bu}–σ correlation or all the others, respectively.

Following the discussion given in the introduction, we consider 12 (sub)samples. The first one (All) is made of the galaxies of Table 1, with the exception of NGC 4486b. This galaxy deviates strongly from every correlation involving its BH mass, despite the fact that our SINFONI BH mass (see Appendix B) is 30% smaller than the value adopted by Kormendy & Ho (2013). As done by Kormendy & Ho (2013), we discard it from all the subsamples and fits discussed below. The other subsamples are core ellipticals (CoreE); core and power-law ellipticals (CorePowerE); core and power-law

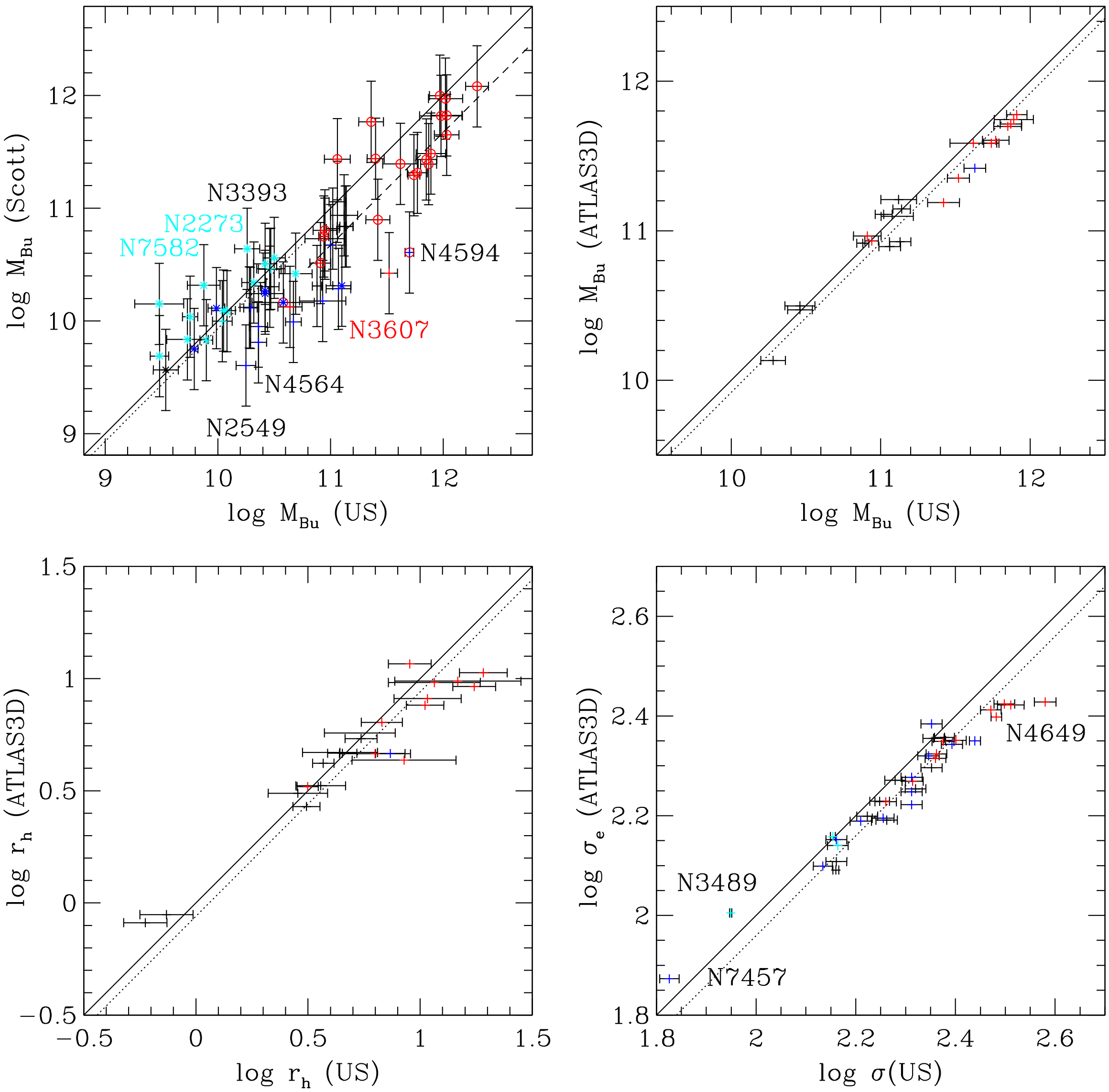

Figure 7. Top left: our bulge masses compared to the values of Scott et al. (2013). We exclude NGC 1399 and NGC 6086, where we subtract the outer halo from the profile. Colors and continuous lines are as in Figure 6. The dotted and dashed lines are shifted to fit the data points at $\log M_{\rm Bu} < 10.8$ and $\log M_{\rm Bu} \geqslant 10.8$, respectively. Circles indicate core-Sérsic galaxies according to the classification of Scott et al. (2013). Asterisks indicate galaxies that we classified as barred. Top right: the bulge masses compared to the values of Cappellari et al. (2013) for the galaxies where we do not apply a decomposition. Bottom left: the half-mass radii compared to the values of Cappellari et al. (2013) for the galaxies where we do not apply a decomposition. Bottom right: the velocity dispersions compared to the σ_e values of Cappellari et al. (2013). The three most deviant galaxies are labeled. Colors and continuous lines are as above. The dotted lines are shifted to the average difference.

ellipticals plus classical bulges (CorePowerEClass); core and power-law ellipticals, classical bulges, and classical bulge components of (composite) pseudobulges (CorePowerEClassPC); the same for just SINFONI measurements (CorePowerEClassPCSINFONI); the same for just measurements from the literature (CorePowerEClassPCLit); the same without barred galaxies (CorePowerEClassnoBars); power-law ellipticals (PowerE); power-law ellipticals and classical bulges (PowerEClass); power-law ellipticals classical bulges, and classical bulge components of pseudo (composite) bulges (PowerEClassPC); and pseudobulges (Pseudo). Furthermore, we consider more or less stringent selection criteria to include or exclude measurements of different quality. Table 8 describes how the subsamples are constructed from Table 1 using the flags listed there.

With this set of subsamples we aim to assess two questions. On the one hand, we want to understand the influence of our SINFONI data set, which provides almost one-quarter of the full database. On the other hand, we want to explore the degree to which we can unify the different types of galaxies in one common picture. Tables 9–12 report the results of the fits obtained for the different families of objects.

Figure 12 shows the correlations between the parameters $M_{\rm Bu}$, $r_{\rm h}$, and $\rho_{\rm h}$ for the galaxies of Table 1 without NGC 4486b; see above. The fourth plot presents the virial relation between $M_{\rm Bu}$, $r_{\rm h}$, and velocity dispersions σ for the same sample. There are no obvious outliers; the galaxies NGC 1332, NGC 3998, and NGC 6861 have denser bulges than expected given their bulge masses, and NGC 7457 and NGC 221 have less dense bulges.

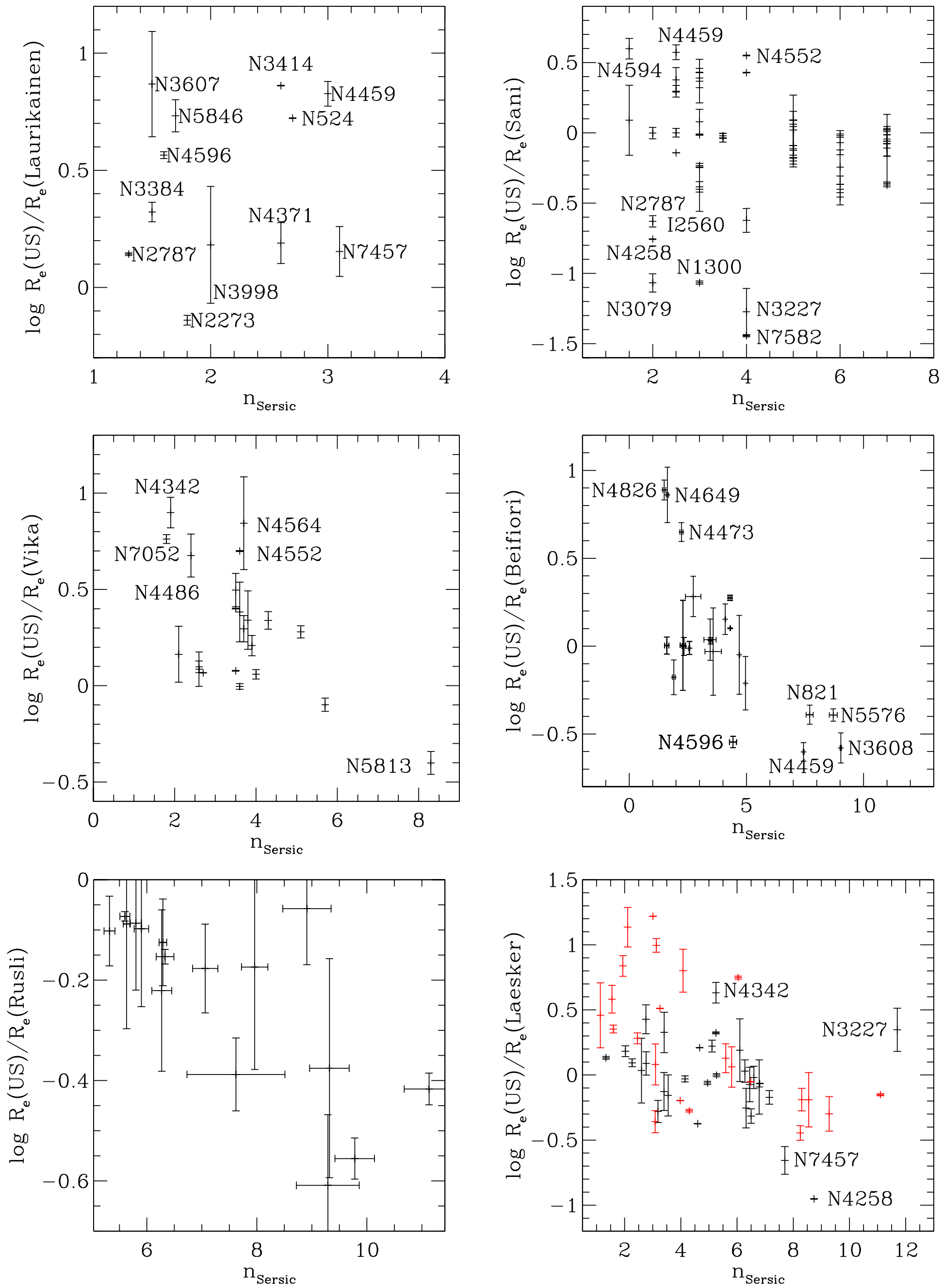

Figure 8. Bulge circularized half-luminosity radius R_e compared to the values of Laurikainen et al. (2010, top left), Sani et al. (2011, top right), Vika et al. (2012, middle left), Beifiori et al. (2012, middle right), Rusli et al. (2013b, bottom left), and Läsker et al. (2014, bottom right) as a function of the fitted Sérsic index $n_{\text{Sérsic}}$. The red points in the comparison to Läsker et al. (2014) indicate their "best" solution.

Bulge masses (see Table 9, sample All) scale as $M_{\rm Bu} \sim r_{\rm h}^{1.3\pm0.04}$ with estimated intrinsic scatter $\epsilon = 0.24 \pm 0.02$ dex, or as $M_{\rm Bu} \sim \rho_{\rm h}^{-0.7\pm0.04}$ with $\epsilon = 0.42 \pm 0.03$. Consistently, bulge average densities scale as $\rho_{\rm h} \sim r_{\rm h}^{-1.72\pm0.04}$. These correlations hold within the errors for all subsamples considered, with no appreciable differences between the literature and the SINFONI sample. The correlations for core ellipticals are tighter. Only pseudobulges follow relations that are different at the 2–3σ level ($M_{\rm Bu} \sim r_{\rm h}^{1.02\pm0.16}$, $M_{\rm Bu} \sim \rho_{\rm h}^{-0.4\pm0.1}$, $\rho_{\rm h} \sim r_{\rm h}^{-1.96\pm0.16}$).

For pressure-supported, self-gravitating systems in virial equilibrium, dynamical masses are expected to scale as

$$M = 10^{6.064}(R_e/\text{kpc})(\sigma/\text{km s}^{-1})^2 M_\odot \qquad (13)$$

(Cappellari et al. 2006). Using spherical half-luminosity radii we find

$$M_{\rm Bu} = 10^{6.67\pm0.38} r_{\rm h}^{0.98\pm0.04} \sigma^{1.65\pm0.17}, \qquad (14)$$

with 40% scatter (see Table 10, sample CorePowerEClassPC). The coefficients are similar within 1–2σ for all the subsamples

Table 5
Error Correlations between the Parameters for Mass-to-light Ratios Derived from Colors

N	Quantity	Mean Value
0	$(\delta \log \sigma)^2$	0.0005
1	$(\delta \log M/L_C)^2 = (\delta M_{\mathrm{Bu},C})^2$	0.008
2	$(\delta \log M_{\mathrm{BH}})^2 = (\delta \log M_{\mathrm{BH}}^{\mathrm{fit}})^2 + (\delta \log D)^2$	0.022
3	$(\delta \log M_{\mathrm{Bu},C})^2 = (\delta \log M_{\mathrm{Bu}}^{\mathrm{ext}})^2 + 4(\delta \log D)^2 + (\delta \log M/L_C)^2$	0.019
4	$(\delta \log r_{\mathrm{h}})^2 = a_{rM}^2 (\delta \log M_{\mathrm{Bu}}^{\mathrm{ext}})^2 + (\delta \log D)^2$	0.013
5	$(\delta \log \rho_{\mathrm{h},C})^2 = a_{\rho M}^2 (\delta \log M_{\mathrm{Bu}}^{\mathrm{ext}})^2 + (\delta \log M/L_C)^2 + (\delta \log D)^2$	0.073
6	$\delta \log M_{\mathrm{BH}} \delta \log \sigma = 2f a_{\mathrm{BH}} (\delta \log \sigma)^2$	-3×10^{-6}
7	$\delta \log M_{\mathrm{BH}} \delta \log M_{\mathrm{Bu},C} = 2(\delta \log D)^2$	0.004
8	$\delta \log M_{\mathrm{BH}} \delta \log r_{\mathrm{h}} = (\delta \log D)^2$	0.002
9	$\delta \log M_{\mathrm{BH}} \delta \log \rho_{\mathrm{h}} = -2(\delta \log D)^2$	−0.002
10	$\delta \log M_{\mathrm{Bu},C} \delta \log \sigma = 0$	0
11	$\delta \log M_{\mathrm{Bu},C} \delta \log r_{\mathrm{h}} = a_{rM} (\delta \log M_{\mathrm{Bu}}^{\mathrm{ext}})^2 + 2(\delta \log D)^2$	0.01
12	$\delta \log M_{\mathrm{Bu},C} \delta \log \rho_{\mathrm{h},C} = a_{\rho M} (\delta \log M_{\mathrm{Bu}}^{\mathrm{ext}})^2 + (\delta M/L_C)^2 - 2(\delta \log D)^2$	−0.01
13	$\delta \log r_{\mathrm{h}} \delta \log \rho_{\mathrm{h},C} = a_{\rho M} a_{rM} (\delta \log M_{\mathrm{Bu}}^{\mathrm{ext}})^2 - 2(\log D)^2$	−0.03
14	$\delta \log \rho_{\mathrm{h},C} \delta \log \sigma = 0$	0

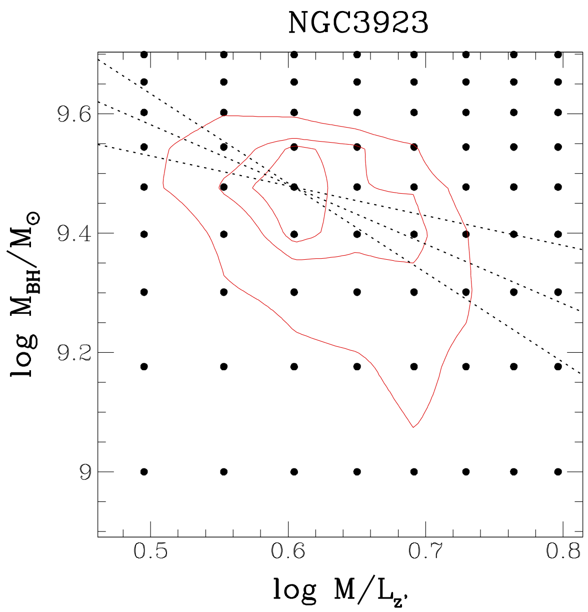

Figure 9. χ^2 contours as a function of $\log M/L$ and $\log M_{\mathrm{BH}}$ for NGC 3923. The filled points show the grid of computed models. The dotted lines show the lines of correlated errors $\Delta \log M_{\mathrm{BH}} = a_{\mathrm{BH}} \Delta \log M/L_{z'}$, for $a_{\mathrm{BH}} = -0.5, -1, -1.5$.

that exclude pseudobulges. In particular, there is no significant difference if we use just the SINFONI or just the literature sample. For pseudobulges, the dynamical masses are roughly a factor of 3 smaller for a given r_{h} and σ with larger scatter. Core ellipticals follow a tighter relation with just 30% intrinsic scatter and a shallower dependence on velocity dispersion ($M_{\mathrm{Bu}} = 10^{7.96 \pm 0.99} r_{\mathrm{h}}^{1.03 \pm 0.13} \sigma^{1.09 \pm 0.44}$). The slope difference is significant only at the 2σ level and could point to the systematic uncertainties in the role of dark matter, as discussed in Thomas et al. (2011). A detailed discussion on the origin of the differences between Equations (13) and (14) goes beyond the scope of this paper.

When we augment the errors on the bulge mass and density by 0.15 dex (see Section 3), the fitted parameters remain essentially the same with somewhat larger errors, except for the estimated intrinsic scatter, which is approximately reduced by 0.15 dex in quadrature and therefore statistically compatible with zero.

5. BH CORRELATION ANALYSIS

We now proceed to examine correlations involving the BH mass. We start by investigating four one-dimensional correlations of the type $y = ax + ZP + N(0, \epsilon)$:

$$M_{\mathrm{BH}} - \sigma\colon \log M_{\mathrm{BH}} = a \log \sigma + ZP, \quad (15)$$

$$M_{\mathrm{BH}} - M_{\mathrm{Bu}}\colon \log M_{\mathrm{BH}} = a \log M_{\mathrm{Bu}} + ZP, \quad (16)$$

$$M_{\mathrm{BH}} - r_{\mathrm{h}}\colon \log M_{\mathrm{BH}} = a \log r_{\mathrm{h}} + ZP, \quad (17)$$

$$M_{\mathrm{BH}} - \rho_{\mathrm{h}}\colon \log M_{\mathrm{BH}} = a \log \rho_{\mathrm{h}} + ZP. \quad (18)$$

Table 11 summarizes the results, giving the number of galaxies in each subsample, the best-fit values of a and ZP with errors, the estimated intrinsic scatter ϵ, and the measured scatter rms. In addition, we list the Spearman coefficient r_{S} and the probability P_{r_s} of its value being greater being caused by chance. Figure 13 presents the correlation plots.

In agreement with the literature, we find that the strongest correlations with the lowest measured and intrinsic scatter are with σ. The correlations with M_{Bu} are strong, except for the pseudobulge subsample. Correlations with sizes or anticorrelations with densities are generally weaker (and nonexistent for pseudobulges) but still robust for several subclasses. The measured slopes of the correlations of Equations (15)–(18) are steeper for the subsamples including core ellipticals. In contrast, all correlations for the subsamples excluding core ellipticals and pseudobulges are similar within the errors. BH masses in pseudobulges correlate (weakly) only with σ, and this with a flatter slope than for the other samples.

As noticed before, when we augment the errors on the bulge mass and density by 0.15 dex (see Section 3), the fitted parameters of the M_{BH}–M_{Bu} and M_{BH}–ρ_{h} correlations remain essentially the same with somewhat larger errors, but the estimated intrinsic scatter is approximately reduced by 0.15 dex in quadrature.

This confirms the results reported in the literature. In particular,

Table 6
Values of the Error Covariance Matrices: Off-diagonal Terms

Galaxy	$a_{\rm BH}$	f	$\delta \log M_{\rm BH}$ $\delta \log \sigma$	$\delta \log M_{\rm BH}$ $\delta \log M_{\rm Bu}$	$\delta \log M_{\rm BH}$ $\delta \log r_{\rm h}$	$\delta \log M_{\rm BH}$ $\delta \log \rho_{\rm h}$	$\delta \log M_{\rm Bu}$ $\delta \log \sigma$	$\delta \log M_{\rm Bu}$ $\delta \log r_{\rm h}$	$\delta \log M_{\rm Bu}$ $\delta \log \rho_{\rm h}$	$\delta \log r_{\rm h}$ $\delta \log \rho_{\rm h}$	$\delta \log \rho_{\rm h}$ $\delta \log \sigma$
MW	0	0	0.00000000	0.00102400	0.00102400	−0.00204800	0.00000000	0.00279996	−0.00360376	−0.00528875	0.00000000
Circinus	0	0	0.00000000	0.00518400	0.00518400	−0.01036800	0.00000000	0.00518913	−0.00772816	−0.01038157	0.00000000
A 1836	0	1	0.00000000	0.00057600	0.00057600	−0.00115200	0.00089280	0.00267647	0.01019260	−0.00828498	0.00089280
IC 1459	−1	0	−0.00000000	0.00117500	0.00313600	−0.00823300	0.00000000	0.00415655	−0.00672214	−0.01005465	0.00000000
IC 4296	0	1	0.00000000	0.00102400	0.00102400	−0.00204800	0.00093300	0.01312244	−0.02733637	−0.05108090	0.00093300
NGC 0221	−2	0	−0.00000000	−0.00005040	0.00025600	−0.00081840	0.00000000	0.00034204	−0.00055272	−0.00077187	0.00000000
NGC 0224	−2	0	−0.00000000	0.00011180	0.00032400	−0.00086020	0.00000000	0.00032516	−0.00054437	−0.00065085	0.00000000
NGC 0524	0	1	0.00000000	0.00160000	0.00160000	−0.00320000	0.00089180	0.00328546	−0.00458597	−0.00968235	0.00089180
NGC 0821	−2	1	−0.00173000	−0.00369240	0.00115600	−0.00716040	0.00086500	0.01497032	−0.03331196	−0.05986855	0.00086500
NGC 1023	0	0	0.00000000	0.00102400	0.00102400	−0.00204800	0.00000000	0.00102543	−0.00204867	−0.00205271	0.00000000
NGC 1068	0	1	0.00000000	0.05954000	0.05954000	−0.11907999	0.00081180	0.05954083	−0.08837061	−0.11908121	0.00081180
NGC 1194	0	1	0.00000000	0.00221800	0.00221800	−0.00443600	0.01009800	0.00229553	0.03497470	−0.00470692	0.01009800
NGC 1300	0	0	0.00000000	0.03386000	0.03386000	−0.06772000	0.00000000	0.03391462	−0.06782499	−0.06786712	0.00000000
NGC 1399	0	0	0.00000000	0.00019600	0.00019600	−0.00039200	0.00000000	0.00043114	−0.00085702	−0.00146191	0.00000000
NGC 2273	0	1	0.00000000	0.00078400	0.00078400	−0.00156800	0.00196240	0.00078465	0.01877527	−0.00156863	0.00196240
NGC 2549	−1	1	−0.00088060	0.00103220	0.00313600	−0.00837580	0.00088060	0.00728061	−0.01419533	−0.02351997	0.00088060
NGC 2748	0	1	0.00000000	0.02250000	0.02250000	−0.04500000	0.00071400	0.02250098	−0.04327431	−0.04500188	0.00071400
NGC 2787	0	0	0.00000000	0.00518400	0.00518400	−0.01036800	0.00000000	0.00563447	−0.01115634	−0.01166805	0.00000000
NGC 2960	0	1	0.00000000	0.00211600	0.00211600	−0.00423200	0.00352600	0.00212848	0.00944793	−0.00427684	0.00352600
NGC 2974	0	0	0.00000000	0.00230400	0.00230400	−0.00460800	0.00000000	0.00309165	−0.00592979	−0.00787469	0.00000000
NGC 3031	0	1	0.00000000	0.00025600	0.00025600	−0.00051200	0.00090540	0.00328737	−0.00558498	−0.00994234	0.00090540
NGC 3079	0	1	0.00000000	0.00115600	0.00115600	−0.00231200	0.00086694	0.00115721	−0.00027405	−0.00231520	0.00086694
NGC 3115	−2	1	−0.00172840	−0.00320566	0.00032400	−0.00417766	0.00086420	0.01652079	−0.03743427	−0.06282222	0.00086420
NGC 3227	−2	0	−0.00000000	−0.00161800	0.00230400	−0.00853000	0.00000000	0.00281822	−0.00389962	−0.00682885	0.00000000
NGC 3245	−2	0	−0.00000000	−0.00232200	0.00160000	−0.00712200	0.00000000	0.00171867	−0.00148446	−0.00346348	0.00000000
NGC 3377	−2	1	−0.00176120	−0.00385340	0.00032400	−0.00482540	0.00088060	0.00908298	−0.02037912	−0.04350170	0.00088060
NGC 3379	−2	0	−0.00000000	−0.00144900	0.00048400	−0.00290100	0.00000000	0.00150424	−0.00245705	−0.00510774	0.00000000
NGC 3384	0	0	0.00000000	0.00078400	0.00078400	−0.00156800	0.00000000	0.00111568	−0.00184045	−0.00253374	0.00000000
NGC 3393	0	1	0.00000000	0.00518400	0.00518400	−0.01036800	0.00172740	0.00518493	−0.00322946	−0.01036968	0.00172740
NGC 3414	0	1	0.00000000	0.00221800	0.00221800	−0.00443600	0.00089803	0.00602675	−0.01155801	−0.02290207	0.00089803
NGC 3585	−2	1	−0.00201560	−0.00465320	0.00129600	−0.00854120	0.00100780	0.03685222	−0.07949613	−0.10677002	0.00100780
NGC 3607	−2	1	−0.00174360	−0.00302320	0.00115600	−0.00649120	0.00087180	0.00517189	−0.01005872	−0.02014504	0.00087180
NGC 3608	−2	0	−0.00000000	−0.00272200	0.00078400	−0.00507400	0.00000000	0.01286058	−0.03004822	−0.06245575	0.00000000
NGC 3842	−2	0	−0.00000000	−0.00676400	0.00250000	−0.01426400	0.00000000	0.03250545	−0.07438256	−0.14378713	0.00000000
NGC 3998	0	0	0.00000000	0.00144400	0.00144400	−0.00288800	0.00000000	0.00171955	0.07136787	−0.00368429	0.00000000
NGC 4026	−1	1	−0.00094460	0.00028330	0.00313600	−0.00912470	0.00094460	0.00380532	−0.00495370	−0.00841749	0.00094460
NGC 4151	0	0	0.00000000	0.00360000	0.00360000	−0.00720000	0.00000000	0.00360226	−0.00524429	−0.00720798	0.00000000
NGC 4258	0	0	0.00000000	0.00090000	0.00090000	−0.00180000	0.00000000	0.00090150	−0.00156229	−0.00180523	0.00000000
NGC 4261	0	0	0.00000000	0.00144400	0.00144400	−0.00288800	0.00000000	0.02379194	−0.05434294	−0.10225459	0.00000000
NGC 4291	−2	1	−0.00185800	−0.00596200	0.00409600	−0.01825000	0.00092900	0.00760714	−0.01171311	−0.02330892	0.00092900
NGC 4342	−2	1	−0.00180600	−0.00525600	0.00067600	−0.00728400	0.00090300	0.00406954	−0.00701535	−0.02018439	0.00090300
NGC 4374	−1	0	−0.00000000	−0.00049100	0.00019600	−0.00107900	0.00000000	0.00367986	−0.00837319	−0.01732530	0.00000000
NGC 4388	0	0	0.00000000	0.00176400	0.00176400	−0.00352800	0.00000000	0.00368642	−0.00062733	−0.00990079	0.00000000
NGC 4459	−1	0	−0.00000000	−0.00049070	0.00019600	−0.00107870	0.00000000	0.00147212	−0.00274696	−0.00532598	0.00000000
NGC 4473	−2	1	−0.00169520	−0.00407760	0.00019600	−0.00466560	0.00084760	0.00595497	−0.01279830	−0.03099224	0.00084760
NGC 4486	0	0	0.00000000	0.00025600	0.00025600	−0.00051200	0.00000000	0.00411383	−0.00725172	−0.02304576	0.00000000
NGC 4526	0	0	0.00000000	0.00221800	0.00221800	−0.00443600	0.00000000	0.00222178	−0.00325176	−0.00444890	0.00000000
NGC 4552	0	1	0.00000000	0.00078400	0.00078400	−0.00156800	0.00085532	0.02151213	−0.05315189	−0.13933082	0.00085532
NGC 4564	0	1	0.00000000	0.00019600	0.00019600	−0.00039200	0.00092140	0.00369338	−0.00625168	−0.01257196	0.00092140
NGC 4594	0	0	0.00000000	0.00129600	0.00129600	−0.00259200	0.00000000	0.00142279	−0.00286399	−0.00310202	0.00000000
NGC 4596	0	1	0.00000000	0.02560000	0.02560000	−0.05120000	0.00073520	0.02631555	−0.05135706	−0.05405618	0.00073520
NGC 4621	0	1	0.00000000	0.00490000	0.00490000	−0.00980000	0.00090143	0.01746883	−0.03815935	−0.06640238	0.00090143
NGC 4649	−2	0	−0.00000000	−0.00427600	0.00025600	−0.00504400	0.00000000	0.01190487	−0.02707213	−0.05537556	0.00000000

Table 6
(Continued)

Galaxy	$a_{\rm BH}$	f	$\delta\log M_{\rm BH}$ $\delta\log\sigma$	$\delta\log M_{\rm BH}$ $\delta\log M_{\rm Bu}$	$\delta\log M_{\rm BH}$ $\delta\log r_{\rm h}$	$\delta\log M_{\rm BH}$ $\delta\log\rho_{\rm h}$	$\delta\log M_{\rm Bu}$ $\delta\log\sigma$	$\delta\log M_{\rm Bu}$ $\delta\log r_{\rm h}$	$\delta\log M_{\rm Bu}$ $\delta\log\rho_{\rm h}$	$\delta\log r_{\rm h}$ $\delta\log\rho_{\rm h}$	$\delta\log\rho_{\rm h}$ $\delta\log\sigma$
NGC 4697	0	0	0.00000000	0.00019600	0.00019600	−0.00039200	0.00000000	0.00290751	−0.00556928	−0.01248113	0.00000000
NGC 4736	0	0	0.00000000	0.00462400	0.00462400	−0.00924800	0.00000000	0.00462492	−0.00728876	−0.00924963	0.00000000
NGC 4826	−1	1	−0.00031400	0.00374480	0.00490000	−0.01095520	0.00031400	0.00503434	−0.00755235	−0.01037050	0.00031400
NGC 4889	−2	1	−0.00015668	−0.00676536	0.00048400	−0.00821736	0.00007834	0.00862240	−0.01555452	−0.03650644	0.00007834
NGC 5077	−2	1	−0.00185520	0.00120360	0.00883600	−0.02530440	0.00092760	0.00949040	−0.01540556	−0.02010439	0.00092760
NGC 5128	0	0	0.00000000	0.00057600	0.00057600	−0.00115200	0.00000000	0.00145456	0.00703146	−0.00324545	0.00000000
NGC 5576	−1	1	−0.00091380	−0.00293260	0.00078400	−0.00528460	0.00091380	0.00242247	−0.00200007	−0.01039793	0.00091380
NGC 5813	0	1	0.00000000	0.00129600	0.00129600	−0.00259200	0.00086279	0.00697637	−0.01302767	−0.02045548	0.00086279
NGC 5845	−2	1	−0.00160040	0.00060800	0.00462400	−0.01326400	0.00080020	0.00861897	−0.01573795	−0.01925507	0.00080020
NGC 5846	0	0	0.00000000	0.00160000	0.00160000	−0.00320000	0.00000000	0.04308930	−0.10483564	−0.19428015	0.00000000
NGC 6086	−1	1	−0.00001492	−0.00109684	0.00129600	−0.00498484	0.00001492	0.00138738	0.00146205	−0.00295196	0.00001492
NGC 6251	−2	1	−0.00176120	−0.00614840	0.00129600	−0.01003640	0.00088060	0.00735691	−0.01364734	−0.02887339	0.00088060
NGC 6264	0	0	0.00000000	0.00221800	0.00221800	−0.00443600	0.00000000	0.00221883	0.00310852	−0.00443722	0.00000000
NGC 6323	0	0	0.00000000	0.00221800	0.00221800	−0.00443600	0.00000000	0.00258465	0.01379189	−0.00569656	0.00000000
NGC 7052	−2	1	−0.00180480	−0.00482760	0.00270400	−0.01293960	0.00090240	0.01062736	−0.01976312	−0.03080237	0.00090240
NGC 7457	0	1	0.00000000	0.00176400	0.00176400	−0.00352800	0.00075740	0.00180232	−0.00160043	−0.00366793	0.00075740
NGC 7582	0	0	0.00000000	0.03460000	0.03460000	−0.06919999	0.00000000	0.03460121	−0.05675261	−0.06920315	0.00000000
NGC 7768	0	1	0.00000000	0.01040000	0.01040000	−0.02080000	0.00388800	0.04072450	−0.08605497	−0.15456009	0.00388800
UGC 3789	0	0	0.00000000	0.00221800	0.00221800	−0.00443600	0.00000000	0.00221885	0.00444446	−0.00443731	0.00000000
NGC 0307	0	1	0.00000000	0.00221800	0.00221800	−0.00443600	0.00008884	0.00221933	−0.00419436	−0.00443999	0.00008884
NGC 1316	0	1	0.00000000	0.00019600	0.00019600	−0.00039200	0.00003881	0.08107346	−0.17447022	−0.21420352	0.00003881
NGC 1332	0	1	0.00000000	0.00129600	0.00129600	−0.00259200	0.00020022	0.00129723	−0.00159565	−0.00259534	0.00020022
NGC 1374	0	0	0.00000000	0.00021900	0.00021900	−0.00043800	0.00000000	0.00436364	−0.00781183	−0.01579101	0.00000000
NGC 1398	−1	0	0.00000000	0.00485370	0.00518400	−0.01069830	0.00000000	0.00518528	−0.01004053	−0.01037162	0.00000000
NGC 1407	0	1	0.00000000	0.00270400	0.00270400	−0.00540800	0.00001586	0.02964143	−0.06433558	−0.09472568	0.00001586
NGC 1550	0	1	0.00000000	0.00221800	0.00221800	−0.00443600	0.00054402	0.01115648	−0.02176448	−0.04509263	0.00054402
NGC 3091	0	1	0.00000000	0.00490000	0.00490000	−0.00980000	0.00057943	0.01205779	−0.02498498	−0.03827811	0.00057943
NGC 3368	0	1	0.00000000	0.00160000	0.00160000	−0.00320000	0.00002028	0.00160095	−0.00021428	−0.00320175	0.00002028
NGC 3489	0	1	0.00000000	0.00090000	0.00090000	−0.00180000	0.00001191	0.00090093	−0.00140569	−0.00180169	0.00001191
NGC 3627	0	0	0.00000000	0.00221800	0.00221800	−0.00443600	0.00000000	0.00221894	−0.00431971	−0.00443770	0.00000000
NGC 3923	−1	0	0.00000000	−0.00001900	0.00313600	−0.00942700	0.00000000	0.00739883	−0.01349074	−0.02458506	0.00000000
NGC 4371	0	1	0.00000000	0.00144400	0.00144400	−0.00288800	0.00004773	0.00145530	−0.00276670	−0.00292754	0.00004773
NGC 4472	0	0	0.00000000	0.00022500	0.00022500	−0.00045000	0.00000000	0.00623316	−0.01395564	−0.02764212	0.00000000
NGC 4486a	0	1	0.00000000	0.00019600	0.00019600	−0.00039200	0.00007537	0.00908209	−0.02046265	−0.03306464	0.00007537
NGC 4486b	0	0	0.00000000	0.00025600	0.00025600	−0.00051200	0.00000000	0.00030891	−0.00018686	−0.00067849	0.00000000
NGC 4501	−2	1	−0.00026617	−0.00013134	0.00090000	−0.00283134	0.00013309	0.00090122	−0.00128698	−0.00180322	0.00013309
NGC 4699	0	1	0.00000000	0.00221800	0.00221800	−0.00443600	0.00019092	0.00221892	−0.00345774	−0.00443764	0.00019092
NGC 4751	0	1	0.00000000	0.00221800	0.00221800	−0.00443600	0.00053312	0.00825643	−0.01720868	−0.02762641	0.00053312
NGC 5018	−2	1	−0.00021631	0.00205479	0.00270400	−0.00605721	0.00010815	0.00451187	−0.00950904	−0.01342547	0.00010815
NGC 5328	−2	1	−0.00002499	−0.00348797	0.00221800	−0.01014197	0.00001249	0.07293955	−0.18097316	−0.39152691	0.00001249
NGC 5419	0	0	0.00000000	0.00221800	0.00221800	−0.00443600	0.00000000	0.00721928	0.00110698	−0.02481270	0.00000000
NGC 5516	0	0	0.00000000	0.00221800	0.00221800	−0.00443600	0.00000000	0.00601705	−0.01328545	−0.01972207	0.00000000
NGC 6861	−2	1	−0.00003291	0.00489019	0.00518400	−0.01066181	0.00001645	0.02407962	−0.05868636	−0.12175512	0.00001645
NGC 7619	−1	1	−0.00010842	0.00106015	0.00384400	−0.01047185	0.00010842	0.02500535	−0.05654635	−0.09997252	0.00010842

Note. Column 1: galaxy name; columns 2 and 3: $a_{\rm BH}$ and f factors, see Section 3; column 4: error covariances between $M_{\rm BH}$ and σ; column 5: error covariances between $M_{\rm BH}$ and $M_{\rm Bu}$; column 6: error covariances between $M_{\rm BH}$ and $r_{\rm h}$; column 7: error covariances between $M_{\rm BH}$ and $\rho_{\rm h}$; column 8: error covariances between $M_{\rm Bu}$ and σ; column 9: error covariances between $M_{\rm Bu}$ and $r_{\rm h}$; column 10: error covariances between $M_{\rm Bu}$ and $\rho_{\rm h}$; column 11: error covariances between $r_{\rm h}$ and $\rho_{\rm h}$; column 12: error covariances between $\rho_{\rm h}$ and σ.

Table 7
Values of the Error Covariance Matrices: Off-diagonal Terms for the Kormendy & Ho (2013) Sample

Galaxy	$\delta \log M_{\rm BH}$ $\delta \log M_{{\rm Bu},C}$	$\delta \log M_{\rm BH}$ $\delta \log \rho_{{\rm h},C}$	$\delta \log M_{{\rm Bu},C}$ $\delta \log r_{\rm h}$	$\delta \log M_{{\rm Bu},C}$ $\delta \log \rho_{{\rm h},C}$	$\delta \log r_{\rm h}$ $\delta \rho_{{\rm h},C}$
IC 1459	0.006272	−0.003136	0.007293	−0.0005831	−0.006919
NGC 0221	0.000512	−0.000256	0.000598	0.009294	−0.0005159
NGC 0224	0.000648	−0.000324	0.0006492	0.00745	−0.0003268
NGC 0524	0.0032	−0.0016	0.004885	0.000887	−0.008082
NGC 0821	0.002312	−0.001156	0.01613	−0.02763	−0.05871
NGC 1023	0.002048	−0.001024	0.002049	0.006049	−0.001029
NGC 1194	0.004436	−0.002218	0.004514	0.003483	−0.002489
NGC 1399	0.000392	−0.000196	0.0006271	0.00713	−0.001266
NGC 2549	0.006272	−0.003136	0.01042	−0.008197	−0.02038
NGC 3115	0.000648	−0.000324	0.01684	−0.0311	−0.0625
NGC 3245	0.0032	−0.0016	0.003319	0.004655	−0.001863
NGC 3377	0.000648	−0.000324	0.009407	−0.01437	−0.04318
NGC 3379	0.000968	−0.000484	0.001988	0.004676	−0.004624
NGC 3585	0.002592	−0.001296	0.03815	−0.07402	−0.1055
NGC 3608	0.001568	−0.000784	0.01364	−0.0237	−0.06167
NGC 3998	0.002888	−0.001444	0.003164	0.004598	−0.00224
NGC 4026	0.006272	−0.003136	0.006941	0.0002975	−0.005281
NGC 4258	0.0018	−0.0009	0.001801	0.006297	−0.0009052
NGC 4291	0.008192	−0.004096	0.0117	−0.00864	−0.01921
NGC 4374	0.000392	−0.000196	0.003876	−0.0009602	−0.01713
NGC 4473	0.000392	−0.000196	0.006151	−0.006832	−0.0308
NGC 4486	0.000512	−0.000256	0.00437	−0.002294	−0.02279
NGC 4526	0.004436	−0.002218	0.00444	0.003655	−0.002231
NGC 4564	0.000392	−0.000196	0.003889	−0.0004435	−0.01238
NGC 4594	0.002592	−0.001296	0.002719	0.005203	−0.001806
NGC 4649	0.000512	−0.000256	0.01216	−0.02124	−0.05512
NGC 4697	0.000392	−0.000196	0.003104	0.001064	−0.01229
NGC 5077	0.01767	−0.008836	0.01833	−0.01112	−0.01127
NGC 5576	0.001568	−0.000784	0.003206	0.002386	−0.009614
NGC 5845	0.009248	−0.004624	0.01324	−0.009713	−0.01463
NGC 6086	0.002592	−0.001296	0.002683	0.005289	−0.001656
NGC 7457	0.003528	−0.001764	0.003566	0.004482	−0.001904
NGC 7768	0.0208	−0.0104	0.05112	−0.08686	−0.1442
NGC 1332	0.002592	−0.001296	0.002593	0.005505	−0.001299
NGC 1374	0.000438	−0.000219	0.004583	−0.002129	−0.01557
NGC 1407	0.005408	−0.002704	0.03235	−0.0594	−0.09202
NGC 1550	0.004436	−0.002218	0.01337	−0.01832	−0.04287
NGC 3031	0.000512	−0.000256	0.003543	0.0007061	−0.009686
NGC 3091	0.0098	−0.0049	0.01696	−0.01886	−0.03338
NGC 4472	0.00045	−0.000225	0.006458	−0.007113	−0.02742
NGC 4486a	0.000392	−0.000196	0.009278	−0.01325	−0.03287
NGC 4751	0.004436	−0.002218	0.01047	−0.01071	−0.02541
NGC 5516	0.004436	−0.002218	0.008235	−0.005464	−0.0175
NGC 6861	0.01037	−0.005184	0.02926	−0.05073	−0.1166
NGC 7619	0.007688	−0.003844	0.02885	−0.05123	−0.09613

Note. Column 1: galaxy name; column 2: error covariances between $M_{\rm BH}$ and $M_{{\rm Bu},C}$; column 3: error covariances between $M_{\rm BH}$ and $\rho_{{\rm h},C}$; column 4: error covariances between $M_{{\rm Bu},C}$ and $r_{\rm h}$; column 5: error covariances between $M_{{\rm Bu},C}$ and $\rho_{{\rm h},C}$; column 6: error covariances between $r_{\rm h}$ and $\rho_{{\rm h},C}$.

a. the slopes of the $M_{\rm BH}$–σ and $M_{\rm BH}$–$M_{\rm Bu}$ relations agree with published results within the quoted errors;
b. core ellipticals have more massive BHs than other classical bulges, at a given σ or bulge mass, when correlations derived using samples including noncore galaxies are adopted; moreover, the smallest intrinsic and measured scatter of the $M_{\rm BH}$–σ and $M_{\rm BH}$–$M_{\rm Bu}$ relations are measured for the sample of core ellipticals;
c. power-law early-type galaxies and classical bulges follow similar $M_{\rm BH}$–σ and $M_{\rm BH}$–$M_{\rm Bu}$ relations;
d. pseudobulges have smaller BH masses than the rest of the sample at a given σ or $M_{\rm Bu}$.

Our sample indicates that the $M_{\rm BH}$–σ relation is possibly a better predictor (i.e., with lower intrinsic scatter) of $M_{\rm BH}$ than the $M_{\rm BH}$–$M_{\rm Bu}$ relation; this remains true even when we augment the errors on the bulge mass by 0.15 dex in quadrature. However, the difference is not statistically significant. Kormendy & Ho (2013) argue on the basis of their KH45 sample that both relations are equivalent (see Table 13 and discussion below).

Graham & Scott (2013) claim that "Sérsic galaxies" follow a quadratic $M_{\rm BH}$–$M_{\rm Bu}$ relation. We disagree with this interpretation: *classical* bulges (all with a Sérsic profile) and core-Sérsic galaxies follow the same linear $M_{\rm BH}$–$M_{\rm Bu}$ relations within the errors. The steepening of the relation at low bulge masses for

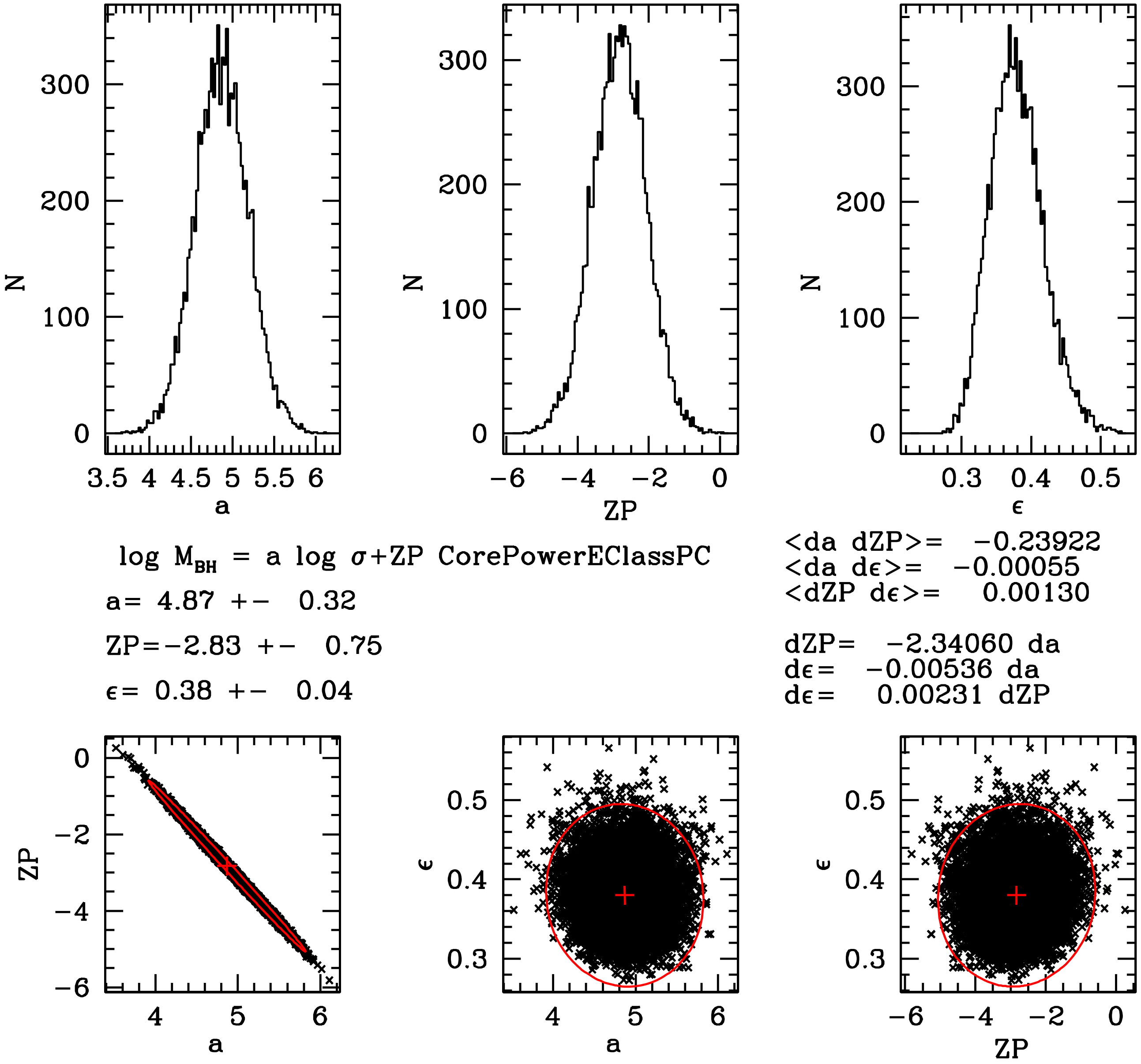

Figure 10. Top row: the posterior probability distributions of the fitted parameters of the correlation between $\log M_{\rm BH}$ and $\log \sigma$ for the subsample CorePowerEClassPC. Middle row: mean values of the parameters and errors, off-diagonal terms of the parameter variance matrix, and resulting correlations between parameter errors. Bottom row: the correlations between all possible pairs of parameters. The red ellipse shows the 3σ contours.

"Sérsic galaxies" seen by Graham & Scott (2013) stems from their possibly uncertain bulge masses (see Figure 7) and the fact that they do not distinguish between pseudo and classical bulges. We also disagree with their interpretation of the role of barred galaxies: considering barred galaxies with classical bulges delivers the same $M_{\rm BH}$–σ and $M_{\rm BH}$–$M_{\rm Bu}$ relations within the errors that we derive for nonbarred classical bulges and early-type galaxies. Again, it is the pseudobulges, not the barred classical bulges, that deviate from the $M_{\rm BH}$–σ and $M_{\rm BH}$–$M_{\rm Bu}$ relations.

The intrinsic and measured scatter of our $M_{\rm BH}$–σ and $M_{\rm BH}$–$M_{\rm Bu}$ relations are generally larger than the values quoted in previous studies, although the coefficients of the relations are compatible within the errors. This stems from the sample of objects that comes from our SINFONI survey, where we deliberately observed objects with extreme properties (i.e., objects with small or large velocity dispersions, particularly compact objects or merger remnants).

Finally, we explicitly show that galaxy sizes and densities correlate with BH masses too, although with larger scatter. This and the discrepant results on the existence of the "BH FP" quoted in Section 1 motivate our next step, which is to investigate five two-parameter correlations of the type $z = ax + by + ZP + N(0, \epsilon)$:

$$M_{\rm BH} - \sigma - \rho_{\rm h}\colon \log M_{\rm BH} = a \log \sigma + b \log \rho_{\rm h} + ZP, \quad (19)$$

$$M_{\rm BH} - M_{\rm Bu} - \rho_{\rm h}\colon \log M_{\rm BH} = a \log M_{\rm Bu} + b \log \rho_{\rm h} + ZP, \quad (20)$$

$$M_{\rm BH} - \sigma - r_{\rm h}\colon \log M_{\rm BH} = a \log \sigma + b \log r_{\rm h} + ZP, \quad (21)$$

$$M_{\rm BH} - M_{\rm Bu} - r_{\rm h}\colon \log M_{\rm BH} = a \log M_{\rm Bu} + b \log r_{\rm h} + ZP, \quad (22)$$

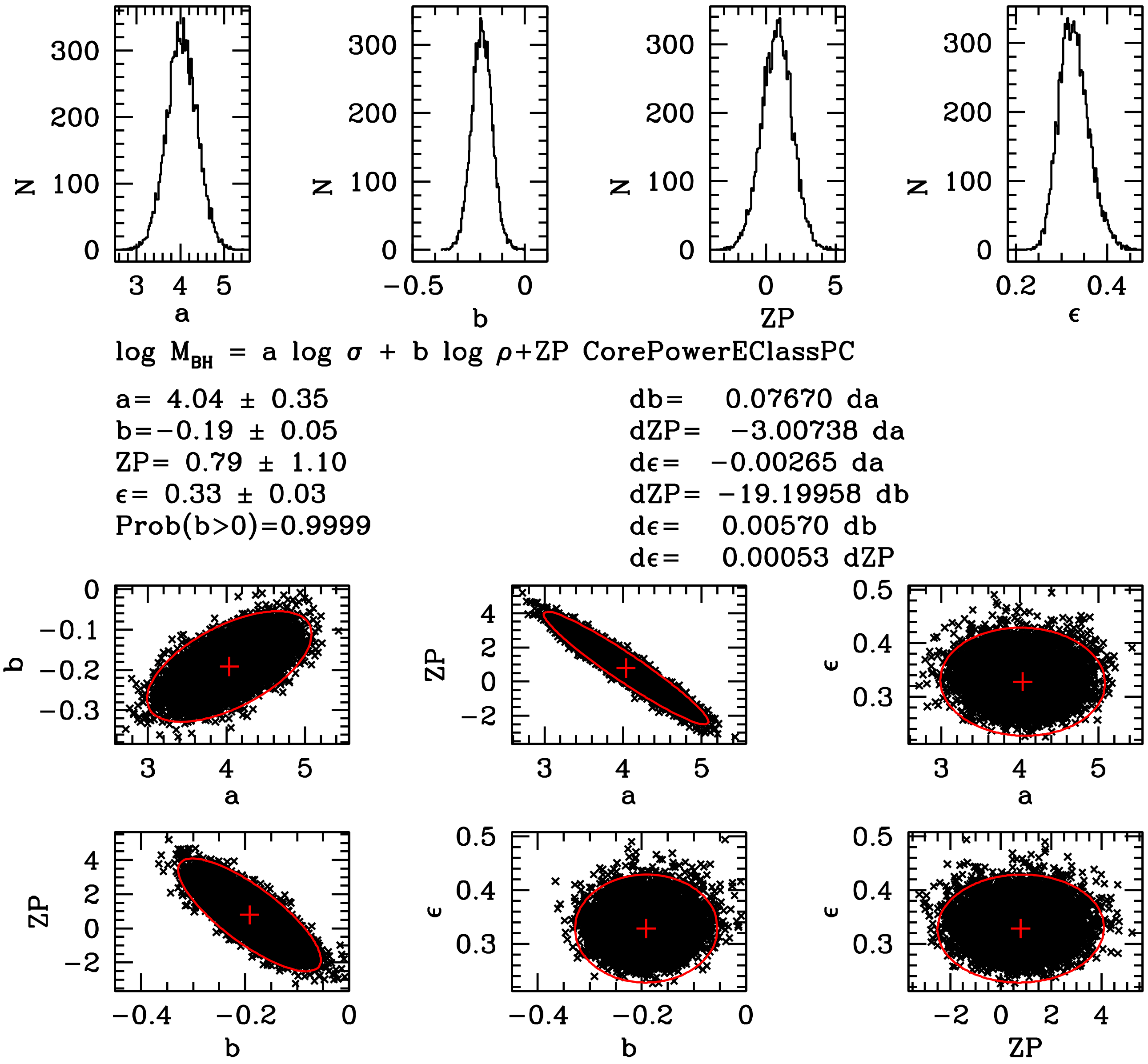

Figure 11. Top row: the posterior probability distributions of the fit to the relation $\log M_{\rm BH} = \alpha\sigma + \beta\rho + ZP$ for the subsample CorePowerEClassPC. Middle row: mean values of the parameters and errors, and correlations between parameter errors. The plots on the bottom show the correlations between all possible pairs of parameters. The red ellipse shows the 3σ contours.

$$M_{\rm BH} - M_{\rm Bu} - \sigma\text{: } \log M_{\rm BH} = a \log M_{\rm Bu} + b \log\sigma + ZP. \tag{23}$$

Table 12 gives the results for the 12 (sub)samples considered above: the values of the best-fit parameters a, b, and ZP with their errors of the correlations of the type $z = ax + by + ZP$, the intrinsic and measured scatter ϵ and rms, the probability of the bivariate correlation $P(b \neq 0)$ of $b \leqslant 0$ (if $b_{\rm fit} > 0$) or of $b \geqslant 0$ (if $b_{\rm fit} < 0$), the value of ΔcAIC and of $RP = \exp(\Delta{\rm cAIC})$ (the relative probability of the mono- and bivariate solutions), the Spearman correlation coefficient of the residuals $z - ax$ with y, and the probability of the latter's value being greater due to chance.

The correlations involving σ ($M_{\rm BH}$–σ–$\rho_{\rm h}$, $M_{\rm BH}$–σ–$r_{\rm h}$, $M_{\rm BH}$–$M_{\rm Bu}$–σ) are established with high confidence for all subsamples except core ellipticals, power-law ellipticals, and pseudobulges (each of these classes have ≈30 or fewer objects). In particular, for the sample CorePowerEClassPC (the 77 galaxies that are not pseudobulges) the relations

$$\log M_{\rm BH} = (4.04 \pm 0.35)\log\sigma - (0.19 \pm 0.05)\log\rho_{\rm h} + (0.79 \pm 1.11), \tag{24}$$

$$\log M_{\rm BH} = (3.74 \pm 0.40)\log\sigma + (0.38 \pm 0.09)\log r_{\rm h} - (0.35 \pm 0.90) \tag{25}$$

and

$$\log M_{\rm BH} = (0.37 \pm 0.09)M_{\rm Bu} + (3.19 \pm 0.52)\log\sigma - (2.93 \pm 0.66) \tag{26}$$

have a measured/intrinsic scatter of just 0.36/0.33 dex, 0.05 dex less than the respective one-dimensional solution $M_{\rm BH}$–σ, a probability $P(b \neq 0) > 0.99$, very negative ΔcAIC values (<-13, or relative probabilities of the mono- and bivariate solutions less than 0.001), and a strong Spearman coefficient value ($|r_{\rm S}| > 0.5$ with $P(r_{\rm S}) < 10^{-6}$) of the

Table 8
(Sub)samples Considered in the Correlation Analysis

Sample	Selection Flags	Explanation
All	$T \leqslant 3$ and $b \leqslant 1$ and $B \leqslant 2$	All galaxies without NGC 4486b
CoreE	$T = 0$	Core ellipticals
CorePowerE	$T \leqslant 1$	Core and power-law ellipticals without NGC 4486b
CorePowerEClass	$T \leqslant 2$	Core and power-law ellipticals plus classical bulges without NGC 4486b
CorePowerEClassPC	$T \leqslant 2$ plus ($T = 3$ and $B = 2$)	Core and power-law ellipticals, classical bulges and classical component of composite bulges without NGC 4486b
CorePowerEClassPCSINFONI	$T \leqslant 2$ and $S = 1$ plus ($T = 3$ and $B = 2$ and $S = 1$))	Core and power-law ellipticals, classical bulges and classical component of composite bulges, only SINFONI measurements without NGC 4486b
CorePowerEClassPCLit	$T \leqslant 2$ and $S = 0$ plus ($T = 3$ and $B = 2$ and $S = 0$)	Core and power-law ellipticals, classical bulges and classical component of composite bulges, only literature measurements
CorePowerEClassnoBars	$T \leqslant 2$ and $b \leqslant 0.5$	Core and power-law ellipticals, classical bulges and classical component of composite bulges but without barred objects and without NGC 4486b
PowerE	$T = 1$	Power-law ellipticals without NGC 4486b
PowerEClass	$1 \leqslant T \leqslant 2$	Power-law ellipticals and classical bulges without NGC 4486b
PowerEClassPC	$1 \leqslant T \leqslant 2$ plus ($T = 3$ and $B = 2$)	Power-law ellipticals classical bulges and classical component of composite bulges without NGC 4486b
Pseudo	$T = 3$ and $B \neq 2$	Pseudobulges

Note. Flags (see also Table 1): T (type, 0 for core ellipticals, 1 for power-law ellipticals, 2 for classical bulges, 3 for pseudobulges), b (0: no bar, 1: barred), B (0 for one-component galaxy, 1 for bulge plus disk galaxy, 2 for galaxy with composite (classical plus pseudo) bulge plus disk).

residuals $z - ax$ with the y variable. We illustrate the three correlations in the top and bottom left-hand panels of Figure 14.

As in the single-variable correlations presented in Figure 13, the subsample of pseudobulges (see Figure 14, bottom right, and Figure 15, top and bottom left) has smaller BH masses for a given velocity dispersion. The smallest offsets are observed at the largest densities and smallest scale lengths, and pseudobulges smaller than 1 kpc or denser than $10^{10}\ M_\odot\ \mathrm{kpc}^{-3}$ roughly follow the correlations defined by the other subsamples. As a consequence, it is not possible to derive a tight bivariate correlation that simultaneously describes the behavior of core, power-law ellipticals, classical bulges, and pseudobulges. If we fit the sample All, we get a steeper σ coefficient and a measured and intrinsic scatter larger by 0.06–0.07 dex than for the subsample without pseudobulges. Nevertheless, the bivariate correlation remains highly significant ($P(b \neq 0) > 0.99$), and the Spearman coefficient value of the correlation of the residuals $z - ax$ with the y variable is strong ($|r_S| > 0.49$, $P(r_S) < 4 \times 10^{-7}$).

The right-hand plots of Figure 5 illustrate what happens if we use the cylindrical densities and radii for pseudobulges that we calculate from Equation (15) and $h_z = 0.2a_e/1.67$. Since densities are increased and scale lengths do not change much, only the density threshold above which pseudobulges follow the scaling relations of the other subsamples changes, to about $10^{11} M_\odot\ \mathrm{kpc}^{-3}$.

The evidence for the correlations M_{BH}–M_{Bu}–ρ_{h} and M_{BH}–M_{Bu}–r_{h} is weaker but still convincing. Here the bivariate correlations derived for the CorePowerEClassPC sample are significant at the 98% level, and the ΔcAIC values are negative (<-2.3) with relative probability of the mono- and bivariate solutions less than 0.32, with large Spearman correlation coefficients ($|r_S| > 0.45$) and low $P(r_S)$ probabilities ($P(r_S) < 4 \times 10^{-5}$ for the residuals $z - ay$), but only a marginal reduction (by 0.01 dex) of the measured scatter compared to the monovariate correlations is achieved. We derive the following relations:

$$\log M_{\mathrm{BH}} = (1.11 \pm 0.14)\log M_{\mathrm{Bu}} + (0.23 \pm 0.11)\log \rho_{\mathrm{h}} - (5.52 \pm 2.42), \tag{27}$$

$$\log M_{\mathrm{BH}} = (1.33 \pm 0.24)\log M_{\mathrm{Bu}} - (0.68 \pm 0.32)\log r_{\mathrm{h}} - (5.74 \pm 2.53). \tag{28}$$

Stronger bivariate correlations are obtained when excluding core ellipticals (the subsample PowerEClassPC); see discussion below.

This lets us present the correlations M_{BH}–M_{Bu}–ρ_{h} and M_{BH}–M_{Bu}–r_{h} in a slightly different fashion in Figure 16. There we plot the two relations separately for the subsamples CoreE, PowerEClassPC, and Pseudo. First, we note that the subsample of CoreE is offset to the left of the PoweEClassPC sequence at lower densities and to the right at larger scale lengths. Indeed, fitting the M_{BH}–M_{Bu}–ρ_{h} and M_{BH}–M_{Bu}–r_{h} relations to the PowerEClassPC sample delivers steeper slopes for both the ρ_{h} and r_{h} dependence.

Second, as found above, the pseudobulges tend to have lower BH masses at any bulge mass. Figure 17 shows that pseudobulges with large densities or small scale lengths tend to be closer to the M_{BH}–M_{Bu}–ρ_{h} and M_{BH}–M_{Bu}–r_{h} relations defined by the other subsamples.

We now discuss the effects of considering different samples. The exclusion of barred objects weakens only slightly the significance of all the bivariate correlations discussed above; we come back to this issue at the end of this section. If we just fit the 22 galaxies with SINFONI BH mass determinations, we find good evidence for the bivariate correlations M_{BH}–σ–ρ_{h}, M_{BH}–σ–r_{h}, and M_{BH}–M_{Bu}–σ ($P(\beta) \neq 0 > 0.97$, ΔcAIC < -0.9), but weaker or no evidence ($P(\beta) \neq 0 > 0.95$ but positive ΔcAIC) for the bivariate correlations M_{BH}–M_{Bu}–ρ_{h} and M_{BH}–M_{Bu}–r_{h}. Similar numbers are found if we fit only the 57 galaxies with BH mass measurements from the literature. The results do not change if we minimize the

Table 9
One-dimensional Correlations within Bulge Parameters

Fit	Sample	N	a	da	ZP	dZP	ϵ	$d\epsilon$	rms
$M_{\rm Bu}$–$r_{\rm h}$	All	96	1.285	0.041	10.35	0.029	0.241	0.02	0.251
	CoreE	31	1.246	0.104	10.41	0.101	0.131	0.028	0.151
	CorePowerE	47	1.37	0.072	10.27	0.062	0.186	0.026	0.2
	CorePowerEClass	71	1.245	0.055	10.4	0.041	0.228	0.022	0.232
	CorePowerEClassPC	77	1.256	0.046	10.39	0.034	0.238	0.022	0.245
	CorePowerEClassnoBars	61	1.261	0.065	10.39	0.052	0.231	0.025	0.228
	CorePowerEClassPCSINFONI	22	1.24	0.094	10.43	0.078	0.268	0.05	0.232
	CorePowerEClassPCLit	57	1.261	0.056	10.38	0.04	0.236	0.026	0.245
	PowerE	16	1.348	0.174	10.25	0.108	0.302	0.073	0.26
	PowerEClass	40	1.204	0.108	10.4	0.053	0.287	0.037	0.278
	PowerEClassPC	46	1.234	0.081	10.39	0.045	0.294	0.035	0.291
	Pseudo	19	1.018	0.156	10.16	0.069	0.234	0.05	0.209
$M_{\rm Bu}$–$\rho_{\rm h}$	All	96	−0.678	0.04	16.78	0.363	0.414	0.033	0.423
	CoreE	31	−0.63	0.101	16.53	0.79	0.219	0.044	0.245
	CorePowerE	47	−0.743	0.078	17.35	0.637	0.332	0.043	0.347
	CorePowerEClass	71	−0.626	0.051	16.42	0.442	0.379	0.036	0.379
	CorePowerEClassPC	77	−0.654	0.044	16.64	0.389	0.401	0.036	0.405
	CorePowerEClassnoBars	61	−0.624	0.061	16.41	0.511	0.386	0.04	0.375
	CorePowerEClassPCSINFONI	22	−0.643	0.087	16.6	0.751	0.443	0.082	0.386
	CorePowerEClassPCLit	57	−0.655	0.053	16.63	0.466	0.401	0.043	0.404
	PowerE	16	−0.666	0.171	16.57	1.48	0.499	0.12	0.442
	PowerEClass	40	−0.514	0.089	15.34	0.812	0.45	0.057	0.434
	PowerEClassPC	46	−0.582	0.074	15.91	0.696	0.479	0.055	0.468
	Pseudo	19	−0.42	0.113	14	1.098	0.345	0.075	0.307
ρ_h–$r_{\rm h}$	All	96	−1.716	0.041	9.428	0.029	0.242	0.02	0.251
	CoreE	31	−1.756	0.105	9.49	0.104	0.133	0.027	0.151
	CorePowerE	47	−1.634	0.072	9.352	0.063	0.187	0.027	0.199
	CorePowerEClass	71	−1.758	0.056	9.48	0.041	0.229	0.022	0.231
	CorePowerEClassPC	77	−1.745	0.047	9.468	0.035	0.238	0.022	0.244
	CorePowerEClassnoBars	61	−1.743	0.065	9.466	0.052	0.231	0.024	0.227
	CorePowerEClassPCSINFONI	22	−1.758	0.093	9.503	0.077	0.264	0.049	0.231
	CorePowerEClassPCLit	57	−1.737	0.055	9.457	0.04	0.236	0.026	0.245
	PowerE	16	−1.662	0.177	9.336	0.111	0.306	0.074	0.259
	PowerEClass	40	−1.795	0.106	9.482	0.052	0.286	0.037	0.277
	PowerEClassPC	46	−1.764	0.082	9.468	0.045	0.294	0.035	0.29
	Pseudo	19	−1.959	0.156	9.249	0.069	0.233	0.051	0.21

Note. Column 1: fit type; column 2: sample type, see Table 8; column 3: number of data points; columns 4 and 5: slope of the correlation and its error; columns 6 and 7: zero point of the correlation and its errors; columns 8 and 9: intrinsic scatter and its errors; column 10: measured scatter.

Table 10
Two-dimensional Correlation $\log M_{\rm Bu} = a \log r_{\rm h} + b \log \sigma + ZP$ for Different Samples

Fit	Sample	a	da	b	db	ZP	dZP	ϵ	$d\epsilon$	rms	$P(b \neq 0)$
$M_{\rm Bu}$–$r_{\rm h}$–σ	All	0.974	0.039	1.638	0.148	6.699	0.33	0.146	0.013	0.157	0.9999
	CoreE	1.033	0.133	1.091	0.443	7.957	0.993	0.117	0.022	0.119	0.9923
	CorePowerE	1.024	0.078	1.487	0.245	6.991	0.54	0.126	0.017	0.128	0.9999
	CorePowerEClass	0.94	0.047	1.633	0.167	6.735	0.375	0.136	0.014	0.136	0.9999
	CorePowerEClassPC	0.978	0.042	1.65	0.17	6.666	0.383	0.146	0.014	0.15	0.9999
	CorePowerEClassnoBars	0.911	0.054	1.721	0.177	6.546	0.395	0.133	0.015	0.131	0.9999
	CorePowerEClassPCSINFONI	0.93	0.084	1.814	0.35	6.271	0.803	0.161	0.032	0.138	0.9999
	CorePowerEClassPCLit	0.993	0.051	1.645	0.202	6.687	0.454	0.147	0.017	0.152	0.9999
	PowerE	0.996	0.13	1.671	0.382	6.575	0.841	0.17	0.043	0.136	0.9995
	PowerEClass	0.966	0.067	1.76	0.195	6.454	0.439	0.15	0.02	0.143	0.9999
	PowerEClassPC	1.012	0.055	1.818	0.2	6.301	0.45	0.161	0.02	0.16	0.9999
	Pseudo	0.975	0.132	1.472	0.604	7.066	1.274	0.185	0.045	0.18	0.988

Note. Column 1: fit type; column 2: sample type, see Table 8; columns 3 and 4: first variable slope of the correlation and its error; columns 5 and 6: second variable slope of the correlation and its error; columns 7 and 8: zero point of the correlation and its errors; columns 9 and 10: intrinsic scatter and its errors; column 11: measured scatter; column 12: probability of the bivariate correlation (see the text).

Table 11
One-dimensional Correlations with Black Hole Masses

Fit	Sample	N	a	da	ZP	dZP	ϵ	$d\epsilon$	rms	r_S	$P(r_S)$
M_{BH}–σ	All	96	5.246	0.274	−3.77	0.631	0.417	0.037	0.459	0.9109	6.59e-38
	CoreE	31	4.772	0.794	−2.476	1.942	0.332	0.06	0.366	0.6936	1.52e-05
	CorePowerE	47	4.713	0.458	−2.393	1.099	0.38	0.05	0.399	0.8005	1.45e-11
	CorePowerEClass	71	4.546	0.33	−2.03	0.78	0.348	0.037	0.38	0.8677	1.24e-22
	CorePowerEClassPC	77	4.868	0.32	−2.827	0.75	0.38	0.038	0.409	0.883	2.42e-26
	CorePowerEClassPCSINFONI	22	4.976	0.72	−3.025	1.72	0.502	0.093	0.446	0.7134	0.000194
	CorePowerEClassPCLit	57	4.829	0.372	−2.756	0.867	0.335	0.044	0.388	0.9015	1.18e-21
	CorePowerEClassnoBars	61	4.566	0.36	−2.05	0.858	0.343	0.04	0.379	0.8501	4.48e-18
	PowerE	16	3.992	0.874	−0.856	2.01	0.496	0.122	0.416	0.6676	0.00471
	PowerEClass	40	3.806	0.442	−0.421	1.016	0.347	0.05	0.35	0.8006	5.58e-10
	PowerEClassPC	46	4.227	0.446	−1.452	1.015	0.397	0.051	0.401	0.8211	2.77e-12
	Pseudo	19	2.129	1.349	2.526	2.832	0.455	0.108	0.45	0.4159	0.0766
M_{BH}–M_{Bu}	All	96	0.962	0.066	−2.099	0.716	0.535	0.044	0.54	0.8505	5.64e-28
	CoreE	31	0.906	0.23	−1.35	2.672	0.431	0.07	0.423	0.5728	0.000759
	CorePowerE	47	0.986	0.114	−2.309	1.293	0.436	0.055	0.442	0.7308	5.49e-09
	CorePowerEClass	71	0.885	0.08	−1.155	0.887	0.424	0.043	0.444	0.7776	1.51e-15
	CorePowerEClassPC	77	0.846	0.064	−0.713	0.697	0.431	0.041	0.447	0.8147	2e-19
	CorePowerEClassPCSINFONI	22	0.945	0.12	−1.643	1.335	0.447	0.086	0.403	0.8557	3.84e-07
	CorePowerEClassPCLit	57	0.794	0.074	−0.231	0.805	0.417	0.049	0.438	0.8081	3.01e-14
	CorePowerEClassnoBars	61	0.925	0.094	−1.618	1.059	0.435	0.048	0.448	0.7512	3.07e-12
	PowerE	16	0.912	0.226	−1.579	2.454	0.55	0.134	0.461	0.43	0.0964
	PowerEClass	40	0.783	0.132	−0.094	1.411	0.448	0.061	0.451	0.5717	0.000116
	PowerEClassPC	46	0.758	0.095	0.166	1.002	0.453	0.056	0.452	0.6782	2.24e-07
	Pseudo	19	0.094	0.298	6.058	2.968	0.519	0.115	0.477	0.0158	0.949
M_{BH}–r_h	All	96	1.149	0.104	7.894	0.074	0.644	0.05	0.628	0.7704	4.49e-20
	CoreE	31	1.05	0.318	8.162	0.319	0.456	0.075	0.444	0.5862	0.000529
	CorePowerE	47	1.3	0.178	7.864	0.158	0.488	0.062	0.489	0.6739	2.08e-07
	CorePowerEClass	71	0.999	0.122	8.122	0.093	0.52	0.05	0.524	0.7057	6.33e-12
	CorePowerEClassPC	77	0.991	0.098	8.119	0.076	0.528	0.048	0.529	0.7482	5.26e-15
	CorePowerEClassPCSINFONI	22	1.096	0.203	8.257	0.171	0.6	0.113	0.514	0.8229	2.57e-06
	CorePowerEClassPCLit	57	0.929	0.109	8.059	0.083	0.501	0.055	0.508	0.7333	8.74e-11
	CorePowerEClassnoBars	61	1.071	0.15	8.064	0.122	0.53	0.056	0.529	0.6853	1.11e-09
	PowerE	16	1.166	0.374	7.804	0.235	0.636	0.151	0.536	0.2647	0.322
	PowerEClass	40	0.726	0.212	8.105	0.105	0.571	0.074	0.555	0.3646	0.0207
	PowerEClassPC	46	0.798	0.155	8.063	0.089	0.575	0.068	0.559	0.4988	0.000419
	Pseudo	19	0.098	0.326	7.022	0.15	0.524	0.111	0.474	0.1299	0.596
M_{BH}–ρ_h	All	96	−0.589	0.07	13.49	0.633	0.734	0.058	0.721	−0.7016	1.71e-15
	CoreE	31	−0.517	0.195	13.21	1.529	0.483	0.08	0.475	−0.4815	0.00609
	CorePowerE	47	−0.7	0.124	14.53	1.008	0.55	0.071	0.564	−0.5899	1.28e-05
	CorePowerEClass	71	−0.472	0.078	12.7	0.674	0.597	0.057	0.599	−0.6346	2.81e-09
	CorePowerEClassPC	77	−0.493	0.064	12.85	0.567	0.612	0.055	0.61	−0.6879	4.77e-12
	CorePowerEClassPCSINFONI	22	−0.539	0.134	13.46	1.16	0.72	0.132	0.614	−0.7811	1.78e-05
	CorePowerEClassPCLit	57	−0.466	0.073	12.53	0.641	0.575	0.063	0.58	−0.6732	9.59e-09
	CorePowerEClassnoBars	61	−0.493	0.094	12.87	0.79	0.614	0.064	0.609	−0.6064	2.23e-07
	PowerE	16	−0.553	0.249	13.07	2.146	0.73	0.178	0.628	−0.2029	0.451
	PowerEClass	40	−0.234	0.125	10.39	1.137	0.631	0.082	0.616	−0.2232	0.166
	PowerEClassPC	46	−0.323	0.097	11.15	0.913	0.657	0.076	0.637	−0.3878	0.00776
	Pseudo	19	−0.065	0.162	7.628	1.58	0.52	0.113	0.472	−0.1869	0.444
M_{BH}–$M_{Bu}^{0.5}\sigma^2$	All	96	1.198	0.061	−3.673	0.613	0.417	0.036	0.439	0.9122	3.37e-38
	CoreE	31	1.185	0.212	−3.492	2.274	0.356	0.062	0.371	0.6802	2.56e-05
	CorePowerE	47	1.168	0.107	−3.336	1.121	0.363	0.048	0.382	0.8032	1.09e-11
	CorePowerEClass	71	1.096	0.075	−2.57	0.769	0.333	0.036	0.363	0.8588	1.01e-21
	CorePowerEClassPC	77	1.093	0.063	−2.538	0.64	0.342	0.034	0.367	0.881	4.36e-26
	CorePowerEClassPCSINFONI	22	1.157	0.125	−3.089	1.295	0.396	0.075	0.359	0.8472	6.55e-07
	CorePowerEClassPCLit	57	1.05	0.072	−2.156	0.723	0.316	0.041	0.356	0.8854	6.01e-20
	CorePowerEClassnoBars	61	1.12	0.085	−2.821	0.885	0.341	0.04	0.372	0.8353	5.75e-17
	PowerE	16	1.059	0.21	−2.292	2.103	0.463	0.115	0.392	0.5971	0.0146
	PowerEClass	40	1.007	0.114	−1.698	1.137	0.343	0.049	0.351	0.745	3.52e-08
	PowerEClassPC	46	1.023	0.093	−1.874	0.913	0.354	0.045	0.359	0.8023	2.04e-11
	Pseudo	19	0.358	0.389	3.719	3.564	0.504	0.114	0.466	0.1975	0.418

Table 11
(Continued)

Fit	Sample	N	a	da	ZP	dZP	ϵ	$d\epsilon$	rms	r_S	$P(r_S)$
M_{BH}–$M_{Bu}\sigma^2$	All	96	0.747	0.042	−3.205	0.648	0.456	0.038	0.468	0.8948	1.08e-34
	CoreE	31	0.743	0.148	−3.083	2.448	0.379	0.065	0.386	0.6505	7.43e-05
	CorePowerE	47	0.746	0.072	−3.161	1.165	0.38	0.05	0.397	0.7847	6.72e-11
	CorePowerEClass	71	0.69	0.05	−2.23	0.789	0.358	0.038	0.385	0.8384	7.39e-20
	CorePowerEClassPC	77	0.673	0.042	−1.963	0.651	0.367	0.036	0.389	0.8644	4.25e-24
	CorePowerEClassPCSINFONI	22	0.726	0.081	−2.662	1.279	0.404	0.077	0.365	0.876	9.19e-08
	CorePowerEClassPCLit	57	0.64	0.049	−1.512	0.756	0.347	0.042	0.38	0.8591	1.25e-17
	CorePowerEClassnoBars	61	0.711	0.059	−2.588	0.935	0.366	0.043	0.392	0.8132	1.71e-15
	PowerE	16	0.687	0.14	−2.3	2.17	0.479	0.119	0.408	0.5765	0.0194
	PowerEClass	40	0.636	0.08	−1.432	1.217	0.373	0.052	0.379	0.7181	1.83e-07
	PowerEClassPC	46	0.629	0.062	−1.321	0.931	0.381	0.048	0.385	0.7827	1.31e-10
	Pseudo	19	0.155	0.244	4.822	3.444	0.522	0.115	0.471	0.06231	0.8

Note. Column 1: fit type; column 2: sample type, see Table 8; column 3: number of data points; columns 4 and 5: slope of the correlation and its error; columns 6 and 7: zero point of the correlation and its errors; columns 8 and 9: intrinsic scatter and its errors; column 10: measured scatter; columns 11 and 12: Spearman coefficient and its probability.

correlated errors by setting $a_{BH} = f = 0$ for all galaxies in the equations of Table 4. Similar to what was noticed for the one-dimensional correlations, we do not see any statistically significant change in the fitted parameters of the M_{BH}–M_{Bu}–ρ_h, M_{BH}–M_{Bu}–σ, and M_{BH}–σ–ρ_h correlations when we augment the errors on the bulge mass and density by 0.15 dex (see Section 3). Only the estimated intrinsic scatter is reduced by approximately 0.15 dex in quadrature.

We also repeat the one-dimensional and bivariate analysis by deleting from the sample NGC 2974, NGC 3414, NGC 4552, NGC 4621, NGC 5813, and NGC 5846, for which only uncertain BH mass determinations are available (Cappellari et al. 2008), and NGC 3079 and NGC 4151, for which Kormendy & Ho (2013) do not trust the BH masses. The results are presented in Appendix D, Tables 36 and 37. The changes are not significant, so we prefer the values derived including these galaxies (Tables 11 and 12) to maximize the size of the sample.

Finally, we repeated the M_{BH}–σ, M_{BH}–M_{Bu}, and M_{BH}–M_{Bu}–σ fits using the BH and bulge masses, plus the velocity dispersions and errors of Kormendy & Ho (2013) for the KH45 sample, to derive the solutions given in their Equations (5) and (10). The results are given in Table 13, third and fourth rows, and demonstrate that our fit methodology recovers the results of Kormendy & Ho (2013) for the M_{BH}–σ and M_{BH}–M_{Bu} correlations in terms of coefficients and intrinsic scatter within the errors.[6] This remains true when we repeat the fits using our estimated covariance matrix (Tables 3 and 7); see the results quoted in the fifth and sixth rows of Table 13. Finally, using our bulge masses and errors (Tables 1 and 4) for the KH45 sample, we get the results listed in the seventh and eighth rows of Table 13. The coefficients agree at the 1σ level, but the estimate of the measured and intrinsic scatter for the M_{BH}–M_{Bu} correlation is larger.

Table 14 reports the results of the bivariate analysis on the same data sets. The first row shows that the M_{BH}–M_{Bu}–σ relation is well established when using the data and errors of Kormendy & Ho (2013). The intrinsic and measured scatter are just 0.26 dex, and the values of $RP = \exp(\Delta\mathrm{cAIC}/2)$, and $P(\Delta\mathrm{cAIC})$ all demonstrate the existence of the bivariate correlation. When we consider Tables 3 and 7, we find results similar to the ones discussed above. The evidence for the M_{BH}–M_{Bu}–σ, M_{BH}–σ–ρ_h, and M_{BH}–σ–r_h correlations is strong, while the M_{BH}–M_{Bu}–ρ_h and M_{BH}–M_{Bu}–r_h correlations are only marginally detected (second to sixth rows of Table 14). The same is true when we consider the bulge masses and errors (Tables 1 and 4) for the KH45 sample (seventh to eleventh rows of Table 14). Also in this case, the coefficients agree at the 1σ levels, but the estimates of the measured and intrinsic scatter for the correlations involving M_{Bu} are larger.

These tests let us conclude that our large, combined SINFONI-plus-literature database establishes Equations (24) to (28) convincingly for the entire population of galaxies where dynamical BH masses have been measured. The “best results” (i.e., lowest measured and intrinsic scatter) are obtained when the list of galaxies of Kormendy & Ho (2013) is considered and bulge masses derived from color-based M/L_C are used.

To a first order, these equations deliver a consistent, unifying description of the relations between BHs on the one hand and core and power-law ellipticals and classical bulges on the other.

The one- and two-dimensional correlations discussed above have substantial intrinsic scatter ($\geqslant$0.3 dex), despite the increased number of structural parameters investigated. This is true even when we increase the errors on the bulge masses by 0.15 dex in quadrature or when we use the bulge masses derived from colors of Kormendy & Ho (2013). The correlations derived for the sample of core ellipticals tend to have the smallest intrinsic and measured scatter, broadly in agreement with the averaging effect described by Peng (2007).

We conclude by clarifying again the role of barred galaxies. In Tables 11 and 12 we quote the results of fitting the CorePowerEClassnoBars sample, where we drop 16 barred galaxies contained in the CorePowerEClassPC sample. The coefficients and scatter of the one-dimensional correlations hardly change within the errors, in particular the ones of Equations (31) or (32). The same is true for the bivariate correlations, but their significance is slightly decreased. This effect is partly due to the reduced number of fitted galaxies. We conclude that the BH FP is not driven solely by barred galaxies, contrary to the suggestion of Graham (2008).

---

[6] We note in passing that the zero-point errors quoted by Kormendy & Ho (2013) are not marginalized but given at the best-fit value of the slope.

Table 12

Two-dimensional Correlations with Black Hole Masses

Fit	Sample	a	da	b	db	ZP	dZP	ϵ	$d\epsilon$	rms	$P(b \neq 0)$	ΔcAIC	RP	r_S	$P(r_S)$
$M_{\rm BH}$–σ–$\rho_{\rm h}$	All	4.511	0.32	−0.183	0.046	−0.449	1.038	0.379	0.035	0.409	0.9999	−13.41	0.001	−0.4934	3.27e-07
	CoreE	4.472	1.035	−0.103	0.181	−0.94	3.593	0.334	0.061	0.354	0.7242	2.328	3.203	−0.2972	0.104
	CorePowerE	3.887	0.533	−0.258	0.101	1.669	1.887	0.345	0.047	0.356	0.9929	−4.153	0.125	−0.4936	0.000422
	CorePowerEClass	3.958	0.348	−0.176	0.052	0.859	1.116	0.314	0.035	0.339	0.9993	−9.336	0.009	−0.4546	6.83e-05
	CorePowerEClassPC	4.037	0.35	−0.191	0.046	0.788	1.101	0.328	0.034	0.349	0.9999	−15.28	0	−0.5152	1.63e-06
	CorePowerEClassPCSINFONI	3.988	0.821	−0.218	0.11	1.201	2.638	0.453	0.087	0.384	0.9749	−0.929	0.629	−0.6477	0.00112
	CorePowerEClassPCLit	4.015	0.37	−0.188	0.047	0.78	1.14	0.275	0.038	0.325	0.9999	−13.66	0.001	−0.4144	0.00135
	CorePowerEClassnoBars	4.085	0.395	−0.154	0.063	0.374	1.288	0.324	0.039	0.349	0.9897	−3.664	0.16	−0.4232	0.000679
	PowerE	3.489	0.863	−0.278	0.165	2.694	2.845	0.448	0.117	0.354	0.9509	0.815	1.503	−0.5588	0.0244
	PowerEClass	3.705	0.421	−0.149	0.068	1.174	1.208	0.324	0.047	0.324	0.9836	−2.344	0.31	−0.3131	0.0491
	PowerEClassPC	3.873	0.414	−0.182	0.058	1.057	1.213	0.348	0.045	0.345	0.9986	−7.559	0.023	−0.4194	0.00371
	Pseudo	2.119	1.419	−0.063	0.154	3.166	3.33	0.48	0.117	0.446	0.6709	3.087	4.682	−0.207	0.395
$M_{\rm BH}$–$M_{\rm Bu}$–$\rho_{\rm h}$	All	1.231	0.148	0.246	0.114	−7.183	2.539	0.535	0.044	0.532	0.9824	−2.51	0.285	0.4218	1.87e-05
	CoreE	1.036	0.52	0.129	0.401	−3.854	8.955	0.436	0.075	0.425	0.6179	2.546	3.572	0.1093	0.558
	CorePowerE	1.082	0.247	0.097	0.214	−4.178	4.414	0.442	0.056	0.442	0.6748	2.19	2.989	0.1333	0.372
	CorePowerEClass	1.128	0.16	0.218	0.116	−5.693	2.674	0.426	0.043	0.435	0.9689	−1.296	0.523	0.3818	0.00102
	CorePowerEClassPC	1.107	0.142	0.225	0.106	−5.522	2.419	0.425	0.042	0.439	0.9823	−2.284	0.319	0.4507	3.9e-05
	CorePowerEClassPCSINFONI	1.307	0.252	0.299	0.185	−8.228	4.269	0.422	0.085	0.382	0.9487	0.386	1.213	0.5257	0.012
	CorePowerEClassPCLit	0.993	0.17	0.18	0.126	−3.96	2.88	0.425	0.05	0.435	0.9261	0.262	1.14	0.3278	0.0128
	CorePowerEClassnoBars	1.193	0.176	0.236	0.131	−6.583	2.965	0.426	0.048	0.441	0.9624	−0.946	0.623	0.3425	0.00689
	PowerE	1.002	0.379	0.105	0.321	−3.464	6.513	0.57	0.146	0.459	0.6349	3.529	5.838	0.07647	0.778
	PowerEClass	1.057	0.18	0.296	0.128	−5.704	2.874	0.431	0.061	0.42	0.9887	−2.89	0.236	0.5073	0.000834
	PowerEClassPC	1.056	0.151	0.291	0.113	−5.664	2.511	0.424	0.055	0.426	0.9931	−4.236	0.12	0.5725	3.22e-05
	Pseudo	−0.138	0.476	−0.13	0.273	9.63	6.998	0.544	0.123	0.47	0.6933	3.03	4.55	−0.2789	0.247
$M_{\rm BH}$–σ–$r_{\rm h}$	All	4.258	0.373	0.358	0.096	−1.616	0.834	0.383	0.035	0.413	0.9999	−11.66	0.003	0.5049	1.55e-07
	CoreE	4.396	1.178	0.181	0.369	−1.734	2.63	0.337	0.062	0.356	0.7034	2.408	3.333	0.275	0.134
	CorePowerE	3.571	0.655	0.488	0.207	−0.043	1.45	0.35	0.047	0.361	0.9885	−3.161	0.206	0.4872	0.000515
	CorePowerEClass	3.706	0.399	0.348	0.106	−0.244	0.905	0.315	0.034	0.342	0.9991	−8.434	0.015	0.4629	4.81e-05
	CorePowerEClassPC	3.738	0.398	0.381	0.092	−0.351	0.903	0.328	0.033	0.35	0.9999	−14.87	0.001	0.5307	6.9e-07
	CorePowerEClassPCSINFONI	3.435	0.924	0.505	0.218	0.383	2.122	0.437	0.086	0.372	0.9859	−2.351	0.309	0.6702	0.000642
	CorePowerEClassPCLit	3.766	0.427	0.353	0.096	−0.434	0.965	0.282	0.038	0.331	0.9998	−11.17	0.004	0.4168	0.00126
	CorePowerEClassnoBars	3.849	0.465	0.311	0.136	−0.555	1.045	0.325	0.039	0.352	0.9877	−2.961	0.227	0.4099	0.00104
	PowerE	3.107	1.025	0.524	0.345	0.951	2.271	0.457	0.117	0.363	0.9394	1.333	1.948	0.2941	0.269
	PowerEClass	3.48	0.454	0.295	0.14	0.261	1.029	0.324	0.048	0.326	0.9808	−1.992	0.369	0.2542	0.113
	PowerEClassPC	3.517	0.452	0.376	0.113	0.131	1.023	0.345	0.044	0.344	0.9989	−8.586	0.014	0.402	0.00561
	Pseudo	2.069	1.459	0.029	0.325	2.66	3.08	0.486	0.118	0.449	0.5369	3.249	5.076	0.04737	0.847
$M_{\rm BH}$–$M_{\rm Bu}$–$r_{\rm h}$	All	1.492	0.254	−0.759	0.341	−7.557	2.631	0.533	0.044	0.532	0.9864	−2.782	0.249	−0.6321	4.97e-12
	CoreE	1.101	0.867	−0.303	1.161	−3.319	9.003	0.436	0.072	0.424	0.5959	2.581	3.635	−0.1863	0.316
	CorePowerE	1.168	0.451	−0.279	0.644	−4.161	4.634	0.443	0.057	0.442	0.6672	2.207	3.015	−0.2394	0.105
	CorePowerEClass	1.353	0.266	−0.661	0.347	−5.971	2.772	0.426	0.044	0.435	0.9705	−1.383	0.501	−0.5733	1.74e-07
	CorePowerEClassPC	1.332	0.243	−0.675	0.317	−5.738	2.528	0.426	0.041	0.439	0.9848	−2.294	0.318	−0.6216	1.62e-09
	CorePowerEClassPCSINFONI	1.612	0.427	−0.906	0.554	−8.556	4.451	0.421	0.085	0.383	0.9525	0.342	1.186	−0.7369	9.17e-05
	CorePowerEClassPCLit	1.169	0.284	−0.533	0.372	−4.081	2.955	0.424	0.05	0.434	0.924	0.263	1.14	−0.5672	4.21e-06
	CorePowerEClassnoBars	1.424	0.296	−0.698	0.395	−6.752	3.08	0.426	0.048	0.441	0.9602	−0.822	0.663	−0.5044	3.4e-05
	PowerE	1.088	0.681	−0.294	0.99	−3.359	6.986	0.574	0.148	0.458	0.6266	3.548	5.894	−0.3088	0.244
	PowerEClass	1.355	0.285	−0.887	0.382	−6.01	2.971	0.431	0.06	0.42	0.9892	−2.91	0.233	−0.6947	6.58e-07

Table 12
(Continued)

Fit	Sample	a	da	b	db	ZP	dZP	ϵ	$d\epsilon$	rms	$P(b\neq 0)$	ΔcAIC	RP	r_S	$P(r_S)$
	PowerEClassPC	1.342	0.251	−0.862	0.339	−5.883	2.609	0.424	0.054	0.426	0.994	−4.064	0.131	−0.7504	1.93e-09
	Pseudo	−0.254	0.727	0.38	0.833	9.613	7.395	0.549	0.123	0.47	0.6899	3.05	4.594	0.3035	0.207
$M_{\rm BH}$–$M_{\rm Bu}$–σ	All	0.307	0.099	3.935	0.509	−4.073	0.599	0.395	0.036	0.426	0.999	−7.502	0.023	0.5157	7.59e-08
	CoreE	0.105	0.315	4.466	1.358	−2.95	2.211	0.336	0.062	0.362	0.6367	2.538	3.558	0.141	0.449
	CorePowerE	0.357	0.192	3.365	0.859	−3.219	1.123	0.361	0.048	0.377	0.9666	−1.047	0.592	0.4339	0.00231
	CorePowerEClass	0.319	0.114	3.309	0.547	−2.654	0.757	0.323	0.035	0.353	0.9971	−5.583	0.061	0.4729	3.12e-05
	CorePowerEClassPC	0.368	0.094	3.186	0.518	−2.927	0.658	0.332	0.033	0.36	0.9999	−13.19	0.001	0.5819	2.86e-08
	CorePowerEClassPCSINFONI	0.588	0.211	2.242	1.147	−3.026	1.41	0.409	0.079	0.359	0.9955	−4.737	0.094	0.7899	1.23e-05
	CorePowerEClassPCLit	0.305	0.102	3.396	0.589	−2.76	0.755	0.296	0.04	0.346	0.9988	−6.574	0.037	0.4514	0.000425
	CorePowerEClassnoBars	0.266	0.141	3.564	0.638	−2.663	0.856	0.33	0.039	0.362	0.9689	−1.295	0.523	0.4019	0.00132
	PowerE	0.38	0.341	2.759	1.433	−2.15	2.206	0.484	0.127	0.388	0.8753	2.392	3.307	0.2091	0.437
	PowerEClass	0.261	0.146	3.021	0.61	−1.422	1.1	0.329	0.048	0.333	0.9615	−0.719	0.698	0.2897	0.0698
	PowerEClassPC	0.357	0.111	2.876	0.574	−2.139	0.909	0.347	0.046	0.351	0.9985	−8.005	0.018	0.5019	0.000379
	Pseudo	−0.158	0.32	2.391	1.632	3.54	3.407	0.485	0.119	0.448	0.7002	3.014	4.514	−0.207	0.395

Note. Column 1: fit type; column 2: sample type, see Table 8; columns 3 and 4: first variable slope of the correlation and its error; columns 5 and 6: second variable slope of the correlation and its error; columns 7 and 8: zero point of the correlation and its errors; columns 9 and 10: intrinsic scatter and its errors; column 11: measured scatter; column 12: probability of the bivariate correlation; columns 13 and 14: ΔcAIC value and $RP = \exp(\Delta{\rm cAIC}/2)$ (the relative probability of the mono- and bivariate solutions); they are computed matching the bivariate solutions of this table to the monovariate solutions of Table 11 of the respective data sets. The pairings are $M_{\rm BH}$–σ–$\rho_{\rm h}$ with $M_{\rm BH}$–σ, $M_{\rm BH}$–$M_{\rm Bu}$–$\rho_{\rm h}$ with $M_{\rm BH}$–$M_{\rm Bu}$, $M_{\rm BH}$–σ–$r_{\rm h}$ with $M_{\rm BH}$–σ, $M_{\rm BH}$–$M_{\rm Bu}$–$r_{\rm h}$with $M_{\rm BH}$–$M_{\rm Bu}$, and $M_{\rm BH}$–$M_{\rm Bu}$–σ with $M_{\rm BH}$–σ; see Section 4. Columns 15 and 16: Spearman coefficient and its probability.

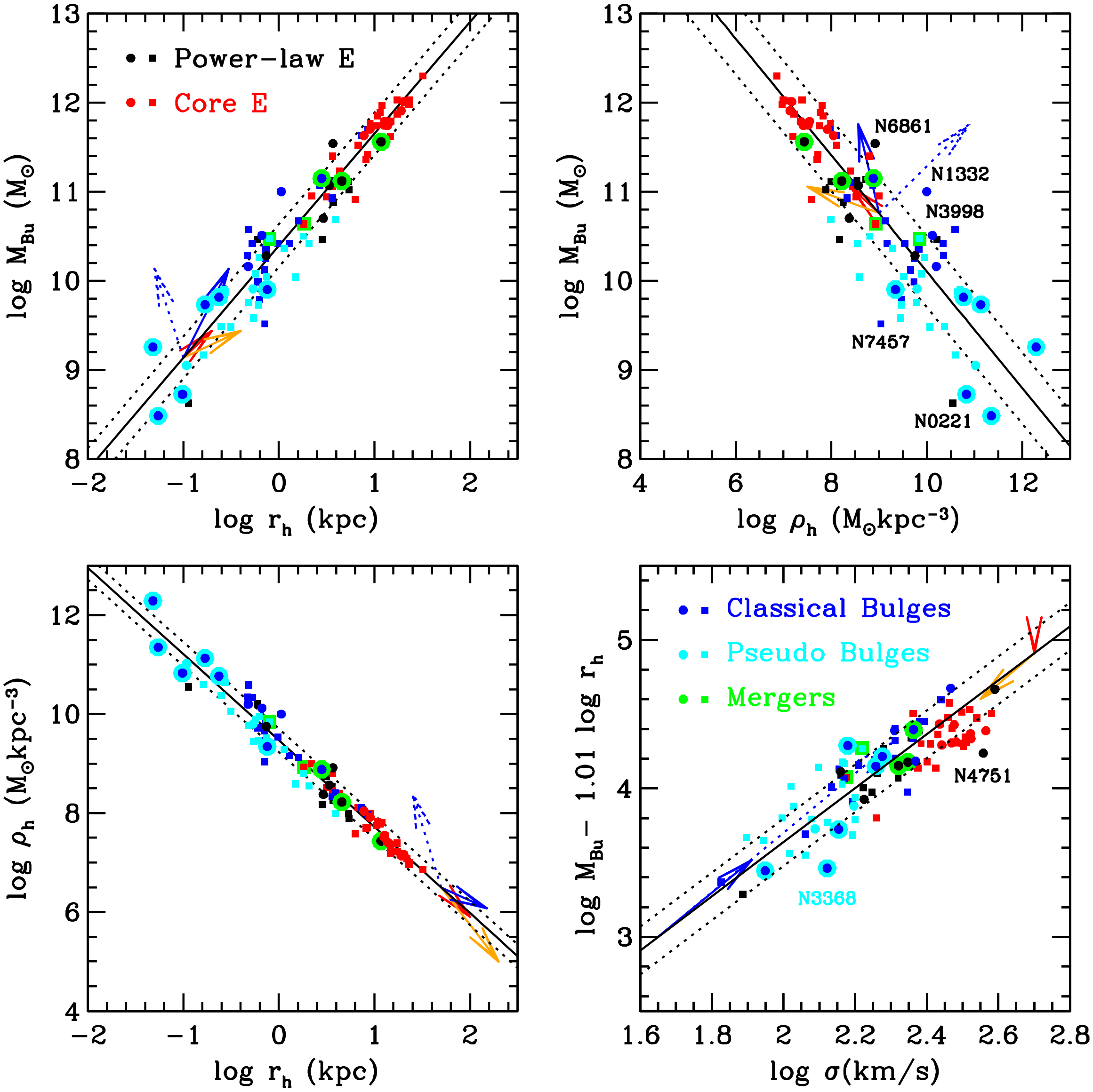

Figure 12. Correlations between the bulge parameters $M_{\rm Bu}$, $r_{\rm h}$, $\rho_{\rm h}$, and σ. Squares are data from the literature, and circles are galaxies from our SINFONI survey. We plot core galaxies in red, power-law ellipticals in black, classical bulges in blue, and pseudobulges in cyan. Mergers have a green annulus. Blue dots with a cyan annulus are the classical bulge components of composite bulges. The labels name particularly deviant galaxies. The solid lines indicate the best-fit relations given in Tables 9 and 10 for the CorePowerEClassPC sample. The dotted lines indicate the estimated intrinsic scatter. Arrows describe the effect of an equal-mass dry merger (red), of a sequence of minor mergers doubling the bulge mass (orange), and an equal-mass, gas-rich merger of two spiral galaxies with 20% bulge mass and bulge-scales ratio $r_{\rm h}^f/r_{\rm h}^i$ of 3 (blue) or 0.5 (dotted blue); see also Section 6 and Table 16. As expected, the red arrow in the bottom right plot has zero length.

6. DISCUSSION

6.1. Comparing $M_{\rm Bu}^{a_{\rm best}}\sigma^{b_{\rm best}}$, $M_{\rm Bu}^{0.5}\sigma^2$, $M_{\rm Bu}\sigma^2$, and $M_{\rm Bu}\sigma$

In Section 1 we reviewed the different physical interpretations proposed to explain the bivariate correlations with $M_{\rm BH}$. Hopkins et al. (2007a, 2007b) concluded that the bivariate correlations mirror the correlation between $M_{\rm BH}$ and $M_{\rm Bu}^{0.5}\sigma^2$, which can be expected on simple physical grounds (see below). Feoli & Mele (2005), Aller & Richstone (2007), and Mancini & Feoli (2012) argued that the bulge's kinetic or gravitational energy $M_{\rm Bu}\sigma^2$ of a galaxy sets its BH mass. Finally, Soker & Meiron (2011) suggested the bulge's momentum $M_{\rm Bu}\sigma$ as the key physical quantity.

We compare the three options $M_{\rm Bu}^{0.5}\sigma^2$, $M_{\rm Bu}\sigma^2$, and $M_{\rm Bu}\sigma$ to our best-fit solutions given in Equation (26) and Table 14 (rows 2 and 7) using the model comparison formalism. Similar to what is discussed in Section 4, we marginalize the posterior probability distribution $P(a, b, ZP, \epsilon)$ over the parameters ZP and ϵ and derive the equivalent of Equation (11) as

$$-2\ln[P(a_{\rm best}, b_{\rm best})/P(a, b)] = (a - a_{\rm best}, b - b_{\rm best})V^{-1}\begin{pmatrix} a - a_{\rm best} \\ b - b_{\rm best} \end{pmatrix}, \qquad (29)$$

where

$$V = \begin{pmatrix} (\delta a_{\rm best})^2 & \langle \delta a \delta b \rangle_{\rm best} \\ \langle \delta a \delta b \rangle_{\rm best} & (\delta b_{\rm best})^2 \end{pmatrix}, \qquad (30)$$

and $a_{\rm best}$, $\delta a_{\rm best}$, $b_{\rm best}$, $\delta b_{\rm best}$ are given in Tables 12 and 14 (as usual dropping the label "best"), and $\langle \delta a \delta b \rangle_{\rm best}$ (see Figure 11) is listed in Table 15. The slopes a and b in Equation (29) obey

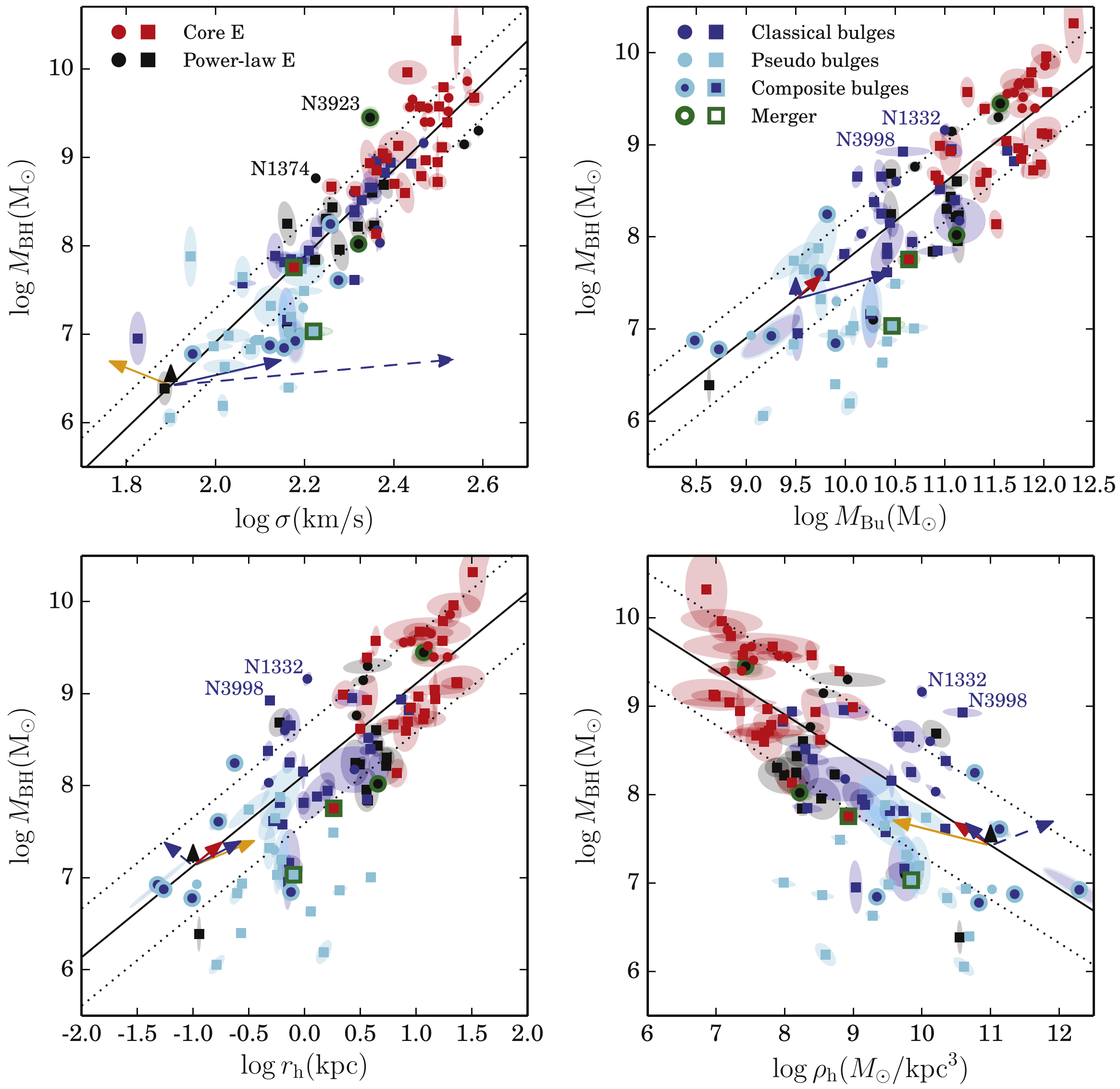

Figure 13. Top: the $M_{\rm BH}$–σ (left) and $M_{\rm BH}$–$M_{\rm Bu}$ (right) relations. Bottom: the $M_{\rm BH}$–$r_{\rm h}$ (left) and $M_{\rm BH}$–$\rho_{\rm h}$ (right) relations. Symbols as in Figure 12. The ellipses show the 1σ errors. The labels name particularly deviant galaxies. The solid lines indicate the relations given in Table 11 for the CorePowerEClassPC sample. The dotted lines indicate the estimated intrinsic scatter. Arrows describe the effect of an equal-mass dry merger (red), of a sequence of minor mergers doubling the bulge mass (orange), an equal-mass, gas-rich merger of two spiral galaxies with 20% bulge mass with bulge-scales ratio $r_{\rm h}^f/r_{\rm h}^i$ 3 (blue) or 0.5 (dotted blue), and doubling the BH mass through accretion or BH merging (black); see Section 6 and Table 16.

$a/b = 0.25, 0.5, 1$ for the cases $M_{\rm Bu}^{0.5}\sigma^2$, $M_{\rm Bu}\sigma^2$, and $M_{\rm Bu}\sigma$, respectively. The values of a and b reported in Table 15 maximize Equation (29) and are identical to the values quoted in Tables 12 and 13 for the $M_{\rm Bu}^{0.5}\sigma^2$ and $M_{\rm Bu}\sigma^2$ fits. Next, we compute ΔcAIC and $RP = \exp(\Delta{\rm cAIC}/2)$. What are the correct values of k to be used in Equation (10)? Since $a_{\rm best}$ is different from zero, we can recast our best-fit solution $M_{\rm BH} \sim (M_{\rm Bu}^{a_{\rm best}}\sigma^{b_{\rm best}})$ as $M_{\rm BH} \sim (M_{\rm Bu}\sigma^{b_{\rm best}/a_{\rm best}})^{a_{\rm best}}$ and argue that $k = 3$ for the four relations $M_{\rm Bu}\sigma^{b_{\rm best}/a_{\rm best}}$, $M_{\rm Bu}^{0.5}\sigma^2$, $M_{\rm Bu}\sigma^2$, or $M_{\rm Bu}\sigma$. The values of $RP^{(3)}$ given in Table 15 are computed following this reasoning. They stem directly from Equation (29) since the terms involving k in Equation (10) are all equal and cancel out. These relative probabilities assess which of the three models $M_{\rm Bu}^{0.5}\sigma^2$, $M_{\rm Bu}\sigma^2$, or $M_{\rm Bu}\sigma$ is nearest to our best solution.

The values of $RP^{(4)}$ given in Table 15 assume instead that our best-fit solution $M_{\rm BH} \sim (M_{\rm Bu}^{a_{\rm best}}\sigma^{b_{\rm best}})$ has $k = 4$, while the $M_{\rm Bu}^{0.5}\sigma^2$, $M_{\rm Bu}\sigma^2$, or $M_{\rm Bu}\sigma$ models have $k = 3$. They assess whether our "complex" best-fit solution $M_{\rm BH} \sim (M_{\rm Bu}^{a_{\rm best}}\sigma^{b_{\rm best}})$ is really needed to describe the data, or whether the "simpler" $M_{\rm Bu}^{0.5}\sigma^2$, $M_{\rm Bu}\sigma^2$, or $M_{\rm Bu}\sigma$ models should be preferred.

If we use $RP^{(3)}$ to rank the $M_{\rm Bu}^{0.5}\sigma^2$, $M_{\rm Bu}\sigma^2$, or $M_{\rm Bu}\sigma$ models with respect to $M_{\rm Bu}\sigma^{b_{\rm best}/a_{\rm best}}$, we find that the $M_{\rm Bu}^{0.5}\sigma^2$ model performs the best (i.e., it has the largest $RP^{(3)}$) when compared with our best-fitting solution, whatever sample is considered (either our reference CorePowerEClassPC sample, or the KH45 sample with the color-based bulge masses, or the same sample with dynamical bulge masses). The $M_{\rm Bu}\sigma$ model performs worst; when using dynamical bulge masses, we get $RP^{(3)} < 10^{-4}$, and only for the KH45 sample with bulge masses derived from M/L_C $RP^{(3)}$ it is not too low (0.33).

Table 13
One-dimensional Correlations Derived Using the KH45 Sample

Fit	Sample	a	da	ZP	dZP	ϵ	$d\epsilon$	rms
$M_{\rm BH}$–σ	Equation (5) Kormendy & Ho (2013)	4.41	0.3	−1.66	0.05	0.28	⋯	⋯
$M_{\rm BH}$–$M_{\rm Bu}$	Equation (10) Kormendy & Ho (2013)	1.16	0.08	−4.07	0.10	0.29	⋯	⋯
$M_{\rm BH}$–σ	Kormendy & Ho (2013)	4.342	0.323	−1.497	0.762	0.309	0.041	0.321
$M_{\rm BH}$–$M_{\rm Bu}$	Kormendy & Ho (2013)	1.153	0.088	−3.98	0.966	0.309	0.043	0.318
$M_{\rm BH}$–$M_{\rm Bu}^{0.5}\sigma^2$	Kormendy & Ho (2013)	1.19	0.073	−3.431	0.745	0.25	0.035	0.263
$M_{\rm BH}$–$M_{\rm Bu}\sigma^2$	Kormendy & Ho (2013)	0.796	0.05	−3.796	0.783	0.256	0.036	0.268
$M_{\rm BH}$–σ	Tables 3 and 7	4.404	0.348	−1.658	0.82	0.323	0.043	0.337
$M_{\rm BH}$–$M_{\rm Bu}$	Tables 3 and 7	1.172	0.089	−4.186	0.98	0.289	0.046	0.321
$M_{\rm BH}$–$M_{\rm Bu}^{0.5}\sigma^2$	Tables 3 and 7	1.204	0.073	−3.577	0.746	0.251	0.036	0.27
$M_{\rm BH}$–$M_{\rm Bu}\sigma^2$	Tables 3 and 7	0.803	0.051	−3.898	0.806	0.256	0.038	0.273
$M_{\rm BH}$–σ	Tables 1 and 4	4.418	0.351	−1.693	0.826	0.325	0.045	0.337
$M_{\rm BH}$–$M_{\rm Bu}$	Table 1 and 4	0.952	0.095	−1.813	1.045	0.404	0.053	0.426
$M_{\rm BH}$–$M_{\rm Bu}^{0.5}\sigma^2$	Tables 1 and 4	1.115	0.079	−2.687	0.813	0.296	0.042	0.324
$M_{\rm BH}$–$M_{\rm Bu}\sigma^2$	Tables 1 and 4	0.715	0.056	−2.554	0.886	0.324	0.045	0.351

Note. Column 1: fit type; column 2: sample type, see text; columns 3 and 4: first variable slope of the correlation and its error; columns 5 and 6: zero point of the correlation and its errors; columns 7 and 8: intrinsic scatter and its errors; column 9: measured scatter.

If we consider $RP^{(4)}$, we conclude that the model $M_{\rm Bu}^{0.5}\sigma^2$ provides a description of the data as good as the one of our best-fitting solution, with $RP^{(4)} = 0.41$ for our reference CorePowerEClassPC sample and $RP^{(4)} = 0.88$ for the KH45 sample with dynamical bulge masses. The model $M_{\rm Bu}^{0.5}\sigma^2$ is statistically preferred with respect to our best-fitting solution when the KH45 sample with color-based bulge masses is considered ($RP^{(4)} = 2.89$). For this sample the same applies to the $M_{\rm Bu}\sigma^2$ model ($RP^{(4)} = 2.82$), while the $M_{\rm Bu}\sigma$ model is statistically indistinguishable ($RP^{(4)} = 1.1$) from the bivariate best-fit model. This conclusion is partially driven by the smaller size (45 versus 77 galaxies) and larger errors (see Section 3) of the KP45 sample, compared to our reference CorePowerEClassPC sample, but it could also reflect the underlying physical difference between color-based and dynamical bulge masses.

In the following we give a closer look to the models that compare best to our best-fitting bivariate solution: the $M_{\rm Bu}^{0.5}\sigma^2$ and $M_{\rm Bu}\sigma^2$ models.

Table 11 presents the results of fitting the relation $\log M_{\rm BH} = a\log(M_{\rm Bu}^{0.5}\sigma^2) + ZP$. For the sample without pseudobulges we find

$$\log M_{\rm BH} = (1.09 \pm 0.06)\log(M_{\rm Bu}^{0.5}\sigma^2) - (2.54 \pm 0.64), \tag{31}$$

with intrinsic and measured scatter slightly lower than the $M_{\rm BH}$–σ relation and slightly larger than the ones given by Equations (19)–(21). Figure 18 (left) shows the relative correlation plot. We recognize the features discussed above: CoreEs are slightly shifted upward, while pseudobulges have systematically lower BH masses than predicted. This confirms that the picture presented by Hopkins et al. (2007a, 2007b) is valid for ellipticals and classical bulges, but breaks down for pseudobulges. The intrinsic scatter is reduced to just 0.25 dex when the KH45 sample with color-based bulge masses is considered.

Figure 18 (right) shows the correlations between the BH mass and the kinetic energy of the bulge $M_{\rm Bu}\sigma^2$ put forward by Feoli & Mele (2005), Aller & Richstone (2007), Feoli & Mancini (2009), and Mancini & Feoli (2012). Table 11 also presents the results of fitting the relation $\log M_{\rm BH} = a\log(M_{\rm Bu}\sigma^2) + ZP$. For the sample without pseudobulges we find

$$\log M_{\rm BH} = (0.67 \pm 0.04)\log(M_{\rm Bu}\sigma^2) - (1.96 \pm 0.65). \tag{32}$$

This is similar to the dependences found by Aller & Richstone (2007), Hopkins et al. (2007b), and Mancini & Feoli (2012). The correlation is strong with an intrinsic scatter slightly better than the one of the $M_{\rm BH}$–σ relation and slightly larger than the one given by Equation (31). In both cases the differences are not statistically significant. When the KH45 sample with color-based bulge masses is considered, the intrinsic scatter is reduced to just 0.256 dex. Again, pseudobulges are offset toward lower BH masses.

To conclude, our analysis shows that the model $M_{\rm Bu}^{0.5}\sigma^2$ is slightly preferred to explain our bivariate correlations, especially when dynamically determined bulge masses are considered. However, the bulge kinetic energy $M_{\rm Bu}\sigma^2$ produces correlations with BH masses with statistically equivalent intrinsic and measured scatter. The bulge momentum $M_{\rm Bu}\sigma$ is highly disfavored in the case of dynamically determined bulge masses.

6.2. A Simple Interpretation Framework

As discussed above, Figure 18 points to some sort of gravitationally induced equilibrium configuration, coupled with a feedback mechanism, that lies behind our empirical findings. Indeed, one could naively expect a correlation between $M_{\rm Bu}\sigma^2$ and $M_{\rm BH}$ as a consequence of an energy balance during the simultaneous growth of bulges and BHs. Why a correlation between $M_{\rm Bu}^{0.5}\sigma^2$ and $M_{\rm BH}$ should exist is less obvious. Hopkins et al. (2007a, 2007b) argue that one needs to equate the momentum of the galactic outflow $p \sim M_{\rm Bu}\sigma$ to the injection of momentum $\dot{p} \sim L_{\rm Edd}/c \sim M_{\rm BH}$ during the dynamical time $t_{\rm soi}^{\rm dyn} \sim R_{\rm soi}/\sigma$ near the BH sphere of influence with radius $R_{\rm soi} \sim GM_{\rm BH}/\sigma^2$. This gives $\dot{p} \times t_{\rm soi}^{\rm dyn} \sim M_{\rm BH}^2/\sigma^3 \sim M_{\rm Bu}\sigma$, or $M_{\rm BH} \sim M_{\rm Bu}^{0.5}\sigma^2$. Clearly this argument applies only if the

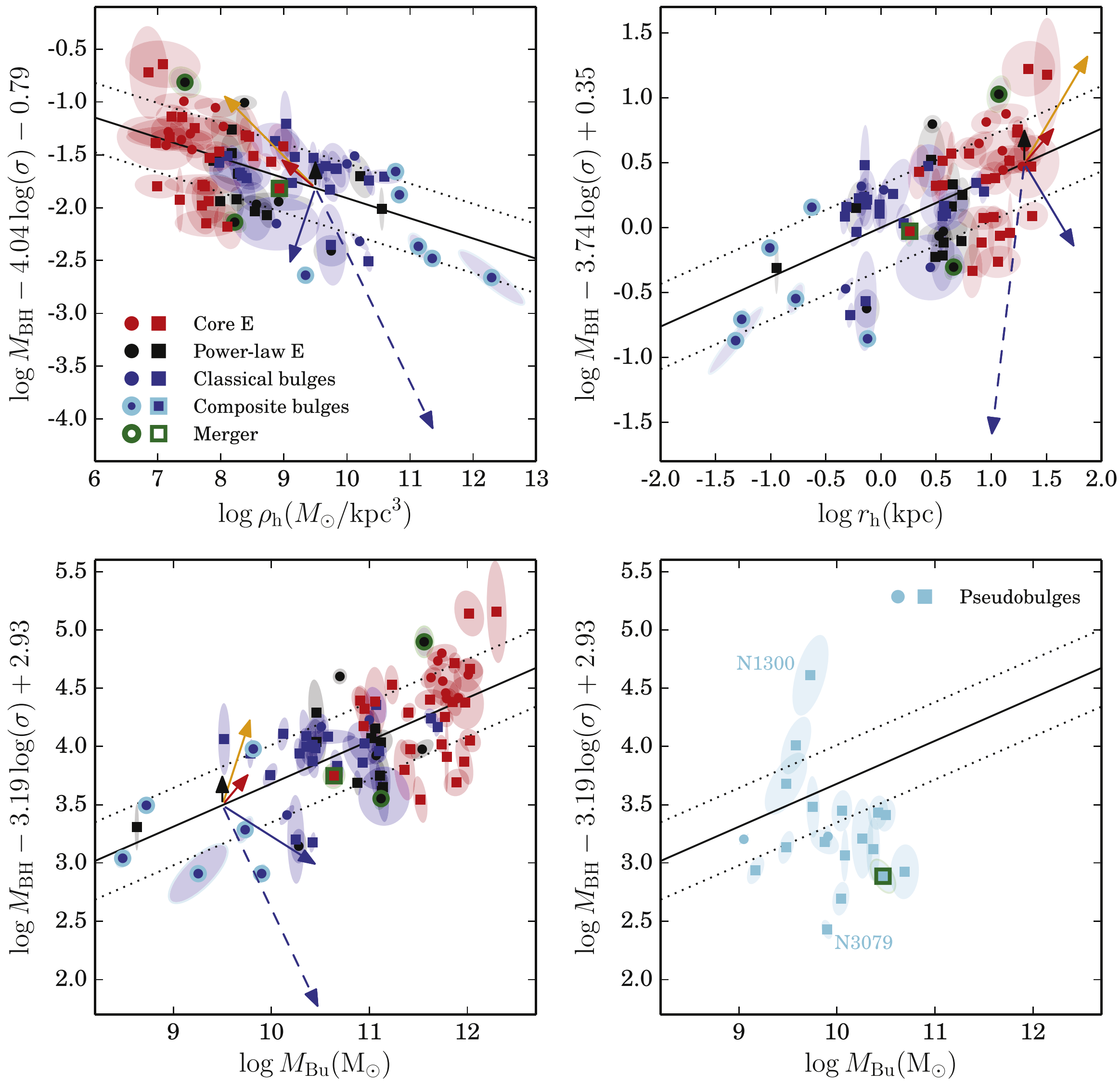

Figure 14. Illustration of the bivariate correlations $M_{\rm BH}$–σ–$\rho_{\rm h}$ (top left), $M_{\rm BH}$–σ–$r_{\rm h}$ (top right), and $M_{\rm BH}$–$M_{\rm Bu}$–σ (bottom left and right). In each panel we plot the corresponding best-fit relations for the CorePowerEClassPC subsample using solid lines, with dotted lines showing the estimated intrinsic scatter. Galaxy data points from the various subsamples are plotted with different colors: core galaxies in red, power-law ellipticals in black, classical bulges in blue, pseudobulges in cyan. Mergers have a green annulus. Blue dots with a cyan annulus are the classical bulge components of (composite) pseudobulges. Squares indicate data from the literature and circles data from our SINFONI survey. The ellipses show the 1σ errors. Arrows describe the effect of an equal-mass dry merger (red), of a sequence of minor mergers that double the bulge mass (orange), an equal-mass, gas-rich merger of two spiral galaxies with 20% bulge mass and bulge-scales ratio $r_{\rm h}^f/r_{\rm h}^i$ of 3 (blue) or 0.5 (dotted blue), and doubling the BH mass through accretion or BH merging (black); see also Section 6 and Table 16.

Eddington luminosity $L_{\rm Edd}$ is high enough. This is probably the case during "wet" mergers of gas-rich galaxies or during violent instabilities in high-density, high-redshift disks, where large amounts of gas could be funneled to the center and accreted quickly while simultaneously forming a classical bulge (Bournaud et al. 2014; Menci et al. 2014). However, this mechanism should not work in the case of "dry" mergers, when gas-poor galaxies coalesce, or for pseudobulges formed by the secular evolution of disks, where only small amounts of gas can flow toward the center at any time (due to, for example, bar torques). Only pseudobulges with particularly high densities could be expected to have been generated in the past with accretion luminosities approaching the Eddington limit. In the following we summarize these statements in a simple quantitative way.

Dry mergers are mergers of (elliptical and S0) galaxies without cold gas and therefore are dissipationless. Equal-mass dry mergers preserve the velocity dispersion σ ($\sigma^f = \sigma^i$, where i and f indicate the initial and final state) of the resulting merged galaxy, doubling the size ($r_{\rm h}^f/r_{\rm h}^i = 2$) and reducing the average density by $1/4$ ($\rho_{\rm h}^f/\rho_{\rm h}^i = 1/4$). They increase the central BH masses through BH merging by a factor of 2 (if both merging galaxies obey the $M_{\rm BH}$–$M_{\rm Bu}$ relation before the merging); see Naab et al. (2009). These effects are indicated by the red arrows in Figures 12 to 18. Dry mergers are also responsible for the formation of the cores of core ellipticals through the binary BH scouring mechanism. The absence of gas implies that the central cusp cannot be re-formed after the merging event.

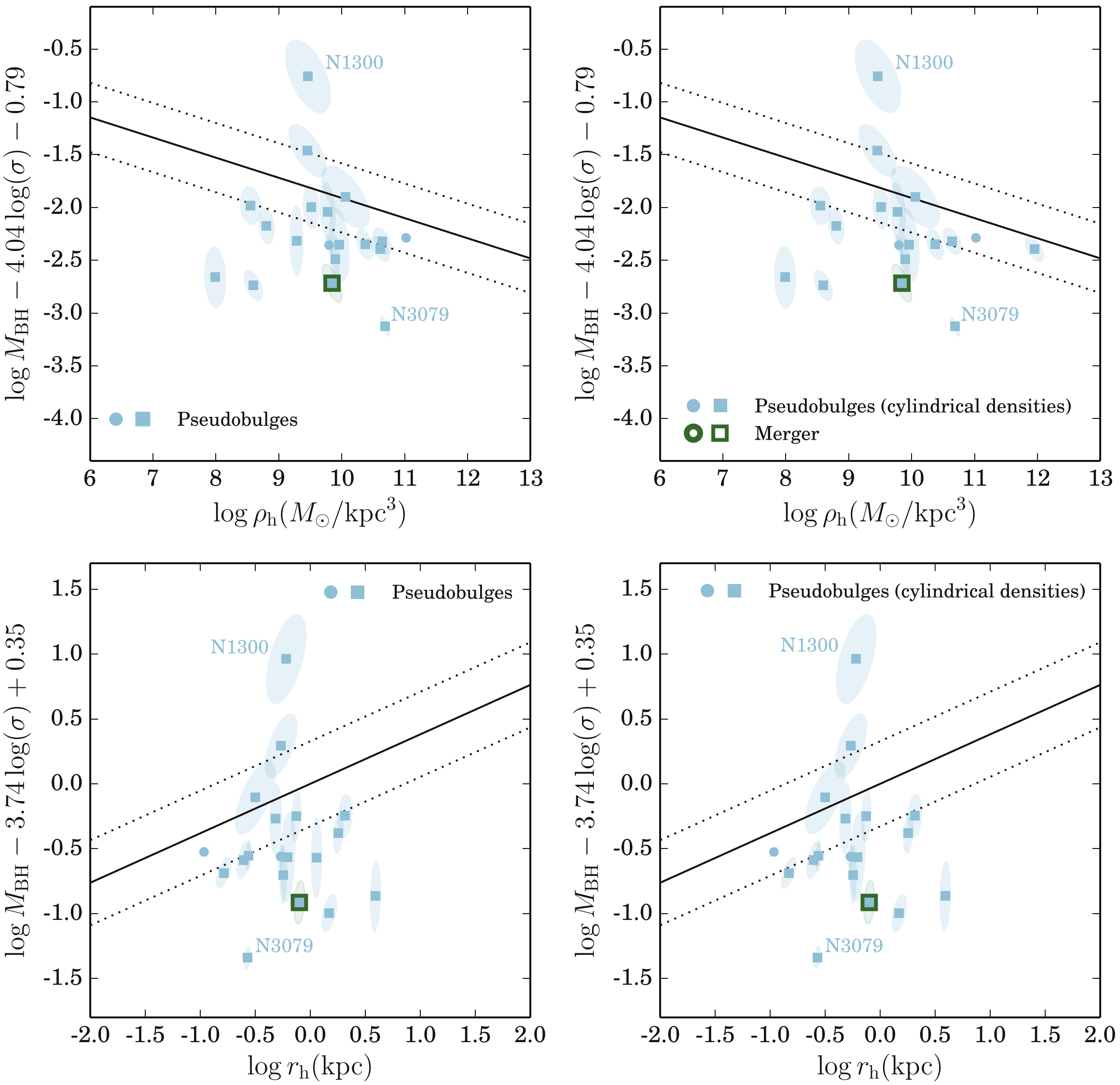

Figure 15. Illustration of the bivariate correlations $M_{\rm BH}$–σ–$\rho_{\rm h}$ (top) and $M_{\rm BH}$–σ–$r_{\rm h}$ (bottom) for pseudobulges (cyan points). Squares indicate data from the literature and circles data from our SINFONI survey. The ellipses show the 1σ errors. Lines and arrows are as in Figure 14. The left plot is for spherical densities and radii (see Equation (4)), the plot to the right for cylindrical densities and radii with $h_z = 0.2a_e/1.67$ (see Equation (5)).

Several minor dry mergers (orange arrows in Figures 12–18) can enlarge sizes and lower average densities even more (for a sequence of minor mergers doubling the mass, the size is increased by 4 and the density is decreased by 1/32), while keeping the $M_{\rm BH}/M_{\rm Bu}$ ratio constant and reducing σ by a factor of $1/2^{0.5}$ (Naab et al. 2009). These combined effects can qualitatively explain the position of the most massive, largest, and least dense core ellipticals in Figures 12, 14, 16, and 18 and the "saturation effect" discussed in Kormendy & Bender (2013). These objects appear to have BH masses ≈0.3 dex larger than the rest of the CorePowerEClassPC sample and could well be the result of dry merging of preexisting power-law or core ellipticals. Moreover, the intrinsic and measured scatter of the correlations defined by core ellipticals alone tend to be the smallest, in line with the averaging effect expectations discussed by Peng (2007).

Wet mergers are mergers of (disk) galaxies with cold gas. Measuring $M_{\rm BH}$ in local galaxies known to be recent mergers of disk galaxies allows one to sketch what could be the evolution with time of this class of objects (Kormendy & Ho 2013). If the merging progenitors follow a BH scaling relation and the BHs do not accrete substantial amounts of gas during the merging process, the merger remnant would now fall below the relation by a factor corresponding to the mean bulge-to-total (B/T) ratio of the progenitors. This is indicated by the blue arrows in Figures 12 to 18 for an equal-mass merger of spirals with $B/T = 0.2$ and a factor of 3 increase in bulge size. The velocity dispersion will change according to the virial theorem, $r_{\rm h}^f\sigma^{f2} = 2r_{\rm h}^i\sigma^{i2}/(B/T)$, while the scale length of the bulge will change by a factor of $r_{\rm h}^f/r_{\rm h}^i = k$. Naab & Trujillo (2006) argue that k can vary between 0.5 and 3 in disk plus bulge mergers without gas. As a consequence, bulge masses and velocity dispersions will generally increase, while scale radii or densities might either increase or decrease. Therefore we could expect recent mergers to lie generally below the BH correlations. This is indeed what we see for NGC 1316, NGC 2960, NGC 5018, and NGC 5128 (plotted in green in Figures 12–18), all rather young, gas-rich merger remnants. NGC 3923 is likely to be (the late phase of) a merger between

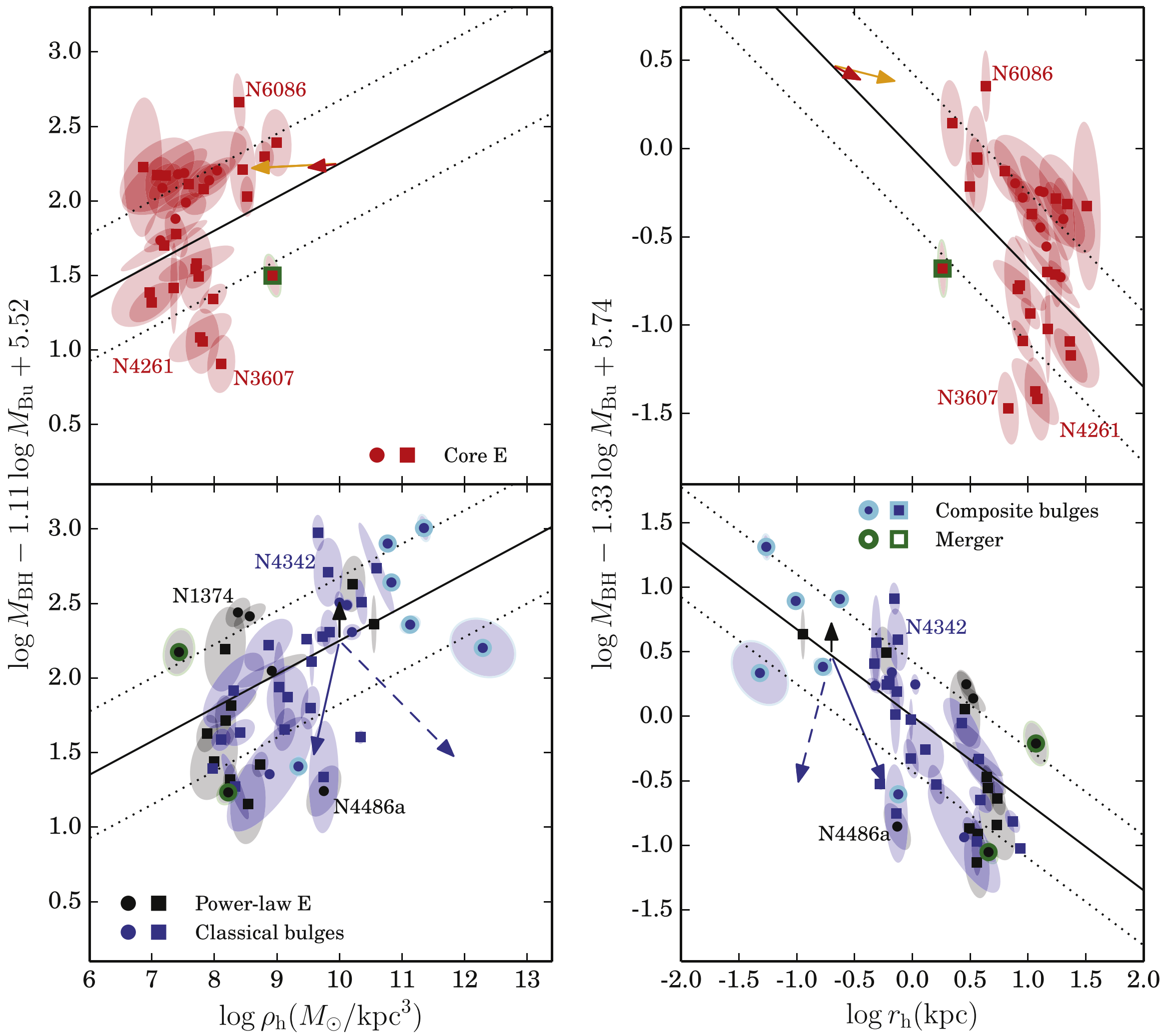

Figure 16. As for Figure 14, but showing how different subsamples relate to the $M_{\rm BH}$–$M_{\rm Bu}$–$\rho_{\rm h}$ (left panels) and the $M_{\rm BH}$–$M_{\rm Bu}$–$r_{\rm h}$ (right panels) bivariate correlations. In each set of panels we plot the corresponding best-fit relations for the CorePowerEClassPC sample using solid lines, with the dotted lines showing estimated intrinsic scatter. Individual panels show different subsamples: core galaxies (top panels) and PowerEClassPC (bottom panels). The labels name particularly deviant galaxies. The ellipses show the 1σ errors. Colors, arrows, and point types are as in Figure 14.

an existing elliptical and a low-velocity-dispersion dwarf galaxy. In general, the distribution of power-law ellipticals and classical bulges in Figures 12–18 is better explained by the solid blue arrow, that is, when the scale length of the bulge resulting from the merger is larger than the original value.

Finally, the BH can increase its mass by accretion. This process has also been proposed for changing sizes and velocity dispersions of galaxies through its feedback (Fan et al. 2008), but it fails to explain the redshift evolution of sizes of early-type galaxies (Saglia et al. 2010). For simplicity we therefore neglect this possible effect on sizes and densities and just mark the importance of BH accretion in itself. The black arrows in Figures 13–18 indicate accretion that doubles the mass of the BH. Table 16 summarizes the mechanisms discussed above. Ultimately, the feedback produced during the accretion event will set the galaxy back to the BH correlations discussed above.

The distribution of power-law ellipticals and classical bulges in Figures 13, 14, and 16 can be seen as the result of the combined effects of wet mergers, BH accretion, and feedback mechanisms. The exact steepness of the blue arrows depends on B/T and the relative amount of (dissipative) gas available. Some gas will be accreted on the BH. Some gas will generate new stars, increasing the density of the newly formed bulge and possibly forming a central power-law cusp.

Because the average gas fraction of galaxies decreases with cosmic time, it is plausible that galaxies that merged earlier had a better chance to grow their BHs in lock step with (or even overgrow) the spheroid than is possible for present-day mergers. Thus, we would expect the $M_{\rm BH}/M_{\rm Bu}$ ratio to increase with increasing redshift (Sijacki et al. 2015). This is indeed observed in various samples of quasars at $z > 2$ (see review in Kormendy & Ho 2013 and references therein).

We can further speculate that those objects that were assembled early and did not undergo late major mergers today harbor the most massive BHs for a given bulge mass. These objects should have formed from very gas-rich material that allowed their BHs to grow efficiently. They also should have high stellar densities because earlier formation implies higher dark matter and gas densities (Thomas et al. 2009). Because dry mergers decrease the mean stellar density, a high density today also implies that the objects did not undergo such events more recently. Examples for such objects could be very

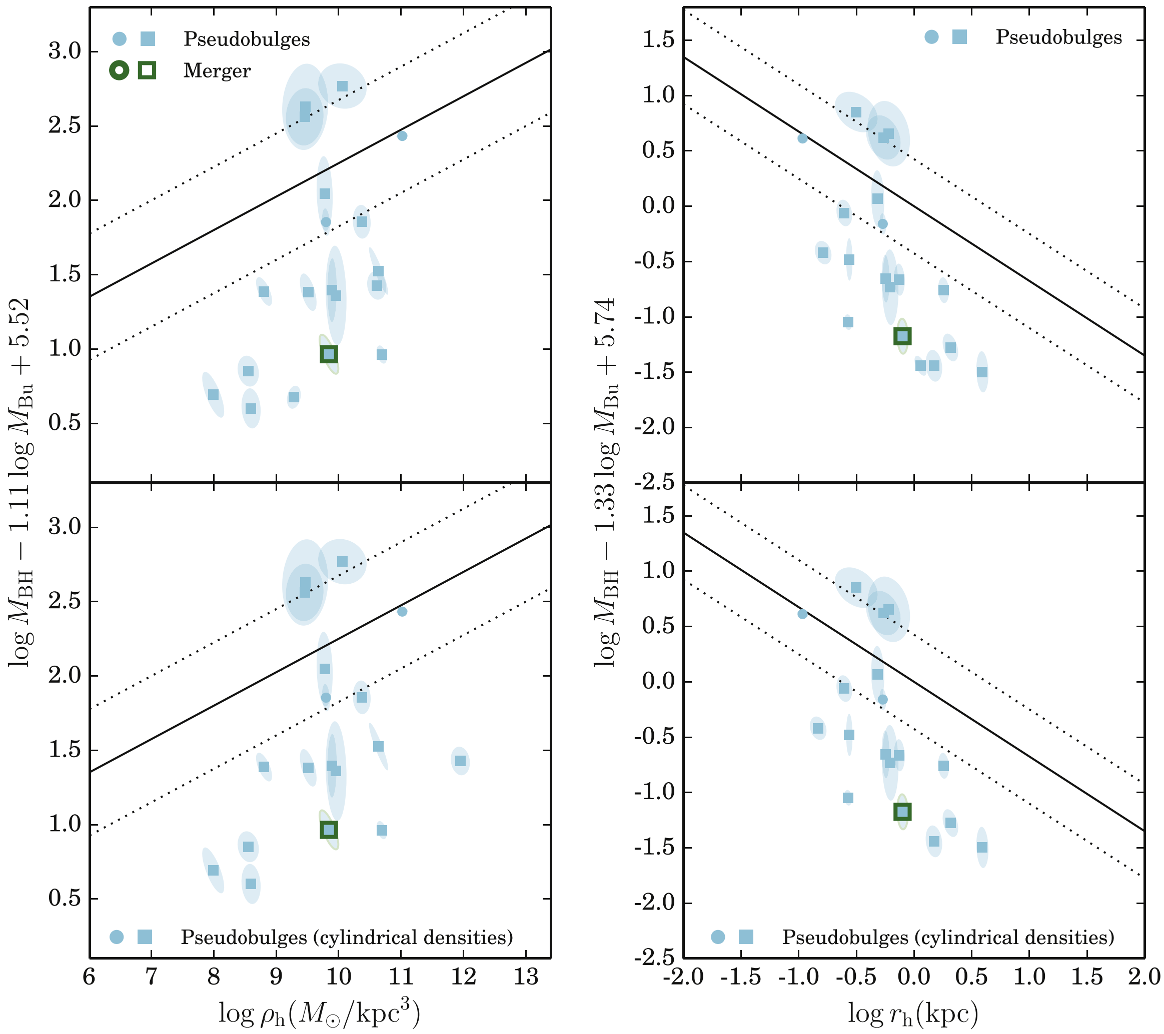

Figure 17. As for Figure 16, but showing pseudobulges only. The plots at the top are for spherical densities and radii (see Equation (4)), the plots at the bottom for cylindrical densities and radii with $h_z = 0.2a_e/1.67$ (see Equation (5)).

compact bulges in old S0s or early-type spirals, where the existence of a substantial disk indicates the lack of late major mergers.

In fact, some of the most compact bulges known (we include NGC 1332, NGC 3998, and NGC 4486b) do harbor unusually large BHs for their bulge mass (see Figure 13). M32 (NGC 221) is also extremely dense, but with a normal BH for its bulge mass. Except for NGC 4486b, these galaxies are not particularly deviant when the $M_{\rm BH}$–σ relation is considered, an indication that the velocity dispersion (through the $M_{\rm BH}$–σ relation) is a more robust BH mass predictor than the bulge mass (through the $M_{\rm BH}$–$M_{\rm Bu}$ relation).

Pseudobulges with spherical densities $\rho_{\rm h} \approx 10^{10}\,M_\odot\,{\rm kpc}^{-3}$ such as NGC 4501 (where we detect molecular gas in noncircular motions; see Mazzalay et al. 2013, 2014) or NGC 3227 (where an active nucleus is present and a recent episode of star formation took place; see Davies et al. 2006) have BHs with masses similar to those predicted by the $M_{\rm BH}$–σ or the $M_{\rm BH}$–$M_{\rm Bu}$ relations of ellipticals and classical bulges. Pseudobulges with lower densities have smaller BHs than the classical-bulges prediction. Therefore, the growth of BHs in galaxies that did not undergo mergers, and therefore do not have a classical bulge, follows a path decoupled from the rest of the galaxy and set by the amount of gas that secular processes (such as bars) manage to funnel toward the galaxy centers. The resulting BH masses are much smaller than the ones measured in early-type galaxies or classical bulges. We speculate that only when the densities involved are above a certain threshold are pseudobulges able to fuel the BHs efficiently enough to approach the feedback mechanism (see above) that sets $M_{\rm BH}/M_{\rm Bu}$ in classical bulges. The exact value of the density threshold is, however, uncertain by an order of magnitude because it depends on the unknown geometry of pseudobulges.

Finally, we also find composite systems where both a classical and a pseudobulge coexist. In Figures 13, 14, and 16 we plot the position of NGC 1068, NGC 2787, NGC 3368, NGC 3489, NGC 4371, and NGC 4699, all galaxies with composite bulges, using the mass of their small classical bulges. These high-density components form the high-density, small-size end of the power-law and classical-bulge bivariate correlations. We speculate that they formed together with their BH at high redshifts. Possibly *every* pseudobulge has a small classical component at its center: Erwin et al. (2015) argue that it is not (yet) possible to present a clear case of a pure pseudobulge where the presence of a small classical component can be excluded without doubt.

Table 14
Two-dimensional Correlations Derived Using the KH45 Sample

Fit	Sample	a	da	b	db	ZP	dZP	ϵ	$d\epsilon$	rms	$P(\beta \neq 0)$	ΔcAIC	RP
$M_{\rm BH}$–$M_{\rm Bu}$–σ	Kormendy & Ho (2013)	0.621	0.164	2.275	0.614	−3.469	0.822	0.255	0.035	0.262	0.9997	−11.98	0.003
$M_{\rm BH}$–$M_{\rm Bu}$–σ	Tables 3 and 7	0.701	0.188	2.027	0.716	−3.77	0.873	0.256	0.037	0.269	0.9995	−11.47	0.003
$M_{\rm BH}$–σ–$\rho_{\rm h}$	Tables 3 and 7	4.02	0.338	−0.141	0.047	0.461	1.028	0.282	0.041	0.308	0.9965	−6.414	0.04
$M_{\rm BH}$–$M_{\rm Bu}$–$\rho_{\rm h}$	Tables 3 and 7	1.298	0.124	0.109	0.067	−6.508	1.807	0.294	0.046	0.312	0.9503	−0.251	0.882
$M_{\rm BH}$–σ–$r_{\rm h}$	Tables 3 and 7	3.621	0.385	0.385	0.113	0	0.874	0.272	0.04	0.295	0.9993	−9.198	0.01
$M_{\rm BH}$–$M_{\rm Bu}$–$r_{\rm h}$	Tables 3 and 7	1.396	0.177	−0.318	0.202	−6.48	1.858	0.297	0.047	0.311	0.9471	−0.062	0.97
$M_{\rm BH}$–$M_{\rm Bu}$–σ	Tables 1 and 4	0.345	0.136	3.157	0.594	−2.534	0.813	0.293	0.042	0.311	0.9951	−4.073	0.13
$M_{\rm BH}$–σ–$\rho_{\rm h}$	Tables 1 and 4	3.91	0.331	−0.194	0.054	1.191	1.067	0.267	0.039	0.291	0.9996	−10.64	0.005
$M_{\rm BH}$–$M_{\rm Bu}$–$\rho_{\rm h}$	Tables 1 and 4	1.159	0.162	0.203	0.119	−5.841	2.681	0.415	0.056	0.41	0.958	−0.512	0.774
$M_{\rm BH}$–σ–$r_{\rm h}$	Tables 1 and 4	3.616	0.386	0.386	0.116	0.011	0.876	0.275	0.04	0.295	0.999	−8.687	0.013
$M_{\rm BH}$–$M_{\rm Bu}$–$r_{\rm h}$	Tables 1 and 4	1.355	0.272	−0.599	0.362	−5.954	2.83	0.415	0.055	0.41	0.9546	−0.319	0.853

Note. Column 1: fit type; column 2: sample type, text; columns 3 and 4: first variable slope of the correlation and its error; columns 5 and 6: second variable slope of the correlation and its error; columns 7 and 8: zero point of the correlation and its errors; columns 9 and 10: intrinsic scatter and its errors; column 11: measured scatter; column 12: probability of the bivariate correlation; columns 13 and 14: ΔcAIC value and $RP = \exp(\Delta{\rm cAIC}/2)$ (the relative probability of the mono- and bivariate solutions). They are computed matching the bivariate solutions of this table to the monovariate solutions of Table 13 of the respective data sets. The pairings are $M_{\rm BH}$–$M_{\rm Bu}$–σ with $M_{\rm BH}$–σ, $M_{\rm BH}$–σ–$\rho_{\rm h}$ with $M_{\rm BH}$–σ, $M_{\rm BH}$–$M_{\rm Bu}$–$\rho_{\rm h}$ with $M_{\rm BH}$–$M_{\rm Bu}$, $M_{\rm BH}$–σ–$r_{\rm h}$ with $M_{\rm BH}$–σ, and $M_{\rm BH}$–$M_{\rm Bu}$–$r_{\rm h}$ with $M_{\rm BH}$–$M_{\rm Bu}$; see Section 4.

As noted in Section 5, all our one- and two-dimensional correlations have sizable intrinsic scatter. The smallest intrinsic scatter (0.26 dex) is derived for the KH45 sample, using *M/L*s derived from colors. On one hand, this could indicate that BH masses correlate best with the baryonic mass of classical bulges. On the other hand, having now explored the influence of all galaxy structure parameters and their errors, we have to conclude that the remaining factor ≈2 uncertainty in the BH mass must stem from the unknown details of the accretion and feedback mechanisms.

7. CONCLUSIONS

We produced a merged SINFONI-plus-literature database of BH masses for 97 galaxies. For this sample, we computed dynamical bulge mass estimates $M_{\rm Bu}$ and determined the bulge spherical half-luminosity radius $r_{\rm h}$ and averaged spherical density $\rho_{\rm h}$ within $r_{\rm h}$, collecting bulge plus disk decompositions from the literature or performing them ourselves (for 16 galaxies). We confirm that there is an almost linear relation between BH mass and the mass of the classical bulge of a galaxy. The quadratic relation suggested by Graham & Scott (2013) for "Sérsic galaxies" is driven by the inclusion of pseudobulges and possibly uncertain bulge masses.

Densities and sizes of classical bulges turn out to be important. We showed that BH masses correlate directly with both densities and sizes, although with larger scatter than the more usual $M_{\rm BH}$–σ or $M_{\rm BH}$–$M_{\rm Bu}$ relations. We established significant bivariate correlations involving σ, $M_{\rm BH}$–σ–$\rho_{\rm h}$, $M_{\rm BH}$–σ–$r_{\rm h}$, and $M_{\rm BH}$–σ–$M_{\rm Bu}$, valid for all classical bulges (core and power-law ellipticals, classical bulges of disk galaxies) with low intrinsic ($\leqslant$0.34 dex) and measured ($\leqslant$0.37 dex) scatter. Two further bivariate correlations involving $M_{\rm Bu}$–$M_{\rm BH}$–$M_{\rm Bu}$–$\rho_{\rm h}$ and $M_{\rm BH}$–$M_{\rm Bu}$–$r_{\rm h}$ are also robustly detected, but with larger intrinsic (≈0.43 dex) and measured (≈0.44 dex) scatter and with core elliptical galaxies slightly offset. The five bivariate correlations are robustly detected also when the KH45 sample is considered. For this sample, with bulge masses scaled from *M/L*s derived from colors, the estimated intrinsic scatter is as low as 0.26 dex. Contrary to the suggestion of Graham (2008), none of these bivariate correlations is driven by the inclusion of barred galaxies. The relations point to a link between BH mass and $M_{\rm Bu}^{0.5}\sigma^2$, as proposed by Hopkins et al. (2007a, 2007b), or the bulge kinetic energy $M_{\rm Bu}\sigma^2$, as first suggested by Feoli & Mele (2005). In contrast, pseudobulges have systematically lower BH masses but approach the predictions of all the above relations at (spherical) densities $\rho_{\rm h} \geqslant 10^{10}\,M_\odot\,{\rm kpc}^{-3}$ or scale lengths $r_{\rm h} \leqslant 1$ kpc. These thresholds are rather uncertain because we do not know the true geometry of pseudobulges.

High densities and small sizes imply a large baryonic concentration near the center and make very efficient mass accretion onto the BH likely. Classical bulge densities and sizes, in turn, are set mainly by two factors: (1) the formation redshift—earlier formation implies higher halo and gas densities—and (2) the merging history—gas-poor mergers reduce the density and increase the size in each merger generation. Factor (1) could explain why compact classical bulges of S0 galaxies have the highest BH masses for their bulge mass; (2) implies that slow-rotator, core ellipticals of a given mass have slightly more massive BHs the lower their average density or the larger their size. The averaging effect of a series of gas-free mergers (Peng 2007) would also make plausible why the correlations derived for the sample of core ellipticals only tend to have the smallest intrinsic and measured scatter. Power-law, fast-rotator early types and classical bulges are the results of dissipational, gas-rich mergers of disk-dominated progenitors. The feedback mechanism triggered by BH accretion, coupled with the gravitationally induced virial equilibrium, creates the correlations between BH mass and galaxy structural parameters. In this case at a given $M_{\rm Bu}$ or σ, objects with larger average densities or smaller sizes have larger $M_{\rm BH}$. The bivariate correlations, however, are not as tight as the mass FP of early-type galaxies (e.g., Hyde & Bernardi 2009). The tightest relation we derive is the $M_{\rm BH}$–$M_{\rm Bu}$–σ relation for the KH45 sample, where the estimated intrinsic scatter is 0.26 dex. The unknown details of the BH accretion

Table 15
Comparison of the $M_{\mathrm{Bu}}^{a_{\mathrm{best}}}\sigma^{b_{\mathrm{best}}}$, $M_{\mathrm{Bu}}^{0.5}\sigma^2$, $M_{\mathrm{Bu}}\sigma^2$, and $M_{\mathrm{Bu}}\sigma$ Models

Model	a	b	Subsample	$\langle\delta a\delta b\rangle_{\mathrm{best}}$	$RP^{(3)}$	ΔcAIC	$RP^{(4)}$
$M_{\mathrm{Bu}}^{0.5}\sigma^2$	0.547	2.186	CorePowerEClassPC	−0.041	0.14	−1.78	0.41
	0.602	2.408	KH45 sample from Tables 3 and 7	−0.123	0.86	2.12	2.89
	0.558	2.230	as above, but from Tables 1 and 4	−0.068	0.26	−0.25	0.88
$M_{\mathrm{Bu}}\sigma^2$	0.673	1.346	CorePowerEClassPC	−0.041	0.002	−10.6	0.005
	0.803	1.606	KH45 sample from Tables 3 and 7	−0.123	0.84	2.07	2.82
	0.715	1.430	as above, but from Tables 1 and 4	−0.068	0.013	−6.31	0.04
$M_{\mathrm{Bu}}\sigma$	0.757	0.757	CorePowerEClassPC	−0.041	1.5×10^{-5}	−19.9	4.7×10^{-5}
	0.965	0.965	KH45 sample from Tables 3 and 7	−0.123	0.33	0.2	1.1
	0.825	0.825	as above, but from Tables 1 and 4	−0.068	4×10^{-4}	−13.2	1.4×10^{-3}

Note. Column 1: tested model; columns 2 and 3: best-fitting values of a and b; column 4: data set used; column 5: see Equation (30); column 6: the probabilities relative to the best-fitting M_{BH}–M_{Bu}–σ correlation, see Section 6.1; column 7: values of ΔcAIC computed matching the models of this table to the $M_{\mathrm{Bu}}^{a_{\mathrm{best}}}\sigma^{b_{\mathrm{best}}}$ model of the corresponding data set, see Tables 12 and 14; column 8: $RP^{(4)} = \exp(\Delta\mathrm{cAIC}/2)$ gives the probability of the models of this table relative to the $M_{\mathrm{Bu}}^{a_{\mathrm{best}}}\sigma^{b_{\mathrm{best}}}$ model of the corresponding data set.

physics and feedback mechanisms are probably responsible for this sizable intrinsic and measured scatter.

Disk galaxies that do not experience major mergers might develop a pseudobulge through secular instabilities such as bars. These may drive gas toward the center and feed the central BH. However, the lack of correlation between M_{BH} and the structural parameters of pseudobulges shows that no efficient consistent feedback mechanism is at work in these objects. Only pseudobulges with extremely high densities or small sizes manage to form BHs with masses approaching those of classical bulges.

We thank the first referee of the paper, John Kormendy, for a careful proof of Table 1; we thank the statistics editor of ApJ for his valuable suggestions on model comparison; we thank the second anonymous referee for comments that helped us improve the presentation of the results. M.O. acknowledges support by the Trans-regional Collaborative Research Centre TR22 "The Dark Universe" of the Deutsche Forschungsgemeinschaft (DFG) and the DFG Cluster of Excellence "Origin and Structure of the Universe." S.P.R. was supported by the DFG Cluster of Excellence "Origin and Structure of the Universe." P.E. was supported by the DFG Priority Programme 1177 "Galaxy Evolution."

Funding for the creation and distribution of the SDSS Archive has been provided by the Alfred P. Sloan Foundation, the Participating Institutions, the National Aeronautics and Space Administration, the National Science Foundation, the US Department of Energy, the Japanese Monbukagakusho and the Max Planck Society. The SDSS website is http://www.sdss.org/. SDSS is managed by the Astrophysical Research Consortium (ARC) for the Participating Institutions. The Participating Institutions are The University of Chicago, Fermilab, the Institute for Advanced Study, the Japan Participation Group, The Johns Hopkins University, the Korean Scientist Group, Los Alamos National Laboratory, the Max-Planck-Institute for Astronomy (MPIA), the Max-Planck-Institute for Astrophysics (MPA), New Mexico State University, University of Pittsburgh, University of Portsmouth, Princeton University, the United States Naval Observatory and the University of Washington. This research made use of the of the NASA/IPAC Infrared Science Archive and the NASA/IPAC Extragalactic Database (NED) which are operated by the Jet Propulsion Laboratory, California Institute of Technology, under contract with the National Aeronautics and Space Administration. It also made use of the Lyon-Meudon Extragalactic Database (LEDA; part of HyperLeda at http://leda.univ-lyon1.fr/).

APPENDIX A
THE EFFECTIVE VELOCITY DISPERSION FOR SINFONI GALAXIES

We determined the effective velocity dispersion σ for the SINFONI sample using long-slit or integral field stellar kinematics and total half-luminosity radii $R = R_{eT}$ taken from the Hyperleda or RC3 (see Table 17) for consistency with previous studies, in combination with the photometry we used for the dynamical modeling. These radii refer to the galaxy as a whole. The half-luminosity radii of the bulge component of a galaxy can be much smaller; see Section 2. The σ values given in Table 1 were obtained by averaging the quantity

$$v(R) = \sqrt{V(r)^2 + \sigma(R)^2}, \tag{33}$$

out to $R = R_{eT}$, where $V(R)$ and $\sigma(R)$ are the stellar line-of-sight mean velocity and velocity dispersion at a distance R from the center:

$$\sigma = \sum_{R \leqslant R_{eT}} v(R)w(R) \Big/ \sum_{R \leqslant R_{eT}} w(R). \tag{34}$$

We weighted each data point with its light contribution. When integral field data were available, this means we set $w(R) = I_c(R)$, where $I_c(R)$ is the circularized surface brightness at the distance R. When only long-slit data were available, we multiplied $I_c(R)$ by the corresponding circumference, $2\pi R$, i.e., $w(R) = 2\pi R I_c(R)$. The errors given in Table 1 for the SINFONI galaxies are the rms of the simple mean of the $v(R)$ (σ^s, obtained by setting $w(R) = 1$ in Equation (34)), divided by the square root of the number of points.

In Table 17 we also list the following quantities:

σ_{col} the velocity dispersion derived by fitting the spectrum obtained by summing together the spectra of the SINFONI data cube

σ_{SIN} the velocity dispersion derived by applying Equation (34) to the SINFONI kinematics

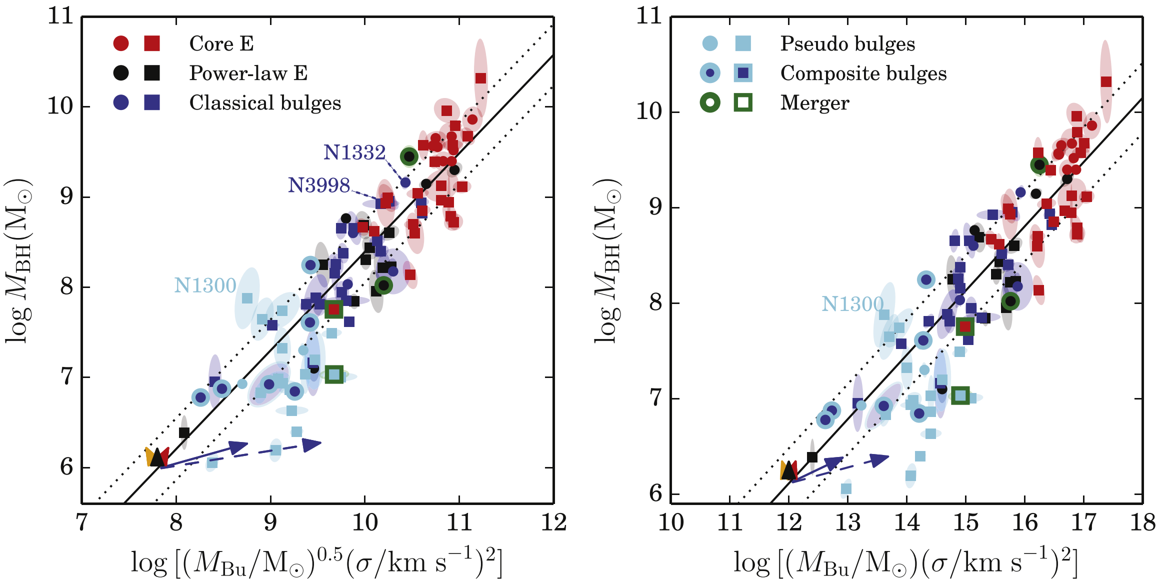

Figure 18. Correlation between $\log M_{\rm BH}$ and $\log M_{\rm Bu}^{0.5}\sigma^2$ (left) and between $\log(M_{\rm BH})$ and $\log M_{\rm Bu}\sigma^2$ (right). The corresponding best-fit relations for the CorePowerEClassPC sample are shown using solid lines, with the dotted lines showing estimated intrinsic scatter. The ellipses show the 1σ errors. Colors, arrows, and point types are as in Figure 14.

Table 16
Fractional Changes in $M_{\rm BH}$, $M_{\rm Bu}$, σ, $r_{\rm h}$, $\rho_{\rm h}$ Expected after a Major or a Minor "Dry" Merger That Doubles the Galaxy and BH Mass, a "Wet" Merger with Initial Bulge-to-total Ratio B/T and Final-to-initial Bulge-scales Ratio k, and Gas Accretion on the BH

Process	$M_{\rm BH}^f/M_{\rm BH}^i$	$M_{\rm Bu}^f/M_{\rm Bu}^i$	$r_{\rm h}^f/r_{\rm h}^i$	$\rho_{\rm h}^f/\rho_{\rm h}^i$	σ^f/σ_i
Major dry merger	2	2	2	1/4	1
Minor dry merger	2	2	4	1/32	$1/2^{0.5}$
Wet merger	2	$\frac{2}{(B/T)}$	κ	$\frac{2}{k^3(B/T)}$	$\left[\frac{2}{k\,(B/T)}\right]^{0.5}$
BH Accretion	2	1	1	1	1

$\sigma_{\rm SIN}$ the velocity dispersion derived by applying Equation (34) with $w(R)=1$ to the SINFONI kinematics
$\sigma_{{\rm e}/2}$ the velocity dispersion derived by applying Equation (34) out to $R_{eT}/2$
$\sigma_{{\rm e}/2}$ the velocity dispersion derived by applying Equation (34) with $w(R)=1$ out to $R_{eT}/2$

Figure 19 compares the quantities listed in Table 17 to σ. On one hand, the velocity dispersion $\sigma_{\rm col}$ derived from the spectrum obtained by summing together the spectra of the SINFONI data cube reproduces within 5% $\sigma_{\rm SIN}$ and within 8% $\sigma_{\rm SIN}^s$ with mean deviations less than 1%. So, averaging the resolved kinematics according to Equation (33) is equivalent to deriving the velocity dispersion from an integrated spectrum of a galaxy. On the other hand, σ matches the other estimates σ_e^s, $\sigma_{e/2}^s$, and $\sigma_{e/2}$ within less than 3% scatter and with mean deviations less than 0.8%. Therefore, neither the exact choice of the cutoff radius nor the weighting scheme plays a big role in the determination of the average velocity dispersion. Moreover, the average fractional error is 0.02, which matches the scatter well. Not surprisingly, the scatter obtained by comparing $\sigma_{\rm col}$ to σ is much larger (14% with a mean difference of 2%) because $\sigma_{\rm col}$ probes the inner regions of the galaxies, where the presence of the supermassive BH or the influence of a compact classical bulge becomes dynamically important.

Kormendy & Ho (2013) give discrepant velocity dispersions for three galaxies of our SINFONI sample. For NGC 1332 they have 328 km s^{-1} (from our previous determination in Rusli et al. 2011), which we now revise to 293.1 km s^{-1} (see Appendix B). For NGC 4486a they quote 111 km s^{-1}, whereas we get 144.5 km s^{-1} using the profiles of Prugniel et al. (2011). For NGC 4486b their value is larger (185 km s^{-1} compared to 148.6 km s^{-1}), but the combination of a steep surface brightness and velocity dispersion radial gradient makes the measurement difficult (see Appendix B).

APPENDIX B
LUMINOSITY PROFILES AND BULGE MASS-TO-LIGHT RATIOS

Many of the profiles come from the ESO Key Programme described in Scorza et al. (1998, hereafter KeyProg) or were derived from images from the SDSS (York et al. 2000). We corrected luminosity profiles and colors for galactic extinction (GE) following Schlegel et al. (1998); however, we quote the results of the fits in Tables 20–33 without correction for GE. The zero points of the profiles derived from SDSS images and corrected for GE are moved to the Johnson-Cousins bands when necessary using the equations of Jordi et al. (2006) and extinction-corrected colors. Most of the colors used in the conversions from one band to the other come from the Hyperleda database (Paturel et al. 2003). For three galaxies we also use the colors of the simple stellar populations (SSP) of Maraston (2005). We discuss how we addressed these cases and how we obtained the bulge luminosity profiles (which coincide with the total luminosity profile in the case of elliptical galaxies) below.

For all the galaxies we managed either to collect the dynamically determined bulge *M/L*s from the literature or to compute our own dynamical estimate by fitting available stellar kinematics (see Appendix C). The ratios and their sources are quoted in Table 34. In most of the cases the literature values do

Table 17
Velocity Dispersions of the SINFONI Sample

Galaxy	$R_{e,T}$ ($''$)	$R_{\rm max}^{\rm kin}/R_{e,T}$ —	$\sigma_{\rm col}$ (km s^{-1})	$\sigma_{\rm SIN}$ (km s^{-1})	$\sigma_{\rm SIN}^{s}$ (km s^{-1})	$\sigma_{e/2}$ (km s^{-1})	$\sigma_{e/2}^{s}$ (km s^{-1})	σ_{e}^{s} (km s^{-1})
NGC 0307	4.755	1.942	233.9	225.9	227.6	209.9	204.9	204.9
NGC 1316	80.75	0.6128	221	216.4	216.5	230.6	230.4	230.4
NGC 1332	28	0.7178	352.4	352.3	373.9	292	290.4	290.4
NGC 1374	24.38	0.4825	191.7	192.9	205.6	167.8	167	167
NGC 1398	52.13	0.693	213.1	207.3	197.1	233.2	235	235
NGC 1407	70.33	0.5436	285.6	287.2	289.4	276.4	277.9	277.9
NGC 1550	25.53	0.965	293.3	302.8	318.8	276.9	260.2	260.2
NGC 3091	32.89	0.3684	315	320.5	332.3	299.7	294.1	294.1
NGC 3368	73.64	1.058	98.5	109.2	102	132.8	130.2	130.2
NGC 3489	20.3	—	91.1	97.72	96.85	—	—	—
NGC 3627	67.16	0.4754	104.7	107.3	95.43	122.4	122.4	122.4
NGC 3923	49.79	0.7626	256.6	245.2	254.1	226.3	211.8	211.8
NGC 4371	23.29	1.099	115.4	111.3	108.1	141.5	142.8	142.8
NGC 4472	225.5	0.3036	289.1	302.1	295.9	303.7	305.9	305.9
NGC 4486a	5.459	1.952	144.8	130.7	118	149.1	141.1	141.1
NGC 4486b	2.495	1.2	200.1	199.8	230.8	159.4	146.3	146.3
NGC 4501	77.11	0.8222	138.7	134.5	135.5	159.1	157.8	157.8
NGC 4699	30.7	0.5416	176.5	175	182	181.3	189.6	189.6
NGC 4751	22.76	0.3563	363.3	382.3	416.7	361.4	363.9	363.9
NGC 5018	22.76	0.9905	188.1	190.3	186	210.1	208.4	208.4
NGC 5328	22.24	1.27	356.1	335	320.1	335	324.3	324.3
NGC 5419	43.36	0.3201	349.9	344.1	354.6	367.2	370.4	370.4
NGC 5516	22.09	0.3944	289.3	267.7	275.7	332.7	339.7	339.7
NGC 6861	17.67	0.4878	345.3	338.8	351.7	389	390.2	390.2
NGC 7619	36.91	1.837	322.2	320.3	321.1	299.9	279.3	279.3

Note. Column 1: galaxy name; column 2: total half-luminosity radius $R_{e,T}$; column 3: ratio between $R_{\rm max}^{\rm kin}$ and $R_{e,T}$, where $R_{\rm max}^{\rm kin}$ is the distance from the center of the most distant available stellar kinematic point; column 4 to 9: see the text in Appendix A.

not include a correction for GE, which we apply here following Schlegel et al. (1998). Exceptions are Saglia et al. (1993, 2000), Moellenhoff et al. (1995), Kronawitter et al. (2000), Bower et al. (2001), Cappellari et al. (2006), Dalla Bontà et al. (2009), Krajnović et al. (2009), and Rusli et al. (2013a), who already published M/L values corrected for GE. The photometric band for which the M/L values were computed does not always coincide with the photometic band we used to derive the bulge luminosity profile (see Table 34). Finally, we adjust distances by adopting the ones given by Kormendy & Ho (2013) or Sani et al. (2011) for the remaining objects.

In general we scale the M/L ratios to our distances and bands using the equation

$$M/L_{\rm us} = M/L_{\rm lit} \times \frac{D_{\rm lit}}{D_{\rm us}} \times 10^{0.4(m_{\rm us}-m_{\rm lit})} \times 10^{0.4(m_{\odot,{\rm lit}}-m_{\odot,{\rm us}})}. \quad (35)$$

The solar magnitudes used below are listed in Table 18. The original M/L values and distances, together with colors and GE values used to transform or compute the M/Ls, are given in Table 19.

Figure 20 shows the derived M/L ratios in the nine bands with more than one galaxy as a function of the dynamical bulge mass. In general, they increase with bulge mass; a comparison with the models of Maraston (2005) shows that SSPs with a Kroupa IMF, solar metallicity, and ages ranging from 2 to 12 Gyr roughly bracket the observed range.

In the following two subsections, we discuss in detail the galaxies with BH masses from the literature and from our SINFONI survey.

B.1. Literature Sample

The surface-brightness values reported in Tables 20–33 are in the Vega system, when Johnson and the 3.6*mu* filters are used, or in the AB system, when SDSS filters are used.

Milky Way: We adopt the axisymmetric bulge density profile of McMillan (2011), scaled as follows. Portail et al. (2015) compute the total mass in the bulge volume ($\pm 2.2 \times \pm 1.4 \times \pm 1.2$) kpc to be $1.84 \times 10^{10}\,M_{\odot}$. A sphere with a 1.92 kpc radius has the same volume. Using the spherically averaged density profile of McMillan (2011), we get a mass within this radius of $7.2 \times 10^{9}\,M_{\odot}$, so we scale up this profile by a factor of 2.54.

Circinus: The bulge photometry in the 3.6*mu* band is taken from the decomposition published by Sani et al. (2011). The M/L is derived as in Appendix C and Figure 37 to match the kinematic profiles of Maiolino et al. (1998). We follow Kormendy & Ho (2013) in classifying the galaxy as barred.

A 1836: The M/L is scaled to the distance of Kormendy & Ho (2013), and the *i*-band image is calibrated to the Cousins *I* using the $(r-i)$ color and the equations in Jordi et al. (2006). McConnell & Ma (2013) and Kormendy & Ho (2013) consider the galaxy a core elliptical; we accept their classification, although strong nuclear dust makes it difficult to determine its core properties (see discussion in Rusli et al. 2013a).

IC 1459: We correct the M/L for GE, scaling it from the R to V band using the $(V-R)$ color from Hyperleda and adjusting it to the distance of Kormendy & Ho (2013). The galaxy is a core elliptical (Rusli et al. 2013a), despite the

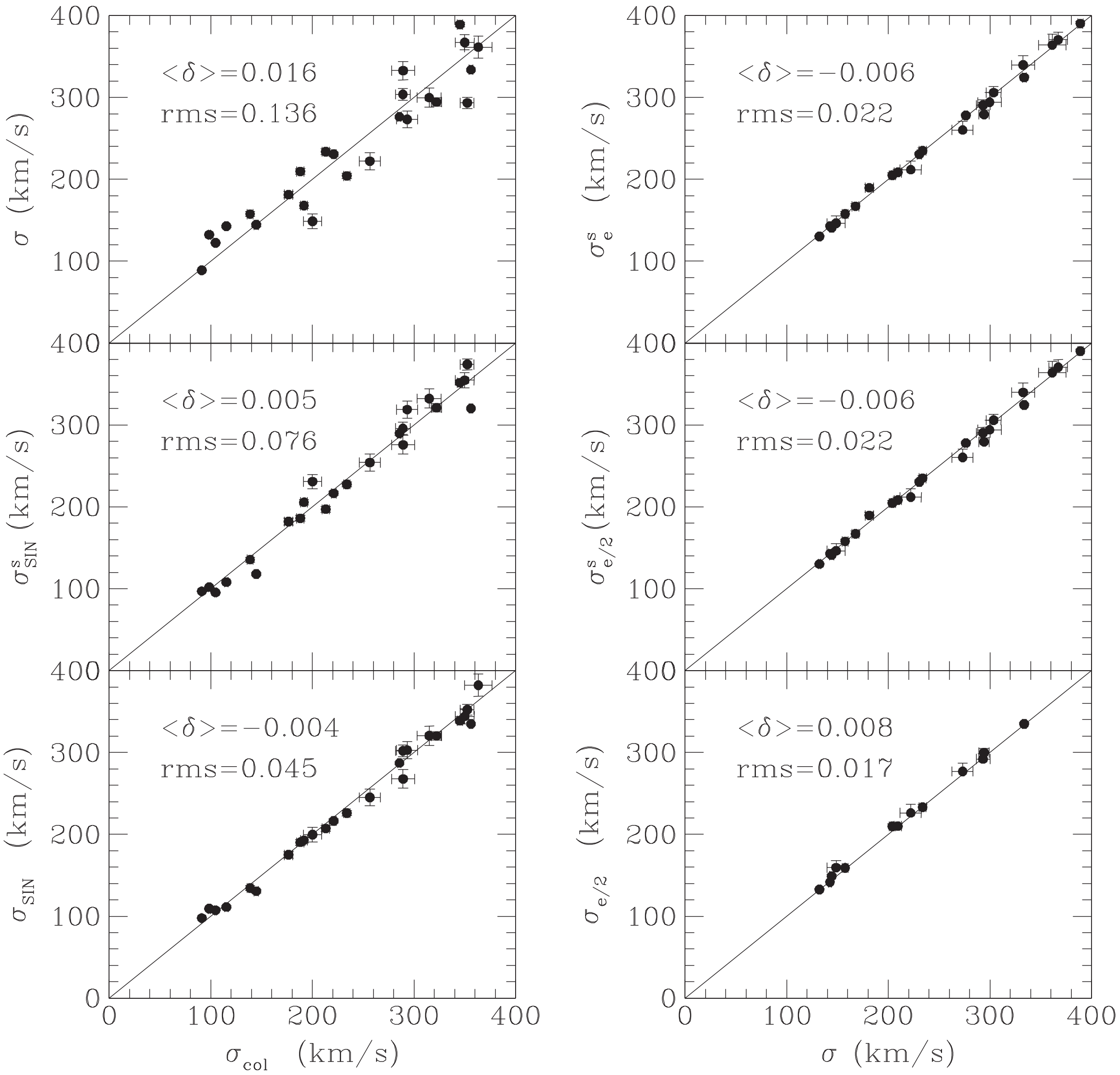

Figure 19. Comparison between the different estimates of the average velocity dispersion of a galaxy and σ for the SINFONI sample.

Table 18
Solar Magnitudes Used in the Conversion of the M/L

$m_{\odot,B}$	5.48
$m_{\odot,V}$	4.83
$m_{\odot,g}$	5.36
$m_{\odot,R}$	4.42
$m_{\odot,r}$	4.67
$m_{\odot,I}$	4.08
$m_{\odot,i}$	4.57
$m_{\odot,z}$	4.52
$m_{\odot,{\rm zACS}}$	3.98
$m_{\odot,H}$	3.32
$m_{\odot,K}$	3.28
$m_{\odot,3.6mu}$	3.24

classification of Kormendy & Ho (2013). We use the profile of Rusli et al. (2013a) and derive $R_e = 18.''6$, while their $n = 7.6$ core-Sérsic fit profile has $R_e = 45.''4$ (see Figure 2). The difference is driven by the extrapolation. The same applies to the result of Sani et al. (2011), who measure $R_e = 53.''3$, and Läsker et al. (2014), who quote $R_e = 38.''4$ for the "classical" fit and $R_e = 51.''9$ for the best fit.

IC 4296: McConnell & Ma (2013) and Kormendy & Ho (2013) consider the galaxy a core elliptical; we accept their classification, although strong nuclear dust makes it difficult to determine its core properties (see discussion in Rusli et al. 2013a). We measure the profile from *I*-band FORS images that we calibrate to Cousins *I* using the photometry of Prugniel & Heraudeau (1998) and finally to the *B* band using the mean $(B - I) = 2.41$ color derived from Goudfrooij et al. (1994) and $A_B = 0.265$. From this profile we measure $R_e = 68.''1$, in agreement with the Läsker et al. (2014, $R_e = 70.''9$) "best fit," but disagreeing with their "classical fit" ($R_e = 28.''9$) or the value reported by Sani et al. (2011, $32.''3$). The M/L (from the model with dark matter and already corrected for GE) is scaled to the distance of Kormendy & Ho (2013).

NGC 221: The M/L is scaled from the V to R band using the $(V - R)$ color from Hyperleda and to the distance of Kormendy & Ho (2013).

Table 19

Original M/L and Distances with Colors and Galactic Extinction (GE) Values Used in the M/L Conversions for the Literature Sample

Galaxy	Comment
Circinus	$M/L_{3.6mu}$ derived fitting the stellar kinematics of Maiolino et al. (1998), $A_{3.6mu} = 0.107$
A 1836	$M/L_I = 5\, M_\odot/L_\odot$, $D = 147.2$ Mpc from Dalla Bontà et al. (2009), GE corrected $A_i = 0.134$, $A_r = 0.176$, $(r - i) = 0.482$, $(I - i) = -0.247 \times [(r - i)_0 + 0.236]/1.007$
IC 1459	$M/L_R = 4.2\, M_\odot/L_\odot$, $D = 29.2$ Mpc from Häring & Rix (2004), not corrected for GE $A_R = 0.042$, $A_V = 0.053$, $(V - R) = 0.621$
IC 2560	$M/L_{3.6mu}$ derived fitting the central σ of Greene et al. (2010), $A_{3.6mu} = 0.015$
IC 4296	$M/L_B = 5.6\, M_\odot/L_\odot$, $D = 75$ Mpc from Saglia et al. (1993), GE corrected $A_B = 0.265$, $A_I = 0.119$, $(B - I) = 2.41$
NGC 0221	$M/L_V = 2.16\, M_\odot/L_\odot$, $D = 0.8$ Mpc from Magorrian et al. (1998), not corrected for GE $A_V = 0.206$, $A_R = 0.166$, $(V - R) = 0.641$
NGC 0224	$M/L_V = 4.83\, M_\odot/L_\odot$, $D = 0.8$ Mpc from Magorrian et al. (1998), not corrected for GE, $A_V = 0.206$
NGC 0524	$M/L_I = 4.99\, M_\odot/L_\odot$, $D = 23.3$ Mpc from Cappellari et al. (2006), GE corrected
NGC 0821	$M/L_I = 3.08\, M_\odot/L_\odot$, $D = 23.44$ Mpc from Cappellari et al. (2006), GE corrected $A_R = 0.294$, $A_I = 0.213$, $(R - I) = 0.6923$
NGC 1023	$M/L_V = 5.56\, M_\odot/L_\odot$, $D = 10.2$ Mpc from Bower et al. (2001), GE corrected $A_V = 0.201$, $A_{3.6mu} = 0.009$, $(V - 3.6mu) = 3.695$
NGC 1068	M/L_K derived fitting the stellar kinematics of Emsellem et al. (2006), $A_K = 0.012$
NGC 1194	M/L_r derived fitting the stellar kinematics of Greene et al. (2010), $A_r = 0.21$
NGC 1300	$M/L_{F606W} = 2.29\, M_\odot/L_\odot$, $D = 18.8$ Mpc from Atkinson et al. (2005), not corrected for GE, $A_V = 0.1$, $A_R = 0.081$, $(V - F606W) = 0.36$
NGC 1399	$M/L_B = 10.2\, M_\odot/L_\odot$, $D = 21.1$ Mpc from Kronawitter et al. (2000), GE corrected
NGC 2273	M/L_R derived fitting the stellar kinematics of Greene et al. (2010), $A_R = 0.189$
NGC 2549	M/L_R from Krajnović et al. (2009), GE corrected $A_V = 0.22$, $A_R = 0.175$, $(V - R)_{SV} = 0.567$, $(R_{SV} - r) = -0.267 \times (V - R)_{SV} - 0.088$ $(R - R_{SV}) = 0.27 \times (R - V)_{SV} - 0.22$
NGC 2748	$M/L_{3.6mu}$ derived fitting the stellar kinematics of Batcheldor et al. (2005), $A_{3.6mu} = 0.004$
NGC2778	$M/L_V = 8\, M_\odot/L_\odot$, $D = 22.9$ Mpc from Gebhardt et al. (2003), not corrected for GE $A_V = 0.069$, $(V - R) = 0.643$, $(B - V) = 0.958$, $(V - r)_0 = -0.63(B - V) + 1.646(V - R) + 0.124 - A_V$
NGC 2787	$M/L_{3.6mu}$ derived fitting the stellar kinematics of Bertola et al. (1995), $A_{3.6mu} = 0.020$
NGC 2960	M/L_r derived fitting the stellar kinematics of Greene et al. (2010), $A_r = 0.123$
NGC 2974	$M/L_I = 4.52\, M_\odot/L_\odot$, $D = 20.89$ Mpc from Cappellari et al. (2006), corrected for GE $A_I = 0.106$, $A_{3.6mu} = 0.008$, $(I - 3.6mu) = 2.374$
NGC 3031	M/L_i derived fitting the stellar kinematics of Fabricius et al. (2012), $A_i = 0.167$
NGC 3079	$M/L_{3.6mu}$ derived fitting the stellar kinematics of Shaw et al. (1993), $A_{3.6mu} = 0.002$
NGC 3115	$M/L_V = 8.04\, M_\odot/L_\odot$, $D = 8.4$ Mpc from Magorrian et al. (1998), not corrected for GE, $A_V = 0.157$
NGC 3227	M/L_{Kp} from Davies et al. (2006), GE corrected, narrow band definition
NGC 3245	$M/L_R = 3.7\, M_\odot/L_\odot$, $D = 20.9$ Mpc from Häring & Rix (2004), not corrected for GE $A_B = 0.108$, $A_V = 0.083$, $A_R = 0.067$, $A_i = 0.052$, $(B - V) = 0.8367$, $(V - R)_{\rm SSP} = 0.508$, $(R - I)_{\rm SSP} = 0.48$, $(R - i) = 1.007 \times (R - I)_{\rm SSP} - 0.267 \times (V - R)_{\rm SSP} - 0.236 - 0.088$
NGC 3377	$M/L_I = 2.22\, M_\odot/L_\odot$, $D = 10.91$ Mpc from Cappellari et al. (2006), GE corrected $A_R = 0.091$, $A_I = 0.066$, $(R - I) = 0.629$
NGC 3379	$M/L_I = 2.8\, M_\odot/L_\odot$, $D = 10.57$ Mpc, from Cappellari et al. (2006), GE corrected
NGC 3384	$M/L_V = 2.2\, M_\odot/L_\odot$, $D = 11.7$ Mpc from Schulze & Gebhardt (2011), not corrected for GE, $A_V = 0.088$, $A_R = 0.071$, $A_I = 0.052$, $A_i = 0.052$, $(R - I) = 0.624$, $(V - I) = 1.18$, $(I - i) = -0.247 \times (R - I)_0 - 0.329$
NGC 3393	M/L_I fitting the stellar velocity dispersion of Greene et al. (2010), $A_I = 0.146$
NGC 3414	$M/L_I = 4.26\, M_\odot/L_\odot$, $D = 24.55$ Mpc from Cappellari et al. (2006), GE corrected $A_r = 0.067$, $A_i = 0.051$, $(r - i) = 0.419$, $(R - I) = [0.236 + (r - i)_0]/1.007$, $(i - I) = -0.247 \times (R - I) - 0.329$
NGC 3585	$M/L_V = 3.4\, M_\odot/L_\odot$, $D = 21.2$ Mpc from Gültekin et al. (2009a), not corrected for GE, $A_V = 0.212$
NGC 3607	$M/L_V = 7.5\, M_\odot/L_\odot$, $D = 19.9$ Mpc from Gültekin et al. (2009a), not corrected for GE $A_B = 0.09$, $A_V = 0.069$, $A_g = 0.079$, $(B - V) = 0.921$, $(V - g) = -0.63 \times (B - V)_0 + 0.124$
NGC 3608	$M/L_V = 3.1\, M_\odot/L_\odot$, $D = 23$ Mpc from Rusli et al. (2013a), GE corrected $A_V = 0.069$, $A_I = 0.041$, $(V - I) = 1.24$

Table 19

(Continued)

Galaxy	Comment
	$A_R = 0.056$, $A_I = 0.041$, $A_i = 0.044$, $(R - I) = 0.608$, $(I - i) = -0.247 \times (R - I)_0 - 0.329$
NGC 3842	M/L_V from Rusli et al. (2013a), GE corrected
NGC 3998	$M/L_V = 6.5\ M_\odot/L_\odot$, $D = 17$ Mpc from de Francesco et al. (2006), not corrected for GE $A_B = 0.069$, $A_V = 0.053$, $A_I = 0.031$, $A_i = 0.034$, $(B - V) = 0.966$, $(V - I)_{\rm SSP} = 1.135$, $(R - I)_{\rm SSP} = 0.555$, $(I - i) = -0.247 \times (R - I)_{\rm SSP} - 0.329$
NGC 4026	$M/L_V = 4.89\ M_\odot/L_\odot$ from Gültekin et al. (2009a), not corrected for GE $A_B = 0.095$, $A_V = 0.073$, $A_g = 0.084$, $(B - V) = 0.962$, $(V - g) = -0.63 \times (B - V)_0 + 0.124$
NGC 4151	$M/L_R = 1.4\ M_\odot/L_\odot$, $D = 13.9$ Mpc from Onken et al. (2007), not corrected for GE, $A_R = 0.074$
NGC 4258	$M/L_V = 3.6\ M_\odot/L_\odot$, $D = 7.28$ Mpc from Häring & Rix (2004), not corrected for GE $A_V = 0.053$, $A_{3.6mu} = 0.002$, $(V - 3.6mu) = 3.629$
NGC 4261	$M/L_V = 9.1\ M_\odot/L_\odot$, $D = 31.6$ Mpc from Rusli et al. (2013a), GE corrected
NGC 4291	$M/L_V = 5.4\ M_\odot/L_\odot$, $D = 25$ Mpc from Rusli et al. (2013a), GE corrected
NGC 4342	$M/L_I = 6.3\ M_\odot/L_\odot$, $D = 15$ Mpc from Cappellari et al. (2006), GE corrected $A_r = 0.056$, $A_i = 0.043$, $A_I = 0.04$, $(r - i) = 0.426$, $(R - I) = [(r - i)_0 + 0.236)]/1.007$, $(I - i) = -0.247 \times (R - I) - 0.329$
NGC 4374	$M/L_I = 4.36\ M_\odot/L_\odot$, $D = 17.86$ Mpc from Cappellari et al. (2006), GE corrected $A_V = 0.134$, $A_I = 0.078$, $(V - I) = 1.26$
NGC 4388	$M/L_{3.6mu}\ M_\odot/L_\odot$ fitting the stellar velocity dispersion Greene et al. (2010), $A_{3.6mu} = 0.005$
NGC 4459	$M/L_I = 2.51\ M_\odot/L_\odot$, $D = 15.7$ Mpc from Cappellari et al. (2006), GE corrected $A_V = 0.153$, $A_I = 0.09$, $(V - I) = 1.306$
NGC 4473	$M/L_V = 6.8\ M_\odot/L_\odot$, $D = 17$ Mpc from Schulze & Gebhardt (2011), not corrected for GE, $A_V = 0.094$
NGC 4486	$M/L_V = 6.3\ M_\odot/L_\odot$, $D = 17.9$ Mpc from Gebhardt & Thomas (2009), not corrected for GE, $A_V = 0.074$
NGC 4526	$M/L_I = 2.65\ M_\odot/L_\odot$, $D = 16.5$ Mpc from Davis et al. (2013), corrected for GE $A_I = 0.043$, $A_{3.6mu} = 0.003$, $(I - 3.6mu) = 2.47$
NGC 4552	$M/L_V = 7.1\ M_\odot/L_\odot$, $D = 15.85$ Mpc from Rusli et al. (2013a), GE corrected
NGC 4564	M/L_V fitting the stellar kinematics of Bender et al. (1994), $A_V = 0.116$
NGC 4594	$M/L_I = 3.4\ M_\odot/L_\odot$, $D = 9.8$ Mpc from Jardel et al. (2011), not corrected for GE $A_I = 0.099$
NGC 4596	$M/L_K\ M_\odot/L_\odot$ fitting the stellar kinematics of Bettoni & Galletta (1997), $A_K = 0.008$
NGC 4621	$M/L_I = 3.03\ M_\odot/L_\odot$, $D = 17.78$ Mpc from Cappellari et al. (2006), GE corrected $A_I = 0.064$, $A_{3.6mu} = 0.005$, $(I - 3.6mu) = 2.515$
NGC 4649	$M/L_V = 7.3\ M_\odot/L_\odot$, $D = 17.3$ Mpc from Rusli et al. (2013a), GE corrected
NGC 4697	$M/L_V = 4.3\ M_\odot/L_\odot$, $D = 12.4$ Mpc from Schulze & Gebhardt (2011), not corrected for GE, $A_V = 0.101$, $A_R = 0.081$, $(V - R) = 0.59$
NGC 4736	$M/L_B = 1.8\ M_\odot/L_\odot$, $D = 6.6$ Mpc from Moellenhoff et al. (1995), GE corrected $A_B = 0.076$, $A_V = 0.059$, $A_R = 0.047$, $A_I = 0.034$, $A_z = 0.026$, $(B - V) = 0.9$, $(V - R) = 0.84$, $(R - I) = 0.74$, $(g - r) = 1.646 \times (V - R)_0 - 0.139$, $(g - B) = -0.37 \times (B - V)_0 - 0.124$, $(r - z) = 1.586 \times (R - I)_0 - 0.386$, $(z - B) = (g - B) - (g - r) - (r - z)$
NGC 4826	M/L_i fitting the stellar kinematics of Héraudeau & Simien (1998), $A_i = 0.086$
NGC 4889	$M/L_r = 6.025 M_\odot/L_\odot$, $D = 103.2$ Mpc from McConnell et al. (2012), not corrected for GE, $A_R = 0.026$, $A_V = 0.032$, $(V - R) = 0.724$, $(r - R) = -0.267 \times (V - R)_0 - 0.088$
NGC 5077	$M/L_B = 4\ M_\odot/L_\odot$, $D = 56$ Mpc from Pizzella et al. (1997), not corrected for GE $A_B = 0.21$, $A_V = 0.161$, $(B - V) = 1.04$
NGC 5128	$M/L_K = 0.65\ M_\odot/L_\odot$, $D = 3.5$ Mpc from Cappellari et al. (2009), GE corrected
NGC 5576	$M/L_V = 3.7\ M_\odot/L_\odot$, $D = 27.1$ Mpc from Gültekin et al. (2009a), not corrected for GE $A_V = 0.104$, $A_R = 0.084$, $(V - R) = 0.553$
NGC 5813	$M/L_V = 4.7\ M_\odot/L_\odot$, $D = 32.2$ Mpc from Rusli et al. (2013a), GE corrected
NGC 5845	$M/L_V = 5.1\ M_\odot/L_\odot$, $D = 28.7$ Mpc from Schulze & Gebhardt (2011), not corrected for GE, $A_V = 0.177$
NGC 5846	$M/L_I = 5.2\ M_\odot/L_\odot$, $D = 24.9$ Mpc from Rusli et al. (2013a), GE corrected
NGC 6086	$M/L_R = 4.2\ M_\odot/L_\odot$, $D = 133$ Mpc from Rusli et al. (2013a), GE corrected
NGC 6251	$M/L_R = 6\ M_\odot/L_\odot$, $D = 106$ Mpc from Häring & Rix (2004), not corrected for GE

Table 19
(Continued)

Galaxy	Comment
	$A_V = 0.29$, $A_R = 0.234$, $A_I = 0.17$, $(R - I) = 0.626$, $(R - I)_{\rm SSP} = 0.643$, $(V - I) = 1.408$
NGC 6264	M/L_r fitting Greene et al. (2010) minor axis velocity dispersion, $A_r = 0.178$
NGC 6323	M/L_r fitting Greene et al. (2010) velocity dispersion, $A_r = 0.047$
NGC 7052	$M/L_R = 3.5\ M_\odot/L_\odot$, $D = 58.7$ Mpc from Häring & Rix (2004), not corrected for GE $A_R = 0.324$
NGC 7457	$M/L_{3.6mu}$ fitting the stellar kinematics of Emsellem et al. (2004), $A_{3.6mu} = 0.008$
NGC 7582	$M/L_{3.6mu}$ fitting the stellar kinematics of Oliva et al. (1995), $A_{3.6mu} = 0.002$
NGC 7768	$M/L_V = 7.8\ M_\odot/L_\odot$, $D = 112.8$ Mpc from Rusli et al. (2013a), GE corrected
UGC 3789	M/L_H fitting the stellar velocity dispersion of Greene et al. (2010), $A_H = 0.037$

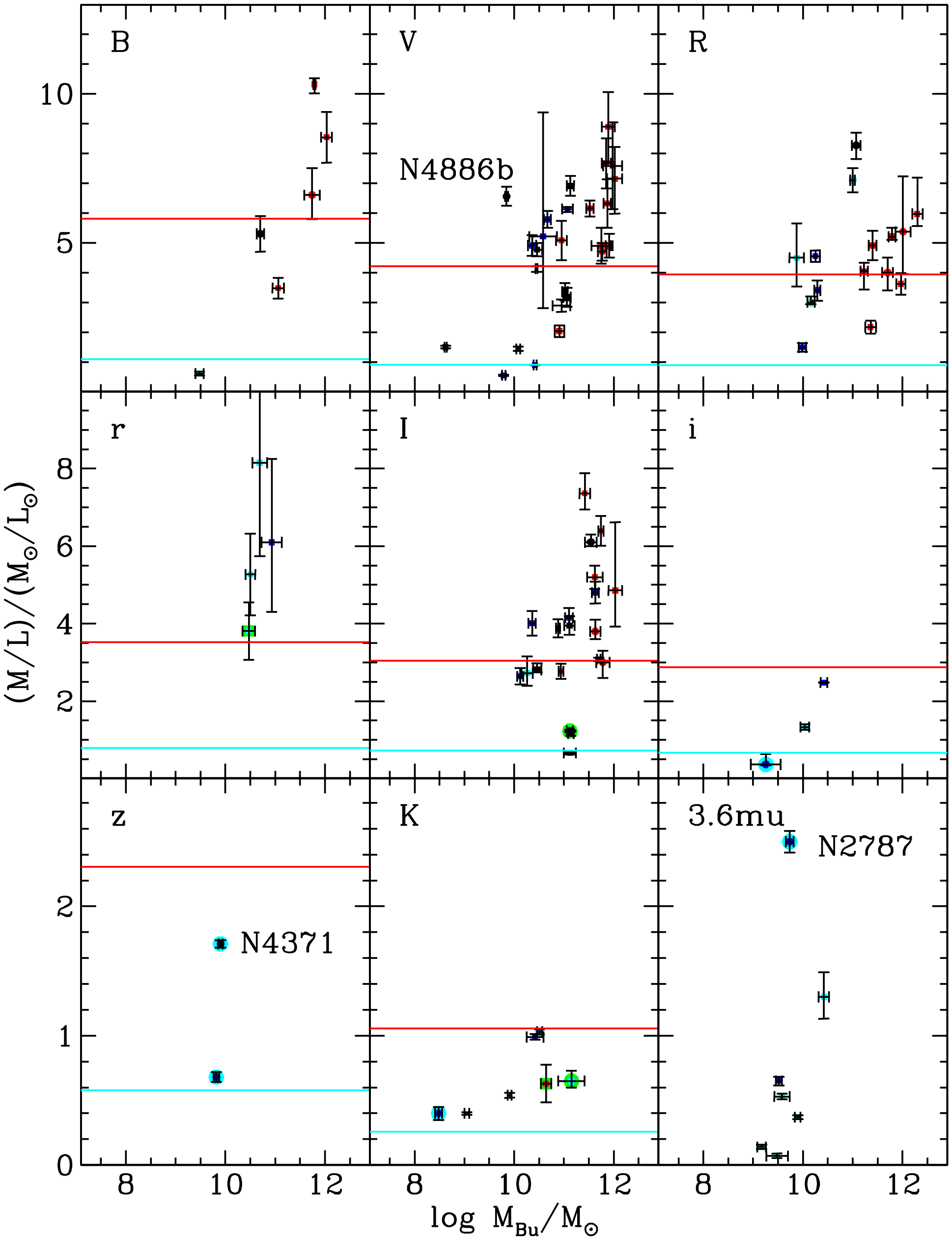

Figure 20. M/L ratios in the nine bands with more than one galaxy as a function of the bulge mass. Colors and point types are as in Figure 14. The lines show the values predicted by the simple stellar population models of Maraston (2005) for a Kroupa IMF, solar metallicity, and age of 2 (cyan) and 12 (red) Gyr.

Table 20
Bulge plus Disk Fits to the Galaxies of Figure 21

Galaxy	b/a	$n^B_{\rm Ser}$	a^B_e (arcsec)	μ_{a_e} (mag arcsec^{-2})	$m^B_{\rm tot}$ (mag)	h^D (arcsec)	μ^D_0 (mag arcsec^{-2})	$m^D_{\rm tot}$ (mag)	Bu/T
NGC 1023	0.75	2.71 ± 0.02	8.61 ± 0.19	14.8 ± 0.03	7.249 ± 0.04	57.6 ± 0.8	16.08 ± 0.04	5.59 ± 0.04	0.18
NGC 4258	0.6	2.91 ± 0.01	17.12 ± 0.21	16.27 ± 0.02	7.43 ± 0.03	87.6 ± 1.05	16.10 ± 0.02	4.95 ± 0.02	0.09
NGC 7457	0.75	3.14 ± 0.02	10.1 ± 0.4	17.43 ± 0.05	9.47 ± 0.07	27.3 ± 0.04	16.63 ± 0.04	7.77 ± 0.04	0.17

Note. We list the galaxy name, column 1; the flattening of the system, column 2; the parameters of the bulge (major axis half-light radius a_e, column 4; surface brightness at a_e, column 5; bulge magnitude, column 6; exponential scale length of the disk, column 7; disk central surface brightness, column 8; disk magnitude, column 9); and the bulge-to-total ratio, column 10. Surface brightnesses and magnitudes are given in the 3.6*mu* band.

Table 21
Parameters of the Bulge plus Disk Decomposition of NGC 2273

Bulge	PA [°]	ell		n	μ_e[mag arcsec^{-2}, R]	a_e[arcsec]	$m_{\rm Bu}$ [R mag]	Bu/T
	34.50 ± 0.03	0.3616 ± 0.0003		0.7937 ± 0.0008	17.2699 ± 0.0008	1.7801 ± 0.0007	13.91	0.08
Bar	PA [°]	ell	c_0	n	μ_e[mag arcsec^{-2}, R]	a_e[arcsec]	$m_{\rm Bar}$ [R mag]	Bar/T
	105.08 ± 0.02	0.4022 ± 0.0003	−0.305 ± 0.002	0.927 ± 0.001	20.2888 ± 0.0009	14.67 ± 0.01	12.43	0.31
Disk	PA [°]	ell			μ_0 [mag arcsec^{-2}, R]	h [arcsec]	$m_{\rm Di}$ [R mag]	Di/T
	63.76 ± 0.03	0.3919 ± 0.0004	⋯	⋯	20.868 ± 0.002	33.94 ± 0.03	11.76	0.57
Inner Ring	PA [°]	ell	⋯	⋯	μ_0 [mag arcsec^{-2}, R]	$r_{\rm ring}$[arcsec]	$m_{\rm Ri}$ [R mag]	Ri/T
	64.65 ± 0.05	0.3069 ± 0.0004			21.884 ± 0.002	20.45 ± 0.02	14.65	0.04
	$\sigma_{\rm in}$ [arcsec]	$\sigma_{\rm out}$ [arcsec]						
	2.14 ± 0.02	4.31 ± 0.01						

Table 22
Parameters of the Bulge plus Disk Decomposition of NGC 2549

Bulge	PA [°]	ell	n	μ_e[mag arcsec^{-2}, R]	a_e[arcsec]	$m_{\rm Bu}$ [R mag]	Bu/T
	179.73 ± 0.02	0.5055 ± 0.0002	3.467 ± 0.004	19.23 ± 0.003	13.09 ± 0.003	11.1	0.77
Edge-On-Disk	PA [°]	μ_0 [mag arcsec^{-2}, R]	h [arcsec]	$\alpha = 2/n$	z_0 [arcsec]	$m_{\rm Di}$ [R mag]	Di/T
	179.31 ± 0.01	20.14 ± 0.002	26.43 ± 0.03	2.38 ± 0.04	5.07 ± 0.03	12.39	0.23

Table 23
Parameters of the Bulge–Bar–Disk Decomposition of NGC 2748

Bulge	PA [°]	ell	n	μ_e[mag arcsec^{-2}, 3.6*mu*]	a_e[arcsec]	$m_{\rm Bu}$ [3.6*mu* mag]	Bu/T
	13.68 ± 0.07	0.386 ± 0.001	1.419 ± 0.003	15.99 ± 0.01	4.447 ± 0.007	10.42	0.15
Disk	PA [°]	ell	⋯	μ_0 [mag arcsec^{-2}, 3.6*mu*]	h [arcsec]	$m_{\rm Di}$ [3.6*mu* mag]	Di/T
	41.27 ± 0.01	0.719 ± 0.001		15.50 ± 0.01	16.75 ± 0.01	8.35	0.69
Inner Ring	PA [°]	ell	⋯	μ_0 [mag arcsec^{-2}, 3.6*mu*]	$r_{\rm ring}$ [arcsec]	$m_{\rm Ri}$ [3.6*mu* mag]	Ri/T
	44.28 ± 0.04	0.589 ± 0.001		17.30 ± 0.01	10.73 ± 0.01	11.87	0.04
	$\sigma_{\rm ring}$ [arcsec]						
	2.126 ± 0.009						
Outer Ring	PA [°]	ell	⋯	μ_0 [mag arcsec^{-2}, 3.6*mu*]	$r_{\rm ring}$ [arcsec]	$m_{\rm Ro}$ [3.6*mu* mag]	Ro/T
	43.3 ± 0.005	0.822 ± 0.001		17.49 ± 0.01	28.80 ± 0.01	9.09	0.12
	$\sigma_{\rm ring}$ [arcsec]						
	6.90 ± 0.01						

NGC 224: The M/L is scaled to the distance of Kormendy & Ho (2013). We classify it as barred following Athanassoula & Beaton (2006).

NGC 524: The M/L is scaled to the distance of Kormendy & Ho (2013). We classify this galaxy with $T = 2$ (a classical bulge). Although the galaxy is circular, significant stellar rotation is nonetheless seen (Simien & Prugniel 2000; Emsellem et al. 2004); therefore the S0 classification is dubious and the galaxy could be a core elliptical (McConnell & Ma 2013). We deproject the multi-Gaussian expansion of the photometry profile as given in Cappellari et al. (2006) and get $R_e = 47\farcs1$. We ignore the possible small disk detected by Sani et al. (2011) ($B/T \approx 0.83$); Kormendy & Ho (2013) give $B/T = 0.92$. Finally, we conclude that the bulge plus disk decomposition with $B/T = 0.28$ and $R_e = 8\farcs9$ of Laurikainen et al. (2010) does not describe the nature of the galaxy.

Table 24
Parameters of the Bulge–Bar–Disk–Ring Decomposition of NGC 3079

Bulge	PA [°]	ell	n	μ_e[mag arcsec^{-2}, 3.6*mu*]	a_e[arcsec]	$m_{\rm Bu}$ [3.6*mu* mag]	Bu/T
	169.4 ± 0.1	0.79 ± 0.01	2.724 ± 0.002	13.00 ± 0.011	4.50 ± 0.01	8.24	0.26
Bar	PA [°]	ell	n	μ_e[mag arcsec^{-2}, 3.6*mu*]	a_e[arcsec]	$m_{\rm Bar}$ [3.6*mu* mag]	Bar/T
	171.6 ± 0.1	0.69 ± 0.01	0.37 ± 0.01	17.43 ± 0.01	40.77 ± 0.01	8.35	0.24
Disk	PA [°]	ell	···	μ_0 [mag arcsec^{-2}, 3.6*mu*]	h [arcsec]	$m_{\rm Di}$ [3.6*mu* mag]	Di/T
	166.9 ± 0.1	0.86 ± 0.01		16.35 ± 0.01	52.87 ± 0.01	7.83	0.38
Ring	PA [°]	ell	μ [mag arcsec^{-2}, 3.6*mu*]	$r_{\rm ring}$ [arcsec]	$\sigma_{\rm ring}$ [arcsec]	$m_{\rm Ri}$ [3.6*mu* mag]	Ri/T
	169.2 ± 0.01	0.90 ± 0.01	16.66 ± 0.01	52.74 ± 0.01	13.11 ± 0.01	9.09	0.12

Table 25
Parameters of the Bulge plus Disk Decomposition of NGC 3393

Bulge	PA [°]	ell		n	μ_e[mag arcsec^{-2}, I]	a_e[arcsec]	$m_{\rm Bu}$ [I mag]	Bu/T
	142.1 ± 0.5	0.107 ± 0.002		1.45 ± 0.01	17.27 ± 0.01	1.91 ± 0.01	13.12	0.17
Bar	PA [°]	ell	c_0	n	μ_e[mag arcsec^{-2}, I]	a_e[arcsec]	$m_{\rm Bar}$ [I mag]	Bar/T
	160.5 ± 0.1	0.429 ± 0.002	−0.35 ± 0.01	0.352 ± 0.004	19.632 ± 0.007	9.98 ± 0.03	13.08	0.18
Disk	PA [°]	ell			μ_0 [mag arcsec^{-2}, I]	h [arcsec]	$m_{\rm Di}$ [I mag]	Di/T
	29 ± 4	0.022 ± 0.003	···	···	20.022 ± 0.005	18.98 ± 0.06	11.66	0.65

Table 26
Parameters of the Bulge plus Disk Decomposition of NGC 3414

Bulge	PA [°]	ell		n	μ_e[mag arcsec^{-2}, I]	a_e[arcsec]	$m_{\rm Bu}$ [I mag]	Bu/T
	176.01 ± 0.01	0.1918 ± 0.0005		5.13 ± 0.01	20.827 ± 0.008	28.04 ± 0.14	9.9	0.79
Bar	PA [°]	ell	c_0	n	μ_e[mag arcsec^{-2}, I]	a_e[arcsec]	$m_{\rm Bar}$ [I mag]	Bar/T
	199.48 ± 0.04	0.8527 ± 0.0006	0.478 ± 0.006	4.7 ± 0.3	22.177 ± 0.006	40.59 ± 0.14	13.2	0.04
Disk	PA [°]	ell			μ_0 [mag arcsec^{-2}, I]	h [arcsec]	$m_{\rm Di}$ [I mag]	Di/T
	35.7 ± 0.3	0.307 ± 0.003	···	···	21.152 ± 0.007	33.2 ± 0.1	11.54	0.17

Table 27
Parameters of the Bulge plus Disk Decomposition of NGC 4026

Bulge	PA [°]	ell	n	μ_e[mag arcsec^{-2}, V]	a_e[arcsec]	$m_{\rm Bu}$ [V mag]	Bu/T
	180.9 ± 0.1	0.402457 ± 0.0004	3.242 ± 0.004	19.222 ± 0.003	10.67 ± 0.02	11.36	0.59
Edge-On-Disk	PA [°]	μ_0 [mag arcsec^{-2}, V]	h [arcsec]	$\alpha = 2/n$	z_0 [arcsec]	$m_{\rm Di}$ [V mag]	Di/T
	177.5 ± 0.1	19.893 ± 0.003	34.34 ± 0.03	1.50 ± 0.01	4.83 ± 0.02	11.76	0.41

Table 28
Parameters of the Bulge plus Disk Decomposition of NGC 4342

Bulge	PA [°]	ell	n	μ_e[mag arcsec^{-2}, I]	a_e[arcsec]	$m_{\rm Bu}$ [I mag]	Bu/T
	164.99 ± 0.07	0.3420 ± 0.0009	7.51 ± 0.02	18.50 ± 0.008	5.79 ± 0.02	11.42	0.65
Disk	PA [°]	ell	···	μ_0 [mag arcsec^{-2}, I]	h [arcsec]	$m_{\rm Di}$ [I mag]	Di/T
	167.46 ± 0.01	0.7680 ± 0.0003		16.22 ± 0.002	5.581 ± 0.005	12.07	0.35

NGC 821: Kormendy & Ho (2013) quote $B/T = 0.95$, so we ignore the possible disk component and use the whole galaxy profile (Graham et al. 2001), getting $R_e = 34''.8$. Beifiori et al. (2012) report $R_e = 85''.4$, and the Läsker et al. (2014) "best fit" gives $3''.5$. The fit of Beifiori et al. (2012) overestimates the measured profile at radii larger than $70''$ by 0.4 mag. Läsker et al. (2014) consider a bulge, a (faint) disk, and a halo, and it is not clear that the bulge and halo should be treated as separate components. The M/L is scaled to the distance of Kormendy & Ho (2013) and from the I to R band using the mean $(R - I)$ color from Hyperleda.

NGC 1023: The M/L of Bower et al. (2001) is already corrected for GE; we scale it to the distance of Kormendy & Ho (2013) and calibrate it from the V band to 3.6*mu* using the V-band aperture photometry from Hyperleda. The *Spitzer* images come from Program 69, PI Giovanni Fazio, Observer ID 2. We perform a Sérsic bulge plus exponential disk decomposition along the major axis of the galaxy following Fisher & Drory (2008) and masking the region where the bar is present (see Figure 21 and Table 20). This gives $R_e = 7''.5$, which agrees with Fisher & Drory (2010). The two-dimensional fit (including a bar) of Sani et al. (2011) gives

Table 29
Parameters of the Bulge–Ring–Disk plus Point Source Decomposition of NGC 4388

Bulge	PA [°]	ell	n	μ_e[mag arcsec^{-2}, 3.6mu]	a_e[arcsec]	$m_{\rm Bu}$ [3.6mu mag]	Bu/T
	93.3 ± 0.1	0.494 ± 0.001	2.886 ± 0.002	18.23 ± 0.01	27.82 ± 0.01	8.53	0.38
Disk	PA [°]	ell		μ_0 [mag arcsec^{-2}, 3.6mu]	h [arcsec]	$m_{\rm Di}$ [3.6mu mag]	Di/T
	88.75 ± 0.01	0.830 ± 0.001	⋯	17.29 ± 0.01	48.64 ± 0.01	8.78	0.31
Ring	PA [°]	ell	⋯	μ_0 [mag arcsec^{-2}, 3.6mu]	$r_{\rm ring}$ [arcsec]	$m_{\rm Ri}$ [3.6mu mag]	Ri/T
	90.97 ± 0.01	0.82 ± 0.01		16.78 ± 0.01	28.99 ± 0.01	9.4	0.17
	$\sigma_{\rm in}$ [arcsec]	$\sigma_{\rm out}$ [arcsec]					
	7.39 ± 0.01	12.28 ± 0.01					
Point Source	PA [°]	ell	⋯	μ_0 [mag arcsec^{-2}, 3.6mu]	σ [arcsec]	$m_{\rm PS}$ [3.6mu mag]	PS/T
	63.55 ± 0.19	0.649 ± 0.002		8.392 ± 0.008	0.38 ± 0.01	9.63	0.14

Table 30
Parameters of the Bulge plus Disk Decomposition of NGC 4526

Bulge	PA [°]	ell	n	μ_e[mag arcsec^{-2}, 3.6mu]	a_e[arcsec]	$m_{\rm Bu}$ [3.6mu mag]	Bu/T
	10.7 ± 1.4	0.15 ± 0.01	2.74 ± 0.03	15.84 ± 0.04	7.3 ± 0.2	8.51	0.11
Inner Disk	PA [°]	ell	n	μ_0 [mag arcsec^{-2}, 3.6mu]	h [arcsec]	$m_{\rm Di}$ [3.6mu mag]	Di/T
	21.58 ± 0.05	0.69 ± 0.02	12.23 ± 0.01	3.78 ± 0.01	8.63	0.10	
Bar	PA [°]	ell	n	μ_e[mag arcsec^{-2}, 3.6mu]	a_e[arcsec]	$m_{\rm Bar}$ [3.6mu mag]	Bar/T
	28.28 ± 0.07	0.368 ± 0.001	0.738 ± 0.005	16.33 ± 0.01	19.54 ± 0.04	7.66	0.25
	c_0						
	1.55 ± 0.03						
Outer Disk	PA [°]	ell	n	μ_0 [mag arcsec^{-2}, 3.6mu]	h [arcsec]	$m_{\rm Do}$ [3.6mu mag]	Do/T
	27.97 ± 0.09	0.710 ± 0.003	1	19.02 ± 0.02	154.9 ± 2.6	7.83	0.21
	c_0						
	−0.92 ± 0.01						
Spur1	PA [°]	ell	n	μ_e[mag arcsec^{-2}, 3.6mu]	a_e[arcsec]	m_{Sp1} [3.6mu mag]	Sp1/T
	16.08 ± 0.06	0.711 ± 0.001	0.971 ± 0.004	18.99 ± 0.01	83.62 ± 0.35	8.05	0.18
	R.A.(Spur1)-R.A. (Center) [arcsec]	Decl.(Spur1)-Decl. (Center) [arcsec]					
	31.2 ± 0.1	−18.1 ± 0.2					
Spur2	PA [°]	ell	n	μ_e[mag arcsec^{-2}, 3.6mu]	a_e[arcsec]	m_{Sp2} [3.6mu mag]	Sp2/T
	17.37 ± 0.06	0.710 ± 0.001	0.756 ± 0.003	18.65 ± 0.01	67.8 ± 0.2	8.27	0.14
	R.A.(Spur2)-R.A. (Center) [arcsec]	Decl.(Spur2)-Decl. (Center) [arcsec]					
	−29.7 ± 0.1	−17.3 ± 0.2					

Table 31
Parameters of the Bulge plus Disk Decomposition of NGC 4736

Bulge	PA [°]	ell	n	μ_e[mag arcsec^{-2}, z]	a_e[arcsec]	$m_{\rm Bu}$ [z mag]	Bu/T
	25.80 ± 0.06	0.1582 ± 0.0003	1.405 ± 0.001	16.004 ± 0.001	8.071 ± 0.007	8.8	0.26
Disk	PA [°]	ell		μ_0 [mag arcsec^{-2}, z]	h [arcsec]	$m_{\rm Di}$ [z mag]	Di/T
	106.14 ± 0.04	0.1850 ± 0.0003	⋯	16.674 ± 0.002	23.80 ± 0.02	8.02	0.54
Outer Ring	PA [°]	ell	⋯	μ_0 [mag arcsec^{-2}, z]	$r_{\rm ring}$[arcsec]	$m_{\rm Ri}$ [z mag]	Ri/T
	94.44 ± 0.06	0.2497 ± 0.0005		21.011 ± 0.001	110.31 ± 0.09	9.1	0.2
	$\sigma_{\rm in}$ [arcsec]	$\sigma_{\rm out}$ [arcsec]					
	23.2 ± 0.1	51.01 ± 0.07					

Table 32
Parameters of the Bulge plus Disk Decomposition of NGC 4826

Bulge	PA [°]	ell	n	μ_e[mag arcsec^{-2}, i]	a_e[arcsec]	$m_{\rm Bu}$ [i mag]	Bu/T
	105.21 ± 0.04	0.2190 ± 0.0003	4.295 ± 0.005	20.106 ± 0.004	36.8 ± 0.1	9.12	0.28
Disk	PA [°]	ell	⋯	μ_0 [mag arcsec^{-2}, i]	h [arcsec]	$m_{\rm Di}$ [i mag]	Di/T
	111.399 ± 0.006	0.4556 ± 0.0001		18.1850 ± 0.0004	56.561 ± 0.009	8.08	0.72

Table 33
Parameters of the Bulge–Bar–Disk Decomposition of NGC 7582

Bulge	PA [°]	ell		n	μ_e[mag arcsec^{-2}, 3.6*mu*]	a_e[arcsec]	$m_{\rm Bu}$ [3.6*mu* mag]	Bu/T
	134.6 ± 0.06	0.419 ± 0.001		2.59 ± 0.01	12.71 ± 0.01	2.38 ± 0.01	8.27	0.29
Bar	PA [°]	ell	c_0	n	μ_e[mag arcsec^{-2}, 3.6*mu*]	a_e[arcsec]	$m_{\rm Bar}$ [3.6*mu* mag]	Bar/T
	140 ± 0.01	0.869 ± 0.001	1.74 ± 0.02	0.211 ± 0.001	17.20 ± 0.01	51.76 ± 0.04	8.58	0.22
Disk	PA [°]	ell	⋯	⋯	μ_0 [mag arcsec^{-2}, 3.6*mu*]	h [arcsec]	$m_{\rm Di}$ [3.6*mu* mag]	Di/T
	141.4 ± 0.03	0.602 ± 0.001			16.54 ± 0.01	37.3 ± 0.04	7.69	0.49

$R_e = 18.''8$, but the peculiar fit residuals suggest that the bar has not been modeled correctly.

NGC 1068: We consider the small classical component of the composite bulge, getting $R_e = 0.''5$ (Erwin et al. 2015). This explains the large difference with Sani et al. (2011), who derive $R_e = 8.''4$ for the pseudobulge of the galaxy. The M/L is derived using the distance of Kormendy & Ho (2013) and fitting the major-axis kinematic profile $\sqrt{\sigma^2 + V^2}$ of Figure 5 of Emsellem et al. (2006), summing the bulge and disk contributions (see Appendix C and Figure 37). The value $M/L_K = 0.7$ derived by Erwin et al. (2015) for the stellar population of the classical bulge is a factor of 1.9 larger. We adopt this as the upper error estimate. The lower error estimate comes from the spherical mass profile derived from Figure 13 of Emsellem et al. (2006) evaluated at $20''$ from the center. We classify the galaxy as "barred" following Erwin (2004). Kormendy & Ho (2013) call it a prototypical oval galaxy.

NGC 1194: The SDSS r-band bulge photometry is taken from the decomposition given in Greene et al. (2010). The M/L is derived following Appendix C to match the velocity dispersion within the effective aperture radius of $1.''38$, using the distance of Kormendy & Ho (2013).

NGC 1300: The bulge model is taken from Fisher & Drory (2008), who correctly discard the bar contribution. The huge difference between our R_e ($4''$) and the value quoted by Sani et al. (2011), $45.''98$, stems from the fact that they do not separately fit the strong bar of the galaxy and thus include it in the bulge component. The M/L is derived by converting the average of the two values in the F160W band given in Table 4 of Atkinson et al. (2005), using the color of Hyperleda. We adopt the distance of Kormendy & Ho (2013).

NGC 1399: The galaxy is a core elliptical (Rusli et al. 2013a); we use their profile and subtract the outer exponential component before deprojecting the galaxy, getting $R_e = 103.''7$. The "classical" best fit of Läsker et al. (2014) gives $R_e = 49.''3$, the "best" one $R_e = 147''$. The M/L is scaled to the distance of Kormendy & Ho (2013). Errors are taken from Kronawitter et al. (2000).

NGC 2273: We performed a bulge plus disk decomposition on an R-band image from Erwin & Sparke (2003) using the Imfit software of Erwin (2015). A Sérsic bulge (function *Sérsic* of *imfit*), a bar (function *Sérsic_GenEllipse* of Imfit), an exponential disk (function *Exponential* of Imfit), and an outer ring (function *GaussianRing2Side* of Imfit) were fit to the image; see Erwin (2015) for a definition of the function parameters. We set $\mu_e = -2.5 \log I_e$ and $\mu_0 = -2.5 \log I_0$. The parameter values of the fit are given in Table 21. Model images of the bar, disk, and inner ring components (see Figures 22 and 35) were subtracted from the original image, and the bulge photometry was derived on the residual image. The M/L is computed as in Appendix C to match the velocity dispersion of Greene et al. (2010) within the effective aperture radius of $1.''38$, using the distance of Kormendy & Ho (2013).

NGC 2549: The M/L (already corrected for GE) is scaled to the distance of Kormendy & Ho (2013). The SDSS r-band image is calibrated to the R band using the aperture photometry in the R_{SV} and V_{SV} bands of Sandage & Visvanathan (1978), using the color transformations of Prugniel et al. (1993) and Jordi et al. (2006). We performed an Imfit bulge (function *Sérsic*) plus disk (function *Edge-OnDisk*) decomposition (see Figures 23 and 35). The parameters of this fit are given in Table 22.

NGC 2748: We performed an Imfit bulge (function *Sérsic*) plus disk (function *Exponential*) plus double ring (functions *GaussianRing*) decomposition of the 3.6*mu* band *Spitzer* image (see Figures 24 and 35). The resulting values of the parameters of the fit are listed in Table 23. The residual image shows that the galaxy has a low-surface-brightness polar ring, which we masked while fitting the main galaxy. The position angle of the bulge component (which contributes 15% of the total light) is different from the rest of the galaxy; this probably stems from the modeling of the combination of a small bar (in which case the two rings make sense as an inner ring and an outer ring) and whatever small pseudobulge the galaxy may have. The *Spitzer* image does not really have the resolution to be sure about that. The "bulge" model of Sani et al. (2011) is 0.8 mag brighter and 3.5 times larger in size than our solution. The $M/L = 0.5 \pm 0.02\, M_\odot/L_\odot$ in the 3.6*mu* band is derived as in Appendix C and Figure 37 using the (circularized) surface brightness of the entire galaxy (i.e., with the polar ring component) to match the kinematic profile of Batcheldor et al. (2005). The distance comes from Kormendy & Ho (2013). If we convert the best-fit value in the F160W band

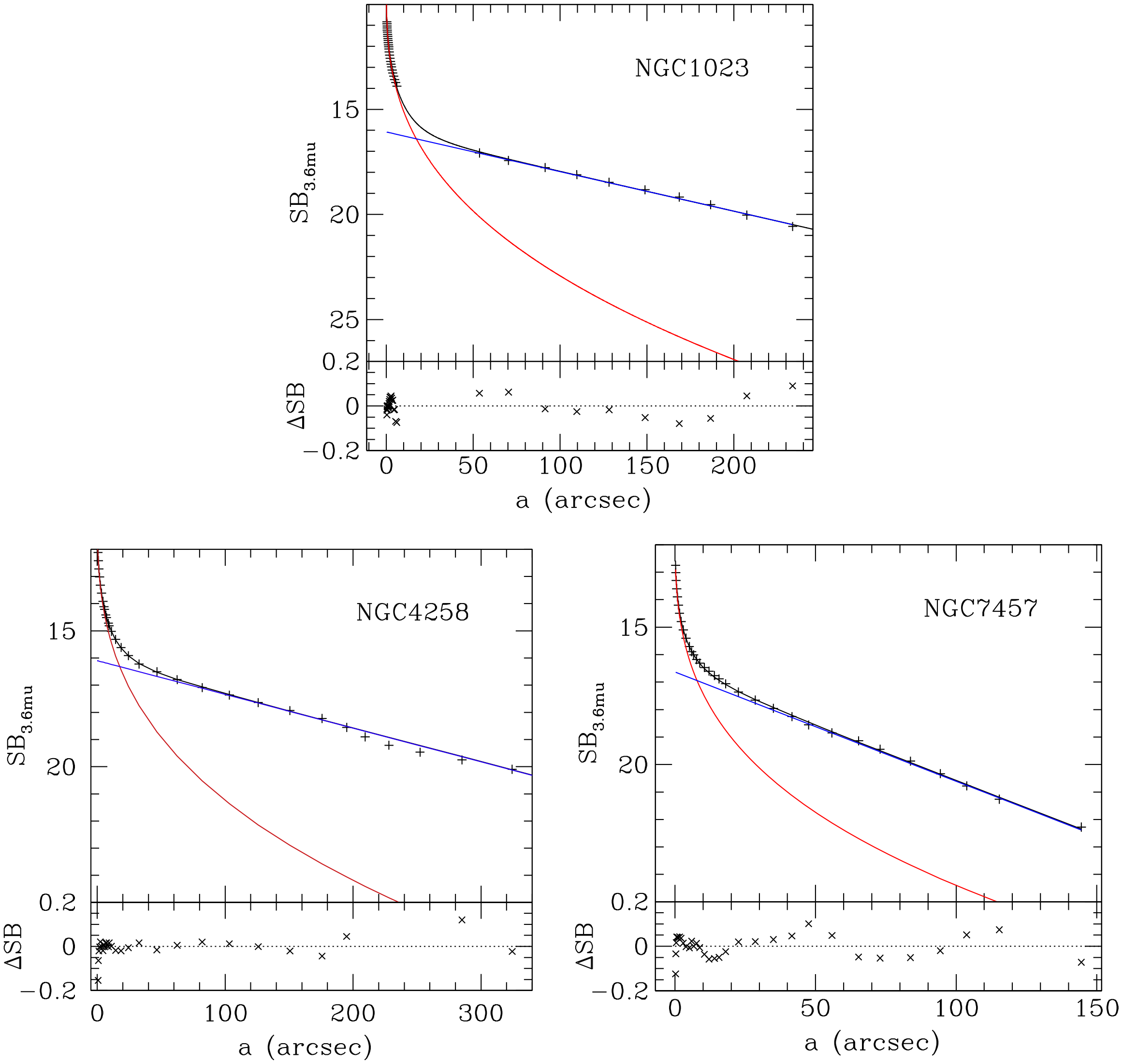

Figure 21. Major-axis bulge plus disk fits to the *Spitzer* 3.6*mu* profiles of NGC 1023, NGC 4258, and NGC 7457 (see the text and Table 20).

given in Table 4 of Atkinson et al. (2005) to the 3.6*mu* band using 2MASS *J*, *H*, and *K* aperture magnitudes and the conversion equation given in Stephens et al. (2000), we get $M/L_{3.6mu} = 0.4 \pm 0.05\, M_\odot/L_\odot$. Since the galaxy is too dusty and edge-on to be sure about the presence or absence of a bar, we set $b = 0.5$ in Table 1.

NGC 2787: Erwin et al. (2003) presented evidence for a composite bulge in this galaxy. Although their "inner disk" may perhaps be better understood as the projected box/peanut structure of the bar (rather than a "disky pseudo-bulge"), we use the parameters of their decomposition (their Table 5) giving $R_e = 3\farcs5$, but shift the resulting total surface brightness to the 3.6*mu* band to match the total profile derived from *Spitzer* images (coming from Program 30318, PI Giovanni Fazio, Observer ID 2; Figure 21). Sani et al. (2011) derive $R_e = 12\farcs3$, not distinguishing between the classical and the pseudo components of the bulge. The M/L is computed by fitting the kinematics of Bertola et al. (1995) (see Appendix C and Figure 37), using the sum of the bulge and disk profiles derived above. The distance comes from Kormendy & Ho (2013).

NGC 2960: We use the bulge plus disk decomposition of Greene et al. (2010) in the *r* band, ignoring the E2 morphology of Kormendy & Ho (2013), but accepting the merger appearance of the galaxy. The M/L is computed as in Appendix C to match the velocity dispersion of Greene et al. (2010) within an effective aperture radius of $1\farcs6$, using the distance of Kormendy & Ho (2013).

NGC 2974: The M/L is scaled to the distance of Sani et al. (2011) and from the *I* to 3.6*mu*-band using the ($I - 3.6mu$) color from Hyperleda. The *Spitzer* images come from Program 30318, PI Giovanni Fazio, Observer ID 2. The BH mass comes from the uncertain determination of Cappellari et al. (2008). We exclude this galaxy from the fits reported in Tables 36 and 37.

NGC 3031: The SDSS *i*-band decomposed bulge profile comes from Beifiori et al. (2012), which gives $R_e = 41\farcs4$. Sani et al. (2011) quote $R_e = 100\farcs2$, probably overestimating the size of the bulge by including the bar of the galaxy as part of the bulge in the fit. Fisher & Drory (2010) are in better agreement with our adopted solution. The M/L is determined using the distance of Kormendy & Ho (2013) and by fitting the kinematics of Fabricius et al. (2012) (see

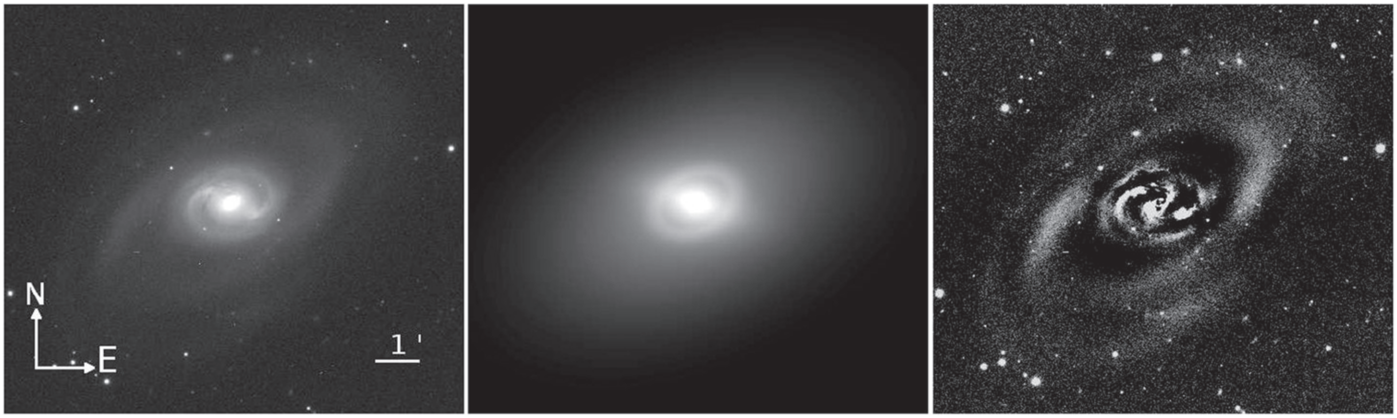

Figure 22. Imfit model for NGC 2273: the galaxy *R*-band image (left), the model (middle), and the residuals (right); see also Figure 35.

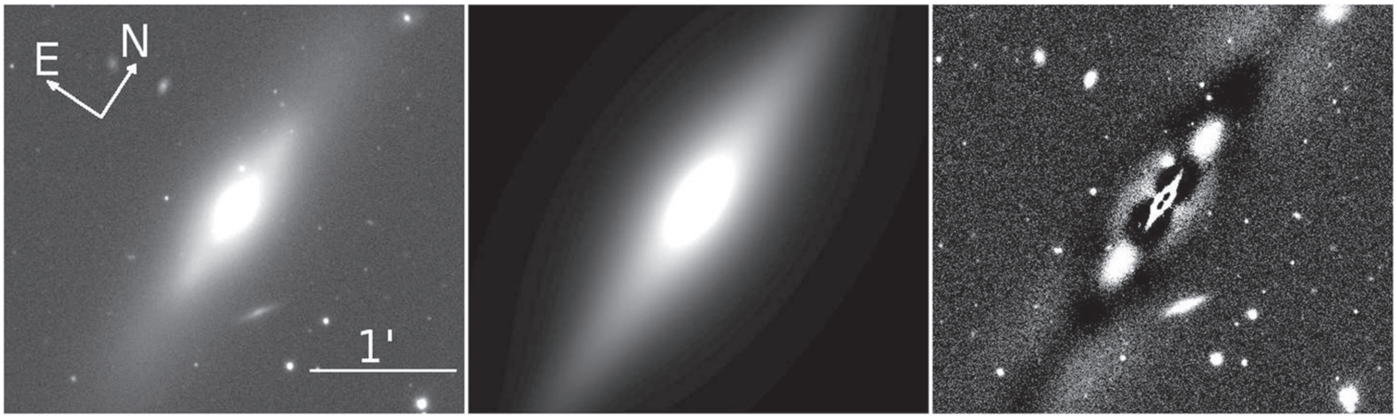

Figure 23. Imfit model for NGC 2549: the galaxy *r*-band image (left), the model (middle), and the residuals (right); see also Figure 35.

Figure 24. Imfit model for NGC 2748: the galaxy 3.6*mu*-band image (left), the model (middle), and the residuals (right); see also Figure 35.

Appendix C and Figure 37), summing the disk and the bulge profiles. We classify the galaxy as barred following Gutiérrez et al. (2011) and Erwin & Debattista (2013). Following Fabricius et al. (2012), we classify the galaxy bulge as classical, even if it is most likely a composite (pseudo plus classical) system.

NGC 3079: We model the *Spitzer*3.6*mu*-band image of this pseudobulge galaxy with four components using Imfit: a pseudobulge (function *Sérsic*), a disk (function *Exponential*), a bar (a second *Sérsic* function), and a ring (function *GaussianRing*). The results are shown in Figures 25 and 35. The parameters of the fit are listed in Table 24. All four components are very flattened and have almost the same position angle. The small ($a_e = 4\farcs5$) pseudobulge component contributes 26% of the total light of the galaxy. This is in contrast to the fit of Sani et al. (2011), who claim the existence of an unrealistically large ($R_e = 74''$) bulge with $B/T = 0.87$. The M/L is computed as in Appendix C to match the stellar kinematic profile of Shaw et al. (1993) (see Figure 37) using the distance of Sani et al. (2011). Kormendy

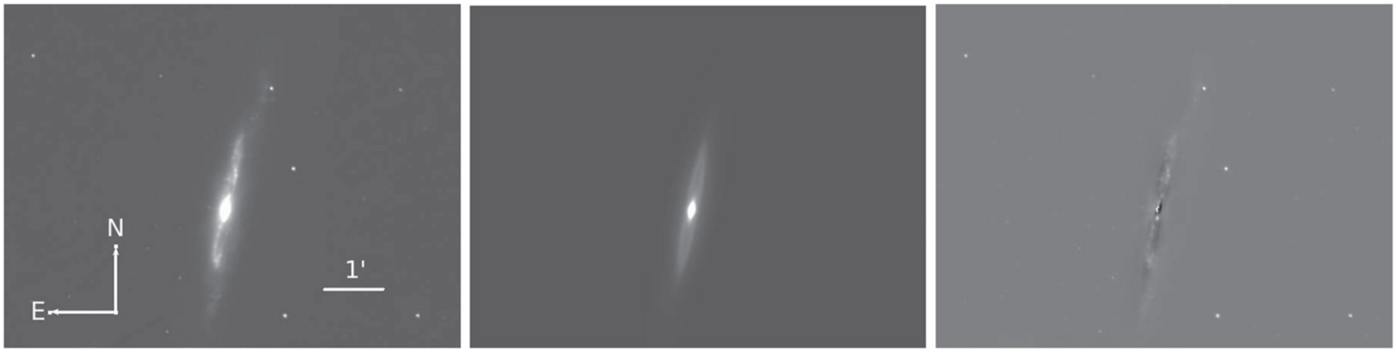

Figure 25. Imfit model for NGC 3079: the galaxy 3.6*mu*-band image (left), the model (middle), and the residuals (right); see also Figure 35.

& Ho (2013) judge the BH mass determination of Kondratko et al. (2005) unreliable, which however agrees with Yamauchi et al. (2004) and matches the value quoted by Sani et al. (2011) we used here. We exclude this galaxy from the fits reported in Tables 36 and 37.

NGC 3115: For this edge-on S0 we prefer the decomposition of Seifert & Scorza (1996) and Scorza et al. (1998), which gives $R_e = 42''$, to the one of Sani et al. (2011, $R_e = 15\farcs7$) that shows systematic residuals. The M/L is scaled to the distance of Kormendy & Ho (2013) and corrected for GE.

NGC 3227: The bulge component is determined in Davies et al. (2006) from a high-resolution SINFONI image, giving $R_e = 3\farcs1$. The "classical fit" of Läsker et al. (2014) delivers $R_e = 1\farcs4$, the "best fit" $R_e = 0\farcs5$; both results are probably affected by insufficient resolution (FWHM $= 0\farcs9$). Sani et al. (2011) quote $R_e = 58''$, which is definitely too large. The K-band M/L (scaled to the distance of Kormendy & Ho 2013) is given in the unusual units quoted by Davies et al. (2006). We mark the "peculiarity" of this definition by referring to the band as "Kp" in Table 34 and by not plotting the galaxy in Figure 20. Kormendy & Ho (2013) exclude the galaxy from their fits, arguing that the active nucleus makes the dynamical modeling challenging.

NGC 3245: We use the decomposition of Beifiori et al. (2012) in the i band, which gives $R_e = 3\farcs5$ (with $B/T = 0.27$) and agrees with the "classical fit" of Läsker et al. (2014). The "best fit" of Läsker et al. (2014), which includes a bar, gives $R_e = 1\farcs5$. Since what Läsker et al. (2014) call a "bar" could also be an "oval" component, we stick to the decomposition of Beifiori et al. (2012). We calibrate the fit to the R band from the original SDSS i band using the $(R-I)$ color estimated as follows and the $(i-R)$ conversion equation in Jordi et al. (2006). Since only the $(B-V)$ color was available in Hyperleda, we derived $(R-I)$ by linearly fitting the $(V-I)$ versus $(B-V)$ correlation of the SSP models of Maraston (2005). The M/L is corrected for GE and scaled to the distance of Kormendy & Ho (2013).

NGC 3377: For this E6 galaxy we use a single profile, which gives $R_e = 39\farcs1$, roughly consistent with Arnold et al. (2014). The multicomponent fit of Läsker et al. (2014) delivers $R_e = 7''$, but their disk component is faint, and the envelope could well be part of the bulge. The M/L is scaled to the distance of Kormendy & Ho (2013) and from the I to R band using the $(R-I)$ color from Hyperleda.

NGC 3379: The galaxy is a core elliptical (Rusli et al. 2013a). We use their profile and M/L, which is scaled to the distance of Kormendy & Ho (2013).

NGC 3384: The decomposed SDSS i-band bulge profile comes from Beifiori et al. (2012). We calibrated it to the I band using the equation of Jordi et al. (2006) and the $(R-I)$ color from Hyperleda. We get $R_e = 7\farcs6$, while Laurikainen et al. (2010) quote $R_e = 3\farcs6$ from a complex fit involving two bars. But Erwin (2004) classified the object as a barred galaxy with an inner disk, rather than double-barred. Moreover, the residuals of the fit of Laurikainen et al. (2010) are not shown, so we keep our reasonable solution. We correct the M/L of the model with dark matter of Schulze & Gebhardt (2011) for GE, and scale it from the V to I band using the $(V-I)$ color of Hyperleda, using the distance of Kormendy & Ho (2013).

NGC 3393: We perfomed an Imfit bulge (function *Sérsic*) plus bar (function *Sérsic_GenEllipse*) plus disk (function *Exponential*) decomposition (see Figures 26 and 35) on an I-band image observed with the 0.9 m CTIO telescope by Schmitt & Kinney (2000). The parameters of the decomposition are given in Table 25. The M/L is computed as in Appendix C to match the velocity dispersion of Greene et al. (2010) within an effective aperture of radius of $1\farcs6$, using the distance of Kormendy & Ho (2013).

NGC 3414: We performed an Imfit bulge (function *Sérsic*) plus bar (function *Sérsic_GenEllipse*) plus disk (function *Exponential*) decomposition on the SDSS i-band image of the galaxy (see Figures 27 and 35). The parameters are listed in Table 26. We converted the i-band zero point into a Cousins I band using two equations in Jordi et al. (2006) and the $(r-i)$ SDSS color. The M/L of Cappellari et al. (2006) is scaled to the distance of Sani et al. (2011). Our decomposition gives $R_e = 23''$ and agrees with Sani et al. (2011). Laurikainen et al. (2010) obtain $R_e = 3\farcs2$ and classify the galaxy as a "spindle." Given the impossibility of verifying the quality of the fit of Laurikainen et al. (2010), we stick to our solution but acknowledge that the galaxy is complex. For consistency with our fit that contains a bar we set $b = 1$ in Table 1. The BH mass comes from the uncertain determination of Cappellari et al. (2008). We exclude this galaxy from the fits reported in Tables 36 and 37.

NGC 3585: For this edge-on S0, we prefer the decomposition of Scorza et al. (1998), giving $R_e = 27\farcs4$, to the one of (Sani et al. 2011, $R_e = 11\farcs5$), which shows systematic residuals. The M/L is corrected for GE and scaled to the distance of Kormendy & Ho (2013).

Table 34
Dynamical M/L Ratios of the Literature and SINFONI Samples

Galaxy	M/L	Band of M/L	$(d\log M/L)^2$	Band of Image	Reference
MW	1.00	…	0.001886	…	…
Circinus	0.14	3.6*mu*	0.002651	3.6*mu*	Sani et al. (2011)
A 1836	4.86	*I*	0.01443	*I*	SDSS
IC 1459	4.91	*V*	0.001961	*V*	Rusli et al. (2013a)
IC 4296	8.54	*B*	0.001961	*I*	P. Erwin et al. (2016, in preparation)
NGC221	1.50	*R*	0.0001532	*R*	Peletier (1993)
NGC224	4.13	*V*	0.0001061	*V*	Kormendy & Bender (1999)
NGC524	4.80	*I*	0.0006592	*I*	Cappellari et al. (2006)
NGC821	3.95	*R*	0.0006942	*R*	Graham et al. (2001)
NGC 1023	0.90	3.6*mu*	2.615e-06	3.6*mu*	*Spitzer*
NGC 1068	0.37	*K*	0.02909	*K*	P. Erwin et al. (2016, in preparation)
NGC 1194	6.10	*r*	0.01975	*r*	SDSS
NGC 1300	2.13	*V*	1.451e-05	*V*	Fisher & Drory (2008)
NGC 1399	10.32	*B*	0.0001133	*B*	Saglia et al. (2000)
NGC 2273	4.50	*R*	0.01044	*R*	Erwin & Sparke (2003)
NGC 2549	4.55	*R*	0.0003426	*r*	SDSS
NGC 2748	0.53	3.6*mu*	0.0003018	3.6*mu*	*Spitzer*
NGC 2787	2.50	3.6*mu*	0.0002153	3.6*mu*	*Spitzer*
NGC 2960	3.81	*r*	0.007132	*r*	SDSS
NGC 2974	1.17	3.6*mu*	0.0005821	3.6*mu*	*Spitzer*
NGC 3031	2.48	*i*	9.922e-07	*i*	Beifiori et al. (2012)
NGC 3079	0.37	3.6*mu*	0.0003067	3.6*mu*	*Spitzer*
NGC 3115	6.13	*V*	3.643e-05	*V*	Scorza et al. (1998)
NGC 3227	19.68	*K*	0.001961	*K*	Davies et al. (2006)
NGC 3245	3.40	*R*	0.001961	*i*	Beifiori et al. (2012)
NGC 3377	2.81	*R*	0.0003275	*R*	Graham et al. (2001)
NGC 3379	2.77	*I*	0.0009665	*I*	Rusli et al. (2013a)
NGC 3384	1.44	*I*	0.0004682	*i*	SDSS
NGC 3393	2.72	*I*	0.003697	*I*	Schmitt & Kinney (2000)
NGC 3414	4.15	*I*	0.0005544	*i*	SDSS
NGC 3585	2.89	*V*	0.000959	*V*	Scorza et al. (1998)
NGC 3607	6.15	*V*	0.000346	*g*	SDSS
NGC 3608	2.04	*I*	0.001753	*i*	SDSS
NGC 3842	7.15	*V*	0.004632	*V*	Rusli et al. (2013a)
NGC 3998	5.21	*I*	0.07487	*i*	SDSS
NGC 4026	4.91	*V*	0.0009635	*g*	SDSS
NGC 4151	1.49	*R*	0.001961	*R*	Gadotti (2008)
NGC 4258	0.55	3.6*mu*	0.0002412	3.6*mu*	*Spitzer*
NGC 4261	8.89	*V*	0.003279	*V*	Rusli et al. (2013a)
NGC 4291	5.08	*V*	0.003171	*V*	Rusli et al. (2013a)
NGC 4342	4.01	*I*	0.00116	*i*	SDSS
NGC 4374	6.39	*V*	0.000687	*V*	Kormendy et al. (2009)
NGC 4388	1.30	3.6*mu*	0.003625	3.6*mu*	*Spitzer*
NGC 4459	3.88	*V*	0.0006867	*V*	Kormendy et al. (2009)
NGC 4473	6.91	*V*	0.0004416	*V*	Kormendy et al. (2009)
NGC 4486	6.32	*V*	0.003142	*V*	Kormendy et al. (2009)
NGC 4526	2.64	*I*	0.001193	3.6*mu*	*Spitzer*
NGC 4552	7.36	*V*	0.0007571	*V*	Kormendy et al. (2009)
NGC 4564	5.78	*V*	0.0004514	*V*	Kormendy et al. (2009)
NGC 4594	3.08	*I*	3.265e-05	*I*	Jardel et al. (2011)
NGC 4596	0.99	*K*	9.111e-05	*K*	Vika et al. (2012)
NGC 4621	0.66	3.6*mu*	0.0006928	3.6*mu*	*Spitzer*
NGC 4649	7.67	*V*	0.002266	*V*	Rusli et al. (2013a)
NGC 4697	3.36	*R*	0.001467	*R*	Erwin et al. (2008)
NGC 4736	0.61	*z*	0.001961	*z*	SDSS
NGC 4826	1.33	*i*	0.0005272	*i*	SDSS
NGC 4889	5.97	*R*	0.003468	*r*	Jorgensen & Franx (1994)
NGC 5077	3.48	*V*	0.001961	*V*	KeyProg
NGC 5128	0.63	*K*	0.01004	*K*	Cappellari et al. (2009)
NGC 5576	3.17	*R*	0.001889	*r*	SDSS
NGC 5813	4.70	*V*	0.0007684	*V*	Rusli et al. (2013a)
NGC 5845	4.77	*V*	0.0004076	*V*	KeyProg
NGC 5846	5.20	*I*	0.0006278	*i*	Rusli et al. (2013a)
NGC 6086	4.05	*R*	0.002363	*R*	Rusli et al. (2013a)

Table 34
(Continued)

Galaxy	M/L	Band of M/L	$(d\log M/L)^2$	Band of Image	Reference
NGC 6251	3.62	*I*	0.001961	*I*	Graham et al. (2001)
NGC 6264	5.27	*r*	0.007546	*r*	Greene et al. (2010)
NGC 6323	8.15	*r*	0.01908	*r*	Greene et al. (2010)
NGC 7052	2.17	*R*	0.001961	*R*	Graham et al. (2001)
NGC 7457	0.65	3.6*mu*	0.0005046	3.6*mu*	*Spitzer*
NGC 7582	0.07	3.6*mu*	0.01245	3.6*mu*	*Spitzer*
NGC 7768	7.58	*V*	0.006975	*V*	Rusli et al. (2013a)
U3789	0.50	*H*	0.008882	*H*	Peletier et al. (1999)
NGC307	1.03	*K*	6.695e-05	*K*	P. Erwin et al. (2016, in preparation)
NGC 1316	0.65	*K*	0.001886	*K*	Nowak et al. (2008)
NGC 1332	7.10	*R*	0.0005986	*R*	Rusli et al. (2011)
NGC 1374	5.30	*B*	0.002417	*B*	Rusli et al. (2013b)
NGC 1398	3.00	*R*	0.0003303	*R*	P. Erwin et al. (2016, in preparation)
NGC 1407	6.60	*B*	0.003128	*B*	Rusli et al. (2013b)
NGC 1550	4.00	*R*	0.003566	*R*	Rusli et al. (2013b)
NGC 3091	3.80	*I*	0.0008164	*I*	Rusli et al. (2013b)
NGC 3368	0.40	*K*	0.002947	*K*	Nowak et al. (2010)
NGC 3489	0.44	*H*	0.0003723	*H*	Nowak et al. (2010)
NGC 3627	0.40	*K*	0.0001181	*K*	P. Erwin et al. (2016, in preparation)
NGC 3923	4.22	*z*	0.003155	*z*	R. Bender et al. (2016, in preparation)
NGC 4371	1.71	*z*	5.221e-05	*z*	P. Erwin et al. (2016, in preparation)
NGC 4472	4.90	*V*	0.001257	*V*	Rusli et al. (2013b)
NGC 4486a	4.00	*zACS*	0.0007368	*zACS*	Nowak et al. (2007)
NGC 4486b	6.56	*V*	0.0004456	*V*	R. Bender et al. (2016, in preparation)
NGC 4501	0.54	*K*	0.0002495	*K*	P. Erwin et al. (2016, in preparation)
NGC 4699	0.68	*z*	0.0005982	*z*	P. Erwin et al. (2016, in preparation)
NGC 4751	8.27	*R*	0.0005339	*R*	Rusli et al. (2013b)
NGC 5018	1.23	*I*	0.0001083	*I*	R. Bender et al. (2016, in preparation)
NGC 5328	4.90	*V*	0.002828	*V*	Rusli et al. (2013b)
NGC 5419	5.37	*R*	0.01759	*R*	Mazzalay et al. (2015)
NGC 5516	5.20	*R*	0.000279	*R*	Rusli et al. (2013b)
NGC 6861	6.10	*I*	0.000114	*I*	Rusli et al. (2013b)
NGC 7619	3.00	*I*	0.002567	*I*	Rusli et al. (2013b)

Note. Column 1, the object name (both literature and SINFONI samples); columns 2 to 4: the dynamical M/L, its band, and its logarithmic error squared; column 5: the band of the related image; column 6: the references of the profiles used. When no errors are available, we set the errors to the average value of all the available errors.

NGC 3607: We calibrate the g-band SDSS image to the V band using the $(B-V)$ color from Hyperleda and the $(g-V)$ transformation of Jordi et al. (2006). McConnell & Ma (2013) and Kormendy & Ho (2013) consider the galaxy a core elliptical; we accept their classification, although strong nuclear dust makes it difficult to determine its core properties (see discussion in Rusli et al. 2013a). From the profile we measure $R_e = 45.''0$, in fair agreement with Beifiori et al. (2012), who measure $R_e = 56.''34$ from a Sérsic fit to the SDSS i-band image. In contrast, Laurikainen et al. (2010) perform a bulge plus disk decomposition, deriving $R_e = 6.''1$ with $B/T = 0.32$. We do not think that this is a good description of the galaxy. The M/L is corrected for GE and scaled to the distance of Kormendy & Ho (2013).

NGC 3608: The galaxy is a core elliptical (Rusli et al. 2013a). We calibrate the i-band SDSS image to the I band using the $(R-I)$ color from Hyperleda and the tranformation of Jordi et al. (2006). This gives a more extended profile than the one derived by Rusli et al. (2013a), which comes from the g-band image. We transform the M/L_V of Rusli et al. (2013a) to the I band using the $(V-I)$ color of Hyperleda and scaling it to the distance of Kormendy & Ho (2013). We measure $R_e = 43''$, while Beifiori et al. (2012) obtain $R_e = 161.''9$. This stems from the systematic overestimation (by 0.4 mag) of the light of the galaxy at radii larger than $60''$ in the fit from Beifiori et al. (2012).

NGC 3842: The galaxy is a core elliptical (Rusli et al. 2013a). We use their profile and M/L, scaled to the distance of Kormendy & Ho (2013).

NGC 3998: The SDSS i-band decomposed bulge profile comes from Beifiori et al. (2012), is calibrated to the I band using the equation of Jordi et al. (2006), and gives $R_e = 5.''2$. This roughly agrees with the $R_e = 3.''4$ of Laurikainen et al. (2010). We prefer this solution to the multicomponent "best fit" of Läsker et al. (2014), which delivers $R_e = 1.''8$, since the size of the fitted bar seems implausible. Since only the $(B-V)$ color was available in Hyperleda, we derived the $(V-I)$ and $(R-I)$ colors by linearly fitting the $(V-I)$ versus $(B-V)$ and $(R-I)$ versus $(B-V)$ correlations of the SSP models of Maraston (2005). We correct the M/L for GE and scaled it to the distance of Kormendy & Ho (2013); moreover, we adapt it to the I band using the above colors. Errors on M/L are one-half of the 2σ values. We classify the galaxy as "barred" following Gutiérrez et al. (2011).

NGC 4026: We correct the M/L for GE and scale it to the distance of Kormendy & Ho (2013). The SDSS g-band image was calibrated to the V band using the transformation

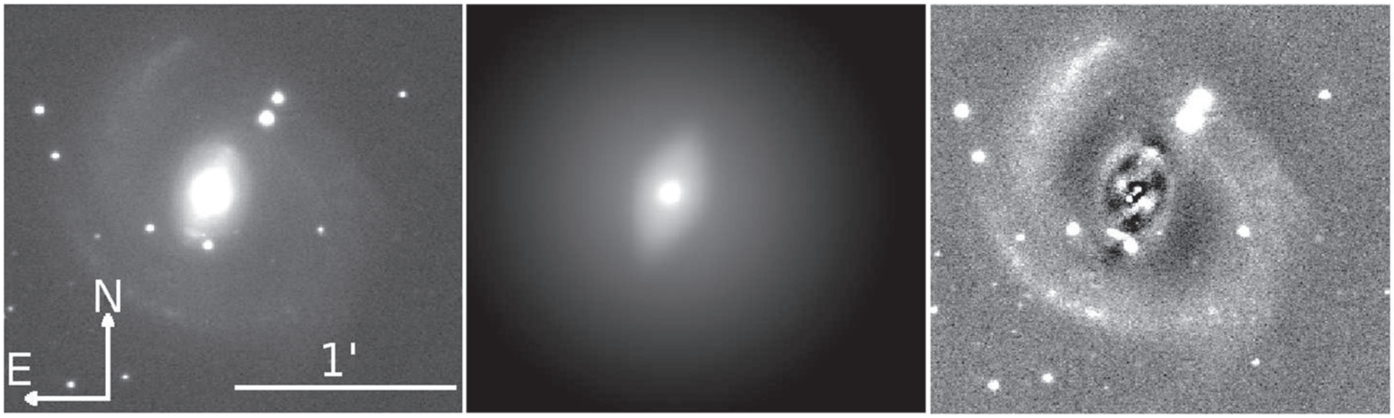

Figure 26. Imfit model for NGC 3393: the galaxy I-band image (left), the model (middle), and the residuals (right); see also Figure 35.

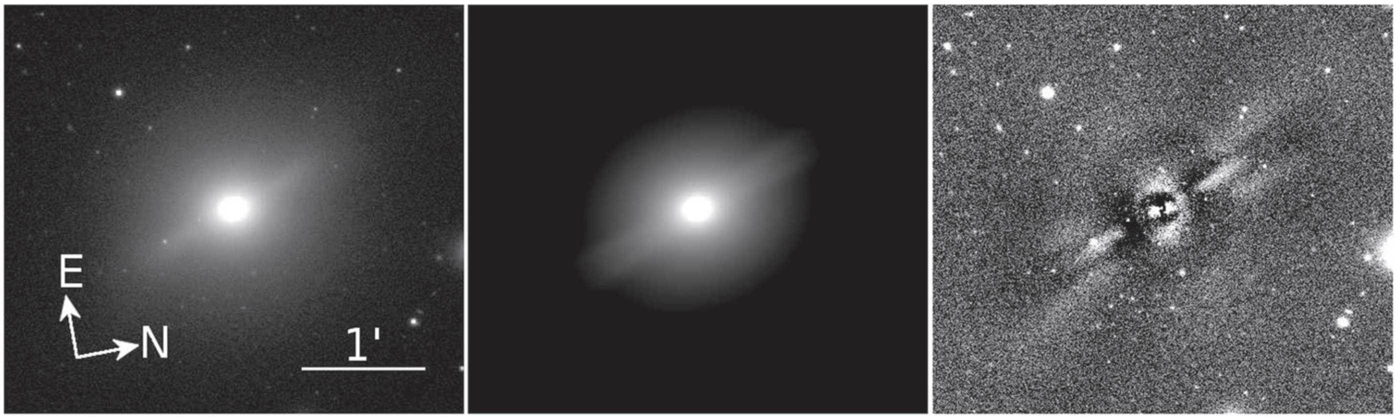

Figure 27. Imfit model for NGC 3414: the galaxy I-band image (left), the model (middle), and the residuals (right); see also Figure 35.

of Jordi et al. (2006) and the mean $(B - V)$ colors from Hyperleda. We performed an Imfit bulge (function *Sérsic*) plus disk (function *EdgeOnDisk*) decomposition (see Figures 28 and 35). The best-fit parameters are given in Table 27. We set $b = 0.5$ in Table 1 since the galaxy is too edge-on to be certain about the presence or the absence of a bar.

NGC 4151: We take the R-band bulge plus bar plus disk decomposition of Gadotti (2008) and set $b = 1$ in Table 1 (Erwin 2005). Sani et al. (2011) ignore the bar of the galaxy in their fit. We use the R-band M/L value (and BH mass) of Onken et al. (2007), which we correct for GE. We follow Ho & Kim (2014) and classify its bulge as classical, but Kormendy (2013) disagrees. Kormendy & Ho (2013) exclude the galaxy from their fits, arguing that the active nucleus makes the dynamical modeling challenging. We exclude this galaxy from the fits reported in Tables 36 and 37.

NGC 4258: The *Spitzer*3.6*mu* images come from Program 20801, PI Seppo Laine, Observer ID 14916. The Sérsic bulge plus exponential disk decomposition is performed using the technique of Fisher & Drory (2008), fitting the major axis profile. The result is shown in Figure 21 and listed in Table 20. This gives $R_e = 13\overset{\prime\prime}{.}3$. The fit of Sani et al. (2011) has $R_e = 75\overset{\prime\prime}{.}8$ with strong residuals; Läsker et al. (2014) quote $R_e = 118\overset{\prime\prime}{.}9$ for the "classical" decomposition with strong residuals and $R_e = 4\overset{\prime\prime}{.}1$ for the six-component fit; we prefer our simpler approach. The M/L is scaled to the distance of Kormendy & Ho (2013) and from the V to 3.6*mu* band using the $(V - 3.6mu)$ color using the V-band photometry of Hyperleda.

NGC 4261: The galaxy is a core elliptical (Rusli et al. 2013a). We use their profile and derive $R_e = 54\overset{\prime\prime}{.}2$, in fair agreement with Beifiori et al. (2012), who measure $R_e = 45\overset{\prime\prime}{.}82$ from a Sérsic fit to the i-band SDSS image. In contrast, Sani et al. (2011) get $R_e = 20''$ from an improbable bulge plus disk decomposition, given the galaxy type, and Vika et al. (2012) derive $R_e = 21\overset{\prime\prime}{.}6$ from a fit with low $n_{\text{Sérsic}}$. The M/L is scaled to the distance of Kormendy & Ho (2013).

NGC 4291: The galaxy is a core elliptical (Rusli et al. 2013a). We use their profile and M/L scaled to the distance of Kormendy & Ho (2013).

NGC 4342: We performed an Imfit bulge (function *Sérsic*) plus disk (function *Exponential*) decomposition on an SDSS i-band image (see Figures 29 and 35), converting the zero point to the Cousins I band using the SDSS $(r - i)$ color and two equations from Jordi et al. (2006). The parameters of the decomposition are given in Table 28. Our fit gives $R_e = 4\overset{\prime\prime}{.}9$, while Vika et al. (2012) quote $R_e = 0\overset{\prime\prime}{.}6$ and Läsker et al. (2014) derive $R_e = 1\overset{\prime\prime}{.}1$ for the classical fit and $R_e = 0\overset{\prime\prime}{.}7$ for the "best" fit. All fits have systematic residuals, but given that the resolution of the images considered by Vika et al. (2012) (FWHM $= 0\overset{\prime\prime}{.}5$ or 1.1 pixels) and Läsker et al. (2014) (FWHM $= 0\overset{\prime\prime}{.}6$) is too near their quoted R_e'', we prefer our solution. The M/L is corrected for GE and scaled to the distance of Kormendy & Ho (2013).

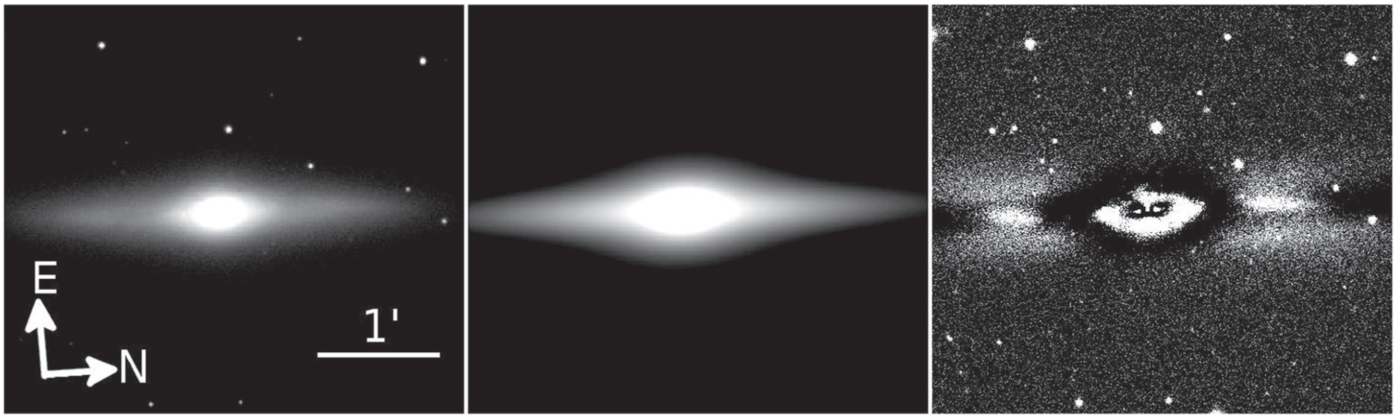

Figure 28. Imfit model for NGC 4026: the galaxy V-band image (left), the model (middle), and the residuals (right); see also Figure 35.

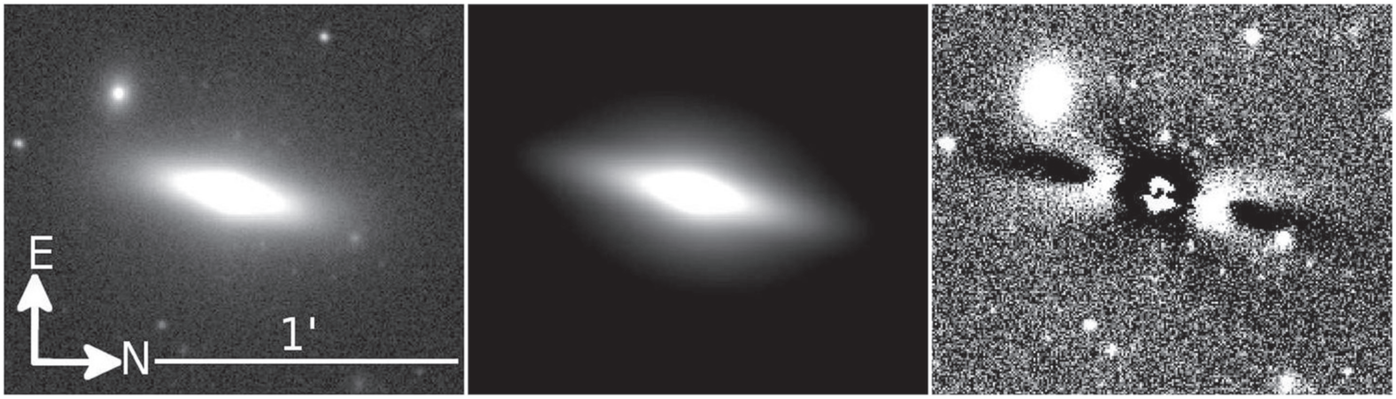

Figure 29. Imfit model for NGC 4342: the galaxy I-band image (left), the model (middle), and the residuals (right); see also Figure 35.

NGC 4374: The galaxy is a giant core elliptical (Rusli et al. 2013a). We measure $R_e = 84\farcs0$, while Vika et al. (2012) derive implausibly small bulge radii from one-component ($R_e = 26\farcs8$) or bulge plus disk ($R_e = 7\farcs2$) fits. The M/L is scaled to the distance of Kormendy & Ho (2013) and from the I to V band using the $(V - I)$ Hyperleda color.

NGC 4388: Our best Imfit decomposition of this pseudobulge galaxy is achieved by fitting a central point source (function *Gaussian*), a pseudobulge (function *Sérsic*), a disk (function *Exponential*), and a ring (function *GaussianRing2-Side*) (see Figures 30 and 35). The parameters of the fit are listed in Table 29. The pseudobulge component contributes 38% of the total light of the galaxy; Greene et al. (2010) give $B/T = 0.5$, while Kormendy & Ho (2013) quote $B/T = 0.096$, which explains most of the discrepancy observed in Figure 6. Despite the use of four components, there are still significant residuals, stemming from the strong nonaxisymmetric galaxy features. The M/L is computed as in Appendix C to match the velocity dispersion of Greene et al. (2010) within an effective aperture radius of $1\farcs6$, by considering the circularized surface brightness of the galaxy without the central point source and using the distance of Kormendy & Ho (2013). We classify the galaxy as barred following Kormendy & Ho (2013). In our decomposition the bar is described by the ring component.

NGC 4459: For this E2 galaxy we measure $R_e = 35\farcs2$ from the whole profile. Beifiori et al. (2012) quote $140\farcs5$, Sani et al. (2011) give $9\farcs4$, and Laurikainen et al. (2010) report $5\farcs2$. The large value of Beifiori et al. (2012) stems from a fit overestimating by 0.4 mag the light of the galaxy at radii larger than $100''$; the fit to a K-band image of the galaxy described by Beifiori (2010) agrees with our value. The discrepancy with the R_e of Sani et al. (2011) and Laurikainen et al. (2010) is driven by their (implausibly large) disk component, which we ignore following Kormendy & Ho (2013). The M/L is scaled to the distance of Kormendy & Ho (2013) and from the I to V band using $(V - I)$ from Hyperleda.

NGC 4473: Contrary to the classification of McConnell & Ma (2013), the galaxy is not a core elliptical (see discussion in Rusli et al. 2013a). We derive $R_e = 35\farcs7$ using a single profile extending to $261\farcs5$. Vika et al. (2012) quote $R_e = 16\farcs3$, fitting a single Sérsic profile to just the inner $70''$. Beifiori et al. (2012) fit two components, which we do not believe to be real, getting $R_e = 8''$. On the other hand, they derive $R_e = 34''$, in agreement with our value, from the isophotal profile (their Table 3). We correct the M/L for GE and scale it to the distance of Kormendy & Ho (2013).

NGC 4486: The galaxy is a giant core elliptical (Rusli et al. 2013a). We derive $R_e = 158\farcs4$, in disagreement with the "classical fit" of Läsker et al. (2014) giving $R_e = 59\farcs1$ and with the fit of Vika et al. (2012), who quote an even smaller $R_e = 34\farcs6$. The M/L is scaled to the distance of Kormendy & Ho (2013) and corrected for GE.

NGC 4526: We considered a *Spitzer*3.6*mu*-band image that we calibrated to the I band using the aperture photometry of Hyperleda. We performed an Imfit decomposition with five structures: a classical bulge (function *Sérsic*), an inner disk

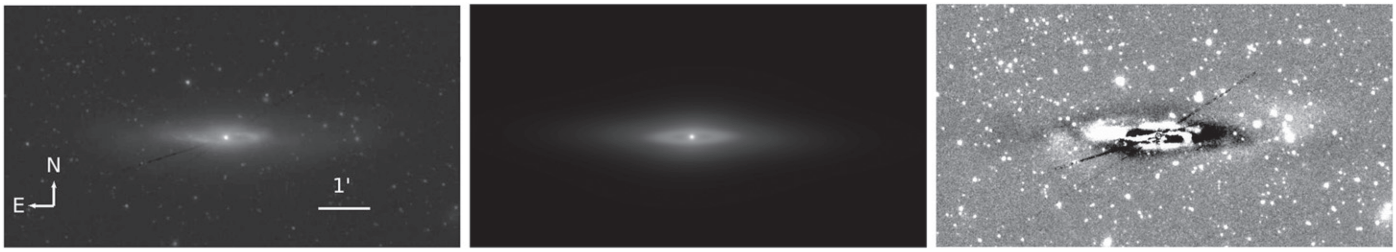

Figure 30. Imfit model for NGC 4388: the galaxy 3.6*mu*-band image (left), the model (middle), and the residuals (right); see also Figure 35.

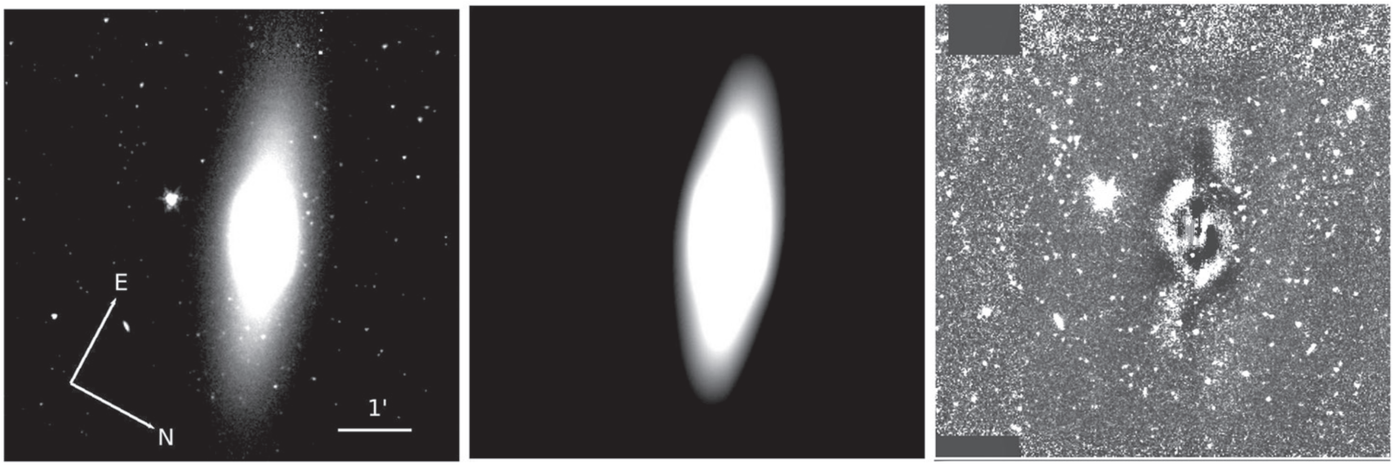

Figure 31. Imfit model for NGC 4526: the galaxy 3.6*mu*-band image (left), the model (middle), and the residuals (right); see also Figure 35.

(function *Exponential*), a bar (function *Sérsic_GenEllipse*), an outer (edge-on and diamond-shaped) disk (function *Exponential_GenEllipse*), and two off-center spurs (function *Sérsic*); see Figures 31 and 35. The parameters of the decomposition are given in Table 30. Our B/T (0.11) is much smaller than the value (0.65) quoted by Kormendy & Ho (2013). The M/L is scaled to the distance of Kormendy & Ho (2013).

NGC 4552: The galaxy is a core elliptical (Rusli et al. 2013a). We use their profile extending to $445\farcs8$ and their M/L scaled to the distance of Sani et al. (2011). We measure $R_e = 82\farcs6$. Sani et al. (2011) and Vika et al. (2012) derive shorter scale lengths ($R_e = 23\farcs3$ and $16\farcs5$ respectively) from a dubious bulge plus disk decomposition (Sani et al. 2011), given the galaxy type, or from a fit to a too-small ($\approx 100''$) image (Vika et al. 2012). The BH mass comes from the uncertain determination of Cappellari et al. (2008). We exclude this galaxy from the fits reported in Tables 36 and 37.

NGC 4564: We take the bulge profile as decomposed by Kormendy et al. (2009). This gives $R_e = 15\farcs32$. We prefer it to the result of Vika et al. (2012, $R_e = 2\farcs2$), who fit a bulge and a bar (without a disk) to an image of average ($1\farcs5$) seeing. The M/L is computed as in Appendix C to match the stellar kinematic profiles of Bender et al. (1994) (see Figure 37), using the distance of Kormendy & Ho (2013).

NGC 4594: We use the Sérsic bulge fit of Jardel et al. (2011) and correct their M/L for GE, scaling it to the distance of Kormendy & Ho (2013). Our $R_e = 133\farcs6$ is much larger than the unreliable value of Sani et al. (2011, $33\farcs7$). We set $b = 0.5$ in Table 1 since the galaxy is too edge-on to be sure about the presence or absence of a bar.

NGC 4596: We use the bulge plus disk plus bar decomposition of Vika et al. (2012), which gives $R_e = 11\farcs9$ with small residuals. We prefer this to Laurikainen et al. (2010), who quote $R_e = 3\farcs2$ but do not show the fit. The fit of Beifiori et al. (2012) gives $R_e = 44\farcs9$ without a bar component. The M/L is computed as in Appendix C to match the stellar kinematic profiles of Bettoni & Galletta (1997), summing the disk, bulge, and bar profiles (see Figure 37) and using the distance of Kormendy & Ho (2013).

NGC 4621: The M/L is scaled to the distance of Sani et al. (2011) and calibrated from the I band to 3.6*mu* using the I-band aperture photometry from Hyperleda. The *Spitzer* images come from Program 13649, PI Patrick Cote, Observer ID 522. The BH mass comes from the uncertain determination of Cappellari et al. (2008). We exclude this galaxy from the fits reported in Tables 36 and 37.

NGC 4649: The galaxy is a core elliptical (Rusli et al. 2013a). We use their profile and get $R_e = 99\farcs5$. Beifiori et al. (2012) quote $R_e = 13\farcs7$, from a fit with two components, which we do not believe are real, given the galaxy type. The same applies to the decompositions put forward by Sani et al. (2011), who quote $R_e = 42\farcs7$, Vika et al. (2012), who get $R_e = 41\farcs2$, or the "best fit" of Läsker et al. (2014), who derive $R_e = 46\farcs8$. The M/L of Rusli et al. (2013a) is scaled to the distance of Kormendy & Ho (2013).

NGC 4697: The profile is measured on R-band images taken during the observations described in Erwin et al. (2008). From this we derive $R_e = 65\farcs8$, in rough agreement with Sani et al. (2011, $R_e = 81''$), Beifiori et al. (2012, $R_e = 107''$), and the "classical" fit of Läsker et al. (2014, $R_e = 118''$). The "best fit" of Läsker et al. (2014) has a bulge with a short scale length ($R_e = 4\farcs8$) but adds an envelope

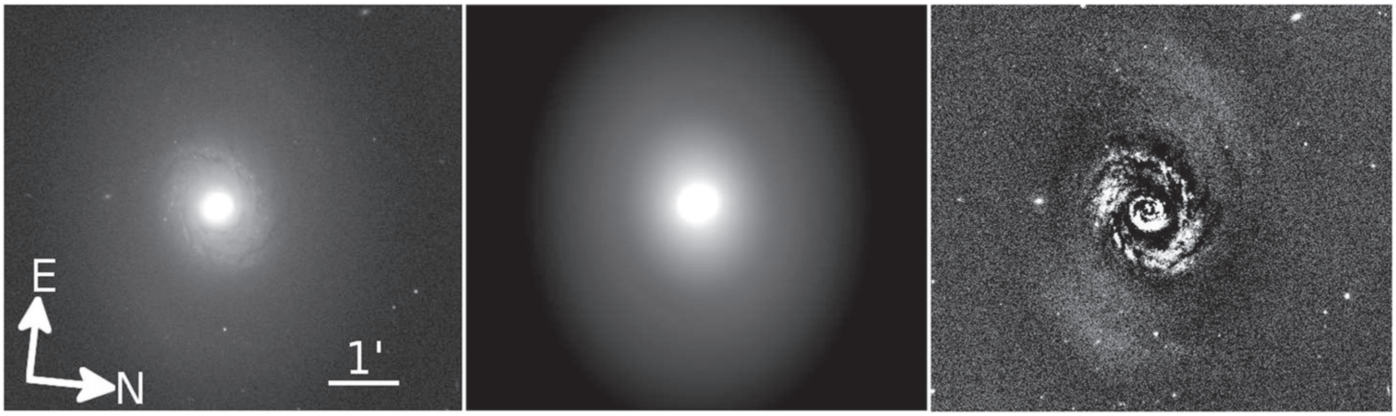

Figure 32. Imfit model for NGC 4736: the galaxy z-band image (left), the model (middle), and the residuals (right); see also Figure 35.

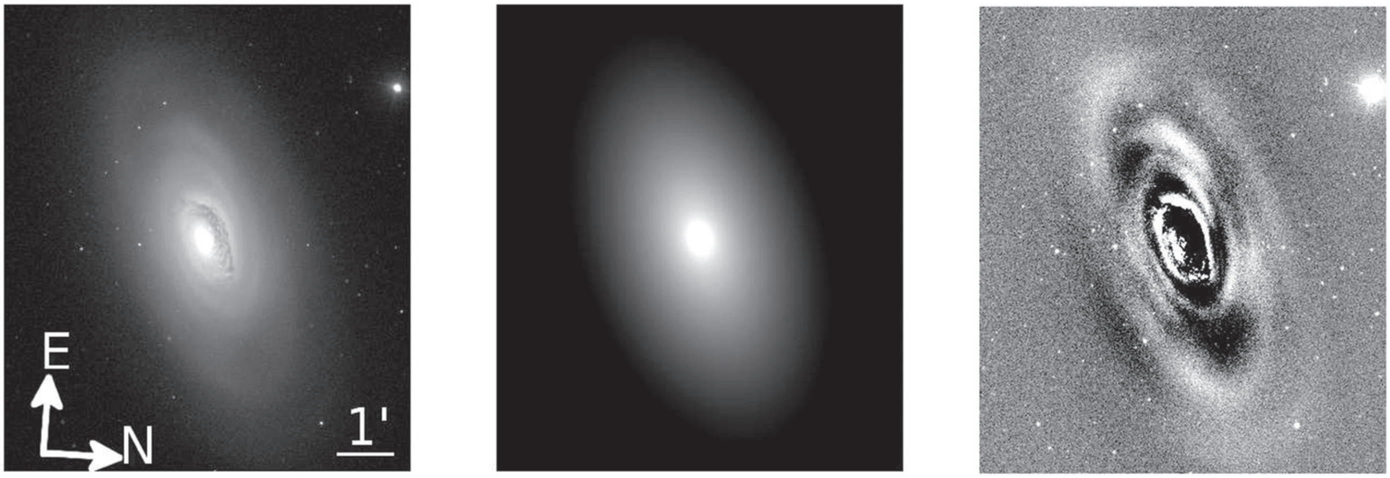

Figure 33. Imfit model for NGC 4826: the galaxy i-band image (left), the model (middle), and the residuals (right); see also Figure 35.

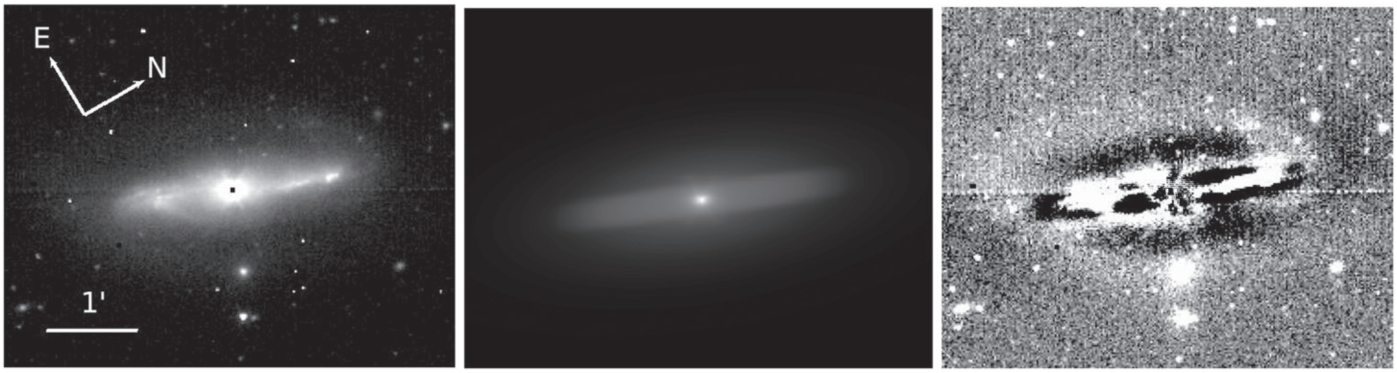

Figure 34. Imfit model for NGC 7582: the galaxy 3.6*mu*-band image (left), the model (middle), and the residuals (right); see also Figure 35.

component. The M/L is scaled to the distance of Kormendy & Ho (2013), calibrated to the R band using $(V - R) = 0.59$ from the aperture photometry in Hyperleda and corrected for GE.

NGC 4736: An Imfit bulge (function *Sérsic*) plus disk (function *Exponential*) plus outer ring (function *GaussianRing2Side*) decomposition was performed on a z-band image from SDSS (see Figures 32 and 35). The parameters of the fit are given in Table 31. A model image of the disk and the outer ring was created, which was then subtracted from the original image. On the residual image an ellipse fit was performed with `IRAF` to get the bulge profile. The M/L of the bulge calculated by Moellenhoff et al. (1995) was converted to the z band using the equations of Jordi et al. (2006) and the B, V, R, I aperture magnitudes provided by Hyperleda, and scaled to the distance of Kormendy & Ho (2013). We classify the galaxy as "barred" following Moellenhoff et al. (1995).

NGC 4826: We performed an Imfit bulge (function *Sérsic*) plus disk (function *Exponential*) decomposition on an SDSS i-band image (see Figure 33) after masking the very strong dust lane. The parameters for the fit are given in Table 32.

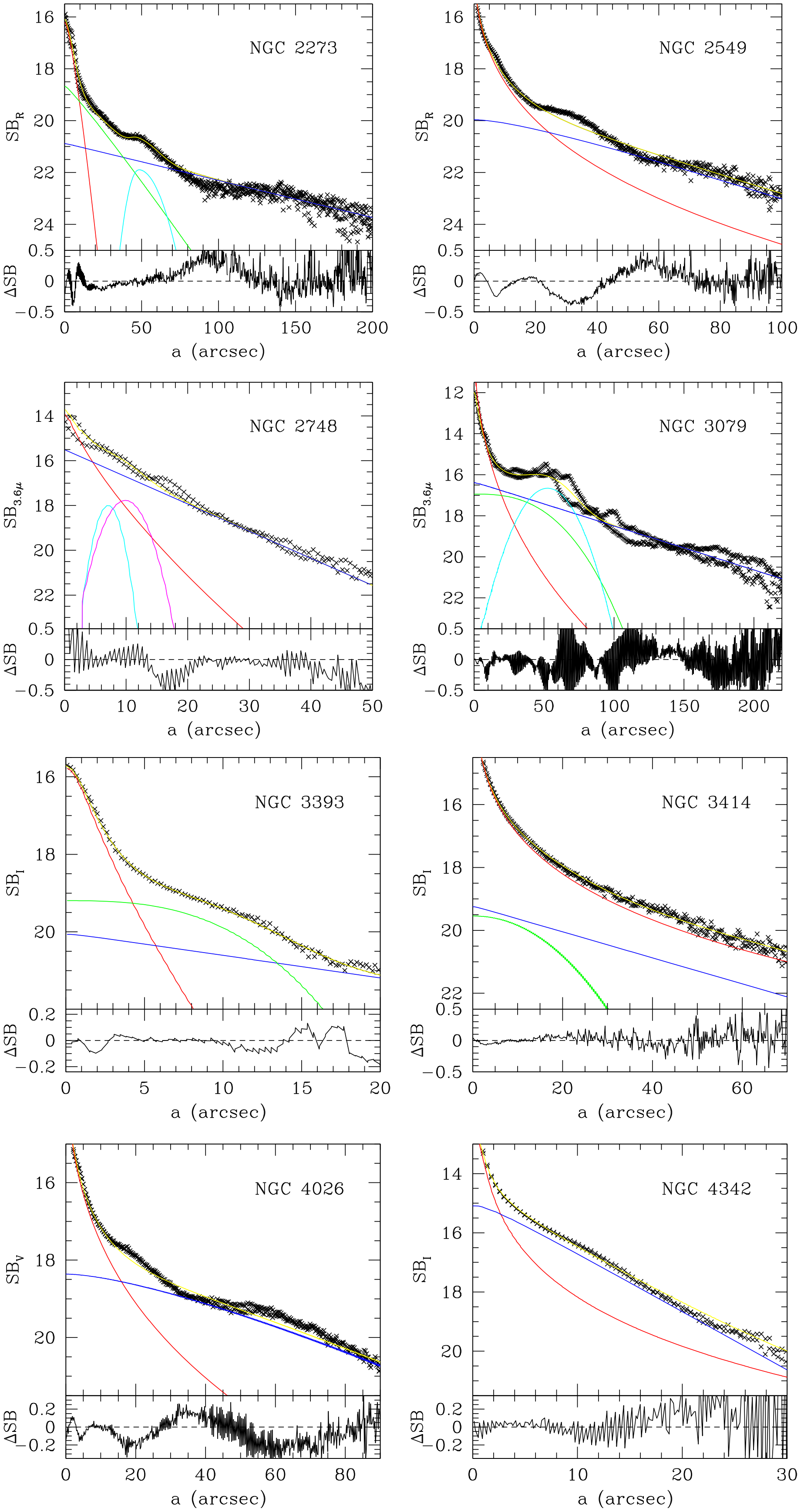

Figure 35. Cuts along the bulge major axis for the galaxies where we performed Imfit decompositions. For each galaxy there are two plots. At the top we show the surface brightness along the bulge major axis (crosses), the resulting point spread function (PSF)-convolved fitted profile (yellow line), and the unconvolved fitted components (red line: bulge; blue line: disk; green line: bar; cyan line: ring or spurs, magenta line: point source), as a function of the distance from the center. At the bottom we show the difference in surface brightness between measured and PSF-convolved fitted profiles.

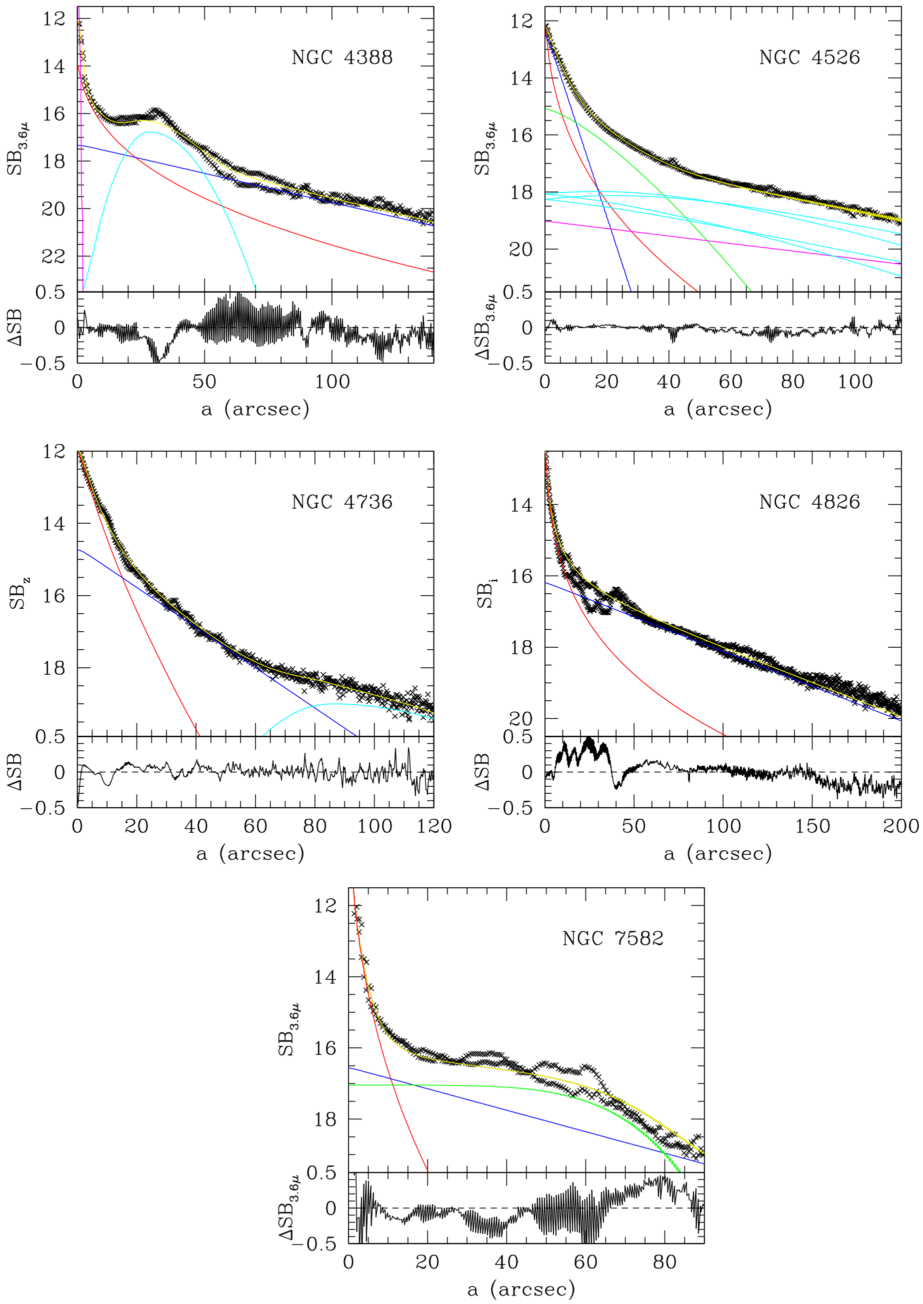

Figure 35. (Continued.)

We subtracted a model image of the disk and performed an ellipse fit on the residual image for the bulge profile. From this we derive $R_e = 31\farcs3$, while Beifiori et al. (2012) get $R_e = 4''$. The fit of Beifiori et al. (2012) fails to reproduce the photometry at large radii, where the disk dominates. Beifiori (2010) discusses an alternative fit to a K-band image of the galaxy that agrees with us. The M/L is computed as in Appendix C to match the stellar kinematic profiles of Héraudeau & Simien (1998), summing the disk and the bulge profiles (see Figure 37) and using the distance of Kormendy & Ho (2013).

NGC 4889: The Gunn r-band photometry of Jorgensen & Franx (1994) was calibrated to Cousins R using the transformation of Jordi et al. (2006) and the $(V - R)$ colors from Hyperleda. The galaxy is a core elliptical (Rusli et al. 2013a). We derive $R_e = 47\farcs1$, while Rusli et al. (2013a) quote $R_e = 169\farcs2$ fitting a $n = 9.8$ core-Sérsic profile. The difference is driven by the extrapolation (see Figure 2). The M/L_R value (scaled to the distance of Kormendy & Ho 2013) is the average of the results for four quadrants given by McConnell et al. (2012) corrected for GE. Rusli et al. (2013a) get $M/L_R = 5.8$ correcting for GE, which is the value quoted in the conclusions of McConnell et al. (2012).

NGC 5077: The surface-brightness profile comes from the observations described in Scorza et al. (1998). The M/L is scaled to the distance of Kormendy & Ho (2013), corrected for GE and converted from the B to the V band using the $(B - V)$ color from Hyperleda. We follow McConnell & Ma (2013) and Kormendy & Ho (2013) and

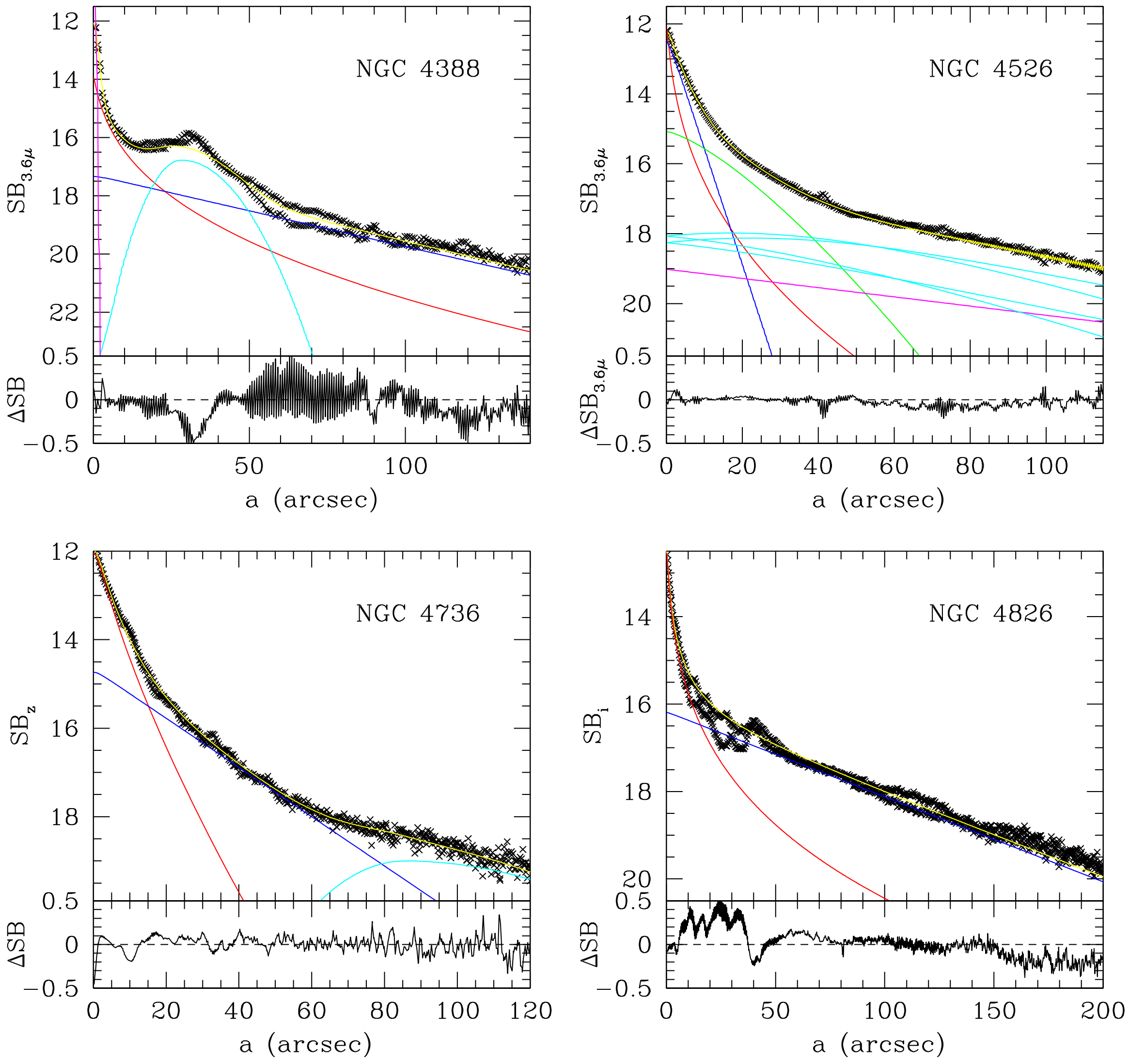

Figure 35. (Continued.)

consider the galaxy a core elliptical, even though the classification is uncertain (see discussion in Rusli et al. 2013a).

NGC 5128 (Cen A): We deprojected the multi-Gaussian expansion of the photometry profile as given in Cappellari et al. (2009) and their M/L_K scaled to the distance of Kormendy & Ho (2013). Despite the strong dust lane and the decomposition proposed by Sani et al. (2011), Cen A does not have a strong stellar disk. McConnell & Ma (2013) and Kormendy & Ho (2013) consider the galaxy a core elliptical; we accept their classification, although the strong nuclear dust makes it difficult to determine its core properties (see discussion in Rusli et al. 2013a).

NGC 5576: We used an *r*-band SDSS image calibrated to the *R* band. For this E6 galaxy we derive $R_e = 26\overset{''}{.}1$ from a profile extending to 200″, while Beifiori et al. (2012) quote 64″ fitting a Sérsic model to an image extending to 120″. Their isophotal profile (Table 3) gives $R_e = 49''$. Our result agrees with Trujillo et al. (2004). Contrary to the classification of McConnell & Ma (2013) and Kormendy & Ho (2013), the galaxy is not a core elliptical (see discussion in Rusli et al. 2013a). The M/L is corrected for GE, scaled from the *V* to the *R* band using the Hyperleda $(V - R)$ color and using the distance of Kormendy & Ho (2013).

NGC 5813: The galaxy is a core elliptical (Rusli et al. 2013a); we use their profile and M/L, scaled to the distance of Sani et al. (2011). The large discrepancy between our $R_e = 42\overset{''}{.}43$ and the values reported by Sani et al. (2011, $R_e = 98\overset{''}{.}33$) and Vika et al. (2012, $R_e = 106\overset{''}{.}8$) stem from the outer component of the galaxy (Rusli et al. 2013a).[7] The BH mass comes from the uncertain determination of Cappellari et al. (2008). We exclude this galaxy from the fits reported in Tables 36 and 37.

NGC 5845: The surface-brightness profile comes from the observations described in Scorza et al. (1998). The M/L is corrected for GE and scaled to the distance of Kormendy & Ho (2013).

NGC 5846: The galaxy is a core elliptical (Rusli et al. 2013a). We use their M/L_i and profile extending to $214\overset{''}{.}5$ from the center and measure $R_e = 89\overset{''}{.}4$. Sani et al.

---

[7] We note that Table 3 of Rusli et al. (2013a) reports wrong values for n, r_e, and μ_e. The parameters corresponding to the fits presented in their Figure 2 there are $n = 2.07$, $r_e = 55\overset{''}{.}98$, and $\mu_e = 21.57$ mag arcsec^{-2}.

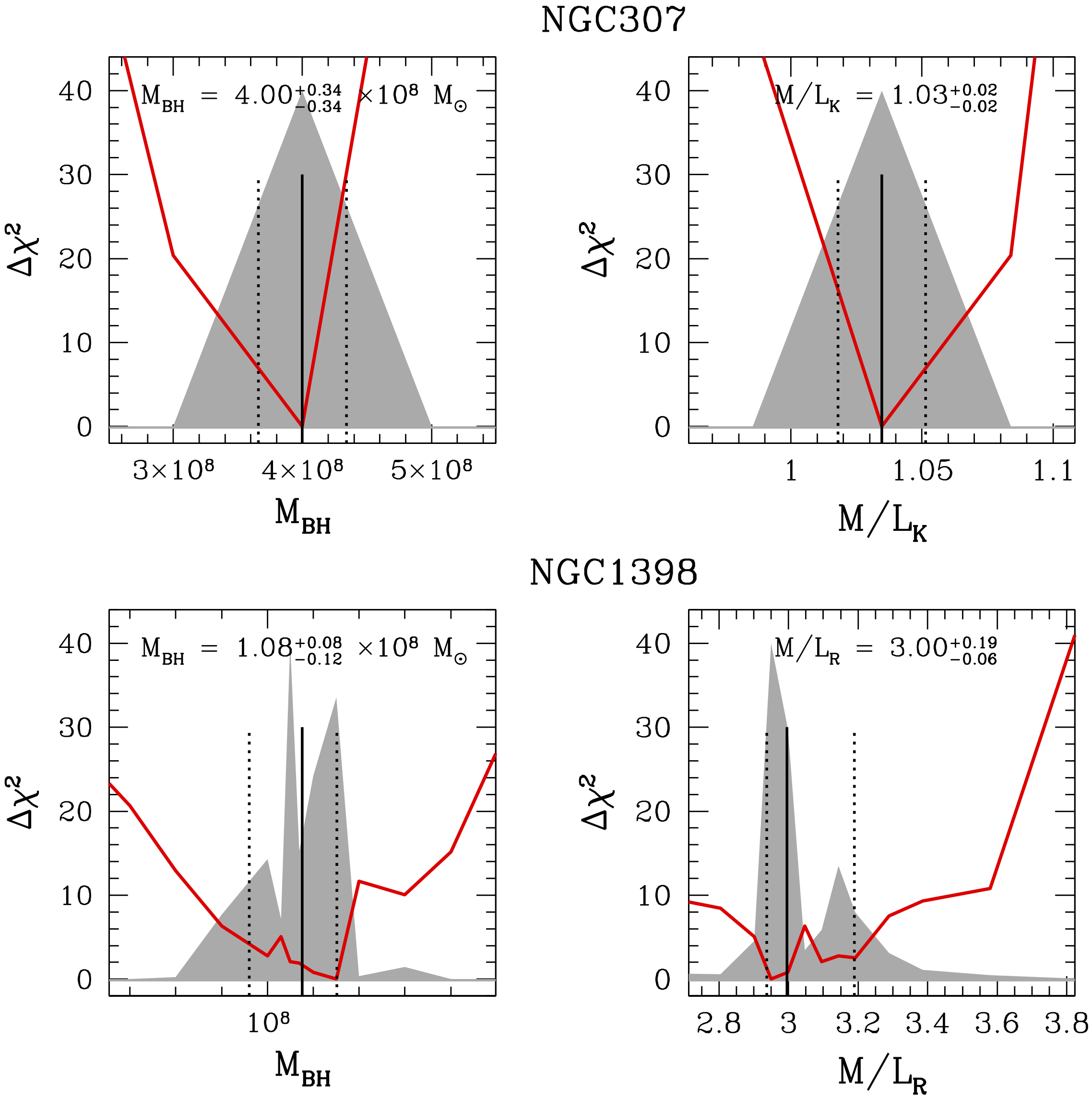

Figure 36. We show two plots for each SINFONI galaxy where we have not yet published a complete analysis of our data. The left plot shows the marginalized posterior probability P, scaled arbitrarily to a maximum value of 40 (shaded; see Equation (4) of Rusli et al. 2013b) and $\Delta\chi^2$ (red lines) versus M_{BH}; the plot to the right shows P and $\Delta\chi^2$ as functions of M/L. The vertical solid lines show the derived values; the vertical dashed lines show the 1σ errors.

(2011) derive $R_e = 36\farcs5$ by fitting (with systematic residuals) an image extending to $\approx 160''$ from the center. Laurikainen et al. (2010) perform an unrealistic bulge plus disk decomposition with $B/T = 0.46$ that delivers $R_e = 15\farcs6$. The BH mass comes from the uncertain determination of Cappellari et al. (2008). We exclude this galaxy from the fits reported in Tables 36 and 37.

NGC 6086: The galaxy is a core elliptical (Rusli et al. 2013a). We use their profile and M/L_R, scaled to the distance of Kormendy & Ho (2013), after subtracting the outer halo component fitted there.

NGC 6251: We confirm the core elliptical classification of the galaxy given by Kormendy & Ho (2013). We derive $R_e = 16\farcs5$, while Sani et al. (2011) quote $R_e = 38\farcs9$ from a Sérsic fit (with $n_{\mathrm{Ser}} = 7$) and a small central point source. The difference is driven by the different amounts of extrapolation. The M/L is corrected for GE and scaled from the R to I band using $(R - I) = 0.63$, using the distance of Kormendy & Ho (2013). There are no $(R - I)$ colors measured for this galaxy, but Hyperleda provides $(V - I)$, so we searched for elliptical galaxies with velocity dispersions and $(V - I)$ colors similar to NGC 6251 and adopted their mean $(R - I)$ value. This matches the predictions of the models of Maraston (2005) for old and metal-rich SSPs.

NGC 6264: We took the bulge plus disk decomposition of J. Kormendy (2016, in preparation), based on the r-band profile of Greene et al. (2010). The M/L is computed by fitting the Jeans equations as in Appendix C to match the average velocity dispersion measured along the minor axis ($118 \pm 10\ \mathrm{km\ s^{-1}}$) within an effective aperture radius of $1\farcs6$, with a 20% error and using the distance of Kormendy & Ho (2013). The velocity dispersion along the major axis is much higher ($166\ \mathrm{km\ s^{-1}}$) and would give an M/L almost a factor of 2 larger.

NGC 6323: We use the bulge plus bar plus disk decomposition of Greene et al. (2010). The M/L is derived as described in Appendix C by matching the velocity dispersion of Greene et al. (2010) within an effective aperture radius of

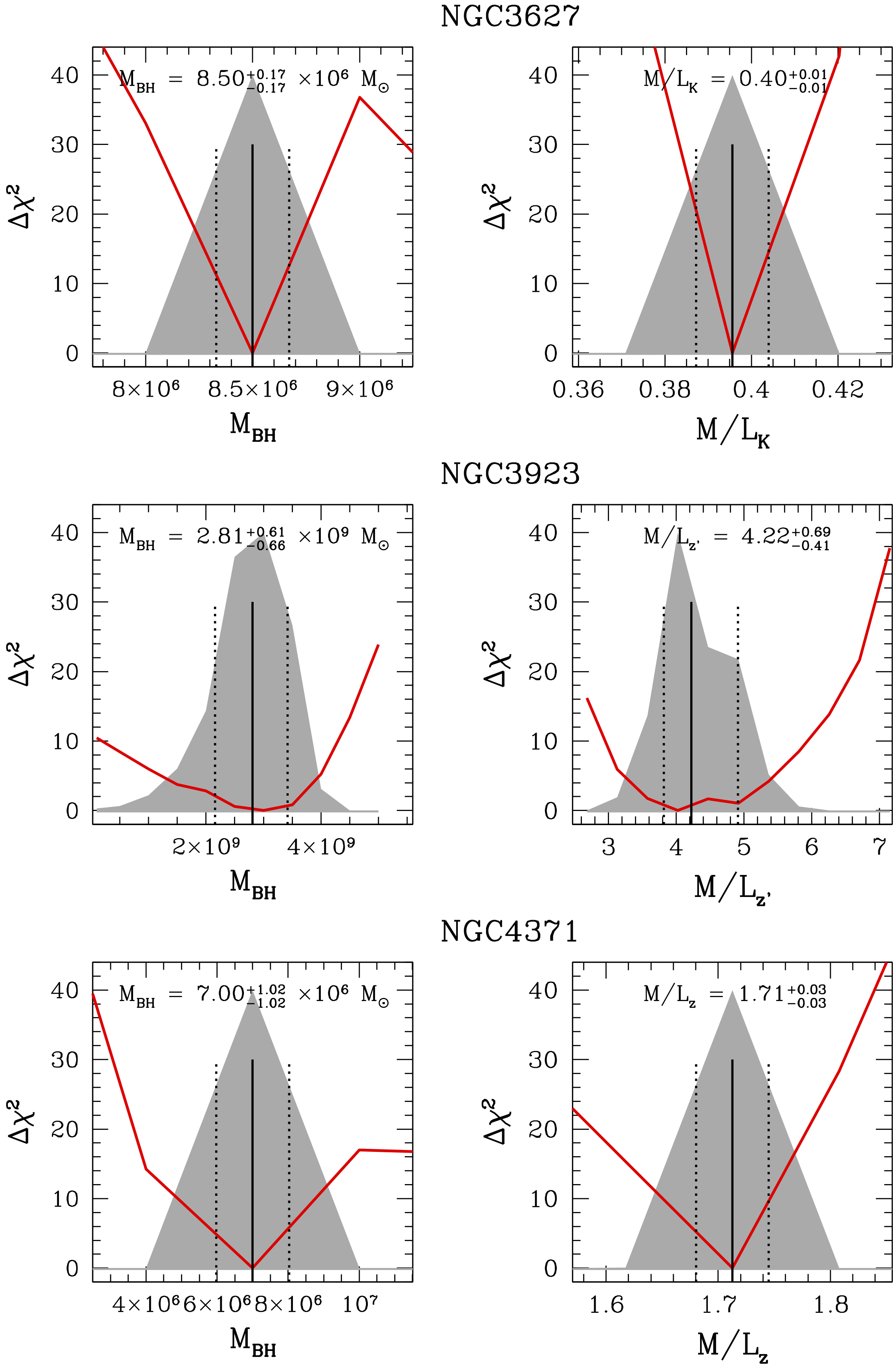

Figure 36. (Continued.)

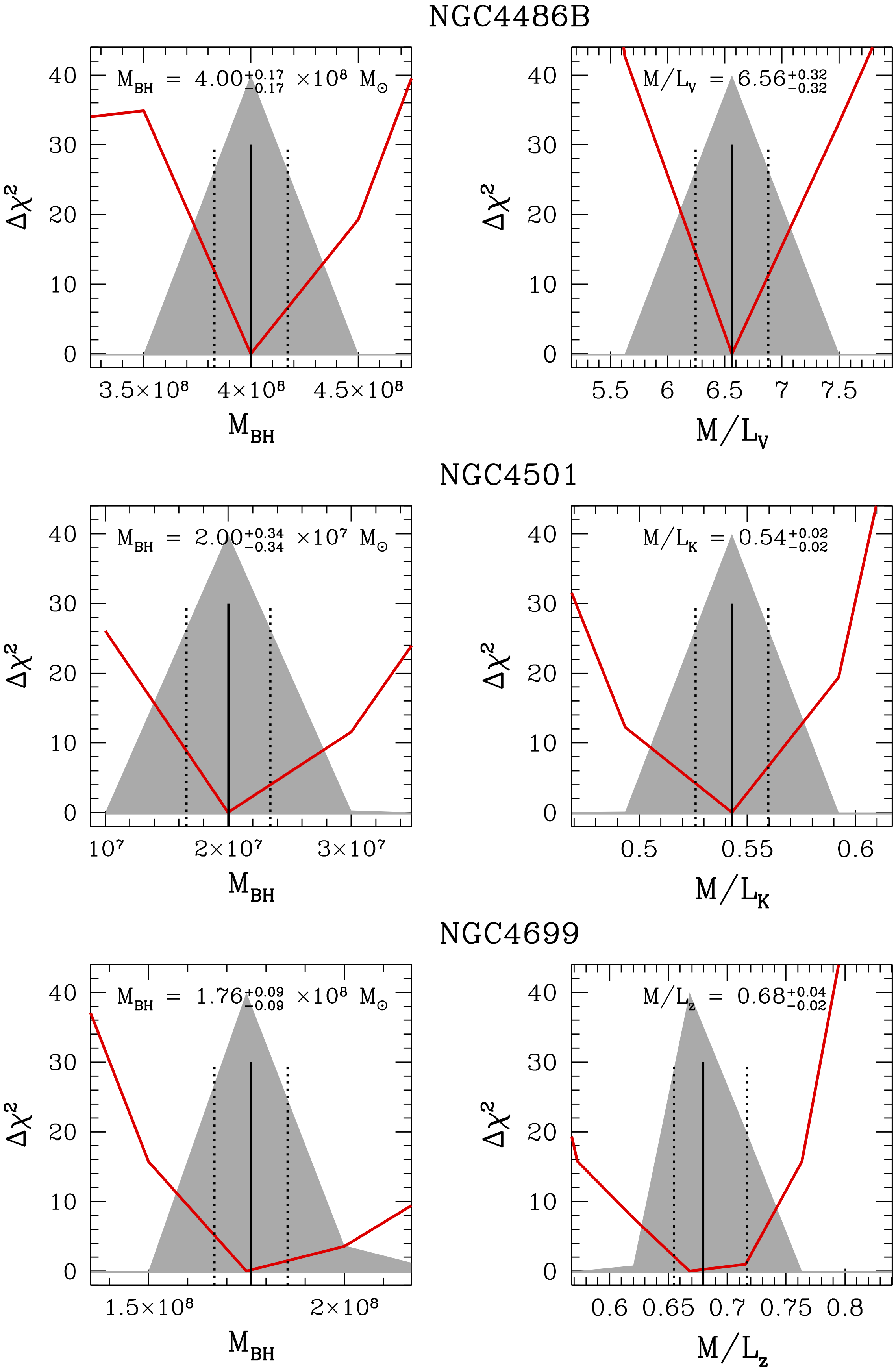

Figure 36. (Continued.)

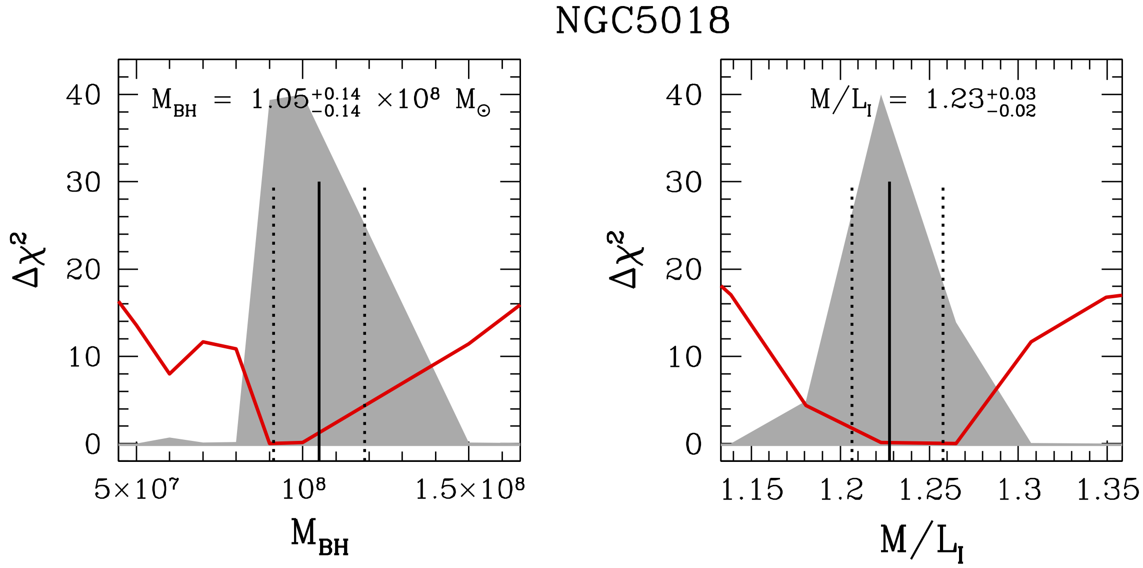

Figure 36. (Continued.)

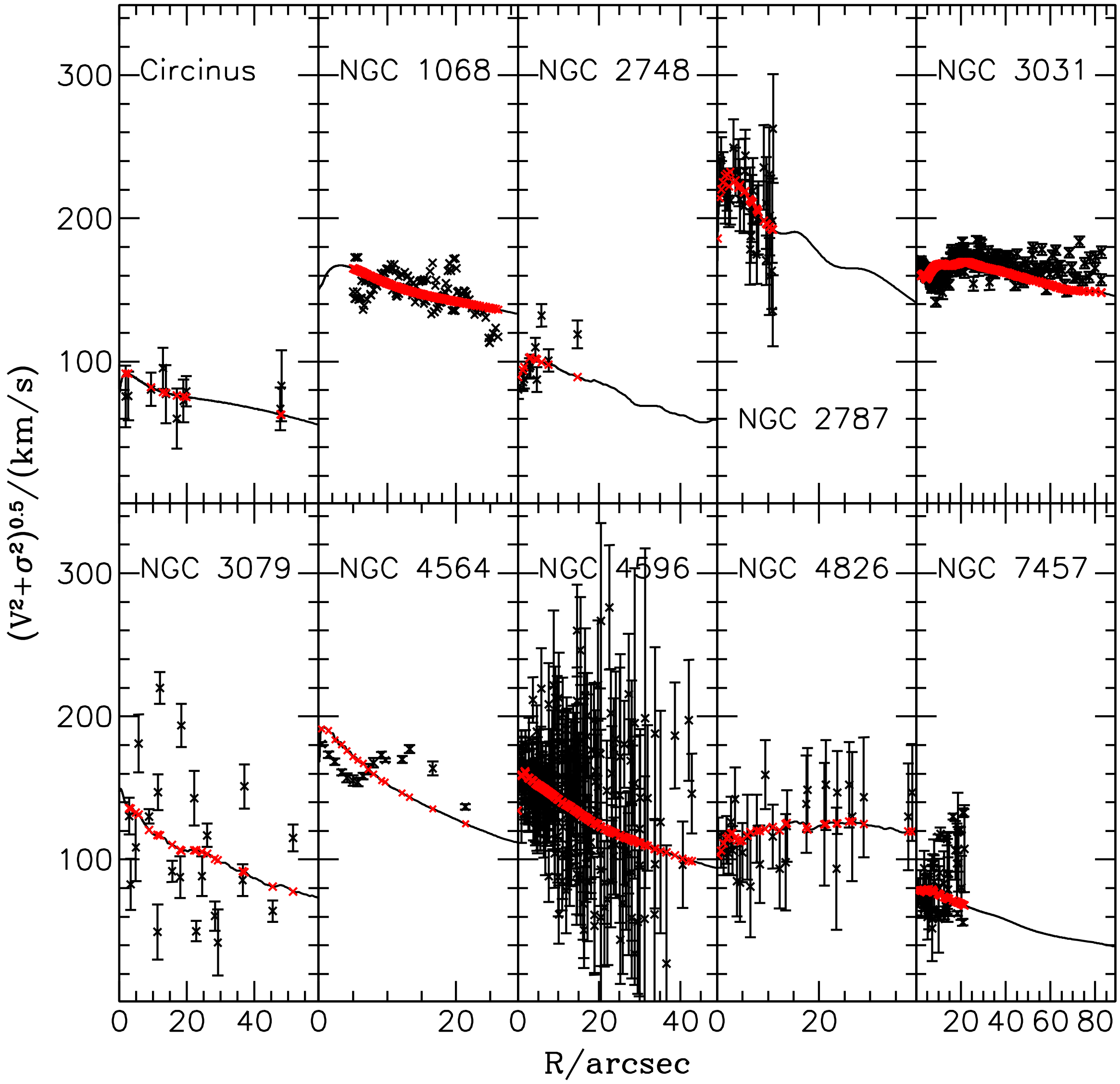

Figure 37. Spherical Jeans fits to the 10 galaxies with extended stellar kinematics, but without dynamical M/L values. The black crosses show the data points, the black line the model, and the red crosses the values of the model at the radii where data are available.

Table 35

Ratios $(M/L)_{\rm kin}/(M/L)_{\rm best}$ and $(M/L)_{\rm ap}/(M/L)_{\rm best}$ for the SINFONI Sample of Galaxies without NGC 3489 (See Appendix C)

Galaxy	$(M/L)_{\rm kin}/(M/L)_{\rm best}$	$(M/L)_{\rm ap}/(M/L)_{\rm best}$
NGC 0307	1.667	1.583
NGC 1316	1.015	0.8354
NGC 1332	0.9507	1.434
NGC 1374	1.336	1.585
NGC 1398	1.45	1.84
NGC 1407	1.618	1.627
NGC 1550	1.328	1.273
NGC 3091	1.353	1.337
NGC 3368	1.275	2.825
NGC 3627	1.35	1.447
NGC 3923	1.13	1.456
NGC 4371	1.251	1.229
NGC 4472	1.592	1.449
NGC 4486a	0.9375	0.81
NGC 4486b	1.101	1.609
NGC 4501	1.358	1.23
NGC 4699	1.467	1.451
NGC 4751	1.493	1.345
NGC 5018	1.04	0.665
NGC 5328	1.455	1.706
NGC 5419	1.33	1.2
NGC 5516	1.386	1.09
NGC 6861	1.19	0.8557
NGC 7619	1.443	1.37

$1\rlap{.}''38$ and using the distance of Kormendy & Ho (2013). In this process we summed the density contributions of the small bulge and the prominent bar. The resulting M/L (8.15 $M_\odot/L_\odot$ in the r band) is suspiciously high, which might explain the discrepancy observed in Figure 6. We classify the galaxy as barred following Graham & Scott (2013).

NGC 7052: McConnell & Ma (2013) and Kormendy & Ho (2013) consider the galaxy a core elliptical. We accept their classification, although strong nuclear dust makes it difficult to determine its core properties (see discussion in Rusli et al. 2013a). We derive $R_e = 17\rlap{.}''4$ in agreement with Läsker et al. (2014, $R_e = 18\rlap{.}''6$) and the one-component fit of Vika et al. (2012, $R_e = 15\rlap{.}''7$) and compatible with Sani et al. (2011, $R_e = 27\rlap{.}''5$), but different from the two-component fit of Vika et al. (2012, $R_e = 3''$). The M/L is scaled to the distance of Kormendy & Ho (2013) and corrected for GE.

NGC 7457: The *Spitzer* images come from Program 30318, PI Giovanni Fazio, Observer ID 2. We perform a Sérsic bulge plus exponential disk decomposition along the major axis, following Fisher & Drory (2008); the results are given in Figure 21 and Table 21. This gives $R_e = 8\rlap{.}''7$, which agrees with Erwin et al. (2015), Laurikainen et al. (2010), and Sani et al. (2011). The "classical fit" of Läsker et al. (2014) is clearly too large a bulge ($R_e = 39\rlap{.}''4$), while their multicomponent "best fit" giving $R_e = 2\rlap{.}''3$ is possibly affected by insufficient resolution (FWHM $= 1\rlap{.}''1$). The M/L is computed as in Appendix C to match the stellar kinematic profiles along the major axis of Emsellem et al. (2004), summing the bulge and the disk profiles (see Figure 37) and using the distance of Kormendy & Ho (2013).

NGC 7582: We perform a (pseudo)bulge plus bar plus disk decomposition using Imfit and the 3.6*mu* *Spitzer* image. A Sérsic bulge (function *Sérsic*), a bar (function *Sérsic_Gen-Ellipse*), and an exponential disk (function *Exponential*) were fit to the image (see Figures 34 and 35). The parameters of the fits are given in Table 33. The inclusion of a central point source does not improve the fit. The pseudobulge contributes 29% of the total light of the galaxy. The large discrepancy with the bulge luminosity and size fitted by Sani et al. (2011) stems from their inclusion in the bulge of the peanut bar present there. The M/L is computed as in Appendix C to match the velocity dispersion of Oliva et al. (1995), measured inside an equivalent $2\rlap{.}''48$ aperture radius and considering the sum of the bulge, the disk, and the bar profiles. The distance is taken from Kormendy & Ho (2013).

NGC 7768: The galaxy is a core elliptical (Rusli et al. 2013a). We use their profile and M/L, scaled to the distance of Kormendy & Ho (2013).

UGC 3789: We use the bulge-disk decomposition of J. Kormendy (2016, in preparation), based on the H-band profile of Peletier et al. (1999). The M/L is computed as in Appendix C to match the average velocity dispersion measured by Greene et al. (2010) within a radius of $1\rlap{.}''4$ (107 ± 12 km s^{-1}) and using the distance of Kormendy & Ho (2013). We classify the galaxy as barred following Graham & Scott (2013); Kormendy & Ho (2013) disagree.

B.2. *SINFONI Sample*

NGC 307: The galaxy has a classical bulge (Thomas et al. 2014; P. Erwin et al. 2016, in preparation). We set $b = 0.5$ in Table 1 since the galaxy is too edge-on to be sure about the presence or absence of a bar. We derive its BH mass in P. Erwin et al. (2016, in preparation), where we model the stellar kinematics allowing for different M/L values for the bulge and the disk components and no dark matter halo; see Figure 36. We adopt the distance derived from the Hyperleda radial velocity corrected for Local Group infall onto Virgo and $H_0 = 75$.

NGC 1316: We consider the galaxy as a merger remnant and power-law elliptical (Nowak et al. 2008). We derive its BH mass in Nowak et al. (2008).

NGC 1332: The galaxy has a prototypical classical bulge (Erwin et al. 2015). We revised our previous velocity dispersion determination of 328 km s^{-1} in Rusli et al. (2011) to 293.1 km s^{-1}. This stems from the larger half-luminosity radius for the whole galaxy ($28''$) that we use now instead of the bulge-only radius ($8\rlap{.}''4$) quoted in Rusli et al. (2011). We derive its BH mass in Rusli et al. (2011).

NGC 1374: The galaxy is a power-law elliptical (Rusli et al. 2013a). We derive its BH mass in Rusli et al. (2013b).

NGC 1398: The galaxy has a classical bulge (P. Erwin et al. 2015, in preparation). We derive its BH mass in P. Erwin et al. (2015, in preparation), where we model the stellar kinematics allowing for different M/L values for the bulge and the disk components, and no dark matter halo; see Figure 36. The distance comes from Tully et al. (2009).

NGC 1407: The galaxy is a core elliptical (Rusli et al. 2013a). We derive its BH mass in Rusli et al. (2013b).

NGC 1550: The galaxy is a core elliptical (Rusli et al. 2013a). We derive its BH mass in Rusli et al. (2013b).

NGC 3091: The galaxy is a core elliptical (Rusli et al. 2013a). We derive its BH mass in Rusli et al. (2013b). We measure $R_e = 22\rlap{.}''4$ using the profile of Rusli et al. (2013a), who get $R_e = 90''$ fitting a $n = 9.3$ core-Sérsic

Table 36

One-dimensional Correlations Derived without Galaxies NGC 2974, NGC 3079, NGC 3414, NGC 4151, NGC 4552, NGC 4621, NGC 5813, and NGC 5846

Fit	Sample	N	a	da	ZP	dZP	ϵ	$d\epsilon$	rms	r_S	$P(r_S)$
$M_{\rm BH}$–σ	All	88	5.175	0.274	−3.594	0.63	0.412	0.04	0.457	0.9111	7.33e-35
	CoreE	28	4.782	0.857	−2.499	2.102	0.351	0.068	0.379	0.6494	0.000185
	CorePowerE	42	4.696	0.48	−2.341	1.155	0.397	0.055	0.411	0.7838	8.33e-10
	CorePowerEClass	64	4.521	0.342	−1.961	0.81	0.365	0.041	0.392	0.8667	2.17e-20
	CorePowerEClassPC	70	4.864	0.333	−2.815	0.781	0.396	0.041	0.423	0.883	5.06e-24
	CorePowerEClassPCSINFONI	22	4.979	0.717	−3.032	1.714	0.501	0.092	0.446	0.7134	0.000194
	CorePowerEClassPCLit	50	4.805	0.393	−2.698	0.912	0.36	0.05	0.406	0.9051	1.88e-19
	CorePowerEClassnoBars	56	4.56	0.359	−2.026	0.855	0.352	0.044	0.388	0.8524	7.82e-17
	PowerE	14	4.052	0.939	−0.974	2.15	0.543	0.146	0.435	0.7231	0.00348
	PowerEClass	36	3.799	0.474	−0.396	1.088	0.369	0.055	0.364	0.817	1.22e-09
	PowerEClassPC	42	4.219	0.469	−1.431	1.067	0.418	0.056	0.417	0.8315	9.14e-12
	Pseudo	18	2.662	1.268	1.449	2.656	0.397	0.113	0.428	0.4556	0.0574
$M_{\rm BH}$–$M_{\rm Bu}$	All	88	0.963	0.07	−2.085	0.75	0.545	0.046	0.548	0.8503	1.07e-25
	CoreE	28	0.915	0.236	−1.418	2.744	0.442	0.078	0.431	0.5566	0.0021
	CorePowerE	42	0.991	0.118	−2.337	1.342	0.455	0.061	0.455	0.7321	3.59e-08
	CorePowerEClass	64	0.905	0.086	−1.342	0.951	0.441	0.047	0.458	0.7822	2.33e-14
	CorePowerEClassPC	70	0.864	0.067	−0.885	0.732	0.445	0.045	0.46	0.8214	3.07e-18
	CorePowerEClassPCSINFONI	22	0.943	0.119	−1.619	1.315	0.446	0.085	0.403	0.8557	3.84e-07
	CorePowerEClassPCLit	50	0.81	0.081	−0.384	0.888	0.45	0.056	0.461	0.8132	7.22e-13
	CorePowerEClassnoBars	56	0.937	0.097	−1.726	1.084	0.446	0.051	0.458	0.7616	9.38e-12
	PowerE	14	0.924	0.254	−1.681	2.744	0.604	0.167	0.484	0.5016	0.0676
	PowerEClass	36	0.809	0.142	−0.362	1.514	0.475	0.069	0.47	0.5808	0.000204
	PowerEClassPC	42	0.779	0.103	−0.033	1.087	0.474	0.063	0.468	0.6927	3.72e-07
	Pseudo	18	0.087	0.297	6.17	2.96	0.512	0.117	0.466	0.003098	0.99
$M_{\rm BH}$–$r_{\rm h}$	All	88	1.141	0.109	7.913	0.08	0.666	0.054	0.647	0.7573	1.37e-17
	CoreE	28	1.068	0.325	8.181	0.328	0.468	0.08	0.451	0.5746	0.00138
	CorePowerE	42	1.304	0.192	7.888	0.172	0.515	0.069	0.508	0.672	1.1e-06
	CorePowerEClass	64	1.014	0.133	8.139	0.101	0.546	0.055	0.545	0.702	1.02e-10
	CorePowerEClassPC	70	1.005	0.105	8.136	0.082	0.552	0.053	0.549	0.7479	1.02e-13
	CorePowerEClassPCSINFONI	22	1.092	0.199	8.26	0.171	0.597	0.112	0.514	0.8229	2.57e-06
	CorePowerEClassPCLit	50	0.945	0.123	8.071	0.092	0.54	0.063	0.538	0.7217	3.34e-09
	CorePowerEClassnoBars	56	1.085	0.156	8.074	0.127	0.55	0.061	0.545	0.6875	4.83e-09
	PowerE	14	1.159	0.423	7.809	0.267	0.714	0.19	0.571	0.3099	0.281
	PowerEClass	36	0.73	0.232	8.119	0.116	0.609	0.083	0.583	0.3441	0.0399
	PowerEClassPC	42	0.807	0.167	8.075	0.097	0.605	0.075	0.583	0.4924	0.000924
	Pseudo	18	0.035	0.345	7.044	0.149	0.522	0.121	0.464	0.01962	0.938
$M_{\rm BH}$–$\rho_{\rm h}$	All	88	−0.576	0.074	13.39	0.669	0.765	0.063	0.747	−0.6849	1.86e-13
	CoreE	28	−0.528	0.2	13.33	1.563	0.498	0.088	0.481	−0.4936	0.00761
	CorePowerE	42	−0.698	0.132	14.55	1.074	0.584	0.08	0.588	−0.5951	3.22e-05
	CorePowerEClass	64	−0.475	0.084	12.74	0.72	0.629	0.064	0.625	−0.632	2.13e-08
	CorePowerEClassPC	70	−0.495	0.068	12.89	0.603	0.641	0.062	0.635	−0.6888	4.35e-11
	CorePowerEClassPCSINFONI	22	−0.535	0.137	13.42	1.185	0.719	0.133	0.614	−0.7811	1.78e-05
	CorePowerEClassPCLit	50	−0.466	0.079	12.53	0.705	0.62	0.072	0.616	−0.6622	1.63e-07
	CorePowerEClassnoBars	56	−0.5	0.1	12.95	0.841	0.64	0.07	0.63	−0.6109	5.72e-07
	PowerE	14	−0.537	0.279	12.92	2.418	0.819	0.217	0.67	−0.2659	0.358
	PowerEClass	36	−0.223	0.135	10.3	1.238	0.674	0.092	0.647	−0.2036	0.234
	PowerEClassPC	42	−0.319	0.105	11.11	0.995	0.696	0.086	0.665	−0.3821	0.0125
	Pseudo	18	−0.008	0.17	7.111	1.647	0.518	0.117	0.465	−0.09086	0.72
$M_{\rm BH}$–$M_{\rm Bu}^{0.5}\sigma^2$	All	88	1.195	0.062	−3.626	0.619	0.415	0.038	0.441	0.9119	5.22e-35
	CoreE	28	1.162	0.225	−3.227	2.416	0.376	0.07	0.384	0.6288	0.000339
	CorePowerE	42	1.16	0.112	−3.232	1.173	0.38	0.053	0.395	0.7848	7.66e-10
	CorePowerEClass	64	1.104	0.079	−2.63	0.813	0.345	0.039	0.374	0.8578	1.39e-19
	CorePowerEClassPC	70	1.103	0.065	−2.62	0.663	0.355	0.037	0.378	0.8822	6.3e-24
	CorePowerEClassPCSINFONI	22	1.153	0.129	−3.051	1.328	0.398	0.077	0.359	0.8472	6.55e-07
	CorePowerEClassPCLit	50	1.062	0.078	−2.263	0.787	0.339	0.045	0.373	0.8959	1.56e-18
	CorePowerEClassnoBars	56	1.12	0.086	−2.8	0.891	0.349	0.043	0.38	0.8365	1.01e-15
	PowerE	14	1.074	0.224	−2.411	2.241	0.497	0.135	0.407	0.6264	0.0165
	PowerEClass	36	1.031	0.121	−1.926	1.204	0.358	0.054	0.362	0.7578	8.72e-08
	PowerEClassPC	42	1.046	0.098	−2.083	0.959	0.366	0.05	0.37	0.8148	5.16e-11
	Pseudo	18	0.41	0.379	3.287	3.463	0.489	0.118	0.452	0.2251	0.369

Table 36
(Continued)

Fit	Sample	N	a	da	ZP	dZP	ϵ	$d\epsilon$	rms	r_S	$P(r_S)$
M_{BH}–$M_{Bu}\sigma^2$	All	88	0.747	0.043	−3.183	0.657	0.458	0.04	0.471	0.8941	9.72e-32
	CoreE	28	0.732	0.154	−2.875	2.546	0.396	0.071	0.397	0.6099	0.000569
	CorePowerE	42	0.745	0.074	−3.106	1.196	0.396	0.055	0.409	0.772	2.15e-09
	CorePowerEClass	64	0.698	0.053	−2.336	0.837	0.371	0.041	0.396	0.8377	6.15e-18
	CorePowerEClassPC	70	0.683	0.043	−2.1	0.671	0.38	0.039	0.4	0.8663	3.5e-22
	CorePowerEClassPCSINFONI	22	0.728	0.079	−2.704	1.258	0.403	0.077	0.365	0.876	9.19e-08
	CorePowerEClassPCLit	50	0.651	0.052	−1.664	0.814	0.37	0.047	0.398	0.868	3.36e-16
	CorePowerEClassnoBars	56	0.715	0.061	−2.613	0.968	0.377	0.046	0.401	0.8153	2.02e-14
	PowerE	14	0.697	0.153	−2.421	2.352	0.52	0.14	0.424	0.6044	0.0221
	PowerEClass	36	0.656	0.085	−1.715	1.301	0.389	0.058	0.392	0.7261	5.37e-07
	PowerEClassPC	42	0.643	0.067	−1.515	1.006	0.398	0.053	0.397	0.794	3.51e-10
	Pseudo	18	0.165	0.24	4.714	3.392	0.508	0.118	0.459	0.06402	0.801

Note. Column 1: fit type; column 2: sample type, see Table 8; column 3: number of data points; columns 4 and 5: slope of the correlation and its error; columns 6 and 7: zero point of the correlation and its errors; columns 8 and 9: intrinsic scatter and its errors; column 10: measured scatter; column 11 and 12: Spearman coefficient and its probability.

profile. The difference is driven by the extrapolation (see Figure 2).

NGC 3368: The galaxy has a composite (classical plus pseudo) bulge (Nowak et al. 2010; Erwin et al. 2015). We derive its BH mass in Nowak et al. (2010).

NGC 3489: Following Nowak et al. (2010), the galaxy has a composite (classical plus pseudo) bulge. We use that decomposition, although it is a bit uncertain (Erwin et al. 2015). We derive its BH mass and velocity dispersion in Nowak et al. (2010) and do not compute $\sigma_{e/2}$, $\sigma^{S}_{e/2}$, σ_{e^S} in Table 17 (see discussion in Nowak et al. 2010).

NGC 3627: The galaxy has a pseudobulge (P. Erwin et al. 2016, in preparation), which we fit without the box-peanut component. We derive its BH mass in P. Erwin et al. (2016, in preparation), where we model the stellar kinematics allowing for different M/L for the bulge and the disk components and no dark matter halo; see Figure 36. We analyze its gas emission and kinematics in Mazzalay et al. (2013, 2014), from which we take the distance.

NGC 3923: The galaxy is a merger remnant (R. Bender et al. 2016, in preparation). We derive the BH mass by fitting the stellar kinematics without a dark matter halo; see Figure 36. We use the mean of the redshift-independent measurements given by NED.

NGC 4371: The galaxy has a composite (classical plus pseudo) bulge (Erwin et al. 2015). We derive its BH mass in P. Erwin et al. (2016, in preparation), where we model the stellar kinematics allowing for different M/L values for the bulge and the disk components and no dark matter halo; see Figure 36.

NGC 4472: The galaxy is a core elliptical (Rusli et al. 2013a). We derive its BH mass in Rusli et al. (2013b).

NGC 4486a: The galaxy is a power-law elliptical (Nowak et al. 2007). We derive its BH mass in Nowak et al. (2007). We derive the velocity dispersions quoted in Tables 1 and 17 using the profiles of Prugniel et al. (2011); see also Appendix A.

NGC 4486b: The galaxy is a compact elliptical (R. Bender et al. 2016, in preparation). We derive the BH mass by fitting the stellar kinematics without a dark matter halo (R. Bender et al. 2016, in preparation); see Figure 36. Our SINFONI black hole mass is 30% smaller than the value used by Kormendy & Ho (2013). We do not use it in the fits since it is the largest outlier in the correlations involving BH masses. We derive the velocity dispersions quoted in Tables 1 and 17 using the profiles of Kormendy et al. (1997) determined at distances between 1.5 and 3 arcsec from the center. This leads to a value of σ different from the one used by Kormendy & Ho (2013); see above. We use the average of the three surface-brightness fluctuation distances reported by NED.

NGC 4501: The galaxy has a pseudobulge (P. Erwin et al. 2016, in preparation). We derive its BH mass in P. Erwin et al. (2016, in preparation), where we model the stellar kinematics allowing for different M/L values for the bulge and the disk components and no dark matter halo; see Figure 36. We analyze its gas emission and kinematics in Mazzalay et al. (2013, 2014).

NGC 4699: The galaxy has a composite (classical plus pseudo) bulge (Erwin et al. 2015). We derive its BH mass in P. Erwin et al. (2016, in preparation), where we model the stellar kinematics allowing for different M/L values for the bulge and the disk components and no dark matter halo; see Figure 36.

NGC 4751: the galaxy is a power-law elliptical (Rusli et al. 2013b). We derive its BH mass in Rusli et al. (2013b), but correct the M/L, having discovered that Rusli et al. (2013b) incorrectly used the magnitude of the Sun in the V band instead of the R band.

NGC 5018: The galaxy is a power-law elliptical. See J. Thomas et al. (2016, in preparation), where we measure M_{BH} allowing for a dark matter halo as in Rusli et al. (2013b); see Figure 36. We take the Tully-Fisher mean distance of Theureau et al. (2007).

NGC 5328: The galaxy is a core elliptical (Rusli et al. 2013a). We derive its BH mass in Rusli et al. (2013b). We find $R_e = 29\farcs4$ using the profile of Rusli et al. (2013a), who get $R_e = 76\farcs8$ fitting a $n = 11.1$ core-Sérsic profile.[8] However, the difference is compatible with our estimated errors due to extrapolation.

---

[8] There is a mistake in their Table 2, where μ_b should read 16.73 instead of 17.07.

Table 37

Two-dimensional Correlations Derived without Galaxies NGC 2974, NGC 3079, NGC 3414, NGC 4151, NGC 4552, NGC 4621, NGC 5813, and NGC 5846

Fit	Sample	a	da	b	db	ZP	dZP	ϵ	$d\epsilon$	rms	$P(b \neq 0)$	ΔcAIC	RP	r_S	$P(r_S)$
M_{BH}–σ–ρ_h	All	4.521	0.315	−0.17	0.047	−0.571	1.036	0.376	0.036	0.412	0.9999	−10.69	0.005	−0.4782	2.46e-06
	CoreE	4.409	1.138	−0.106	0.196	−0.757	3.94	0.356	0.069	0.367	0.7228	2.448	3.4	−0.295	0.127
	CorePowerE	3.906	0.576	−0.246	0.109	1.537	2.05	0.367	0.052	0.369	0.9865	−2.59	0.274	−0.4889	0.00102
	CorePowerEClass	3.948	0.365	−0.179	0.054	0.917	1.165	0.328	0.037	0.35	0.9991	−8.611	0.013	−0.4624	0.00012
	CorePowerEClassPC	4.019	0.355	−0.195	0.047	0.868	1.124	0.343	0.036	0.36	0.9999	−14.76	0.001	−0.5261	2.91e-06
	CorePowerEClassPCSINFONI	3.994	0.819	−0.219	0.109	1.196	2.632	0.453	0.088	0.384	0.9734	−1.02	0.6	−0.6477	0.00112
	CorePowerEClassPCLit	4.014	0.4	−0.19	0.05	0.815	1.226	0.296	0.044	0.34	0.9994	−12	0.002	−0.4256	0.00206
	CorePowerEClassnoBars	4.081	0.407	−0.152	0.067	0.373	1.349	0.335	0.042	0.357	0.9881	−2.816	0.245	−0.4217	0.00121
	PowerE	3.545	0.963	−0.271	0.185	2.529	3.169	0.495	0.145	0.371	0.9322	1.903	2.589	−0.5473	0.0428
	PowerEClass	3.73	0.441	−0.16	0.075	1.228	1.261	0.341	0.052	0.335	0.9824	−2.027	0.363	−0.3544	0.0339
	PowerEClassPC	3.91	0.432	−0.191	0.061	1.066	1.252	0.364	0.05	0.356	0.998	−7.31	0.026	−0.4466	0.00303
	Pseudo	2.656	1.319	0.016	0.149	1.307	3.214	0.424	0.123	0.428	0.5521	3.351	5.341	−0.08566	0.735
M_{BH}–M_{Bu}–ρ_h	All	1.3	0.15	0.311	0.116	−8.467	2.572	0.534	0.046	0.536	0.9955	−4.943	0.084	0.505	5.23e-07
	CoreE	1.135	0.576	0.212	0.438	−5.624	9.905	0.449	0.081	0.436	0.6864	2.505	3.499	0.2271	0.245
	CorePowerE	1.16	0.274	0.171	0.239	−5.635	4.919	0.461	0.065	0.455	0.7693	1.94	2.637	0.2388	0.128
	CorePowerEClass	1.164	0.168	0.232	0.12	−6.198	2.797	0.441	0.048	0.447	0.9724	−1.465	0.481	0.4145	0.000661
	CorePowerEClassPC	1.128	0.15	0.228	0.11	−5.761	2.541	0.441	0.044	0.45	0.9806	−2.016	0.365	0.4739	3.42e-05
	CorePowerEClassPCSINFONI	1.301	0.252	0.296	0.185	−8.124	4.276	0.423	0.085	0.382	0.9466	0.464	1.261	0.5257	0.012
	CorePowerEClassPCLit	1.022	0.182	0.195	0.135	−4.393	3.088	0.453	0.057	0.456	0.9271	0.291	1.157	0.3678	0.0086
	CorePowerEClassnoBars	1.228	0.183	0.255	0.137	−7.123	3.088	0.435	0.051	0.449	0.9684	−1.172	0.557	0.4162	0.00142
	PowerE	1.064	0.444	0.16	0.373	−4.573	7.628	0.632	0.185	0.479	0.6838	3.861	6.893	0.2088	0.474
	PowerEClass	1.08	0.187	0.295	0.132	−5.939	2.956	0.453	0.068	0.436	0.989	−2.485	0.289	0.5151	0.00131
	PowerEClassPC	1.073	0.159	0.29	0.117	−5.828	2.619	0.445	0.06	0.44	0.9928	−3.688	0.158	0.5756	6.67e-05
	Pseudo	0.065	0.516	0.033	0.315	6.069	7.819	0.537	0.128	0.466	0.5463	3.352	5.343	0.009288	0.971
M_{BH}–σ–r_h	All	4.288	0.371	0.334	0.098	−1.662	0.832	0.381	0.036	0.414	0.9999	−9.437	0.009	0.4902	1.25e-06
	CoreE	4.374	1.305	0.184	0.398	−1.678	2.925	0.358	0.068	0.37	0.6843	2.526	3.535	0.2682	0.168
	CorePowerE	3.583	0.681	0.47	0.219	−0.044	1.508	0.37	0.053	0.374	0.9837	−2.171	0.338	0.4684	0.00176
	CorePowerEClass	3.699	0.42	0.355	0.114	−0.217	0.952	0.331	0.037	0.353	0.9987	−7.459	0.024	0.4636	0.000114
	CorePowerEClassPC	3.7	0.413	0.397	0.098	−0.262	0.938	0.343	0.036	0.361	0.9999	−14.31	0.001	0.5438	1.14e-06
	CorePowerEClassPCSINFONI	3.434	0.925	0.508	0.215	0.385	2.125	0.436	0.084	0.372	0.9885	−2.541	0.281	0.6702	0.000642
	CorePowerEClassPCLit	3.744	0.459	0.363	0.104	−0.377	1.039	0.305	0.044	0.346	0.9997	−9.84	0.007	0.4231	0.0022
	CorePowerEClassnoBars	3.85	0.49	0.305	0.144	−0.541	1.101	0.337	0.042	0.36	0.982	−2.179	0.336	0.4033	0.00205
	PowerE	3.163	1.12	0.524	0.384	0.843	2.474	0.507	0.151	0.38	0.9217	2.184	2.98	0.3011	0.296
	PowerEClass	3.469	0.474	0.314	0.153	0.297	1.075	0.343	0.052	0.337	0.9798	−1.68	0.432	0.2659	0.117
	PowerEClassPC	3.538	0.468	0.388	0.121	0.097	1.061	0.361	0.048	0.355	0.9986	−7.89	0.019	0.4198	0.00564
	Pseudo	2.709	1.357	−0.114	0.3	1.327	2.862	0.422	0.119	0.427	0.6603	3.219	4.999	−0.1063	0.675
M_{BH}–M_{Bu}–r_h	All	1.609	0.262	−0.926	0.353	−8.74	2.706	0.532	0.047	0.536	0.9955	−4.688	0.096	−0.7317	5.59e-16
	CoreE	1.342	1.035	−0.621	1.381	−5.776	10.74	0.449	0.082	0.436	0.6692	2.537	3.555	−0.4439	0.018
	CorePowerE	1.336	0.492	−0.518	0.705	−5.848	5.043	0.46	0.064	0.455	0.7712	1.91	2.598	−0.4098	0.00704
	CorePowerEClass	1.399	0.281	−0.701	0.365	−6.447	2.927	0.442	0.048	0.448	0.9743	−1.402	0.496	−0.6084	9.65e-08
	CorePowerEClassPC	1.351	0.251	−0.681	0.327	−5.921	2.608	0.441	0.045	0.45	0.9816	−2.091	0.352	−0.6483	1.3e-09
	CorePowerEClassPCSINFONI	1.6	0.42	−0.896	0.548	−8.434	4.381	0.421	0.084	0.382	0.9514	0.344	1.188	−0.7222	0.000148
	CorePowerEClassPCLit	1.218	0.308	−0.579	0.404	−4.59	3.199	0.454	0.057	0.455	0.9223	0.319	1.173	−0.6116	2.37e-06
	CorePowerEClassnoBars	1.483	0.307	−0.771	0.409	−7.344	3.189	0.434	0.052	0.449	0.9717	−1.226	0.542	−0.558	7.9e-06
	PowerE	1.204	0.799	−0.451	1.143	−4.528	8.181	0.636	0.183	0.478	0.6698	3.889	6.99	−0.4769	0.0846
	PowerEClass	1.375	0.295	−0.882	0.393	−6.207	3.073	0.453	0.067	0.435	0.9871	−2.499	0.287	−0.7027	1.77e-06

Table 37

(Continued)

Fit	Sample	a	da	b	db	ZP	dZP	ϵ	$d\epsilon$	rms	$P(b \neq 0)$	ΔcAIC	RP	r_S	$P(r_S)$
	PowerEClassPC	1.361	0.262	−0.865	0.352	−6.083	2.726	0.445	0.06	0.44	0.9934	−3.603	0.165	−0.7618	4.66e-09
	Pseudo	0.027	0.82	0.021	0.96	6.78	8.331	0.55	0.131	0.464	0.5035	3.362	5.371	0.009288	0.971
$M_{\rm BH}$–$M_{\rm Bu}$–σ	All	0.298	0.099	3.933	0.508	−3.949	0.606	0.392	0.038	0.425	0.9985	−6.793	0.033	0.5174	2.44e-07
	CoreE	0.058	0.366	4.617	1.604	−2.773	2.409	0.361	0.071	0.377	0.5656	2.714	3.885	0.1191	0.546
	CorePowerE	0.348	0.209	3.365	0.937	−3.1	1.175	0.382	0.054	0.389	0.9519	−0.323	0.851	0.4401	0.00354
	CorePowerEClass	0.33	0.123	3.254	0.582	−2.633	0.795	0.339	0.039	0.365	0.9954	−4.909	0.086	0.4953	3.16e-05
	CorePowerEClassPC	0.381	0.099	3.14	0.537	−2.954	0.69	0.347	0.037	0.371	0.9999	−12.51	0.002	0.6067	2.59e-08
	CorePowerEClassPCSINFONI	0.589	0.211	2.247	1.154	−3.045	1.397	0.409	0.081	0.359	0.9955	−4.78	0.092	0.7899	1.23e-05
	CorePowerEClassPCLit	0.314	0.111	3.377	0.618	−2.808	0.812	0.319	0.045	0.362	0.9965	−5.709	0.058	0.4788	0.000436
	CorePowerEClassnoBars	0.265	0.149	3.569	0.667	−2.649	0.896	0.34	0.042	0.37	0.9632	−0.855	0.652	0.406	0.00191
	PowerE	0.391	0.377	2.745	1.573	−2.213	2.433	0.528	0.155	0.402	0.8659	2.971	4.416	0.2596	0.37
	PowerEClass	0.286	0.158	2.986	0.631	−1.59	1.211	0.348	0.053	0.346	0.9639	−0.726	0.696	0.3532	0.0346
	PowerEClassPC	0.374	0.118	2.848	0.605	−2.241	0.965	0.363	0.05	0.362	0.9984	−7.546	0.023	0.5449	0.00019
	Pseudo	−0.219	0.287	3.068	1.523	2.769	3.091	0.423	0.122	0.423	0.7966	2.778	4.01	−0.2673	0.284

Note. Column 1: fit type; column 2: sample type, see Table 8; columns 3 and 4: first variable slope of the correlation and its error; columns 5 and 6: second variable slope of the correlation and its error; columns 7 and 8: zero point of the correlation and its errors; columns 9 and 10: intrinsic scatter and its errors; column 11: measured scatter; column 12: probability of the bivariate correlation; columns 13 and 14: ΔcAIC value and $RP = \exp(\Delta\mathrm{cAIC}/2)$ (the relative probability of the mono- and bivariate solutions); they are computed matching the bivariate solutions of this table to the monovariate solutions of Table 36 of the respective data sets. The pairings are $M_{\rm BH}$–σ–$\rho_{\rm h}$ with $M_{\rm BH}$–σ, $M_{\rm BH}$–$M_{\rm Bu}$–$\rho_{\rm h}$ with $M_{\rm BH}$–$M_{\rm Bu}$, $M_{\rm BH}$–σ–$r_{\rm h}$ with $M_{\rm BH}$–σ, $M_{\rm BH}$–$M_{\rm Bu}$–$r_{\rm h}$ with $M_{\rm BH}$–$M_{\rm Bu}$, and $M_{\rm BH}$–$M_{\rm Bu}$–σ with $M_{\rm BH}$–σ; see Section 4. Columns 15 and 16: Spearman coefficient and its probability.

NGC 5419: The galaxy is a core elliptical (see Mazzalay et al. 2016, where we measure its BH mass). We derive the distance from the radial velocity corrected for Local Group infall onto Virgo from Hyperleda using $H_0 = 72$.

NGC 5516: The galaxy is a core elliptical (Rusli et al. 2013a). Kormendy & Ho (2013) use a BH mass slightly different from our value published in Rusli et al. (2013b).

NGC 6861: The galaxy is a power-law elliptical (Rusli et al. 2013b). We derive its BH mass in Rusli et al. (2013b).

NGC 7619: The galaxy is a core elliptical (Rusli et al. 2013a). We derive $R_e = 42''$ using the profile of Rusli et al. (2013a), who get $R_e = 100''$ fitting a $n = 9.3$ core-Sérsic profile. The difference is driven by the extrapolation (see Figure 2). Kormendy & Ho (2013) use a BH mass slightly different from our value published in Rusli et al. (2013b).

APPENDIX C
M/L VALUES FROM STELLAR KINEMATICS

For a number of galaxies in Table 34, no dynamically determined M/L is available in the literature. Nevertheless, for all of these objects, stellar kinematics of some sort is available, either as stellar velocity and velocity dispersion profiles or central velocity dispersions. In these cases we determine the M/L by solving the Jeans equations for a self-consistent, isotropic, nonrotating spherical system, using the spherically deprojected surface-brightness profiles determined in Section 2. If radially extended stellar kinematics is available, we fit $\sigma_{\rm kin}(R) = \sqrt{v(R)^2 + \sigma(R)^2}$. Figure 37 shows the resulting fits for the 10 galaxies with extended kinematics. When the bulge and disk profiles are of similar luminosity in the radial range where the stellar kinematics is available, we solve the Jeans equations by summing the two deprojected contributions and determining the M/L value (equal for both components) that minimizes χ^2. The errors on M/L are computed by looking at $\chi^2 = \chi^2_{\rm min} + 1$. When only a "central" velocity dispersion is available, we select the M/L that predicts a line-of-sight velocity dispersion $\sigma_{\rm ap} = \sqrt{\langle \sigma^2 L\rangle_{\rm ap}/\langle L\rangle_{\rm ap}}$, luminosity-averaged over the effective aperture with radius $r_{\rm ap} = \sqrt{\text{slitwidth} \times \text{slitlength}/\pi}$, matching the observed value. The percentage error on M/L is twice the percentage error on the observed velocity dispersion.

This approach is a drastic simplification of the appropriate dynamical modeling of the galaxies, which would need to take into account the geometry of the objects and the dynamical effects of the central BH and dark matter halos, not to mention the presence of bars. In order to estimate how wrong our simple dynamical estimates of M/L can be, we apply both methods (i.e., $(M/L)_{\rm kin}$ from the spherical Jeans modeling of $\sqrt{V^2 + \sigma^2}$, or $(M/L)_{\rm ap}$ from modeling of the single aperture velocity dispersion) to the sample of SINFONI galaxies where we performed the full Schwarzschild modeling of the available extended stellar kinematics, deriving $(M/L)_{\rm best}$. To compute $M/L_{\rm ap}$ we consider the $\sigma_{\rm col}$ of Table 17, obtained by fitting the SINFONI collapsed spectrum. Since the SINFONI field of view is 3×3 arcsec^2, the radius of the equivalent aperture is $r_{\rm ap} = 3/\pi^{1/2} = 1.7$ arcsec.

In Table 35 we report the ratios $(M/L)_{\rm kin}/(M/L)_{\rm best}$ and $(M/L)_{\rm ap}/(M/L)_{\rm best}$. On average, our simple methods tend to overestimate the true M/L values by 40% with similar scatter (≈0.15 dex). There are no trends with $M_{\rm Bu}$, σ, $r_{\rm h}$ or $\rho_{\rm h}$.

APPENDIX D
FITS WITHOUT NGC 2974, NGC 3079, NGC 3414, NGC 4151, NGC 4552, NGC 4621, NGC 5813, NGC 5846

Tables 36 and 37 report the results of the mono- and bivariate correlations involving BH masses, excluding the galaxies NGC 2974, NGC 3079, NGC 3414, NGC 4151, NGC 4552, NGC 4621, NGC 5813, and NGC 5846, for which only uncertain BH masses are available. No significant differences with the results reported for the full sample (see Tables 11 and 12) are found.

REFERENCES

Akaike, H. 1973, in 2nd Int. Symp. on Information Theory, Information Theory and an Extension of the Maximum Liklihood Principle, ed. B. Petrov, & F. Csaki (Budapest: Akadémiai Kiadó), 267
Aller, M. C., & Richstone, D. O. 2007, ApJ, 665, 120
Arnold, J. A., Romanowsky, A. J., Brodie, J. P., et al. 2014, ApJ, 791, 80
Athanassoula, E., & Beaton, R. L. 2006, MNRAS, 370, 1499
Atkinson, J. W., Collett, J. L., Marconi, A., et al. 2005, MNRAS, 359, 504
Barway, S., & Kembhavi, A. 2007, ApJL, 662, L67
Batcheldor, D., Axon, D., Merritt, D., et al. 2005, ApJS, 160, 76
Beifiori, A. 2010, PhD thesis, Univ. Padova
Beifiori, A., Courteau, S., Corsini, E. M., & Zhu, Y. 2012, MNRAS, 419, 2497
Beifiori, A., Sarzi, M., Corsini, E. M., et al. 2009, ApJ, 692, 856
Bender, R. 1988, A&A, 193, L7
Bender, R., Saglia, R. P., & Gerhard, O. E. 1994, MNRAS, 269, 785
Bertola, F., Cinzano, P., Corsini, E. M., Rix, H.-W., & Zeilinger, W. W. 1995, ApJL, 448, L13
Bettoni, D., & Galletta, G. 1997, A&AS, 124, 61
Bonnet, H., Ströbele, S., Biancat-Marchet, F., et al. 2003, Proc. SPIE, 4839, 329
Bournaud, F., Perret, V., Renaud, F., et al. 2014, ApJ, 780, 57
Bower, G. A., Green, R. F., Bender, R., et al. 2001, ApJ, 550, 75
Cappellari, M., Bacon, R., Bureau, M., et al. 2006, MNRAS, 366, 1126
Cappellari, M., Bacon, R., Davies, R. L., et al. 2008, in IAU Symp. 245, Formation and Evolution of Bulges, ed. M. Bureau, E. Athanassoula, & B. Barbuy (Cambridge: Cambridge Univ. Press), 215
Cappellari, M., Neumayer, N., Reunanen, J., et al. 2009, MNRAS, 394, 660
Cappellari, M., Scott, N., Alatalo, K., et al. 2013, MNRAS, 432, 1709
Dalla Bontà, E., Ferrarese, L., Corsini, E. M., et al. 2009, ApJ, 690, 537
Davies, R. I., Thomas, J., Genzel, R., et al. 2006, ApJ, 646, 754
Davis, T. A., Bureau, M., Cappellari, M., Sarzi, M., & Blitz, L. 2013, Natur, 494, 328
de Francesco, G., Capetti, A., & Marconi, A. 2006, A&A, 460, 439
Dressler, A. 1989, in IAU Symp. 134, Proc. of Active Galactic Nuclei, ed. D. E. Osterbrock, & J. S. Miller (Dordrecht: Kluwer), 217
Ebisuzaki, T., Makino, J., & Okumura, S. K. 1991, Natur, 354, 212
Eisenhauer, F., Abuter, R., Bickert, K., et al. 2003, Proc. SPIE, 4841, 1548
Emsellem, E. 2013, MNRAS, 433, 1862
Emsellem, E., Cappellari, M., Krajnović, D., et al. 2007, MNRAS, 379, 401
Emsellem, E., Cappellari, M., Peletier, R. F., et al. 2004, MNRAS, 352, 721
Emsellem, E., Fathi, K., Wozniak, H., et al. 2006, MNRAS, 365, 367
Erwin, P. 2004, A&A, 415, 941
Erwin, P. 2005, MNRAS, 364, 283
Erwin, P. 2015, ApJ, 799, 226
Erwin, P., & Debattista, V. P. 2013, MNRAS, 431, 3060
Erwin, P., Pohlen, M., & Beckman, J. E. 2008, AJ, 135, 20
Erwin, P., Saglia, R. P., Fabricius, M., et al. 2015, MNRAS, 446, 4039
Erwin, P., & Sparke, L. S. 2003, ApJS, 146, 299
Erwin, P., Vega Beltrán, J. C., Graham, A. W., & Beckman, J. E. 2003, ApJ, 597, 929
Faber, S. M., Tremaine, S., Ajhar, E. A., et al. 1997, AJ, 114, 1771
Fabricius, M. H., Saglia, R. P., Fisher, D. B., et al. 2012, ApJ, 754, 67
Fan, L., Lapi, A., De Zotti, G., & Danese, L. 2008, ApJL, 689, L101
Feoli, A., & Mancini, L. 2009, ApJ, 703, 1502
Feoli, A., & Mele, D. 2005, IJMPD, 14, 1861
Ferrarese, L., & Merritt, D. 2000, ApJL, 539, L9
Fisher, D. B., & Drory, N. 2008, AJ, 136, 773
Fisher, D. B., & Drory, N. 2010, ApJ, 716, 942

Gadotti, D. A. 2008, MNRAS, 384, 420
Gebhardt, K., Bender, R., Bower, G., et al. 2000, ApJL, 539, L13
Gebhardt, K., Richstone, D., Tremaine, S., et al. 2003, ApJ, 583, 92
Gebhardt, K., & Thomas, J. 2009, ApJ, 700, 1690
Goudfrooij, P., Hansen, L., Jorgensen, H. E., et al. 1994, A&AS, 104, 179
Graham, A. W. 2008, ApJ, 680, 143
Graham, A. W., Erwin, P., Caon, N., & Trujillo, I. 2001, ApJL, 563, L11
Graham, A. W., & Scott, N. 2013, ApJ, 764, 151
Greene, J. E., Peng, C. Y., Kim, M., et al. 2010, ApJ, 721, 26
Greenhill, L. J., Moran, J. M., & Herrnstein, J. R. 1997, ApJL, 481, L23
Gültekin, K., Richstone, D. O., Gebhardt, K., et al. 2009a, ApJ, 695, 1577
Gültekin, K., Richstone, D. O., Gebhardt, K., et al. 2009b, ApJ, 698, 198
Gutiérrez, L., Erwin, P., Aladro, R., & Beckman, J. E. 2011, AJ, 142, 145
Häring, N., & Rix, H.-W. 2004, ApJL, 604, L89
Héraudeau, P., & Simien, F. 1998, A&AS, 133, 317
Ho, L. C., & Kim, M. 2014, ApJ, 789, 17
Hopkins, P. F., Hernquist, L., Cox, T. J., Robertson, B., & Krause, E. 2007a, ApJ, 669, 45
Hopkins, P. F., Hernquist, L., Cox, T. J., Robertson, B., & Krause, E. 2007b, ApJ, 669, 67
Hurvich, C., & Tsai, C.-L. 1989, Biometrika, 76, 297
Hyde, J. B., & Bernardi, M. 2009, MNRAS, 396, 1171
Jardel, J. R., Gebhardt, K., Shen, J., et al. 2011, ApJ, 739, 21
Jordi, K., Grebel, E. K., & Ammon, K. 2006, A&A, 460, 339
Jorgensen, I., & Franx, M. 1994, ApJ, 433, 553
Kelly, B. C. 2007, ApJ, 665, 1489
King, A. 2003, ApJL, 596, L27
Kondratko, P. T., Greenhill, L. J., & Moran, J. M. 2005, ApJ, 618, 618
Kormendy, J. 1993, in Proc. Mtg on the Nearest Active Galaxies, The Nearest Active Galaxies, ed. J. Beckman, L. Colina, & H. Netzer (Madrid: Consejo Superior de Investigaciones Cientificas), 197
Kormendy, J. 2013, in Secular Evolution in Disk Galaxies, ed. J. Falcón-Barroso, & J. H. Knapen (Cambridge: Cambridge Univ. Press), 1
Kormendy, J., & Bender, R. 1996, ApJL, 464, L119
Kormendy, J., & Bender, R. 1999, ApJ, 522, 772
Kormendy, J., & Bender, R. 2009, ApJL, 691, L142
Kormendy, J., & Bender, R. 2013, ApJL, 769, L5
Kormendy, J., Bender, R., & Cornell, M. E. 2011, Natur, 469, 374
Kormendy, J., Bender, R., Magorrian, J., et al. 1997, ApJL, 482, L139
Kormendy, J., Fisher, D. B., Cornell, M. E., & Bender, R. 2009, ApJS, 182, 216
Kormendy, J., & Gebhardt, K. 2001, in AIP Conf. Ser. 586, 20th Texas Symp. on Relativistic Astrophysics, ed. J. C. Wheeler, & H. Martel (Melville, NY: AIP), 363
Kormendy, J., & Ho, L. C. 2013, ARA&A, 51, 511
Kormendy, J., & Richstone, D. 1995, ARA&A, 33, 581
Krajnović, D., McDermid, R. M., Cappellari, M., & Davies, R. L. 2009, MNRAS, 399, 1839
Kronawitter, A., Saglia, R. P., Gerhard, O., & Bender, R. 2000, A&AS, 144, 53
Läsker, R., Ferrarese, L., & van de Ven, G. 2014, ApJ, 780, 69
Lauer, T. R. 2012, ApJ, 759, 64
Laurikainen, E., Salo, H., Buta, R., & Knapen, J. H. 2011, MNRAS, 418, 1452
Laurikainen, E., Salo, H., Buta, R., Knapen, J. H., & Comerón, S. 2010, MNRAS, 405, 1089
Magorrian, J., Tremaine, S., Richstone, D., et al. 1998, AJ, 115, 2285
Maiolino, R., Krabbe, A., Thatte, N., & Genzel, R. 1998, ApJ, 493, 650
Mancini, L., & Feoli, A. 2012, A&A, 537, A48
Maraston, C. 2005, MNRAS, 362, 799
Marconi, A., & Hunt, L. K. 2003, ApJL, 589, L21
Mathur, S., Fields, D., Peterson, B. M., & Grupe, D. 2012, ApJ, 754, 146
Mazzalay, X., Maciejewski, W., Erwin, P., et al. 2014, MNRAS, 438, 2036
Mazzalay, X., Saglia, R. P., Erwin, P., et al. 2013, MNRAS, 428, 2389
Mazzalay, X., Thomas, J., Saglia, R. P., et al. 2016, MNRAS, submitted
McConnell, N. J., & Ma, C.-P. 2013, ApJ, 764, 184
McConnell, N. J., Ma, C.-P., Gebhardt, K., et al. 2011, Natur, 480, 215
McConnell, N. J., Ma, C.-P., Murphy, J. D., et al. 2012, ApJ, 756, 179
McMillan, P. J. 2011, MNRAS, 414, 2446
Menci, N., Gatti, M., Fiore, F., & Lamastra, A. 2014, A&A, 569, A37
Merloni, A., Heinz, S., & di Matteo, T. 2003, MNRAS, 345, 1057
Milosavljević, M., & Merritt, D. 2001, ApJ, 563, 34
Moellenhoff, C., Matthias, M., & Gerhard, O. E. 1995, A&A, 301, 359
Naab, T., Johansson, P. H., & Ostriker, J. P. 2009, ApJL, 699, L178
Naab, T., & Trujillo, I. 2006, MNRAS, 369, 625
Nieto, J.-L., & Bender, R. 1989, A&A, 215, 266
Nieto, J.-L., Bender, R., & Surma, P. 1991, A&A, 244, L37
Nowak, N., Saglia, R. P., Thomas, J., et al. 2007, MNRAS, 379, 909
Nowak, N., Saglia, R. P., Thomas, J., et al. 2008, MNRAS, 391, 1629
Nowak, N., Thomas, J., Erwin, P., et al. 2010, MNRAS, 403, 646
Oliva, E., Origlia, L., Kotilainen, J. K., & Moorwood, A. F. M. 1995, A&A, 301, 55
Onken, C. A., Valluri, M., Peterson, B. M., et al. 2007, ApJ, 670, 105
Paturel, G., Petit, C., Prugniel, P., et al. 2003, A&A, 412, 45
Peletier, R. F. 1993, A&A, 271, 51
Peletier, R. F., Knapen, J. H., Shlosman, I., et al. 1999, ApJS, 125, 363
Peng, C. Y. 2007, ApJ, 671, 1098
Pizzella, A., Amico, P., Bertola, F., et al. 1997, A&A, 323, 349
Portail, M., Wegg, C., Gerhard, O., & Martinez-Valpuesta, I. 2015, MNRAS, 448, 713
Prugniel, P., Bica, E., Klotz, A., & Alloin, D. 1993, A&AS, 98, 229
Prugniel, P., & Heraudeau, P. 1998, A&AS, 128, 299
Prugniel, P., Zeilinger, W., Koleva, M., & de Rijcke, S. 2011, A&A, 528, A128
Rusli, S. P., Erwin, P., Saglia, R. P., et al. 2013a, AJ, 146, 160
Rusli, S. P., Thomas, J., Erwin, P., et al. 2011, MNRAS, 410, 1223
Rusli, S. P., Thomas, J., Saglia, R. P., et al. 2013b, AJ, 146, 45
Saglia, R. P., Bertin, G., Bertola, F., et al. 1993, ApJ, 403, 567
Saglia, R. P., Kronawitter, A., Gerhard, O., & Bender, R. 2000, AJ, 119, 153
Saglia, R. P., Sánchez-Blázquez, P., Bender, R., et al. 2010, A&A, 524, A6
Sandage, A., & Visvanathan, N. 1978, ApJ, 223, 707
Sani, E., Marconi, A., Hunt, L. K., & Risaliti, G. 2011, MNRAS, 413, 1479
Savorgnan, G., Graham, A. W., Marconi, A., et al. 2013, MNRAS, 434, 387
Schlegel, D. J., Finkbeiner, D. P., & Davis, M. 1998, ApJ, 500, 525
Schmitt, H. R., & Kinney, A. L. 2000, ApJS, 128, 479
Schulze, A., & Gebhardt, K. 2011, ApJ, 729, 21
Schwarz, G. 1978, AnSta, 6, 461
Scorza, C., Bender, R., Winkelmann, C., Capaccioli, M., & Macchetto, D. F. 1998, A&AS, 131, 265
Scott, N., Graham, A. W., & Schombert, J. 2013, ApJ, 768, 76
Seifert, W., & Scorza, C. 1996, A&A, 310, 75
Shaw, M., Wilkinson, A., & Carter, D. 1993, A&A, 268, 511
Sijacki, D., Vogelsberger, M., Genel, S., et al. 2015, MNRAS, 452, 575
Simien, F., & Prugniel, P. 2000, A&AS, 145, 263
Soker, N., & Meiron, Y. 2011, MNRAS, 411, 1803
Stephens, A. W., Frogel, J. A., Ortolani, S., et al. 2000, AJ, 119, 419
Theureau, G., Hanski, M. O., Coudreau, N., Hallet, N., & Martin, J.-M. 2007, A&A, 465, 71
Thomas, J., Saglia, R. P., Bender, R., et al. 2004, MNRAS, 353, 391
Thomas, J., Saglia, R. P., Bender, R., et al. 2005, MNRAS, 360, 1355
Thomas, J., Saglia, R. P., Bender, R., et al. 2009, ApJ, 691, 770
Thomas, J., Saglia, R. P., Bender, R., et al. 2011, MNRAS, 415, 545
Thomas, J., Saglia, R. P., Bender, R., Erwin, P., & Fabricius, M. 2014, ApJ, 782, 39
Trujillo, I., Erwin, P., Asensio Ramos, A., & Graham, A. W. 2004, AJ, 127, 1917
Tully, R. B., Rizzi, L., Shaya, E. J., et al. 2009, AJ, 138, 323
van den Bosch, R. C. E., Gebhardt, K., Gültekin, K., et al. 2012, Natur, 491, 729
Vika, M., Driver, S. P., Cameron, E., Kelvin, L., & Robotham, A. 2012, MNRAS, 419, 2264
Yamauchi, A., Nakai, N., Sato, N., & Diamond, P. 2004, PASJ, 56, 605
York, D. G., Adelman, J., Anderson, J., et al. 2000, AJ, 120, 1579